POLITECNICO DI MILANO

Department of Chemistry, Materials and Chemical Engineering

“Giulio Natta”

H-benzimidazoles as n-type dopants of naphtalenediimide copolymers: relationship between design, processing, and performance

Supervisor: Prof. Chiara BERTARELLI

Tutor: Prof. Chiara CASTIGLIONI

PhD Thesis of:

Simone CIMO’

Matr. No. 10341243

XXXIII PhD CYCLE

SUMMARY

0. ABSTRACT

This work aims to investigate the n-type doping mechanism of the naphthalene diimide - bithiophene copolymer P(NDI2OD-T2) by the 1H-benzimidazole dopant DiPrBI for the development of the field of organic thermoelectric applications.

The first part of this work clarifies the interactions between DiPrBI and P(NDI2OD-T2). In particular, it aims to establish whether the n-doping of P(NDI2OD-T2), by DiPrBI is a thermally activated process. The study of both spin-coated and drop-casted films of either pristine and doped samples with different annealing conditions is carried out. The analysis interestingly demonstrates that a three orders of magnitude increase of electrical conductivity, occurs before the annealing process takes place, revealing that benzimidazole-derived dopants are already active at room temperature. Furthermore, despite annealing time and temperature affect the electrical conductivity of the system, their contribution is less relevant, with the increase of electrical conductivity limited to three times. The results from the electrical characterization of the samples are supported by GIWAXS, revealing a dramatic structural change between the undoped and the just-doped not annealed P(NDI2OD-T2) films, accompanied by only minor modifications during the annealing process. Time dependent IR spectroscopy further confirms these results, showing a rise of the intensity of the characteristic polaronic band that occurs at room temperature. Finally, based on the results of density functional theory simulations, it is proposed a new doping mechanism that involves a conformational modification of the dopant molecules, triggered by the interaction with the polymer, that it is already effetive at room temperature.

In the second part of this work it is reported the design, the synthesis, and the electrical characterization of new 1H-benzimidazole dopants whose electron density is modified by chemically introducing donor or acceptor substituents to the benzimidazole moiety. According to density functional theory simulations, the newly designed dopants exhibit a higher HOMO energy level which is directly connected with the dopant effectiveness. This is confirmed by the electrical characterization of the samples that show a direct correlation between the HOMO energy level of the pristine dopant and the highest electrical conductivity achieved by doped P(NDI2OD-T2).

1. INTRODUCTION

The ever-increasing energy consumption and the subsequent carbon emission generate concerns regarding the long-term availability of natural resources and the impact of carbon emissions on global climate. The development of a successful mitigation policy requires a descriptive growth theory. [1] Growth models generally describe mid-term projection of carbon emissions and energy consumption in a top-down approach. By interpreting on a global scale macroeconomic data such as total world population, production and consumption rates of resources and gross domestic product (GDP), it is possible to obtain a good valuation of annual averages. [2]- [3] The world and the per capita energy consumption can be expressed as [4] - [5] :

Equation 1 $$\boldsymbol{e = g\left(\frac{e}{g}\right) = g\,\eta_e}$$

Equation 2 $$\boldsymbol{E = eP = G\eta_e}$$

where *e* is the annual fossil fuel consumption per capita, *E* is the annual world fossil fuel consumption, *P* is the world population, *g* is the GDP per capita, *G* is the world GDP, and η_e is the energy consumption per GDP unit defined as energy intensity factor. The fossil fuel consumption is directly connected to the carbon emission per capita as expressed by the Kaya Identity: [6].

Equation 3 $$\boldsymbol{c = g\left(\frac{e}{g}\right)\left(\frac{c}{e}\right) = g\,\eta_e\,i_c}$$

Equation 4 $$\boldsymbol{C = cP = P\,\frac{G}{P}\,\frac{E}{G}\,\frac{C}{E} = P\,g\,\eta_e i_c}$$

where *c* and *C* are the annual carbon emission per capita and the annual global carbon emission, respectively; i_c is named carbonization index, also known as “carbon footprint” and defines the quantity of CO_2 emissions per unit of spent energy. It is important to notice that although greenhouse gasses include CH_4, N_2O and CO_2, carbon emissions are always expressed as CO_2 equivalents. Greenhouse gasses are compared on the base of their global warming potential (GWP). A CO_2 equivalent is obtained by converting a given quantity of a certain gas to the amount of CO_2 with the same GWP. [7] For example: CH_4 and N_2O have 25 GWP and 298 GWP, respectively; therefore, 1 kg of CH_4 and N_2O are equivalent to 25 kg and 298 kg of CO_2, respectively (Table 1).

Common Name	**Chemical Formula**	**GWP** [8], [9]
Carbon dioxide	CO_2	1
Methane	CH_4	25
Nitrous Oxide	N_2O	298
Dimethyl Ether	CH_3OCH_3	1
Methylene Chloride	CH_2Cl_2	9
Methyl Chloride	CH_3Cl	13
Chloroform	$CHCl_3$	31
Ethane	C_2H_6	6
Propane	C_3H_8	3
Trifluoromethane	CHF_3	14800
Difluoromethane	CH_2F_2	675
Tetrafluoromethane	CF_4	7390
Fluoromethane	CH_3F	92
Hexafluoroethane	C_2F_6	12200
Octafluoropropane	C_3F_8	24000
Octafluorocyclobutane	$c\text{-}C_4F_8$	10300
1,1,1,2-tetrafluoroethane	CH_2FCF_3	1430
1,1,2-trifluoroethane	CH_2FCHF_2	353
Sulphur hexafluoride	SF_6	22800
Pentafluorodimethylether	CHF_2OCF_3	14900
Isofluorane	$CHF_2OCHClCF_3$	350
pentafluoropropanol	$CF_3CF_2CH_2OH$	42
bis(trifluoromethyl)-methanol	$(CF_3)_2CHOH$	195
Nitrogen trifluoride	NF_3	17200
Ethylene	C_2H_4	4
Propylene	C_3H_6	2
Cyclopentane	$C_{10}H_{10}$	5
Ammonia	NH_3	0

Table 1: list of some greenhouse gasses defined by the European Union in 2014. GWP is the global warming potential of each compound referred to the global warming potential of CO_2 which is defined as 1. **[8]**

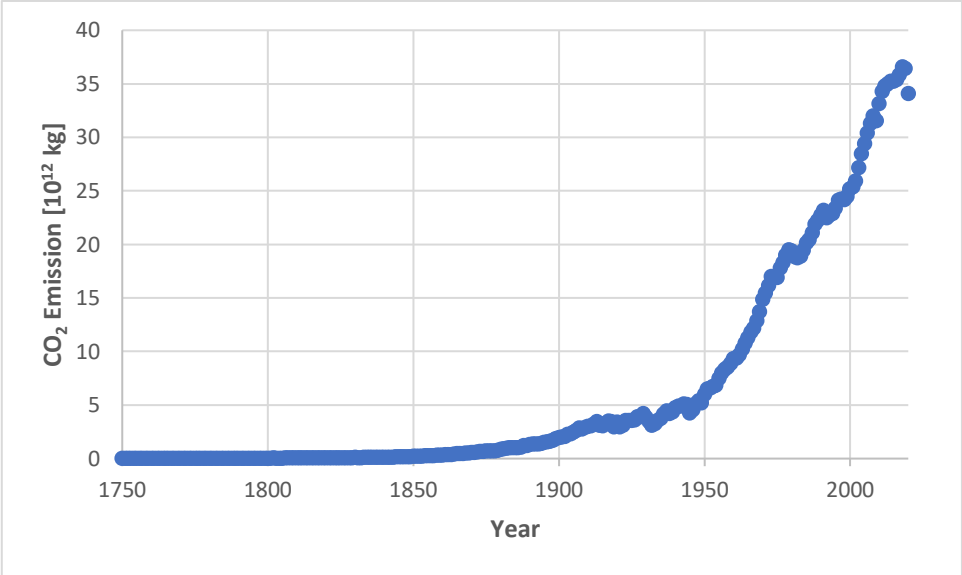

Figure 1: historical CO_2 emissions per year expressed in billions of metric tonnes. Worth to notice the sharp decrease in CO_2 emissions caused by Coronavirus pandemic in 2019-2020. **[10]**, **[11]**

According to the Paris agreement, the global response to climate change must be strengthened to maintain the world mean temperature below 2°C with respect to the pre-industrial level. [12] To achieve this goal, greenhouse gasses (GHG) emissions must be reduced at least 80% below GHG emissions of 1990 (Figure 1). [13] To achieve such GHG emission reduction goal, International Energy Agency (IEA) has proposed different strategies, which consist in the decrease of one or more factors of the Kaya identity (Equation 4). However, the first two factors (P and g) are socio-economic, and they are practically difficult to decrease. The third and fourth factors (η_e and i_c) are technologically related, and their reduction requires more efficient energy processes and the decarbonisation of energy sources, respectively. Another possibility to directly decrease C is the implementation of carbon capture and storage systems (CCS). [14], [15]

According to IEA, comparing the predicted 2025 and 2050 scenarios (Figure 2, Figure 3), it is possible to notice a remarkable decrease in the demand of fossil fuels by -31%, -57% and -27% for oil, coal and natural gas, respectively; meanwhile, an increase in the other energy sources is expected. [13] However, such decarbonization of energy sources is accompanied by a rise of around 30% in the demand of raw materials. As underlined by A. Valero et al. [16], the availability and the production rate of raw materials might hinder the development of green technologies. Indeed, the construction and the operation of renewable energy plants is associated with a cost of raw materials. It is therefore possible to define a material intensity parameter as the amount of material consumed per MW of energy produced by the power plant (

Table 2). Such parameter must be taken into consideration while elaborating predictive models. For example, according to the authors, in 2027 the global production of Ni will be insufficient to fulfil the demand of such material, hence creating a bottleneck that will slow the diffusion of carbon-free technologies. [16]

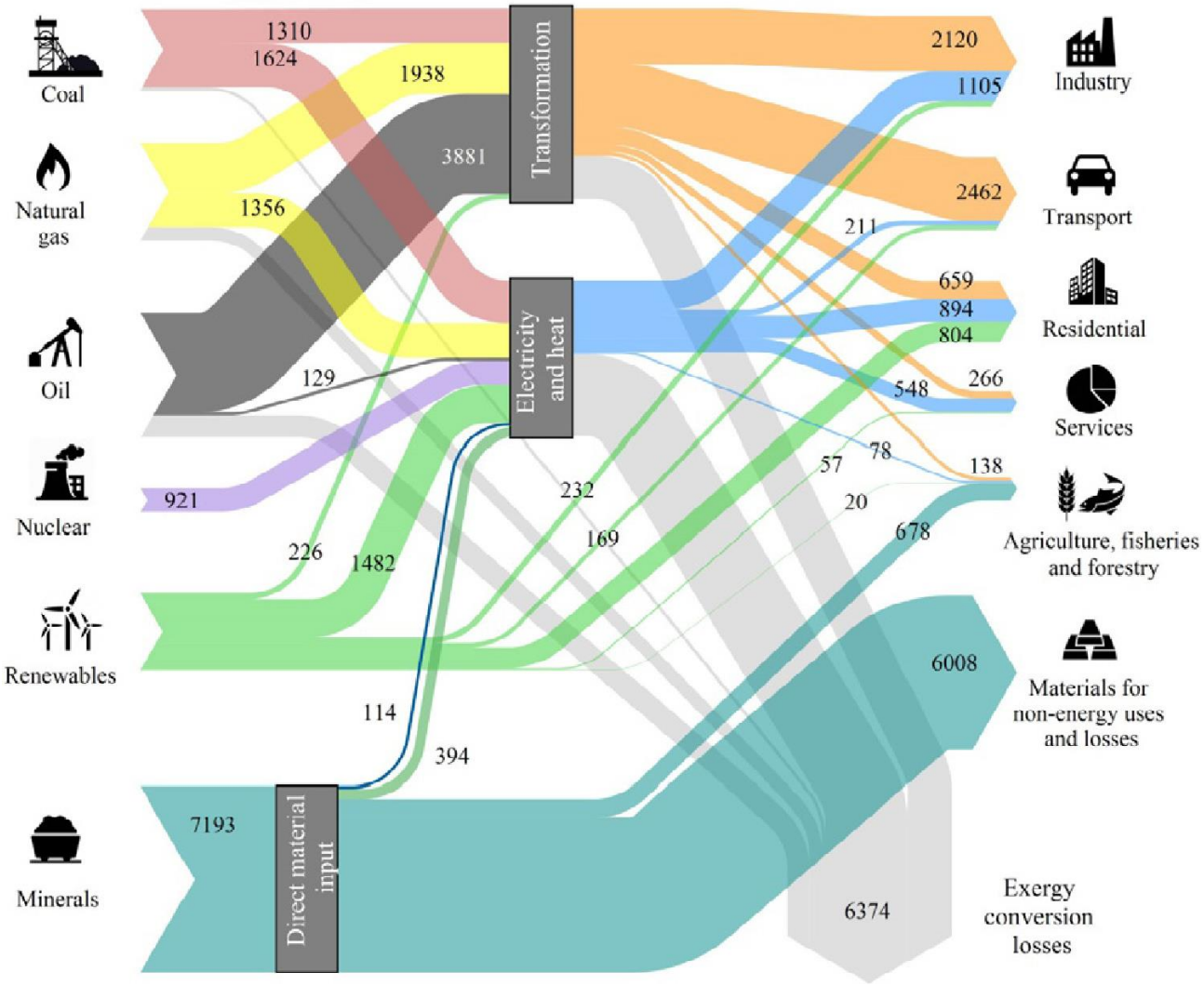

Figure 2: world energy flow predicted by International Energy Agency (IEA) for 2025. Energy path is traced from primary energy sources (on the left), through energy transformation to the end-use device final conversion (on the right). Line thickness represents the amount of energy flow. All data are expressed in Mtoe (millions of tonnes of oil equivalent, 1Mtoe ≈ 4.2 x 10^{16}J) Image adapted from **[13]**.

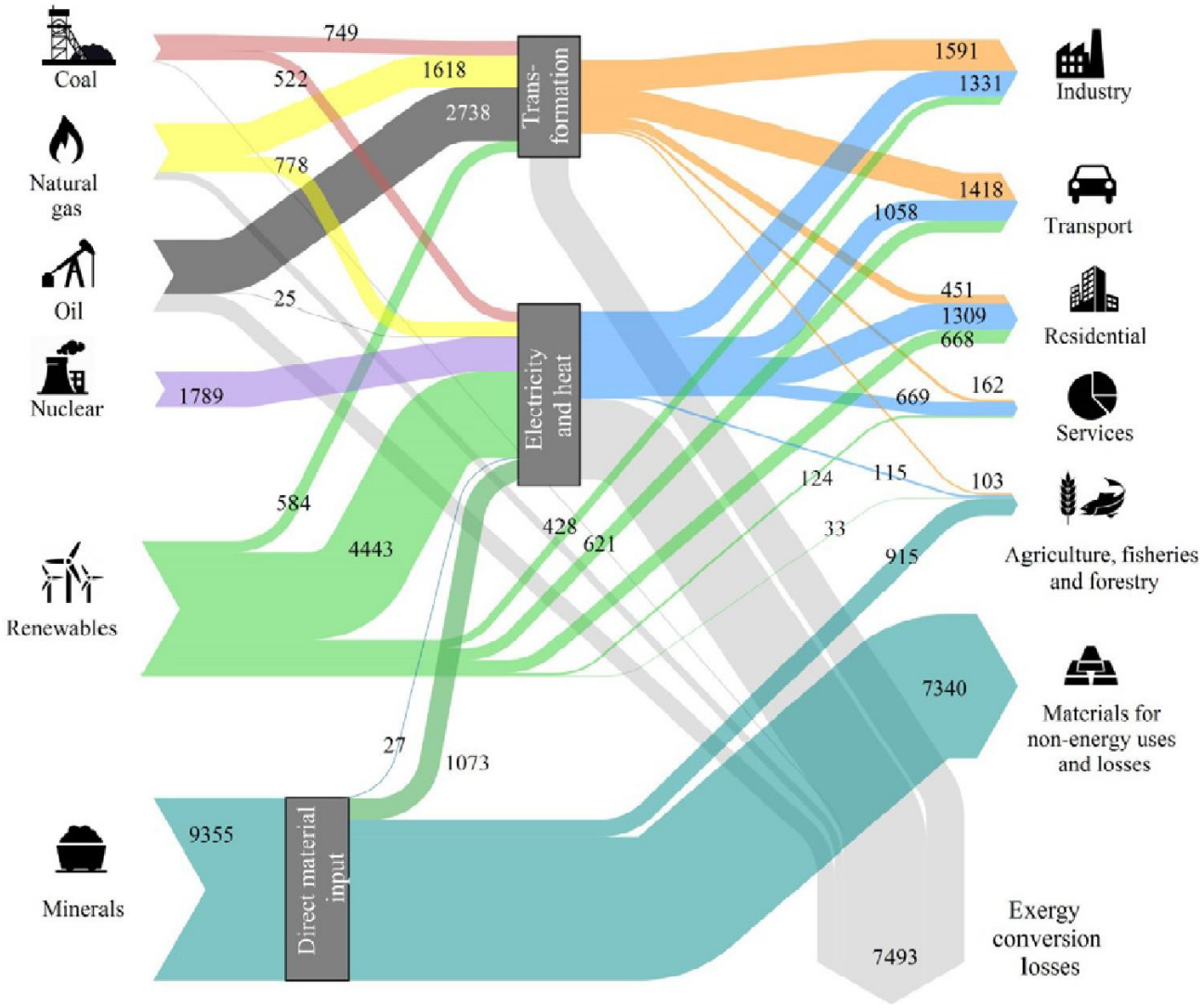

Figure 3: world energy flow predicted by IEA for 2050. Energy path is traced from primary energy sources (on the left), through energy transformation to the end-use device final conversion (on the right). Line thickness represents the amount of energy flow. All data are expressed in Mtoe (millions of tonnes of oil equivalent, 1Mtoe ≈ 4.2 x 10^{16}J) Image adapted from **[13]**.

Material	Wind	Solar			Geother.	Gas power	Nuclear	Hydro power
		PV	CSP	Thermal				
Mg		45.84	2840	149.86				
Al	784	125111	9644	228.38	6790	750	200	
Si		5377.53		1615.29				
P				14.62				
K				37.3				
Ti			15	21.2				
V			2					
Cr			2800	3249.33	200		2190	96000
Mn			3480	324.94			75.19	5760
Fe	160214	116358	851200	28390	14900	5500	58904	1242000
Ni	111	0.94	1284	162.5	240			
Cu	2060	3554	2480	2988.57	2440	750	1470	
Zn		4.29	950	4.72	110			
Ga		0.35						
Ge		0.74						
As				0.01				
Mo		9.74	141.4	162.46				
Ag		113.08	14.2					
Cd		8.54						
In		5.78						
Sn		442		0.04	3.6			
Te		7.27						
Nd	85.29							
Dy	6.80							
Pb		151,82		0.36				

Table 2: material intensity of different technologies. PV column refers to solar photovoltaic and CSP to concentration solar power. All data are reported as kg/MW. **[13]**- **[16]**

As previously discussed, the decarbonization of energy sources reduces the i_c factor of the Kaya identity (Equation 4). Traditionally, emission reduction strategies mainly focus on the change of energy supply

sources, such as swapping from fossil fuels to renewable energies or nuclear power, but this approach might be insufficient or too slow to achieve the desired objectives of the Paris agreement.

It is important to consider that to be useful for any practical human application, the energy harvested from a supply source is usually converted many times in other types of energies that are easier to store, to transport or to use. Unfortunately, since 100% efficiency is thermodynamically impossible in any process, each energy conversion step is accompanied by a remarkable energy loss (Figure 4). A huge portion of energy is transformed into thermal energy, and it is lost due to the lack of an efficient process to convert thermal energy into other types of energy [17]. By reducing energy waste, it is possible to decrease the η_e factor of the Kaya Identity (Equation 4). For this reason, thermoelectric (TE) devices, which are systems that can convert thermal energy into electricity, have gathered a lot of attention in the recent years for their potential to reduce CO_2 emissions and to provide clean energy.

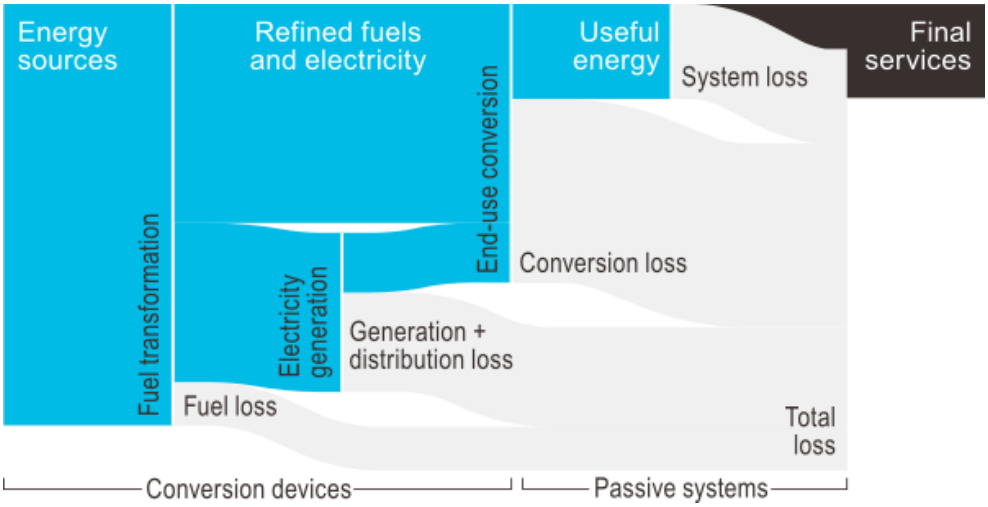

Figure 4 Path of energy and its losses. Conversion devices transform sources into more useful energy (e.g., hydroelectric power plant from potential to mechanical and then to electrical). Each conversion is associated to an energy loss. Image adapted from [18].

While a more formal description of TE materials is discussed in the next chapters, here is reported an example of how TE devices could decrease energy losses and GHG emissions.

The steel manufacturing industry requires an enormous amount of electric power and fuel. According to JFE Steel Corporation, the second biggest steel corporation in Japan, that produces around 380 million of tons of steel per year; the production of 1 ton of steel is associated with a heat waste of 10^{10} J. Therefore, every year, the company wastes around 3.8 x 10^{18} J of energy as heat during the manufacturing process. [19] In order to

decrease environmental impact, JFE Steel Corporation has applied heat-recovery technologies to its production line recovering the 0.05% of energy waste, around 1.9 x 10^{15}J per year. [19] The thermoelectric generators (TEG) applied in the reported case are based on Bi_2Te_3, measure 50 x 50 x 4.2 mm and weight 47g (Figure 5). The size of the applied TEG system is around 4m x 2m and contains 896 TEG modules distancing 2m from the steel slab whose temperature is 1188K (Figure 6). [19] The state-of-the-art TEGs available on the market for high temperature applications (i.e. T > 600°C) are mainly based on Bi_2Te_3 and on the alloy class $(GeTe)_x(AgSbTe_2)_{100-x}$, (where 80 < x < 90), commonly known as TAGS-x [20]. However, recent studies have been conducted on $BaAgAs_{0.95}Bi_{0.05}$ [21] and on $BiAgSeS_{0.97}Cl_{0.03}$ [22].

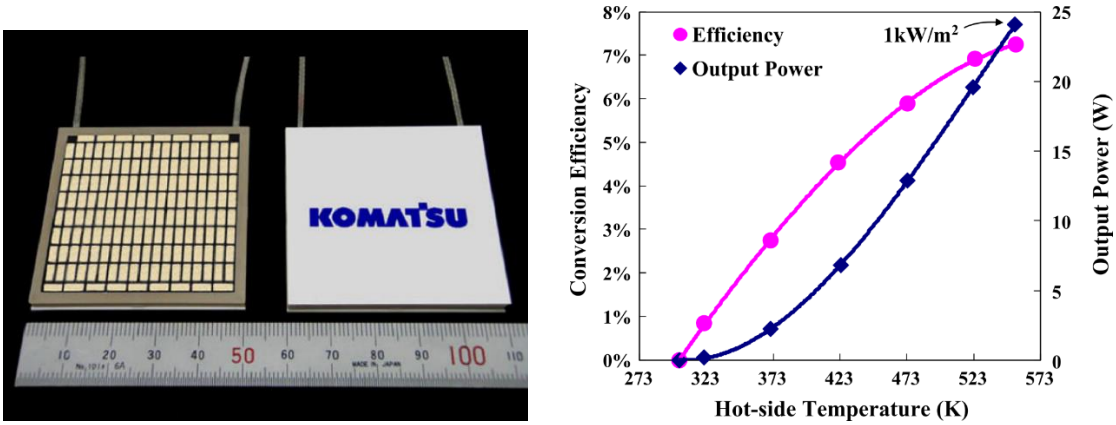

Figure 5: on the left thermoelectric generator module. On the right: Efficiency and generated power for the thermoelectric generator as a function of the hot side temperature (the cold side is kept at 303K by a water-cooled copper plate). Image adapted from **[19]**.

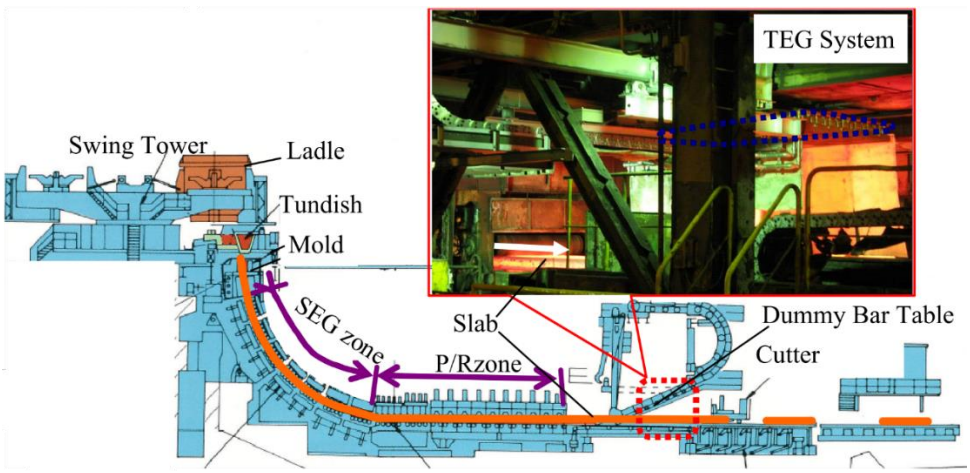

Figure 6: TE generator installed along the continuous casting line by JFT Steel Corporation. Image adapted from [19].

2. TERMOELECTRIC EFFECT

2.1 ORIGINS OF THERMOELECTRIC

In 1821, T. J. Seebeck discovered that a thermocouple, a device made by the junction of two different metals, under a temperature gradient deflects the magnet of a compass, due to the magnetic field generated by the electric current flow (Figure 7). The temperature difference acts as a driving force that makes charge carriers drifting from the hot side to the cold side of the junction. Since charge carriers carry thermal energy, Seebeck noticed that the process is accompanied by a gradual decrease of temperature of the hot side (T_h) and a gradual increase of temperature of the cold side (T_c). At the equilibrium when $T_h = T_c$, the charge carrier flow is null. This was the first observation of the coupling of electrochemical potential and temperature. [23], [24]

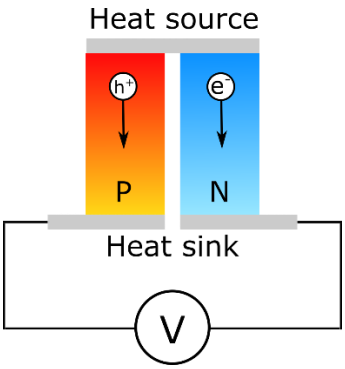

Figure 7. On the left: Thomas Johann Seebeck (1770 – 1831). Image taken from **[25]**. On the right: Seebeck effect in a thermocouple. The Seebeck voltage is related to the difference of temperature, therefore a thermocouple can be used as a thermometer. Image adapted from **[26]**.

Experimentally, Seebeck demonstrated that the current density in the circuit is given by:

Equation 5

$$\vec{\imath} = \boldsymbol{\sigma}\left(\vec{\boldsymbol{E}}_{\boldsymbol{ext}} - \boldsymbol{\alpha}\,\vec{\boldsymbol{\nabla}}\boldsymbol{T}\right)$$

where $\vec{\imath}$ is the electron current density, σ is the electrical conductivity, $\vec{E}_{ext}$ is the external electric field, T is the temperature and α is the Seebeck coefficient which is generally measured in μVK^{-1}. [27]

In 1834, J. C. A. Peltier (Figure 8) observed that a current applied across a junction of two different conductive materials results in heating or cooling of the junction. Furthermore, when the current flow is reversed, the opposite phenomenon is observed. This demonstrated the coupling between heat flux and electrical current. [28]

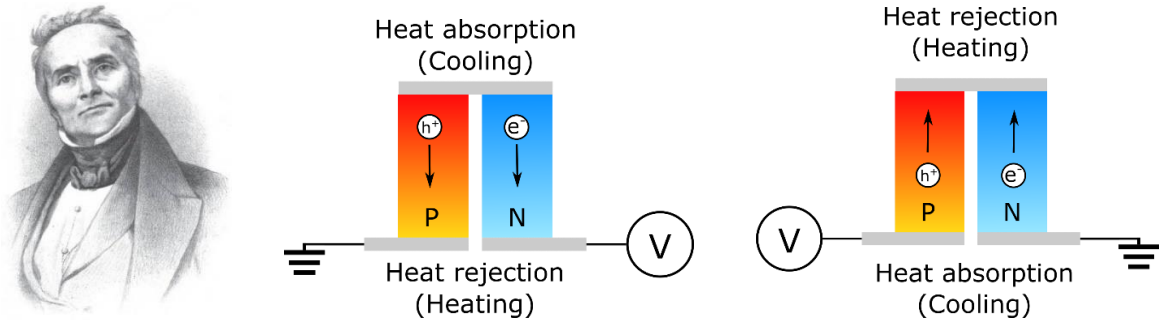

Figure 8. On the left: Jean Charles Athanase Peltier (1785 – 1845). Image taken from [25]. According to the current flow direction, the thermoelectric junction is cooled (center) or heated (right) through Peltier effect. Image adapted from [26].

Electric current is carried by electrons (e^-) in n-type materials and by holes (h^+, travelling in the opposite direction) in p-type materials. Connection of a n-type material and a p-type material is called p-n junction. When a voltage is applied in a certain direction across the p-n junction (Figure 8 center) e^- / h^+ pairs are created within the junction region and both charge carriers flow away from the junction: e^- flows into the n-type material and h^+ flows into the p-type material. Since charge carriers leave the junction, they remove thermal energy, hence, the junction is cooled. On the other hand, if the voltage is reversed, charge carriers move toward the junction and this process heats the junction (Figure 8, on the right). Experimentally, the Peltier heat per time unit generated at the junction is given by:

Equation 6

$$\dot{\vec{Q}} = (\prod_A - \prod_B)\vec{\imath}$$

where $\vec{\imath}$ is the electric current from A to B and $\prod_A$ and $\prod_B$ are the Peltier coefficients of A and B materials. [29].

Few years later, in 1855, W. Thompson demonstrated, using thermodynamics, that Seebeck and Peltier effects are not independent. [30], [31], [32]

2.2 THE ONSAGER-CALLEN THEORY

In 1931, L. Onsager provided a theoretical description of the out of equilibrium thermodynamic systems. [33], [34] Finally, 1948, H. B. Callen expanded the Onsager theory in the case of electrical and thermal coupled fluxes. [35] Onsager was awarded the Nobel prize in 1968 for "for the discovery of the reciprocal relations" [36].

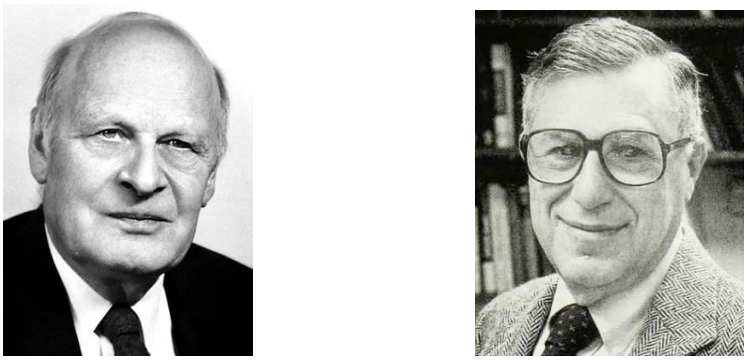

Figure 9: On the left: Lars Onsager (1903 – 1976). On the right Herbert Bernard Callen (1919 – 1993) Images taken from **[25]**.

A thermoelectric (TE) material has some analogies with a steam engine (Figure 10): [37] in both cases the entropy is carried by a fluid which, in the case of a TE material, consists in a gas of electrons, also known as Fermi gas that can be approximated to a perfect gas [38]. The electrochemical potential (μ_e) is:

Equation 7

$$\boldsymbol{\mu_e = \mu_c + eV}$$

where e is the electron charge (≈1.6 x 10^{-19}C), V is the electrical potential and μ_c is the chemical potential.

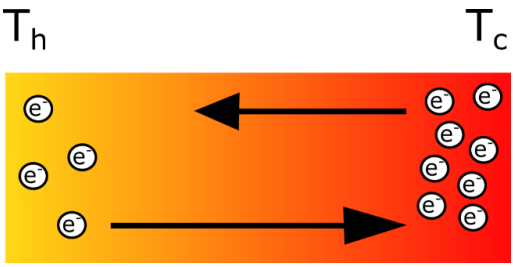

Figure 10: scheme of thermoelectric "engine". On side of the material is maintained at T_h and the other at T_c, where $T_h > T_c$. On the hot side there is a lower concentration of particles which have a higher velocity. Image adapted from **[39]**.

The two sides of the material are maintained at T_h and T_c, with $T_h > T_c$. According to simple gas kinetic theory, there is a lower density of electrons which move at high speed at the hot side, while at the cold side the electron density is higher, but the speed of the particles is lower. While $t_h \neq t_c$ the heat flows from the hot side toward the cold side and the thermodynamic system is not under equilibrium; the temperature difference is directly connected to the gradient of electron density. Furthermore, since electrons are charged particles, the temperature difference generates an electrochemical difference. Therefore, charge carriers and heat fluxes are coupled. The thermodynamical cycle can be described as a Carnot cycle with two isothermal branches and two adiabatic branches. The sources of entropy are the non-adiabatic movement of charge carriers between the two sides caused by electrons colliding with the lattice and the non-isothermal heat transfers, in both cases, entropy is carried by the electrons of the Fermi gas. According to the first principle of thermodynamic, the conservation of energy imposes that:

Equation 8
$$\overrightarrow{J_E} = \overrightarrow{J_Q} + \mu_e \overrightarrow{J_N}$$

where J_E is the energy flux, J_Q is the heat flux and J_N is the particles flux. Furthermore, each of those fluxes is directly correlated to the gradient of its thermodynamic potential that acts as a driving force. In the case of a Fermion gas, the potentials are:

Equation 9
$$\overrightarrow{F_N} = \vec{\nabla}\left(-\frac{\mu_e}{T}\right) \quad \text{for particles}$$

Equation 10
$$\overrightarrow{F_E} = \vec{\nabla}\left(\frac{1}{T}\right) \quad \text{for energy}$$

From Equation 9 and Equation 10 it is possible to get the transport of particles and energy as two coupled equations [40]:

Equation 11
$$\begin{bmatrix}\overrightarrow{J_N}\\ \overrightarrow{J_E}\end{bmatrix} = \begin{bmatrix}L_{NN} & L_{NE}\\ L_{EN} & L_{EE}\end{bmatrix}\begin{bmatrix}\vec{\nabla}\left(-\frac{\mu_e}{T}\right)\\ \vec{\nabla}\left(\frac{1}{T}\right)\end{bmatrix}$$

Under the assumption of minimal entropy production during out-of-equilibrium conditions, and in the absence of external magnetic field, it is possible to consider $L_{NE} = L_{EN}$ [41]. The symmetry of the elements on the anti-diagonal of the matrix also agrees with the Le Châtelier principle. It is also possible to express Equation 11 using J_Q instead of J_E. From Equation 8 [39]:

Equation 12
$$\begin{bmatrix}\overrightarrow{J_N}\\ \overrightarrow{J_Q}\end{bmatrix} = \begin{bmatrix}L_{11} & L_{12}\\ L_{21} & L_{22}\end{bmatrix}\begin{bmatrix}-\frac{1}{T}\vec{\nabla}(\mu_e)\\ \vec{\nabla}\left(\frac{1}{T}\right)\end{bmatrix}$$

where:
$$L_{11} = L_{NN}$$

$$L_{12} = L_{21} = L_{NE} - \mu_e L_{NN}$$

$$L_{22} = L_{EE} - \mu_e(L_{EN} + L_{NE}) + \mu_e L_{NN}$$

From Equation 12 it is now possible to derive the expressions of both coupled (Seebeck and Peltier effects) and uncoupled (Ohm's Law and Fourier Law) transport processes.

2.2.1 The Ohm's Law

The Ohm's law states that the electric current through an electrical conductor is proportional to the voltage, with a proportionality constant called resistance (the inverse of conductance). The Ohm's Law can be obtained with the Onsager-Callen theory. From Equation 12, under isothermal conditions, in the case of charged particles, the current density J can be expressed as:

Equation 13 $$\vec{J} = -e\frac{1}{T}L_{11}\vec{\nabla}(\mu_e)$$

The electric field E is obtained from the electrochemical potential:

Equation 14 $$\vec{E} = -\frac{\vec{\nabla}(\mu_e)}{e}$$

From Equation 13 and Equation 14 it is possible to obtain the Ohm's Law. And then the expression of the first Onsager Coefficient L_{11} of the conductivity matrix:

Equation 15 $$\vec{J} = e^2 L_{11}\frac{1}{T}\vec{E}$$

$$\sigma_T = e^2 L_{11}\frac{1}{T} \qquad L_{11} = \frac{T}{e^2}\sigma_T$$

2.2.2 The Fourier Law

The Fourier Law, also known as the Law of Heat Conduction, states that the heat transfer across a material is proportional to the temperature gradient. In a similar way to what previously discussed for the Ohm's Law, Fourier Law can also be obtained from the Onsager-Callen theory. To estimate the thermal conductivity, it is easier to study J_Q while imposing $J_N = 0$ (absence of any particle/charge transport)

Equation 16 $$\overrightarrow{J_N} = \vec{0} = -L_{11}\left(\frac{1}{T}\vec{\nabla}(\mu_e)\right) + L_{12}\vec{\nabla}\left(\frac{1}{T}\right)$$

$$\left(\frac{1}{T}\vec{\nabla}(\mu_e)\right) = \frac{L_{12}}{L_{11}}\vec{\nabla}\left(\frac{1}{T}\right)$$

Therefore, the heat flux J_Q can be expressed as:

Equation 17 $$\overrightarrow{J_{Q_J}} = \frac{1}{T^2}\left(\frac{L_{21}L_{12} - L_{11}L_{22}}{L_{11}}\right)\vec{\nabla}(T)$$

Therefore, the thermal conductivity k, in absence of electric current ($J_N = 0$) is:

Equation 18 $$k_J = \frac{1}{T^2}\left(\frac{L_{21}L_{12} - L_{11}L_{22}}{L_{11}}\right)$$

With a similar approach it is also possible to express the thermal conductivity in the absence of and electrochemical gradient ($J_Q = 0$):

Equation 19 $$\overrightarrow{J_{Q_E}} = \frac{L_{22}}{T^2}\vec{\nabla}(T) = k_E\,\vec{\nabla}(T) \qquad k_E = \frac{L_{22}}{T^2}$$

2.2.3 Seebeck Coefficient

As discussed in the previous section, the Seebeck coefficient is defined as the ratio between electrochemical and temperature gradients:

Equation 20 $$\alpha \equiv -\frac{1}{e}\frac{\vec{\nabla}(\mu_e)}{\vec{\nabla}(T)}$$

Therefore, it is possible to obtain an expression of the Seebeck coefficient from Equation 16 and Equation 20 connecting α to the conductivity matrix terms:

Equation 21 $$\alpha = \frac{1}{eT}\frac{L_{12}}{L_{11}}$$

According to Equation 21 α depends on the charge of the charge carrier, therefore, in a p-type (holes conducting material) the Seebeck coefficient is positive, while in a n-type material (electron conducting material) the Seebeck coefficient is negative.

2.2.4 Peltier Coefficient

The Peltier Coefficient ∏ is the coupling term between heat flux and current density. Under isothermal conditions, from Equation 13 and Equation 12:

Equation 22 $$\vec{J} = eL_{11}\left(-\frac{1}{T}\vec{\nabla}(\mu_e)\right)$$

Equation 23 $$\vec{J}_Q = eL_{21}\left(-\frac{1}{T}\vec{\nabla}(\mu_e)\right)$$

Equation 24 $$\vec{J}_Q = \frac{1}{e}\frac{L_{21}}{L_{11}}\vec{J} \qquad \vec{J}_Q = \prod \vec{J} \qquad \prod = \frac{1}{e}\frac{L_{21}}{L_{11}}$$

It is finally interesting to notice from Equation 24 and Equation 21 that the Seebeck and the Peltier effects are strongly related:

Equation 25 $$\prod = T\,\alpha$$

2.2.5 Entropy per carrier

As previously discussed, the electrons of the Fermi gas carry entropy during the thermoelectric cycle. Indeed, to the heat flux J_Q is associated an entropy flux J_S:

Equation 26 $$\vec{J}_S = \frac{\vec{J}_Q}{T} = \frac{1}{T}\left[L_{21}\left(-\frac{1}{T}\vec{\nabla}(\mu_e)\right) + L_{22}\,\vec{\nabla}\left(\frac{1}{T}\right)\right]$$

From Equation 13:

Equation 27 $$\vec{\nabla}(\mu_e) = -\vec{J}\frac{T}{eL_{11}}$$

From Equation 26 and Equation 27:

Equation 28 $$\vec{J}_S = \frac{L_{21}}{TeL_{11}}\vec{J} + \frac{1}{T}L_{22}\,\vec{\nabla}\left(\frac{1}{T}\right)$$

According to Equation 28, the entropy flux is composed of two terms, namely i) the electrochemical contribution and ii) the thermal contribution. Therefore, the amount of entropy per carrier is:

Equation 29 $$S_J = \frac{L_{21}}{TL_{11}}$$

Comparing the Equation 21, Equation 25 and Equation 29 it is also interesting to notice that there is a close relation between Seebeck coefficient, Peltier coefficient and carrier entropy:

Equation 30 $$S_J = e\alpha \qquad S_J = e\frac{\prod}{T}$$

Finally, from Equation 15, Equation 18 and Equation 29, it is possible to complete the list of all the L_{xy} coefficients of Equation 12:

Equation 31 $$L_{11} = \frac{T}{e^2}\sigma_T \qquad L_{12} = \frac{T^2}{e^2}\sigma_T S_J \qquad L_{22} = \frac{T^3}{e^2}\sigma_T {S_J}^2 + T^2 k_J$$

From Equation 19, Equation 29, Equation 30 and Equation 31, the electron thermal conductivity can be expressed as the sum of two terms:

Equation 32 $$\boldsymbol{k_E = T\,\alpha^2\,\sigma_T + k_J}$$

where k_J is a conductive term and represents the thermal conductivity associated with the electric current.

2.2.6 General conductivity matrix

Thanks to Equation 31 and Equation 32, It is now possible to rewrite Equation 12 as follows:

Equation 33 $$\begin{bmatrix}\overrightarrow{J_N}\\ \overrightarrow{J_Q}\end{bmatrix} = \begin{bmatrix}\frac{T}{e^2}\sigma_T & \frac{T^2}{e^2}\sigma_T S_J\\ \frac{T^2}{e^2}\sigma_T S_J & T^2 k_E\end{bmatrix}\begin{bmatrix}-\frac{1}{T}\vec{\nabla}(\mu_e)\\ \vec{\nabla}\left(\frac{1}{T}\right)\end{bmatrix}$$

Equation 34 $$\begin{bmatrix}\overrightarrow{J_N}\\ \overrightarrow{J_Q}\end{bmatrix} = \begin{bmatrix}\frac{T}{e^2}\sigma_T & \frac{T^2}{e^2}\sigma_T S_J\\ \frac{T^2}{e^2}\sigma_T S_J & T^3\alpha^2\sigma_T + T^2 k_J\end{bmatrix}\begin{bmatrix}-\frac{1}{T}\vec{\nabla}(\mu_e)\\ \vec{\nabla}\left(\frac{1}{T}\right)\end{bmatrix}$$

Equation 35 $$\begin{bmatrix}\overrightarrow{J_N}\\ \overrightarrow{J_Q}\end{bmatrix} = \begin{bmatrix}\frac{T}{e^2}\sigma_T & \frac{T^2}{e^2}\sigma_T S_J\\ \frac{T^2}{e^2}\sigma_T S_J & \frac{T^3 {S_J}^2\sigma_T}{e^2} + T^2 k_J\end{bmatrix}\begin{bmatrix}-\frac{1}{T}\vec{\nabla}(\mu_e)\\ \vec{\nabla}\left(\frac{1}{T}\right)\end{bmatrix}$$

From Equation 14, Equation 33 and considering that $\vec{\nabla}\left(\frac{1}{T}\right) = -\frac{1}{T^2}\vec{\nabla}(T)$:

Equation 36 $$\begin{bmatrix}\vec{J}\\ \overrightarrow{J_Q}\end{bmatrix} = \begin{bmatrix}\sigma_T & \alpha\sigma_T\\ T\alpha\sigma_T & k_E\end{bmatrix}\begin{bmatrix}\vec{\mathbf{E}}\\ -\vec{\nabla}(T)\end{bmatrix}$$

The conductivity matrix [σ] is therefore defined as:

Equation 37 $$[\sigma] = \begin{bmatrix}\sigma_T & \alpha\sigma_T\\ T\alpha\sigma_T & k_E\end{bmatrix}$$

Equation 38 $$[\sigma]_{\alpha=0} = \begin{bmatrix}\sigma_T & 0\\ 0 & k_E\end{bmatrix}$$

In Equation 37, the Seebeck coefficient α is present only on the terms of the anti-diagonal of the conductivity matrix. Therefore, in the case of α = 0 the conductivity matrix diagonalizes and the Ohm law and the Fourier law are completely decoupled (Equation 38). This gives an important meaning to the Seebeck coefficient (and to the entropy per carrier, as defined in Equation 30): it is the coupling parameter between thermal and electrical fluxes.

So far, the Onsager model only considers the electron gas and neglects any lattice contribution to the thermal conductivity. Such lattice contribution, k_L, might be added as a corrective term in the L_{22} term in the Equation 36.

Equation 39 $$\boldsymbol{k = k_E + k_L = T\,\alpha^2\,\sigma_T + k_J + k_L}$$

Equation 40 $$\begin{bmatrix} \vec{J} \\ \overrightarrow{J_Q} \end{bmatrix} = \begin{bmatrix} \sigma_T & \alpha\sigma_T \\ T\alpha\sigma_T & k \end{bmatrix} \begin{bmatrix} \vec{\mathrm{E}} \\ -\vec{\nabla}(T) \end{bmatrix}$$

2.2.7 Thermoelectric Potential

The relative current density *u* is defined as:

Equation 41 $$\boldsymbol{u \equiv -\frac{J}{k_J \nabla T}}$$

Combining Equation 32, Equation 36 and Equation 41,

Equation 42 $\vec{J} = \sigma_T \vec{\mathrm{E}} - \alpha\sigma_T\,\vec{\nabla}(T)$ and $\overrightarrow{J_Q} = T\alpha\sigma_T \vec{\mathrm{E}} - k_E \vec{\nabla}(T)$

$\sigma_T \vec{\mathrm{E}} = \vec{J} - \alpha\sigma_T\,\vec{\nabla}(T)$ therefore: $\overrightarrow{J_Q} = T\alpha\left(\vec{J} - \alpha\sigma_T\,\vec{\nabla}(T)\right) - k_E \vec{\nabla}(T)$

since: $k_E = T\,\alpha^2\,\sigma_T + k_J$

Equation 43 $$\boldsymbol{\overrightarrow{J_Q} = T\alpha\vec{J} - k_J\vec{\nabla}(T)}$$

$\overrightarrow{J_Q} = T\alpha\vec{J} - \frac{\vec{J}}{u}$ $\overrightarrow{J_Q} = \left(T\alpha - \frac{1}{u}\right)\vec{J}$ $\overrightarrow{J_Q} = \Phi^*\vec{J}$

where Φ^* was firstly defined by Snyder et al. [42] and it is called thermoelectric potential which directly connects the heat and the charge carrier fluxes, leading to a more concise description of TE process. The thermoelectric potential Φ^* allows to directly access the total entropy and heat production: $\vec{\nabla}\left(\frac{\Phi^*}{T}\right)$ and $\vec{\nabla}(\Phi^*)$, respectively. [42]

2.3 THERMOELECTRIC GENERATOR

The efficiency of a TE device is a function of the final and the initial state of the material. The efficiency is the relative change of the thermoelectric potential [42], [43]:

Equation 44 $$\boldsymbol{\eta = \frac{\Delta\Phi^*}{\Phi_h^*} = \frac{\Phi_h^* - \Phi_c^*}{\Phi_h^*} = 1 - \frac{\Phi_c^*}{\Phi_h^*}}$$

It is interesting to notice that $\Delta\boldsymbol{\Phi}^*$ is measured in Volts and it is also the voltage produced by the thermoelectric generator **[42]**.

Equation 45 $$\boldsymbol{\eta = \eta_c \eta_r}$$

where $\eta_c = \frac{T_h - T_c}{T_h}$ is the Carnot efficiency, the maximum possible efficiency in a reversible thermodynamic process. For practical issues, the most efficient process is not useful: the ideal condition $\eta = \eta_c$ can be achieved only in a reversible process that would last an infinite amount of time. The factor η_r in Equation 45 is the relative efficiency with respect to η_c ($\eta_r \leq 1$). From Equation 44 it is possible to demonstrate that the efficiency of a TE device is directly connected to a dimensionless parameter called figure of merit: [42], [40]

Equation 46 $$\boldsymbol{\eta_r = \frac{\sqrt{1+ZT}-1}{\sqrt{1+ZT}+1}}$$

Equation 47 $$\boldsymbol{ZT \equiv \frac{\alpha^2 \sigma_T}{k} T}$$

Equation 47 underlines that ZT is a key TE parameter: it relates the most important TE variables (α, σ and k) with the TE efficiency η_r. Generally, a higher ZT value is directly related to more desirable TE properties. Furthermore, the maximum output power P_{max} and the efficiency of a thermoelectric generator delivering P_{max} can be expressed as: [44]

Equation 48 $$\boldsymbol{P_{max} = \frac{1}{4} \alpha^2 \sigma_T (\Delta T)^2}$$

Equation 49 $$\boldsymbol{\eta_{P_{max}} = \frac{\eta_c}{2} \frac{ZT}{ZT+2}}$$

From Equation 46 and Equation 49 (Figure 11):

Equation 50 $$\boldsymbol{\lim_{ZT \to 0} \eta(ZT) = 0} \qquad \boldsymbol{\lim_{ZT \to \infty} \eta(ZT) = \eta_c}$$

Equation 51 $$\boldsymbol{\lim_{ZT \to 0} \eta_{P_{max}}(ZT) = 0} \qquad \boldsymbol{\lim_{ZT \to \infty} \eta_{P_{max}}(ZT) = \frac{\eta_c}{2}}$$

The curves in Figure 11 demonstrate that the difference between the maximum efficiency and the efficiency at maximum power is neglectable when ZT<1

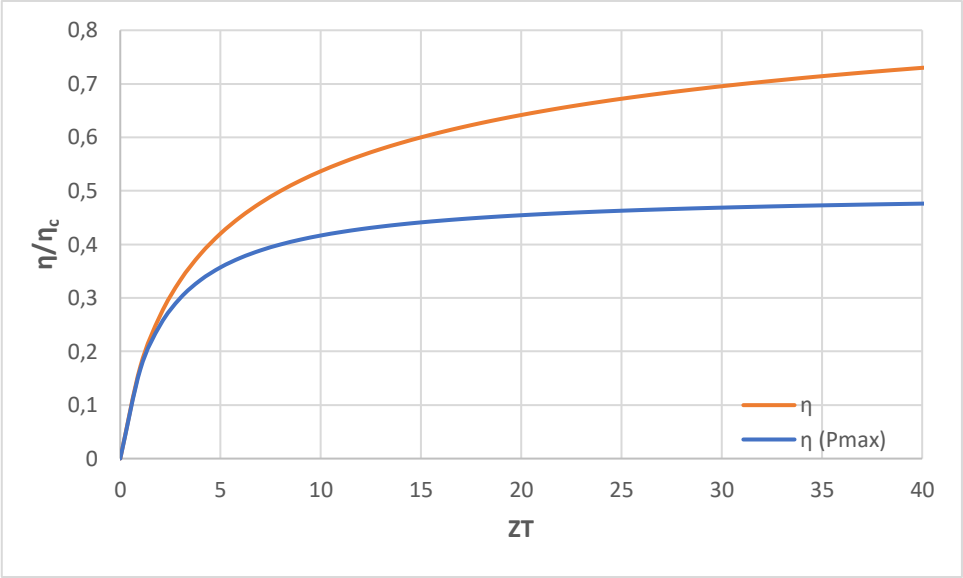

Figure 11: maximum efficiency η (orange) and efficiency at maximum power η_{Pmax} (blue), both curves are normalized over η_c

As previously discussed, thermocouples are the simplest thermoelectric devices and, since their efficiency is generally very low, they are usually implied as a cheap and simple way to measure temperature. However, by connecting multiple thermocouples electrically in series and thermally in parallel the output of the final device is increased. Such device is called thermoelectric generator (TEG, Figure 12).

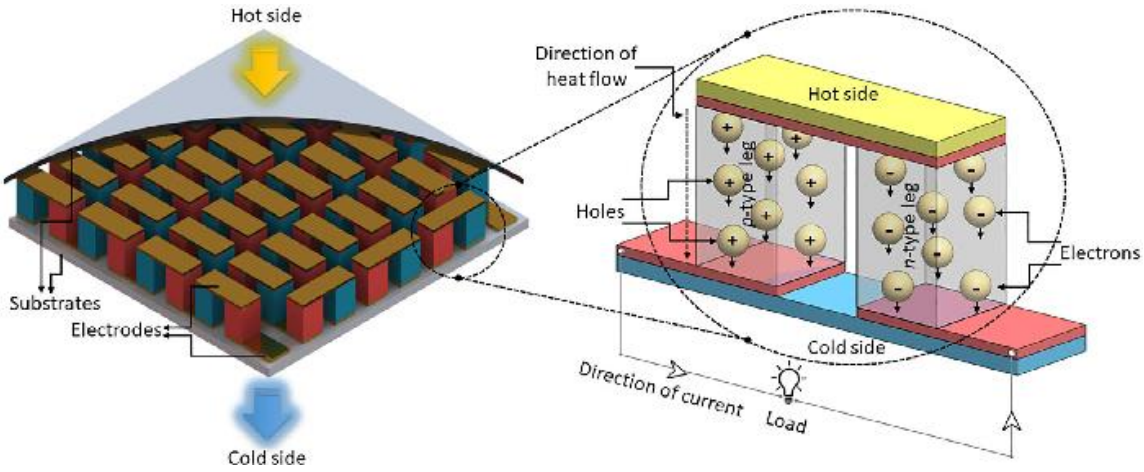

Figure 12. Thermoelectric generator: connection of multiple thermocouples thermally in parallel and electrically in series. Image adapted from [45].

2.4 INORGANIC AND ORGANIC THERMOELECTRICS

In principle, according to Equation 47 and Equation 46, to maximize TE properties, Seebeck coefficient and electrical conductivity must be maximized (i.e. PF must be maximized) while thermal conductivity must be minimized. Unfortunately, since heat is carried by both phonons and charge carriers, a good electrical conductor is usually a good heat conductor as well. For example, a metal is both a good electrical and thermal conductor (Figure 13).

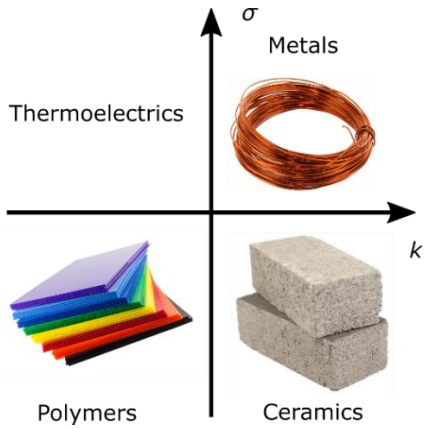

Figure 13. Coarse classification of materials as function of their electrical and thermal conductivity. To be suitable for TE application, materials must have low thermal conductivity and high electrical conductivity.

The design of a TE material requires the optimization of conflicting properties that are interrelated to material properties. An ideal TE material could be described as a phonon glass and an electron crystal. Good TE materials are therefore crystalline materials that scatter phonons without interfering with the electrical conductivity.

2.4.1 Inorganic Thermoelectric materials

According to Equation 47, ZT is a function of α, σ and k. However, these three parameters are not independent.

To maximize α, a TE material should have a single type of charge carriers: in fact, a mixed p-type and n-type conduction mechanism would result in both charge carriers be driven toward the cold side, hence reducing the induced Seebeck voltage. For metals and degenerate semiconductors (parabolic band and energy independent scattering approximation [46]), α can be described by the equations of metallic conductor

transport [47]. Materials with low charge carrier concentration usually exhibit large α (Equation 52). Seebeck coefficients are in the order of 10^{-6} VK^{-1} for metals and 10^{-3} VK^{-1} for electrical insulators:

Equation 52 $$\boldsymbol{\alpha = \frac{8\pi^2 k_b^2}{3eh^2} m^* T \left(\frac{\pi}{3n}\right)^{2/3}}$$

where n is the charge carrier concentration, m^* is the charge carrier effective mass, k_b is the Boltzmann constant (1.38×10^{-23} m^2 kg s^{-2} K^{-1}), and h is the plank constant (6.62×10^{-34} m^2 kg s^{-1}).

However, also electrical conductivity depends on charge carrier concentration, and in particular, low charge carrier concentration leads to low electrical conductivity (Equation 53):

Equation 53 $$\boldsymbol{\sigma = \frac{1}{\rho} = ne\mu}$$

where n is the charge carrier concentration, σ is the electrical conductivity, ρ is the electrical resistivity and μ is the charge carrier mobility.

Thermal conductivity (Equation 39) arises from two different sources: e^- and h^+ transporting heat (electronic thermal conductivity, k_e) and phonons moving through the lattice (lattice thermal conductivity, k_l). According to Wiedemann-Frantz law:

Equation 54 $$\boldsymbol{k = k_e + k_l}$$

Equation 55 $$\boldsymbol{\frac{k_e}{\sigma} = LT}$$

Equation 56 $$\boldsymbol{k_e = \sigma LT = ne\mu LT}$$

where k is the thermal conductivity, σ is the electrical conductivity, L is Lorentz factor (2.44×10^{-8} $W\Omega K^{-2}$ or 2.44×10^{-8} $J^2K^{-2}C^{-2}$ for free electrons) and T is the absolute temperature. Wiedemann-Frantz equation is valid under the approximation of elastic scattering. Variations to the k value occur in materials with low charge carrier concentration where the Lorentz factor is around 20% smaller than in the free electron case, and in materials that exhibit a mixed conduction which introduces a bipolar factor in the thermal conductivity expression [48]. The lowest thermal conductivities are typical of glasses. However, glasses are very poor TE materials because they lack the required electrical properties: in fact, compared to crystalline semiconductors, glasses have poor charge carrier mobility caused by higher electron scattering.

According to Equation 47, Equation 52 and Equation 53, there is a compromise between α, σ and k that must be achieved in order to maximize ZT (Figure 14). The maximum peak of ZT usually occurs at charge carrier densities around 10^{19} and 10^{21} charge carriers per cm^3. These values are typical in heavily doped semiconductor materials.

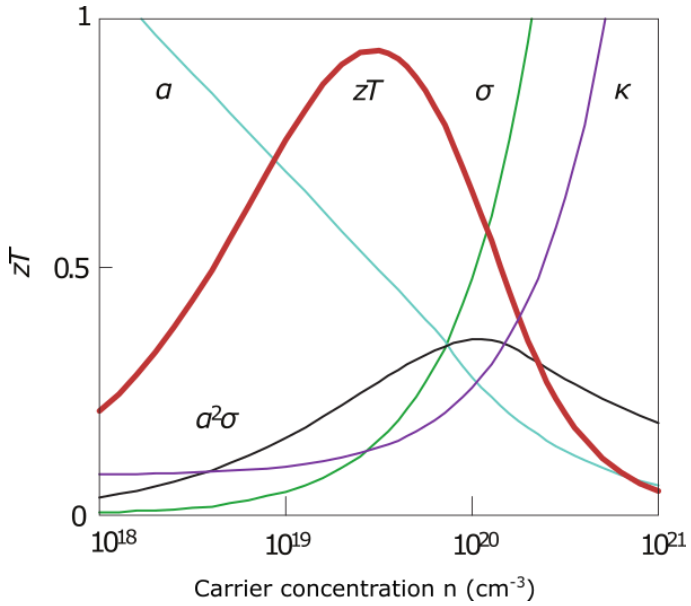

Figure 14. Thermoelectric figure of merit (ZT) as function of charge carrier concentration n. Image adapted from [48].

A lot of attention has been focussed on inorganic materials due to their generally high electrical conductivity and Seebeck coefficient. Furthermore, they are stable at high temperatures (900-1000K, Figure 15), which is ideal for massive TE energy recovery. However, the broad application of inorganic TE materials is hindered by drawbacks such as: high density, high thermal conductivity, and high cost. Common inorganic TE materials are Bi_2Te_3 [49], $CoAs_3$ [50], PbTe [51], Sb_2Te_3 [52] and other alloys [53] (Figure 16).

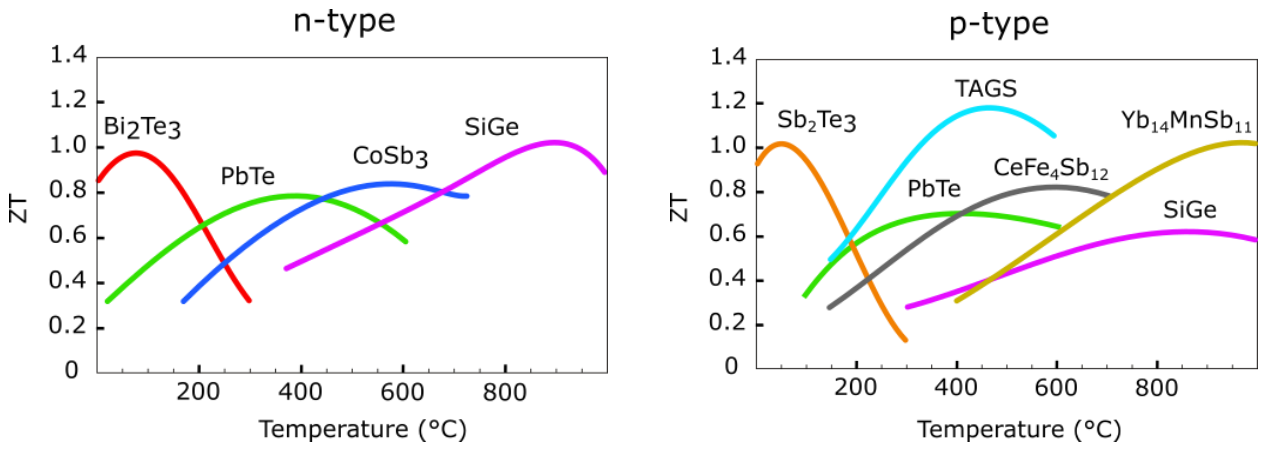

Figure 15: Figure of merit in and working temperature ranges of commercial inorganic TE materials. Image adapted from **[48]**.

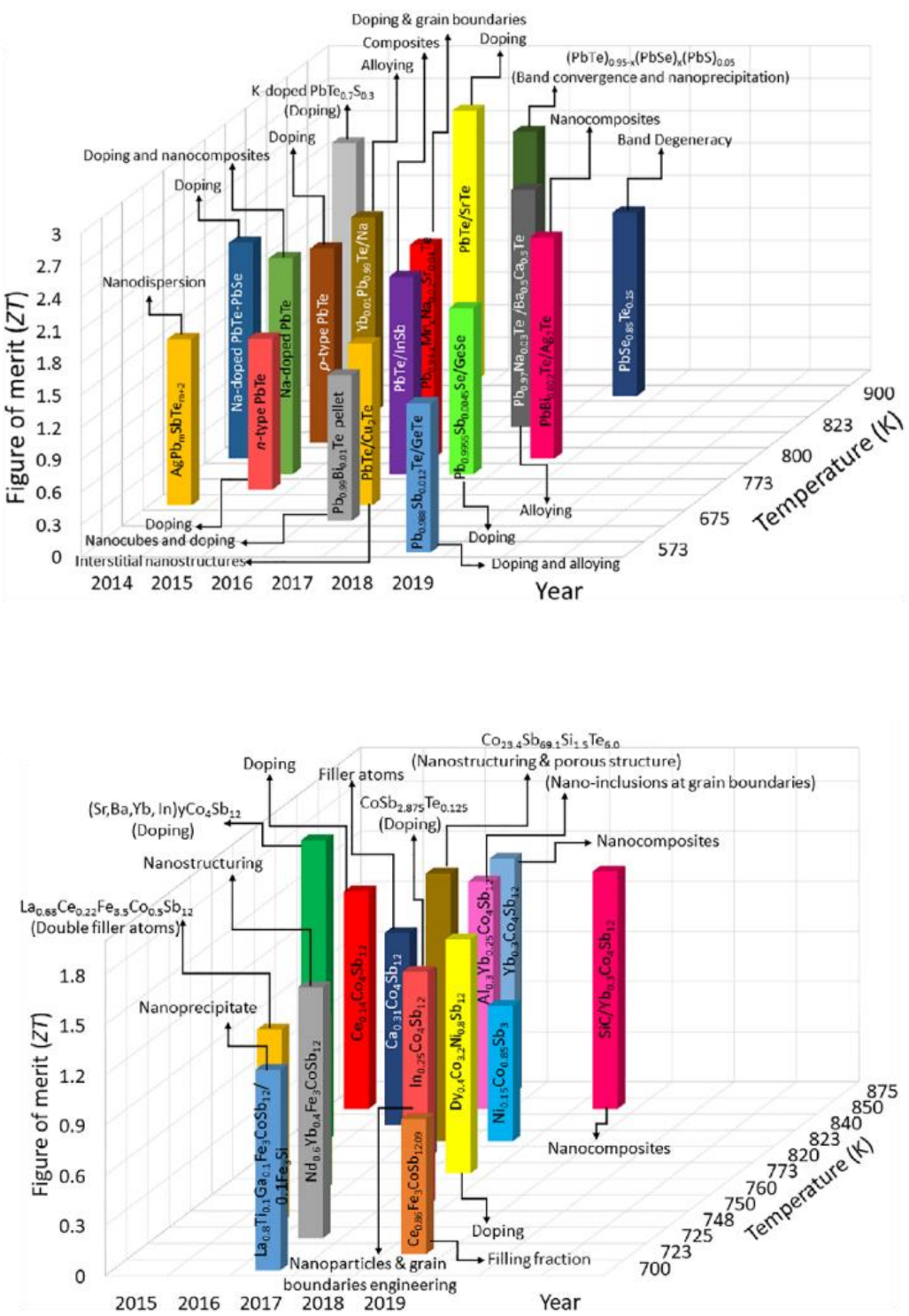

Figure 16 Best performing inorganic TE alloys based on PbTe (on the top) and on $CoAs_3$ (on the bottom). In both graphs the optimization techniques to enhance ZT are labelled. Image adapted from **[50]**.

2.4.2 Organic Thermoelectric materials

Compared to inorganic TE materials, organic TE materials are lighter, flexible, cheaper, easier to process; they have a lower thermal conductivity (around 10^{-1} $Wm^{-1}K^{-1}$) and a lower working temperature (compatible with human body conditions). However, organic TE materials suffer from two major disadvantages: they tend to be unstable at hight temperatures and they have a generally lower efficiency if compared with inorganic counterparts (1-3 orders of magnitude lower [54]). Generally, organic TE materials are intrinsically conducting polymers that will be briefly introduced in the following chapter.

Given their peculiar features, organic and inorganic TE materials do not directly compete each other, but rather cooperate to fulfil two different needs to solve the thermal energy harvesting problem. An interesting application of organic TEG is in flexible wearable electronics (Figure 17, [55], [56]).

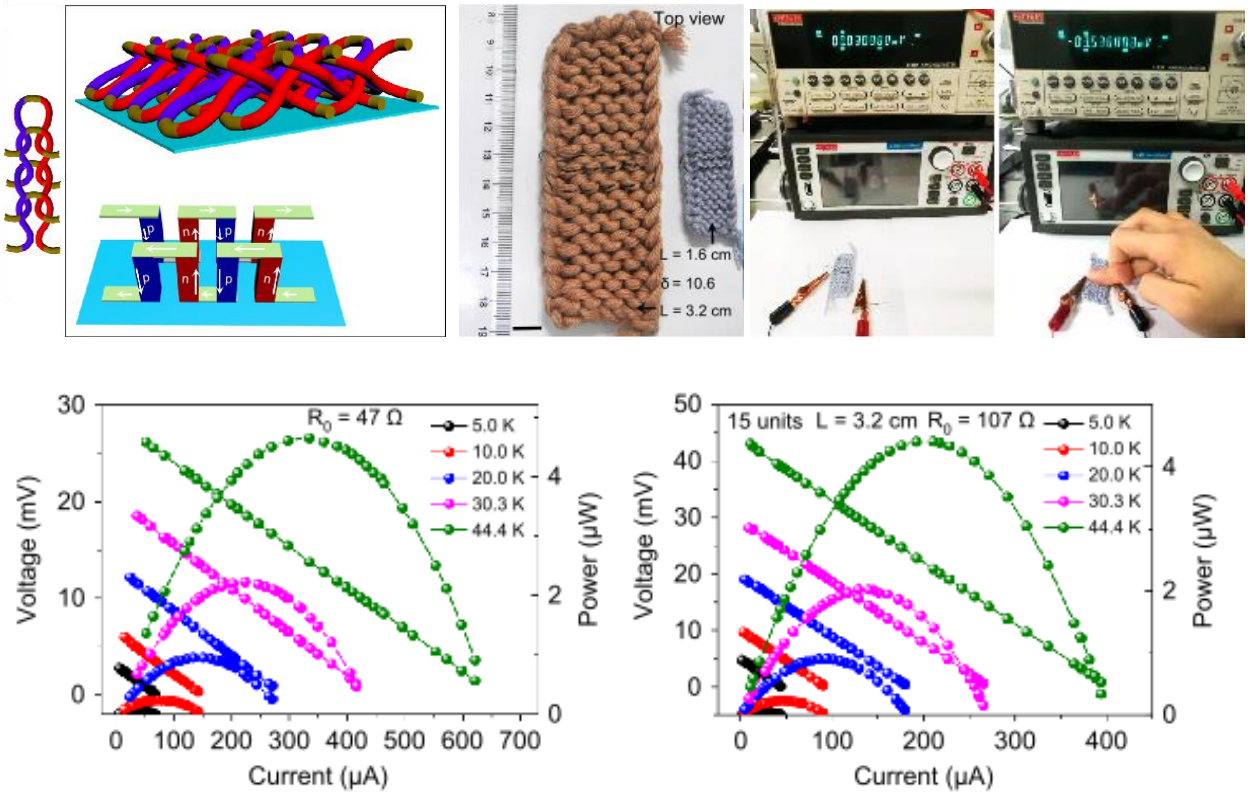

Figure 17: Carbon nanotube fibers wrapped among acrylic fibers can be woven into stretchable thermoelectric modules. Images adapted from **[55]**.

In the case of organic materials, there is a lack of a predictive model that relates PF, α and σ. An interesting approach has been proposed by Russ et al. [57], who suggest analysing the Seebeck coefficient as a function

of electrical conductivity based on experimental observations. Thanks to the wide range of doped organic materials described in the literature, it is possible to underline an empirical relation between the electrical conductivity and the Seebeck coefficient (Figure 18).

Equation 57 $$\boldsymbol{\alpha \propto \sigma^{-1/4}}$$

Equation 58 $$\mathrm{PF} \propto \sigma^{1/2}$$

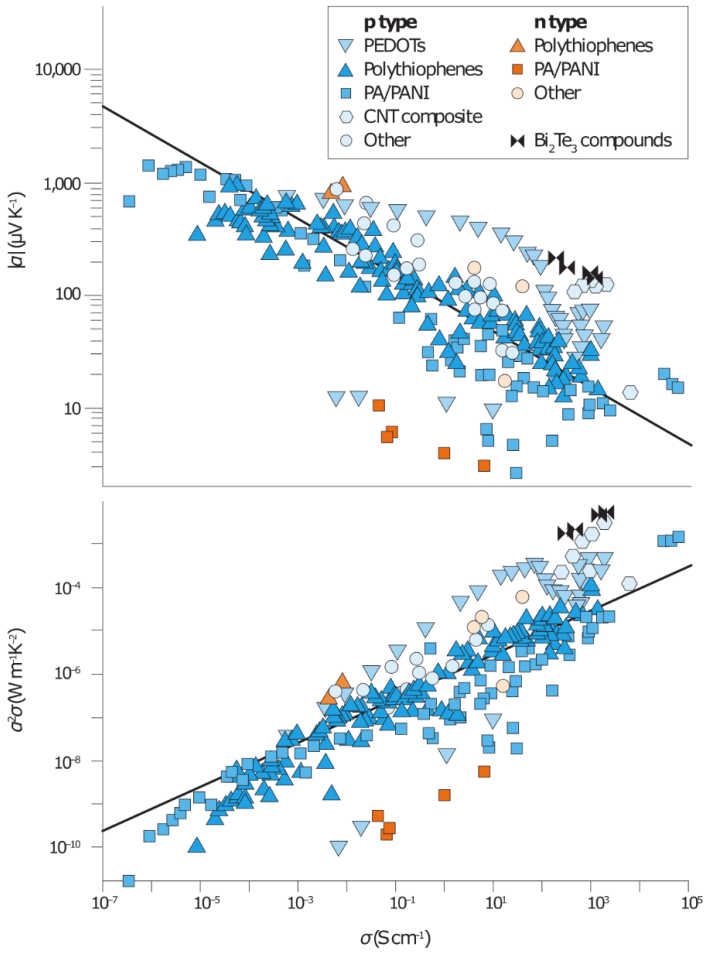

Figure 18. Thermoelectric properties of different organic materials reported in literature: Seebeck coefficient (α), on top, power factor (PF = $\alpha^2\sigma$), on bottom. Both values are plotted as function of electrical conductivity (σ). The solid black line indicates the empirical relation $\alpha \propto \sigma^{-1/4}$ (top) and $PF \propto \sigma^{1/2}$ (bottom). The data regarding the best inorganic thermoelectric material (Bi_2Te_3) are also included, for reference. Image adapted from [57].

Finally, it is worth mentioning that in the recent years, attempts have been made to create hybrid organic-inorganic TE systems [54], [58][59][60][61]- [62].

3. DOPED CONJUGATED MATERIALS

Polyacetylene, the polymer obtained by the polymerization of acetylene (Figure 19) was firstly reported by Natta et al. in 1958. However, despite many initial attempts, polyacetylene has not attracted great interest for a long time because the material is insoluble and infusible and highly reactive [63].

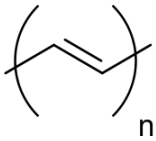

Figure 19 chemical structure of polyacetylene

In 1967 polyacetylene was studied by Hideki Shirakawa, who obtained a polyacetylene film using a high amount of Ziegler Natta catalyst, which could easily be handled and partially characterized. The first report on a highly conducting polyacetylene was published in 1977 by Alan J. Heeger, Alan G. MacDiarmid, Hideki Shirakawa [64] (Figure 20). The authors demonstrated that polyacetylene exposed to iodine vapours becomes highly conductive through a redox (doping) reaction. Indeed, the electrical conductivity of the trans-polyacetylene increased from 10^{-9} S cm^{-1} to 10^{5} S cm^{-1} with the formation of a metal-like material that they called "synthetic metal" [65], [63], [66] (Figure 21). This can be considered as the beginning of the era of organic electronics.

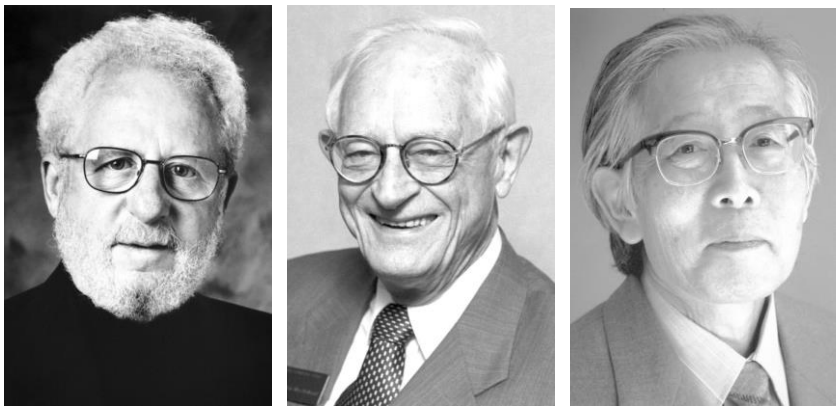

Figure 20: The Noble laureates of 2000, Alan J. Heeger (left), Alan G. MacDiarmid (center), Hideki Shirakawa (right). Pictures taken from [36].

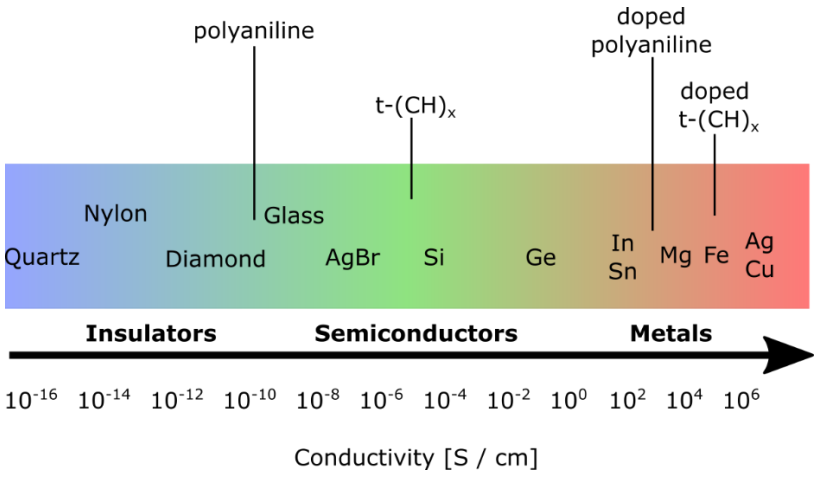

Figure 21. Conductivity ranges of different common materials. It is remarkable to notice the change in conductivity of conjugated polymers before and after the doping process.

Nowadays, conjugated organic materials are gathering increasing interest [67] for their potential to manufacture flexible [68],[[69] and easy to process [70], [71] electronic devices. Conjugated materials can either be small molecules or polymers. Both classes have been extensively studied in the past.

Recently, thanks to the development of new synthetic techniques [72], [73] conductive polymers have made remarkable results as active materials for organic TE generators and have attracted increasing interest ([67], Figure 22).

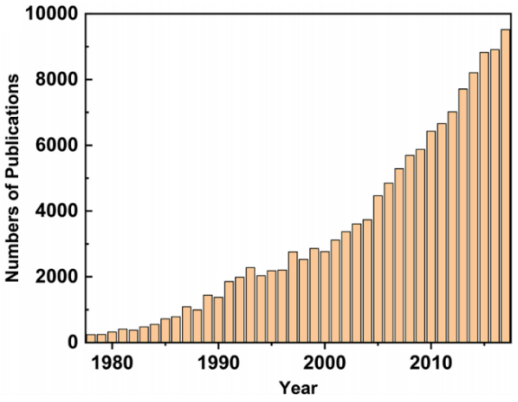

Figure 22. Number of publications on the topic of “conjugated polymer” in the last 40 years. Image adapted from **[67]**.

For practical applications, polyacetylene is not suitable due to its instability and poor processability. Indeed, polyacetylene, as well as several unsubstituted conjugated polymers, have a drawback: due to π-

delocalization, their chains are rigid, and they effectively interact through p-stacking, making conjugated materials poorly soluble in common organic solvents, hindering their processability. For these reasons, flexible side chains are often added to the conjugated backbone to improve solubility. The rigidity of conjugated chains and their weak non-covalent Wan der Waals interactions promote the formation of aggregates in solution and the formation of crystalline domains within polymer films. Hence, monomer units can be engineered to modify polymer behaviour such as either preventing [33] or controlling over [32] π-π stacking. Some conjugated polymers are shown in Figure 23.

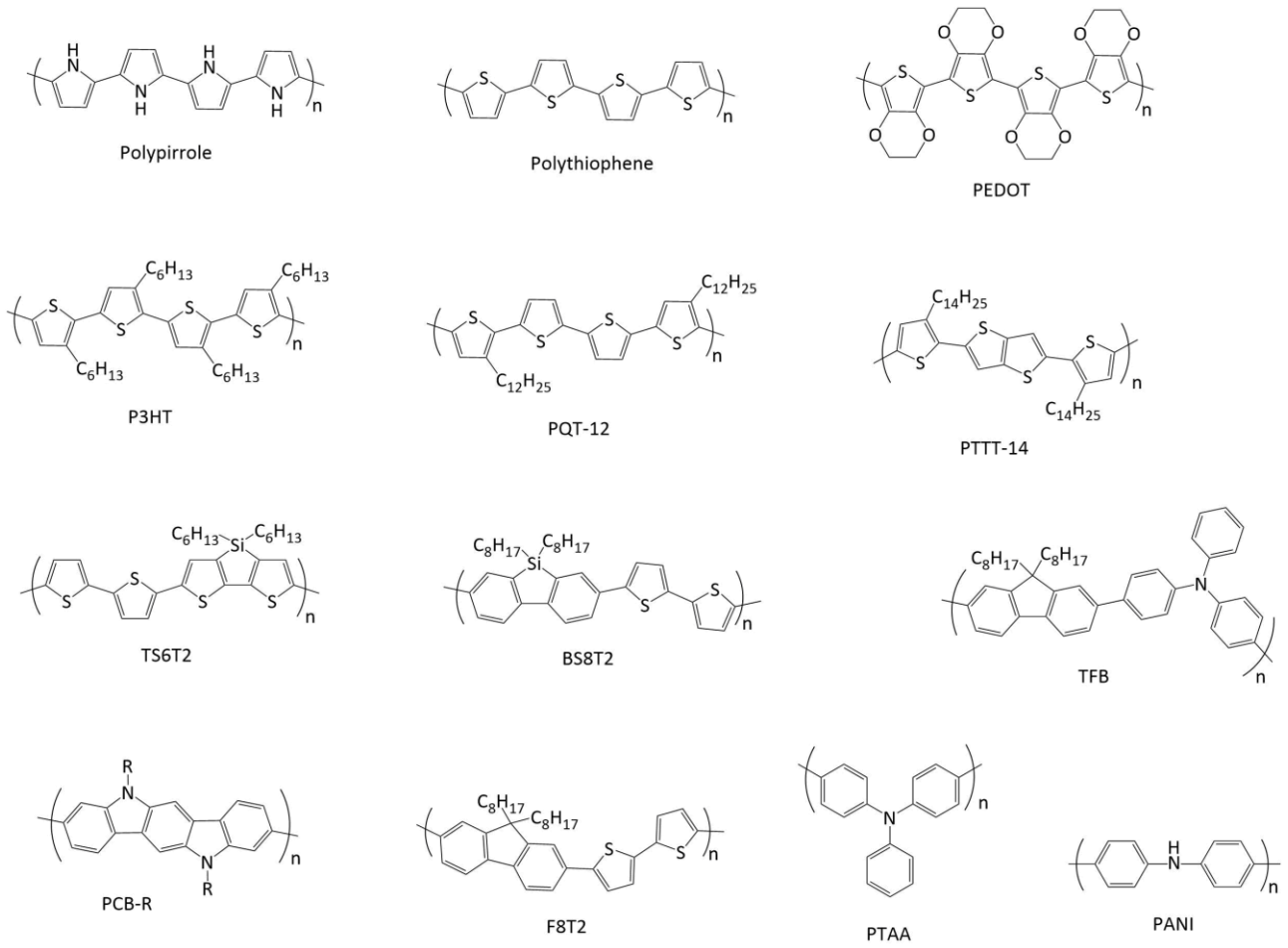

Figure 23: chemical structure of some conjugated polymers.

Like inorganic semiconductors, organic semiconductors can be classified in p-type and n-type materials [74]. P-type materials have an electron-rich conjugated structure often composed of multiple conjugated aromatic rings and/or polycyclic aromatic compounds. N-type materials have an electron-poor structure and are characterized by electron withdrawing substituents. Both classes will be further analysed in the next chapters.

3.1 DOPING

Because of rather low charge carrier concentration ($<10^{20}$ /m^3 [75]), conjugated materials tend to have a rather low electrical conductivity (Equation 53). Therefore, to increase electrical conductivity, it is necessary to increase charge carrier density. The process of injecting additional charge carriers (h^+ or e^-) in the conjugated structure is called "doping" because of its strong analogy with inorganic semiconductors. However, there are two major differences between inorganic and organic doping. The first one is the doping level (amount of dopant species within the host semiconductor): inorganic dopant concentration is around few ppm while organic polymers can be doped up to 100%$_{mol/mol}$. The second one is the actual doping mechanism which, in the case of organic materials, is a redox reaction. There are two main ways to increase polymer conductivity through doping:

- Electrochemical doping

  The conjugated polymer is in contact with an electrolyte and a metal, and charge carriers are injected from the metal electrode. To maintain electro-neutrality, small counterions penetrate the polymer structure. The oxidation/reduction of a conjugated polymer occurs when the metal electrochemical potential is equal to the ionization potential / electron affinity of the polymer.
- Chemical doping

  In this case, the polymer is exposed to an oxidizing/reducing species, which leads to the introduction of positive/negative charges on the polymer backbone, respectively, with the dopant being co-product of this reaction which remains as counterion to balance the charge carriers formation.

After doping, the electrostatic interactions between the new charges of the systems (i.e. counterions and charge carriers) increase the polymer cohesive energy. Therefore, highly doped conjugated polymers are even less soluble than their undoped form. A common solution to enhance solubility is to either use a soluble polymeric counterion such as polystyrene sulfonate in the case of poly 3,4-ethylenedioxythiophene (PEDOT – PSS, [76], Figure 33) or using a ionic surfactant as a counterion such as camphor sulfonic acid in the case of polyaniline [77].

According to the simple integer transfer model (Figure 24) doping process is classified into two classes: p-type and n-type doping. A p-type dopant is an oxidizing compound that removes an e^- from the HOMO (Highest Occupied Molecular Orbital) of a conjugated polymer, hence introducing a positive charge to the polymer backbone. On the other hand, a n-type dopant is a reducing molecule that donates an e^- to the LUMO (Lowest Unoccupied Molecular Orbital), thus introducing a negative charge carrier. Integer charge transfer model is useful to have a rough idea of the doping mechanism, but a more accurate analysis of the

process describes the doping mechanism with the formation of a charge transfer state originated from the mixing of both donor and acceptor orbitals (hybrid charge transfer model) [78], [79].

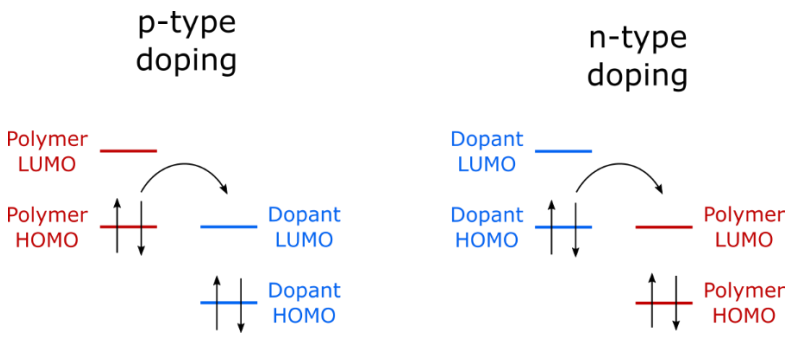

Figure 24. p-type and n-type doping of an organic semiconductor according to the integer charge transfer model. Image adapted from [80].

The charge introduced by doping generates a perturbation of the polymer electronic structure, which displaces the surrounding nuclei from their equilibrium positions and generates a local defect named "polaron". Indeed, the chain structure of neutral conjugated polymers made of cyclic monomers (such as polythiophene) usually has an aromatic character, while the polaron deformation alters the single/double bond alternation and has a more pronounced quinoid character (Figure 25, [81]). Such distortion is usually 3-4 repeating units long and it is associated with two new energy levels within the band gap (Figure 26b [27], [81]). A polaron can be defined as a quasi-particle composed of a charge and its related polarization and distortion effects, which is generated at very low doping ratio. [82], [83] Conjugated polymers also exhibit another type of local defect, which is usually predominant at high doping ratio: the bipolaron (Figure 25). A bipolaron is a quasi-particle that carries two charges, it has a clear quinoid character and it originates two bipolaronic energy levels within the band gap with a higher energy compared to the polaron levels (Figure 26c).

By further increasing the doping level an increased number of defects is created, and the overlapping of their wave functions generates new bands (either intra- or inter chain) within the band gap (Figure 26d). The width of these bands strongly depends on the doping level, and it increases with increasing dopant amount. Some intrinsically conducting polymers show metallic-like electrical behaviour even at room temperature [77]. Doping is also associated to a remarkable change not only of the electrical properties of the material, but also of the optical properties: electrochemical doping and undoping can turn into a reversible change of colour, known as electrochromism, which is applied for smart windows.

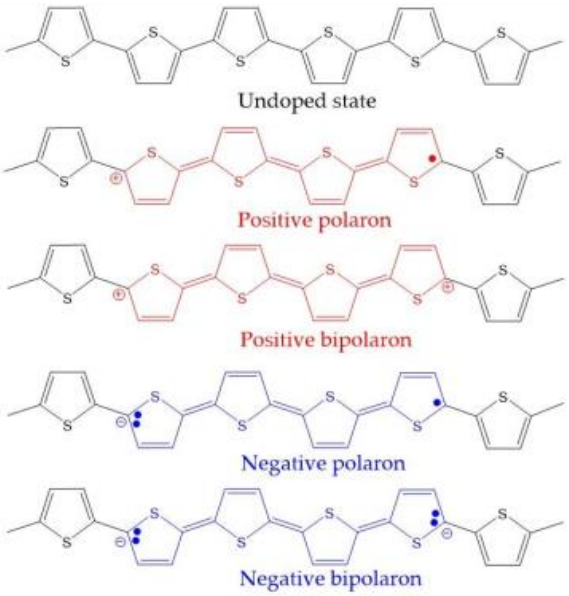

Figure 25. In order from the top: chemical structure of pristine polythiophene, polythiophene with positive polaron and positive bipolaron, polythiophene with negative polaron and negative bipolaron. Locally the conjugated backbone bond alternation changes from aromatic to quinoid. Image adapted from **[81]**.

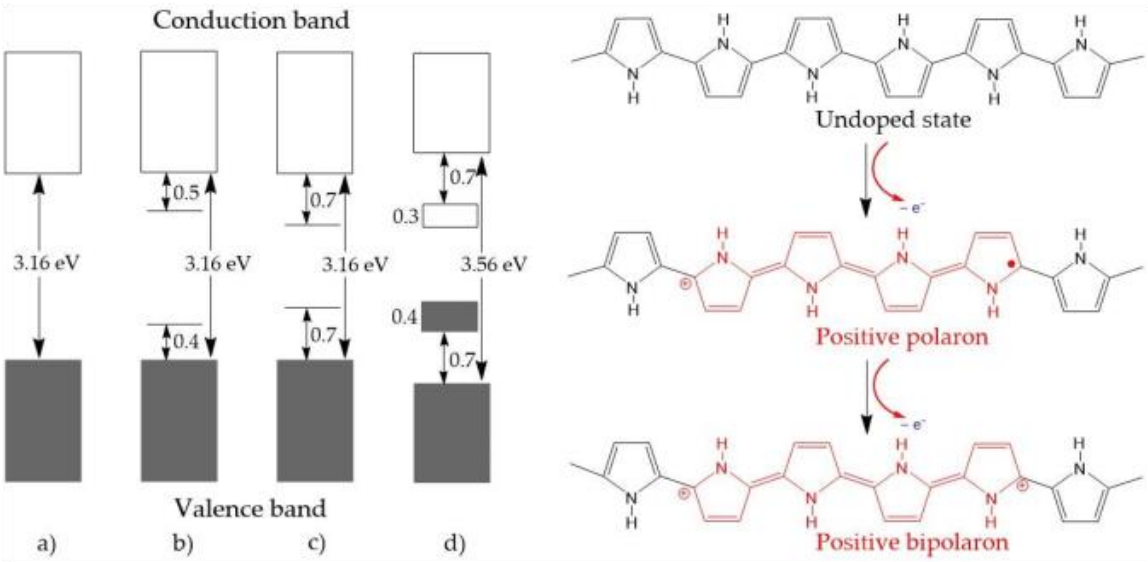

Figure 26. On the left: electronic structure of undoped polypyrrole with a band gap of 3.16 eV (a), positive polaron (b), positive bipolaron (c) and new bands originated by the overlapping of multiple defect wave functions that reduce the band gap to around 1.46 eV (d). On the right: chemical structures of pristine, positive polaron and positive bipolaron backbone of polypyrrole. Image adapted from **[81]**.

In the case of polymer-based semiconductors with spatial and energetic disorder, the charges in the conjugated polymer chain, are trapped by counterions attractive Coulomb potentials. Therefore, the charge transport requires the charge carrier to tunnel from a spatially localized site to another. This type of transport is called hopping mechanism while the charge movement is often informally referred as a "jump" between the two states. [83] Since the typical values of dielectric constant in organic materials are very low (ε ≈3 [84]), the Coulomb traps have a rather large radius (≈ 20 nm), often including many hopping sites [27], [85]. The hopping transition between two localized sites depends on the energy difference, the distance, and the overlap of the wave functions of the two sites. A low dopant concentration is associated with a low density of hopping sites, which are far from each other. Such condition is insufficient to overcome trapping phenomenon and to effectively enhance the charge carrier transport. At higher doping concentrations (> 10^{17} cm^{-3}), Coulomb traps begin to overlap with each other, and the energy barrier (Δ) against the hopping process decreases. At high doping levels (around 30%), the average distance between counterions decreases and the electrostatic potential becomes smooth, facilitating charge hopping (Figure 27). Conjugated polymers e^- [86] and h^+ [87] mobility can vary from ≈ 10^{-5} $cm^2V^{-1}s^{-1}$ to ≈ 1 $cm^2V^{-1}s^{-1}$.

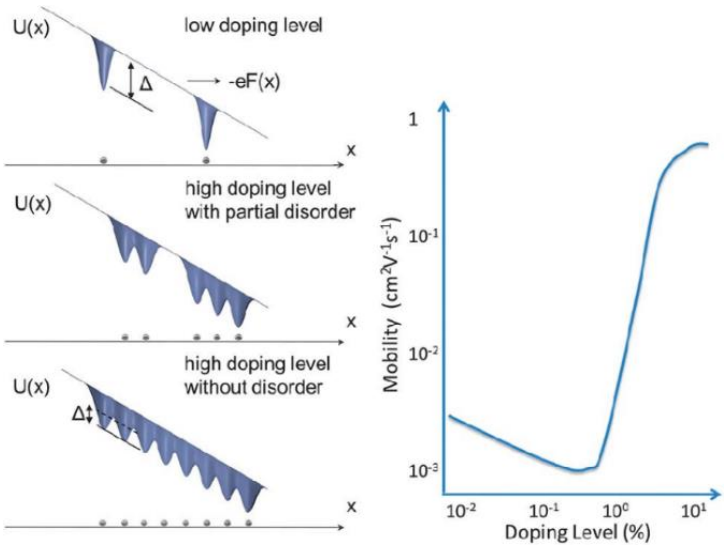

Figure 27. On the left: increasing dopant concentration reduces the energy barrier Δ for the charge transport process to occur, under an external electric field F(x). On the right: the charge carrier mobility at different doping levels. Image adapted from [27].

To sum up, whether the charge transport mechanism is described by the hopping model or by the formation of new defect bands, understanding the complex relation between the dopant and the polymer is crucial to design efficient TE materials.

4. P-TYPE MATERIALS

As previously discussed, the first conducting polymer to be studied was the *trans*-polyacetylene. Conductivities of about 560 Scm^{-1} and mobilities of 1 $cm^2V^{-1}s^{-1}$ have been reported when *trans*-polyacetylene was p-doped with AsF_5 (arsenic pentafluoride). When doped with I_2 vapor, electrical conductivity can be further increased to 10^4 S cm^{-1}. Electrical conductivities as high as $3x10^4$ S cm^{-1} can be measured in oriented polyacetylene at 220K with power factor around 2 x 10^{-4} Scm^{-1} [88], [80]. Unfortunately, despite the initial very promising results, *trans*-polyacetylene is not suitable for electronic applications as it is not soluble in any solvent, and it is unstable at normal environment. Nevertheless, in the last 50 years, many p-type polymers, mainly consisting of 5 or 6 membered aromatic rings, have been reported. The most important for TE applications are: polythiophenes, polypyrroles, polycarbazoles, polyphenylenevinylenes, poly(3,4-ethylenedioxythiophene) and polyaniline.

4.1 POLYTHIOPHENE

Polythiophenes (PT) are polymers obtained from the 2,5- polymerization of thiophene. Worth noting, a chain of unsubstituted thiophene rings is unsoluble, and for this reason, the thiophene monomers are often functionalized in the 3-position with side alkyl chains to enhance both polymer solubility and processability (Figure 28). For example, poly-3-alkylthiophenes exhibit good solubility in common organic solvents such as chloroform, tetrahydrofuran and toluene. [89] Common examples of poly-alkyl thiophenes are poly(3-octylthiophene) (P3OT), poly(3-methylthiophene) (P3MeT) and poly 3-hexylthiophene (P3HT).

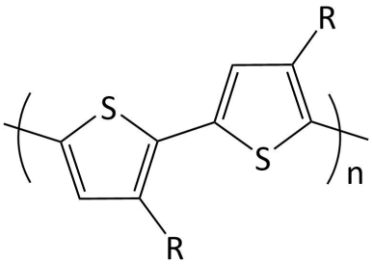

Figure 28. Chemical structure of polythiophene (R = H) and of poly(alkyl thiopene)s (R = alkyl chain).

PTs are often synthetised *via* electrolytic polymerization, which is a process that proceeds by anodic oxidation during which both the polymerization and the doping occur simultaneously on the electrode interface. The films can subsequently be undoped by chemical or electrochemical reduction. Typically, nitrobenzene and

tetra-butylammonium perchlorate ($TBAClO_4$) were used as solvent and electrolyte, respectively. [90] By changing the polymerization conditions such as monomer and electrolyte concentration, electric current, solvent, and temperature, it is possible to tune the PT film structure and its TE properties [91]. For instance, a high monomer or electrolyte concentration (more than 1 M) can originate side reactions that shorten the polymer molecular weight, while a too high deposition rate might generate a rough film with more defects. [92] High crystallinity PT films obtained by electrolytic polymerization of thiophene (0.5 M) using $TBAClO_4$ (0.018 M) as electrolyte exhibit electrical conductivity as high as 200 S cm^{-1} and PF of 10 µW m^{-1} K^{-2}. [91] Li et al. [92] reported the synthesis of PT films on a stainless-steel electrode with a high mechanical strength (around 117MPa which is higher than aluminium) and an electrical conductivity of 49 Scm^{-1}, using a solution of borontrifluoride diethyl etherate (BFEE) and a low monomer concentration (10 mM). Similarly, P3OT films have also been prepared from a BFEE solution, achieving the remarkably high tensile strength of 127MPa. [93] Xu et al. have modified the classic electrolytic polymerization of PT, P3MeT and P3OT by adding 2,6-di-tert-butylpyridine (DTBP) to the BFEE solution, which acts as a H^+ scavenger lowering acidity and prevents acid catalysed reactions that could shorten the polymeric conjugation length. The authors demonstrated an increase between 5 and 30% of the TE power factor due to the DTBP addiction. [94]

4.1.1 Poly 3-hexylthiophene

Thanks to its facile synthesis, processability, environmental stability and relatively high hole mobility (ranging from 10^{-5} – 10^{-1} $cm^2V^{-1}s^{-1}$), the poly-3-hexylthiophene (P3HT) has found many applications in different fields such as TEGs [95], organic field effect transistors [96] and solar cells. Several studies have been conducted on chemically doped P3HT with the p-type dopant F4TCNQ either by solution or vapour doping. In both cases, the electrical conductivity remains in the order of 1 S cm^{-1} [97], [98]. However, as highlighted by Chabynic et al. [99], the TE performances are slightly better in the case of vapor doping (PF 20 $\mu Wm^{-1}K^{-2}$) than in the case of solution doping (PF 0.5 $\mu Wm^{-1}K^{-2}$).

Xuan et al. have evaluated the TE properties of P3HT doped with nitrosonium hexafluorophosphate (F_6NOP). At low dopant concentrations, the bulky counterions disturb the order of the system; however, by increasing the dopant concentration, the order of the polymer matrix increases with a subsequent increase in both the Seebeck coefficient and electrical conductivity. The maximum power factor (0.1 µW m^{-1} K^{-2}) is reached at doping levels between 20 and 31% [100]. A higher PF (2 µW m^{-1} K^{-2}) has been reported when doping P3HT with ferric salt $TFSI^-$. [101]

4.1.2 Polythiophene derived polymers

An interesting PT derived polymer is poly(diketopyrrolopyrroleterthiophene) (PDPP3T, Figure 29) [102]. The presence of the diketopyrrolopyrrole bicyclic γ-lactam ring generates a more planar structure than PT, with an improved molecular order. Jung et al. [103] have doped PDPP3T with $FeCl_3$, obtaining a PF of 276 μW m^{-1} K^{-2}. Zhu et al. [104] compared several polymers including PDPP3T, poly[(4,4'-bis(2-ethylhexyl)dithieno[3,2-b:2',3-d] silole)-2,6-diyl-alt-(2,1,3 benzothiadiazole)-4,7-diyl] (PSBTBT and poly(2,5-bis(3-dodecylthiophen-2-yl)-thieno[3,2-b]thiophene) (PBTTTC12) (Figure 29), obtaining PF of 25, 4 and 14 μW m^{-1} K^{-2} , respectively. Katz et al. [105] have synthesized PDTDE12, PDTDES12 and PQTS12 (Figure 30). The ethylenedioxy groups and the sulfur atoms raise the HOMO and facilitate the oxidation of the polymer. However, while the presence of sulfur atoms does not affect the overall planarity of the polymer, ethylenedioxy groups have a non-negligible steric effect on the conjugated backbone. For this reason, while PQTS12 films have an ordered packing structure, PDTDE12, PDTDES12 have a distorted backbone. The TE properties of some PT materials are reported in Table 3.

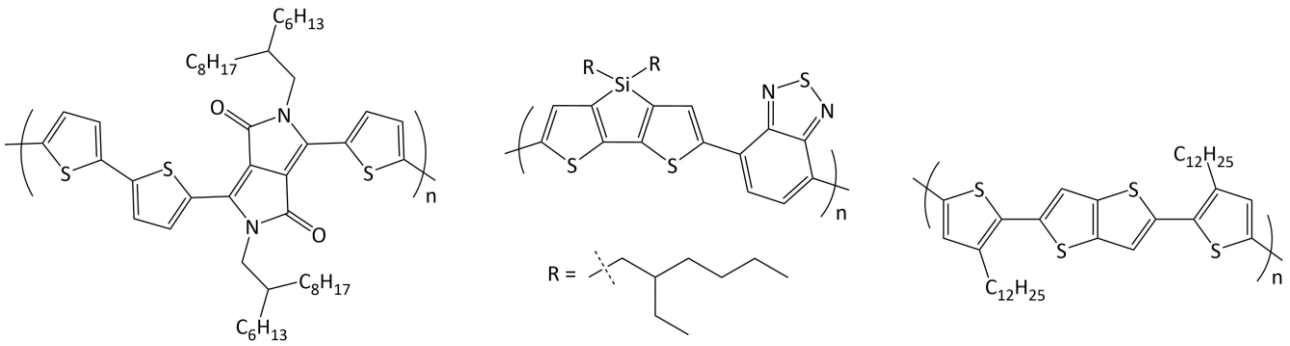

Figure 29. chemical structure of PDPP3T (left), PSBTBT (centre) and PBTTTC12 (right).

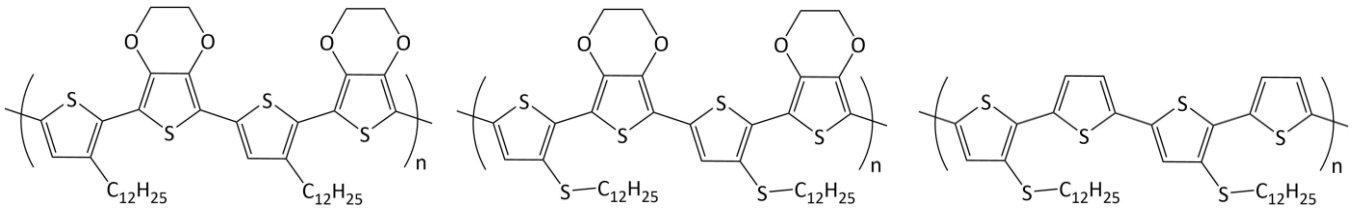

Figure 30. chemical structure of PDTDE12 (left), PDTDES12 (centre) and PQTS12 (right).

Material	Treatment	α (μVK^{-1})	σ (Scm^{-1})	PF ($\mu Wm^{-1}K^{-2}$)	Ref.
PT	Doped with ClO_4^-	26	201	10	[106]
P3HT	Immersion doping with $TFSI^-$	48	87	20	[101]
PBTTTC14	Vapor doping with FTS	23	466	25	[107]
PBTTTC15	Vapor doping with F4TCNQ	42	670	120	[108]
PDPP3T	Spin coating doping with $FeCl_3$	226	55	276	[103]
PDPP3T	Immersion doping with $TFSI^-$	45	62	25	[104]
PDTDE12	Drop doping with F4TCNQ	30	120	10	[105]

Table 3: TE properties of PT derived materials

4.2 PEDOT

Poly(3,4-ethylenedioxythiophene) (PEDOT, Figure 31) is a conjugated polymer obtained from the oxidative polymerization [76] of the 3,4-ethylenedioxythiophene (EDOT), which is a thiophene unit functionalized with an ethylenedioxy group that connects the 3- and 4- thiophene positions. PEDOT was originally reported in 1991 [109] and today, thanks to its properties such as optical transparency as a thin film [110], chemical and environmental stability, relatively low toxicity [111], [112] and versatile deposition techniques, [113] it is one the most important p-type conducting polymer. PEDOT has found applications in many fields such as TEG [114], organic solar cells [115], biosensors [116] and electrochromic switches [117] (Figure 32).

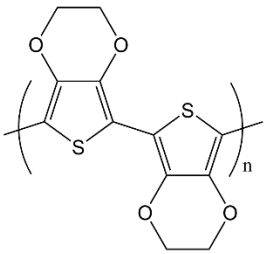

Figure 31. chemical structure of PEDOT.

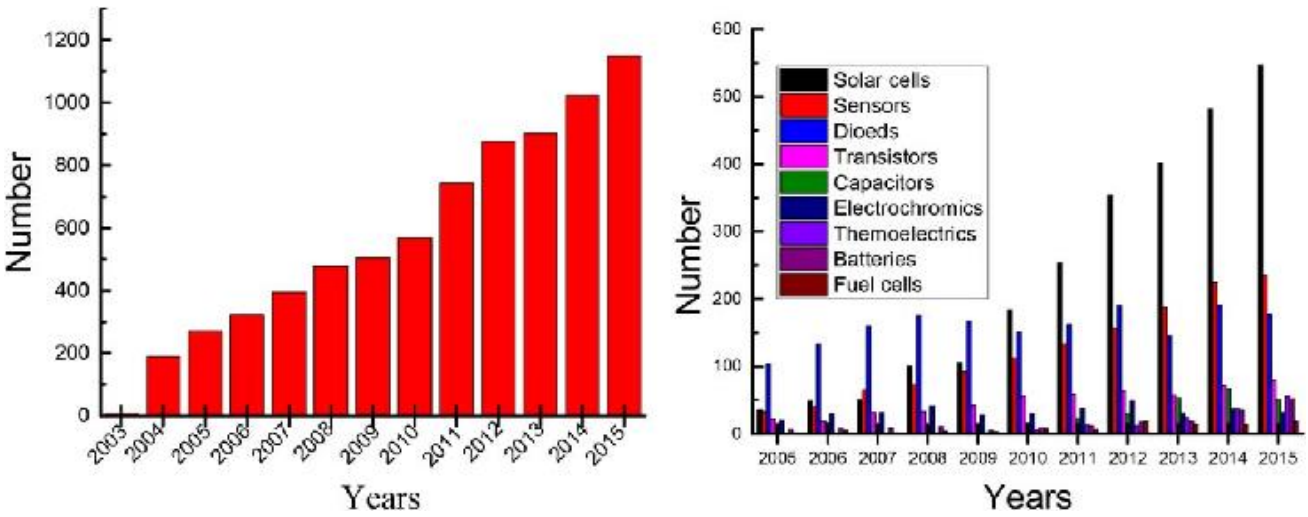

Figure 32 On the left: total number of publications about PEDOT in the period 2005-2015. On the right: number of publications regarding PEDOT divided for each field of application in the period 2005-2015. Image adapted from **[113]**.

Although PEDOT has been doped with many different small molecules, such as (O-tosylate)$_3$ (PEDOT:TOS,), ClO_4^-, bis(trifluoromethylsulfonyl)imide (BTFMSI$^-$) and $PF6^-$ [118], [119] , [120], the PEDOT:PSS system (Figure 33) has received the greatest attention thanks to its remarkable solution processability. Poly(styrenesulfonate) (PSS) is a sulfonated derivative of polystyrene that acts as a solubilizing counter ion when it is deprotonated. Aqueous PEDOT:PSS dispersions are commercially available, and this makes the material a good candidate for ink-based processing such as dip-coating [121], ink-jet printing [122] and spin-coating [123]. PEDOT:PSS properties can be tuned changing the PEDOT:PSS ratio, the dopant and the solvent used for film fabrication [124].

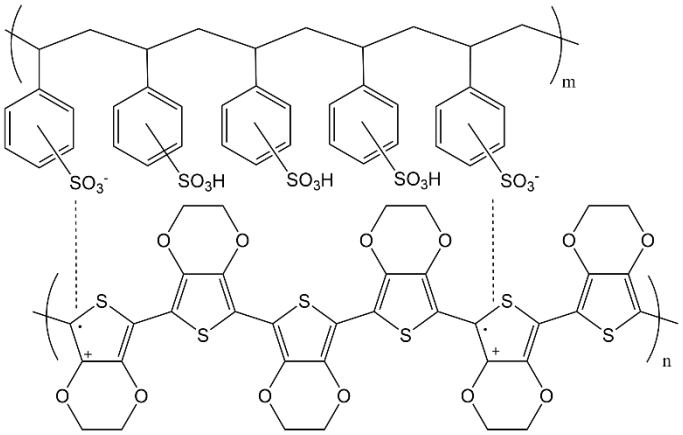

Figure 33. PEDOT:PSS structure. Image adapted from [115].

It is important to consider, that after PEDOT:PSS deposition from an aqueous solution, TE properties are not ideal ($\sigma < 1$ Scm^{-1} , $\alpha \approx 15$ μVK^{-1} and PF ≈ 10^{-3} μWK^{-2}m^{-1} [114], [125]). Such poor performance is caused by the excess of PSS required to disperse PEDOT in water [125]. Removing excess PSS after film deposition remarkably increases electrical conductivity [126], and this process is called “dedoping”. Dedoping increases Seebeck coefficient, however, it reduces electrical conductivity. Therefore, it is important to find the best compromise to reach an optimal conductivity and Seebeck coefficient. Dedoping can be done both electrochemically [127] and chemically with reducing compounds such as hydrazine [128], tetrakis(dimethylamino)ethylene (TDAE), ammonium formate, hydroiodic acid and sodium borohydride [129]. Furthermore, a secondary doping can be performed, aimed at increasing electrical conductivity by changing film morphology and/or composition without altering the doping level [130]. It consists of the addition of a chemical species into the aqueous solution or to treat the PEDOT:PSS film with a vapor, a solvent or a solution. Kim et al. [131] used different solvents such as tetrahydrofuran (THF), N,N-dimethyl formamide (DMF), dimethyl sulfoxide (DMSO) and water, obtaining an increase of electrical conductivity from 0.8 S cm$^-$

[1] (in water) to 80 S cm^{-1} (in DMSO). The relation between the use of DMSO and the electrical conductivity has been explored in [132], where conductivities around 600 S cm^{-1} (a figure of merit of 9.2 x 10^{-3}) have been found for by adding DMSO (5% vol) to the aqueous PEDOT : PSS solution. Gong et al. [133] reported that the addition of DMSO (5%) and polyethylene oxide (PEO, 0.4%) to the aqueous PEDOT : PSS solution dramatically increases electrical conductivity (up to 1300 S cm^{-1}), Seebeck coefficient (up to 40 μVK^{-1}) and PF (157 $\mu WK^{-2}m^{-1}$). Secondary doping can be also achieved through post processing the PEDOT:PSS film. Chu et al. [134] have post-treated PEDOT:PSS films with different organic compounds. When exposed to formic acid, PEDOT:PSS films exhibit an electrical conductivity of 1900 S cm^{-1}, Seebeck coefficient of 21 $\mu V\ K^{-1}$ and a PF of 81 $\mu W\ m^{-1}\ K^{-2}$. A remarkable electrical conductivity of 3 x 10^3 S cm^{-1} has been reported when a PEDOT:PSS film (24nm thick) was treated with a 1M solution of sulfuric acid (H_2SO_4) at 160°C [135]. Some TE properties of PEDOT materials are reported in Table 4.

Material	Treatment	A (μVK^{-1})	Σ (Scm^{-1})	PF ($\mu Wm^{-1}K^{-2}$)	Ref.
PEDOT:PSS	PEO and DMSO addition	38	1060	157	[133]
PEDOT:PSS	Posttreatment with formic acid	21	1900	81	[134]
PEDOT:PSS	Posttreatment with a solution of $ZnCl_2$ in DMF	26	1400	98	[136]
PEDOT:PSS	Electrochemical dedoping	100	20	23,5	[127]
PEDOT:PSS	Chemical dedoping with ammonium formate	436	0,036	0,69	[137]
PEDOT:PSS	Treated with EMIM-BF_4 and DMSO	23	700	38	[138]
PEDOT:PSS	Treated with DMSO and hydrazine	41	677	115	[128]
PEDOT:PSS	Treated with NaOH	16	800	20	[139]
PEDOT:PSS	Treated with hydrazine	67	578	112	[140]
PEDOT:PSS	Treated with TSA and then hydrazine and DMSO	50	1300	318	[141]
PEDOT:PSS	Treated with H_2SO_4 and then NaOH	39	2170	334	[142]
PEDOT:TFSI	Dedoped with hydrazine	37	1100	147	[118]
PEDOT:TOS	DMF addition	35	640	79	[143]
PEDOT:TOS	Posttreatment with p-Tos	15	1570	34	[144]
PEDOT:TOS	Posttreatment with MeOH	24	1200	70	[145]
PEDOT:TOS	Electrochemical dedoping	117	923	1270	[146]
PEDOT:TOS	Chemical dedoping with TDAE	220	67	324	[147]
PEDOT:TOS	Treated with NaOH	20	650	26	[148]
PEDOT:TOS	Treated with a $NaBH_4$ solution in DMSO	40	580	98	[149]
PEDOT:TOS	Treated with HI	20	1690	70	[150]

Table 4: TE properties of some PEDOT materials.

4.3 OTHER POLYMERS

Polyaniline (PANI, Figure 34) is another important conjugated polymer due to its easy synthesis and good stability. PANI synthesis can follow a chemical or an electrochemical route yielding material with different electrical conductivities. Chemical synthesis leads to higher conductivities (6.3 x 10^{-4} S cm^{-1}) than electrochemical synthesis (1.7 x 10^{-4} S cm^{-1}) [151]. In neither case, PANI exhibits TE performance comparable to other p-type polymers [114]. It has been demonstrated that the cross-linking of PANI monomers enhances the order of the structure and increases the electrical conductivity (+25%, Figure 34). [152] At high doping concentrations, PANI shows temperature dependent metallic behaviour and conductivities around 601 S cm^{-1} (at around 300 K). The maximum value of ZT for PANI doped with HCl is 2.7 x 10^{-4} (measured at 423K [153]).

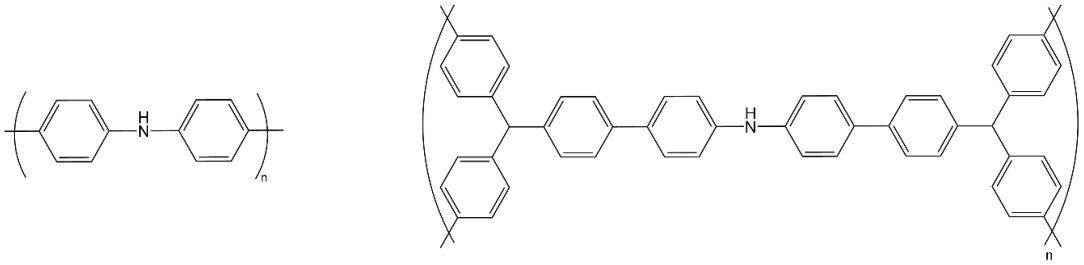

Figure 34. on the left: chemical structure of polyaniline. On the right: chemical structure of cross-linked polyaniline

Another polymer that has received some interest due to its good solubility and facile synthesis is polypyrrole (PPy, Figure 35). Films of polypyrrole prepared by freezing interfacial polymerization can reach electrical conductivity in the order of 2 x 10^3 S cm^{-1} [154]. Depending on the synthetic protocol and on the dopant used, the Seebeck coefficient of polypyrroles can be over 1 μV K^{-1} at 250 K [155].

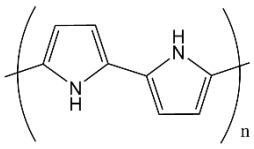

Figure 35. chemical structure of polypyrrole.

Polycarbazoles (Figure 36 left) usually exhibit lower electrical conductivity, but higher Seebeck coefficient than PANI and PPy [114]. The addition to the backbone of vinylene and electron donors such as thiophene

or EDOT, dramatically increase the electrical conductivity in polycarbazole derivatives [156]. Leclerc et al. [157] reported a polycarbazole derivate (PCDTBT, Figure 36 right) that shows an electrical conductivity up to 160 cm^{-1}, Seebeck coefficient of 34 $\mu V\ K^{-1}$ and PF of 20 $\mu W\ m^{-1}\ K^{-2}$.

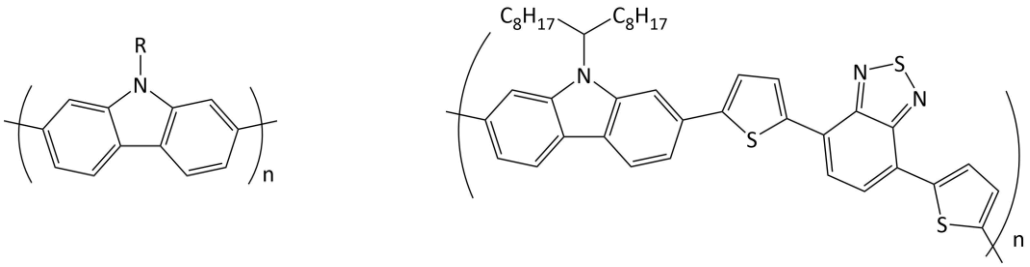

Figure 36. on the left: chemical structure of polycarbazole. On the right: chemical structure of PCDTBT.

5. N-TYPE MATERIALS

As previously discussed, a TE device is composed of two legs made of different materials: a p-type and a n-type (Figure 12). In the past, research has primarily focussed on the development and understanding of p-type materials (Figure 37). The reduced attention on n-type conductive materials is due to two main reasons:

1. The study of n-type TE materials is more complex than the study of p-type TE materials due to their instability to oxygen and humidity. This affects their processability and technological applications.
2. There is still a lack of high performing and commercially available n-type organic polymers.

So far, the performances obtained by p-type materials are out of reach (Figure 37).

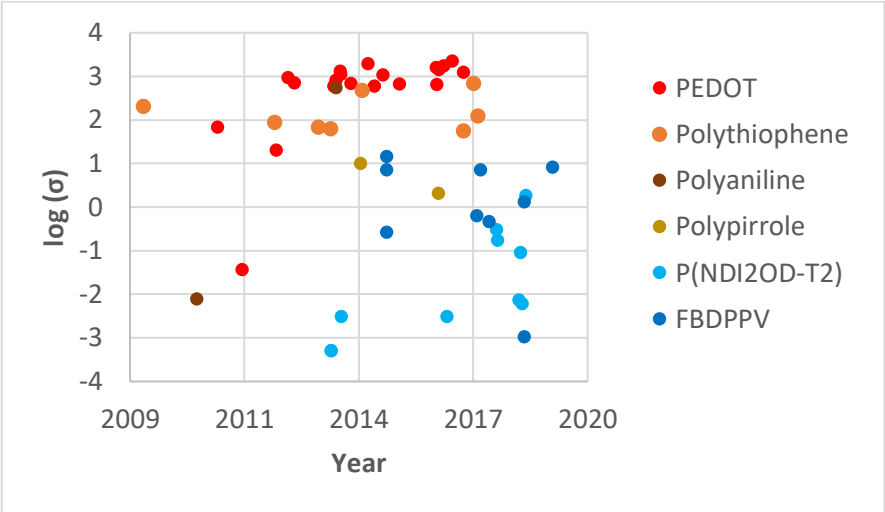

Figure 37. comparison between the electrical conductivity of p-type (orange dots) and n-type polymers (blue dots) developed in the last 10 years.

The LUMO level is a key parameter of a n-type material. A low LUMO favours the n-type doping mechanism (this will be discussed in the following chapters), and it also increases the environmental stability of the molecule. Indeed, after an e^- is injected in the lowest unoccupied molecular orbital by doping, a n-type material should be thermodynamically stable to redox reactions with oxygen and moisture, which might generate e^- traps that hinder the charge transport process. [158]. As water is reduced at a potential below -0.66 V (-3.7eV), and oxygen undergoes reduction at 0.57 V (-4.9 eV), [159] a n-doped (reduced) material should exhibit a LUMO lower than -3.7eV (with respect to vacuum) to be stable in the presence of water and lower than -4.9 eV to be stable in presence of oxygen. By taking into consideration redox kinetics, recent

studies have demonstrated that the threshold to achieve stability in atmosphere is slightly less restrictive: n-doped LUMO should be lower than -4.0 eV. [160]

LUMO level can be deepen by introducing electron withdrawing groups in the structure. Some common n-type molecules are naphthalenetetracarboxylic dianhydrides (NDA) [161], perylene bisimides [162], naphthodithiophenediimides [163] and fullerenes [164]. In case of n-type polymers, they are often obtained by the polymerization of such molecules in combination with a conjugated π-bridge spacer such as bithiophene.

5.1 FULLERENES

Fullerenes (Figure 38) are among the best n-type molecular semiconductors: high charge carrier mobilities, low thermal conductivities (around 0.4 W/m K, [165]) and good thermal stability make them ideal for organic electronic applications.

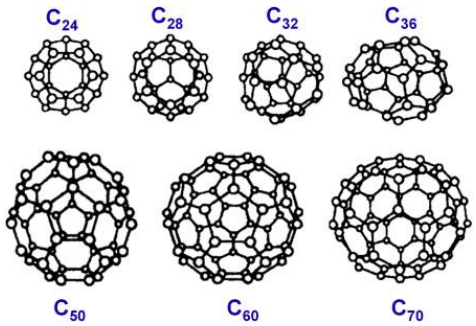

Figure 38. different sizes of fullerenes. Fullerenes are named as C_x, where x is the number of carbon atoms in their structure. Image adapted from [166].

The n-doping of fullerenes can be accomplished by dopant vacuum deposition [167]. A power factor of 20.5 x 10^{-6} W m^{-1} K^{-2} was obtained using a Cs_2CO_3/C_{60} bilayer device [168]. Similar values have been obtained for C_{60} samples doped with $Cr_2(hhpp)_4$ or $W_2(hhpp)_4$ (where hhpp = 1,3,4,6,7,8-hexahydro2H-pyrimido [1,2-a] pyrimidinate) [164], organometallic complexes [169], hydride donors [170], and tetrabutylammonium salts. However, the greatest problem afflicting n-type extrinsic dopants is their reactivity to atmospheric oxidants such as humidity and oxygen. An interesting approach to solve this problem is to promote the formation of an active dopant specie *in situ* through photo or thermal activation. Bao et al. [171] used 1,3-dimethyl-2-phenyl-2,3-dihydro-1H-benzoimidazole (DMBI, Figure 39 left) as a solution-processable air-stable n-type dopant for a well-known n-type system such as [6,6] - phenyl C_{61} butyric acid methyl ester (PCBM, Figure 39 right), obtaining an increase of electrical conductivity from 8.1 x 10^{-8} S cm^{-1} to 1.9 x 10^{-3} S cm^{-1} upon an

overnight thermal treatment at 80°C to activate the dopant. Fullerene derivatives with glycol side chains doped with DMBI have been reported to achieve electrical conductivity around 10 S cm^{-1} and a figure of merit ZT around 0.3. [172]

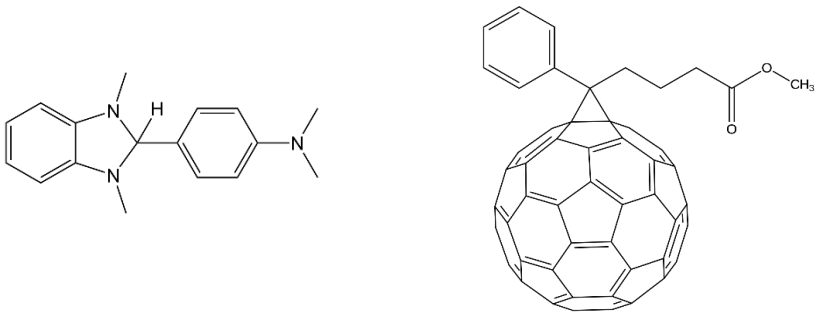

Figure 39. on the left: chemical structure of 1,3-Dimethyl-2-phenyl-2,3-dihydro-1H-benzoimidazole (DMBI). On the right: chemical structure of [6,6] - phenyl C_{61} butyric acid methyl ester (PCBM).

5.2 p-PHENYLENE VINYLENE POLYMERS

Poly p-phenylene vinylene (PPV) is a conjugated polymer (

Figure 40 left) and its derivatives have been applied in the first polymer-based light emitting diodes [173] and in the first bulk heterojunction solar cells [174]. Low charge carrier mobility in PPV (10^{-4} cm^2 $V^{-1}s^{-1}$) is mainly due to i) the trans-cis isomerization (both in solid state and in solution) induced by irradiation with UV light, ii) the free rotation of the single bonds with subsequent formation of conformational isomers, iii) the weak interchain interactions, resulting in slow interchain charge transport, and iv) a too high LUMO level (usually between -2.7 and -3.2eV [175]). To solve these issues, Pei et al. [176], have synthetized a benzodifurandione-based PPV (BDPPV, Figure 40 right). BDPPV is characterized by the presence of strong electron withdrawing carbonyl groups that, on one side, lower the LUMO level and, on the other, form H-bonds to prevent isomerization of the conjugated backbone. Furthermore, side chains (R = 4-octadecyldocosyl groups) improve solubility and processability. BDPPV has a mobility of 4 orders of magnitude higher than PPV (1 cm^2 $V^{-1}s^{-1}$).

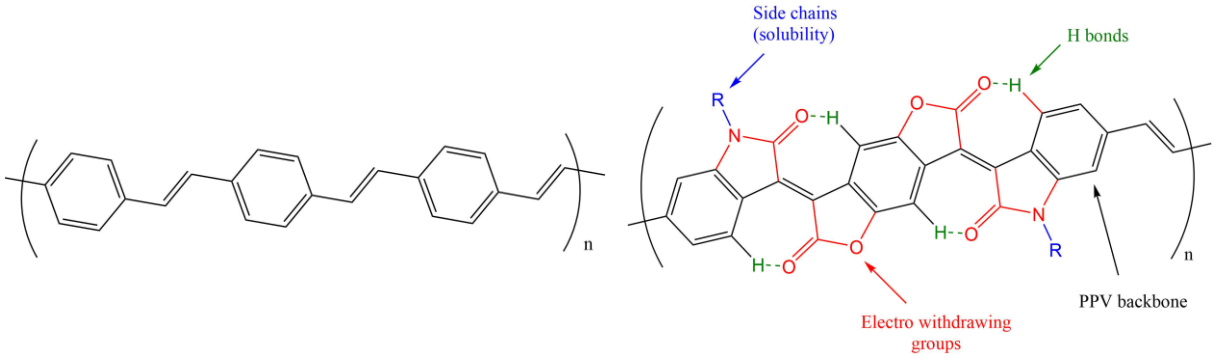

Figure 40. on the left chemical structure of poly p-phenylene vinylene polymer (PPV). On the right: chemical structure of benzodifurandione-based PPV (BDPPV) [176].

Pei et al. [177] doped BDPPV with DMBI, $(RuCp^*mes)_2$ and $DMBI_2$ (Figure 41). According to the authors, $DMBI_2$ dimer shows better doping performances than DMBI (Figure 39) and $(RuCp^*mes)_2$ because it shares both their key features: $DMBI_2$ has the same small size planar cation of DMBI while keeping the good reducibility and absence of side reactions typical of $(RuCp^*mes)_2$ dimer. However, it is important to consider that DMBI-doped BDPPV reaches almost the same conductivity of $DMBI_2$-doped BDPPV, for a higher dopant concentration.

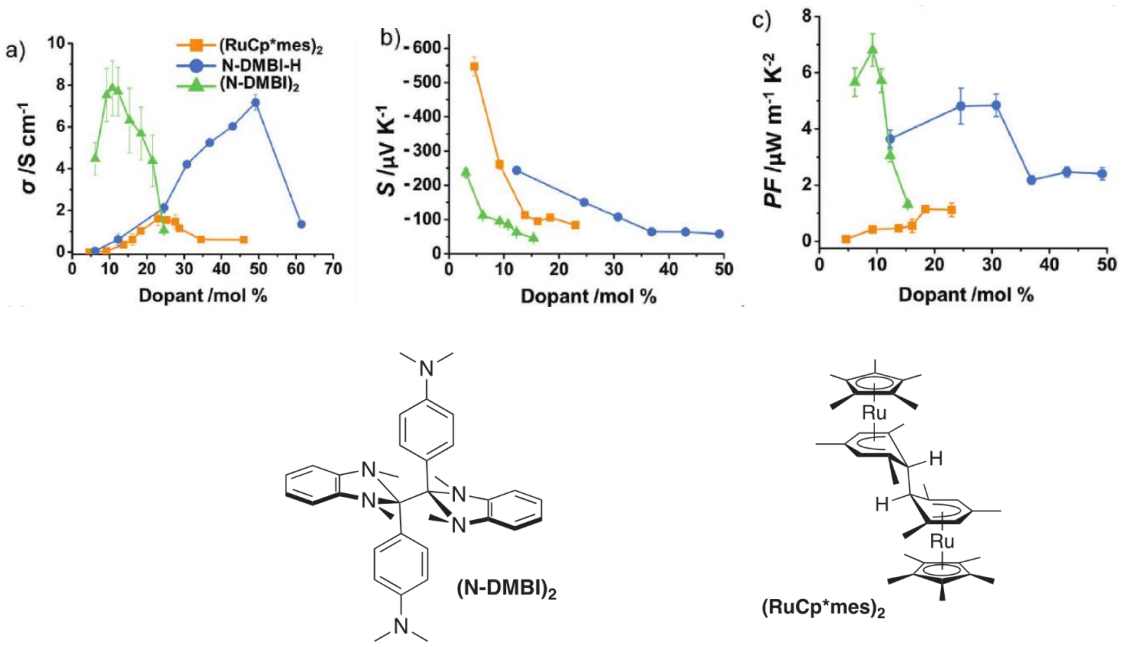

Figure 41. (a) electrical conductivity; (b) Seebeck coefficient and (c) power factor of BDPPV doped with different molecules versus the dopant concentration. On the bottom: chemical structure of $DMBI_2$ (on the left) and $(RuCp^*mes)_2$ (on the right). Image adapted from: [177].

5.3 ORGANOMETALLIC COORDINATION POLYMERS

Organometallic coordination polymers (OMCP) are macromolecules composed of metal ions connected with different organic ligands. Zhu et al. [178] studied the TE properties of poly [A_x(M-ett)] systems, where A is an ion, M is a coordination metal and ett is 1,1,2,2-ethenetetrathiolate (Figure 42), obtaining relatively high electrical conductivities (between 6 and 40 S cm^{-1}) and ZT around 0.1. In their work, they have used different counter cation such as Na^+, K^+, Cu^{2+}, Ni^{2+}, tetrabutylammonium and tetradecyltrimethyl ammonium; and different coordination metals such as Ni or Cu.

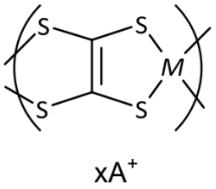

Figure 42. poly [A_x(M-ett)] structure. Image adapted from [178].

Poly [A_x(M-ett)] materials (where A is Na^+ or K^+ and M is Ni^{2+}) have excellent n-type TE properties. Poly [K_x(Ni-ett)] shows electrical conductivities up to 63 S cm^{-1} (at 440K) with a Seebeck coefficient between -50 and -200 x 10^{-6} VK^{-1}. A TE generator with poly [Na_x(Ni-ett)] as n-type leg material and poly [Cu_x(Cu-ett)] as p-type leg material leads to a power output of 750 µW and a figure of merit of 0.1 at 400K. Further studies on OMCP investigated Cu 7,7,8,8-tetracyanoquinodimethane (Cu-TCNQ, Figure 43) coordinated polymers [179]. Nanocrystals of Cu-TCNQ (NC-CuTCNQ) deposited by chemical vapor deposition on a glass substrate exhibit an electrical conductivity around 1.5 x 10^{-2} S cm^{-1} (at room temperature) and 3.7 x 10^{-2} S cm^{-1} (at 370K), and a Seebeck coefficient between -6.77x 10^{-1} V K^{-1} and 6.30 x 10^{-1} V K^{-1}. On the other hand, nanorod arrays of CuTCNQ (NrA-CuTCNQ) exhibit a far worse performance (only 5 x 10^{-3} S cm^{-1}) due to the poor packing of nanorods that hinders the charge transport along the in-plane direction.

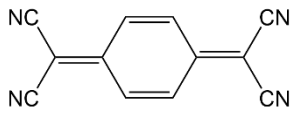

Figure 43. 7,7,8,8–tetracyanoquinodimethane molecule (TCNQ).

5.4 PERYLENE AND NAPHTALENE COMPOUNDS

Perylene bisimide (PDI, Figure 44 C) and naphthalene diimide (NDI, Figure 44 D) derive from perylene dianhydride (PDA Figure 44 A) and naphtalene dianhydride (NDA Figure 44 B), respectively. The main difference between NDI and PDI and their dianhydride counterparts consists in the presence of two functionalization groups (-R) that can provide additional customization such as solubility and crystallization tailoring. As a matter of fact, [180] the π molecular orbital has nodes in the two nitrogen positions of the diimide rings, and this characteristic allows for an easy R- substituents change without significantly altering the electronic structure. For this reason, and for their easy single-step synthesis, a huge amount of different NDI (and PDI) molecules has been studied in the past. [181] Variations in the chain length, functional group polarity, self-segregation and intramolecular binding have been explored [182]. Napthodithiophenediimide molecules (NDTI, Figure 44 E) consist in core-extended NDI derivatives [183]. They have slightly lower LUMO levels (around -4.0eV) and smaller HOMO-LUMO gaps than their NDI counterparts. These molecules are as planar as PDI derivatives, but they have less steric hinderance and an increased solubility. Furthermore, they can undergo chemical modifications on both the imide nitrogen atoms, where it is possible to insert solubilizing alkyl chains, and on the thiophene-fused α-positions, which is usually functionalized with electro-withdrawing groups to further tune the electronic structure of the molecule. As reported by Takimiya et al., N,N'-dioctyl2,7-dichloro-NDTI is an air-stable n-type semiconductor with electron mobility of 0.73 $cm^2 V^{-1}s^{-1}$ [184].

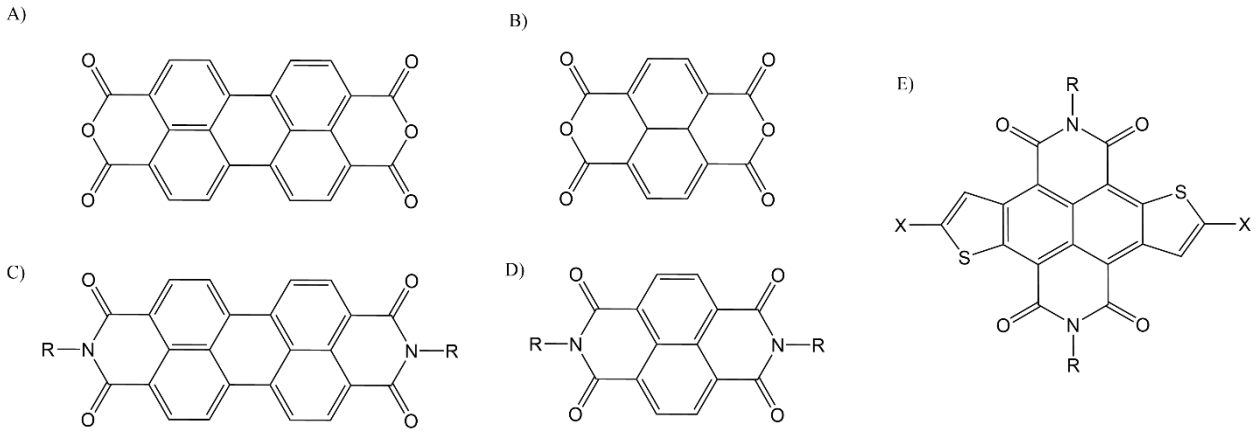

Figure 44. chemical structure of: perylene dianhydride (A), naphthalene dianhydride (B), perylene bisimide (C), napthalen diimide (D) and napthodithiophenediimide (E)

Recently, PDI derived molecules have attracted interest, as for their high electron affinity (EA, around 4eV) and for the possibility to extensively tune their properties by structural modifications [185]. PDI core can be

tethered to a tertiary amine functional group, achieving a self-doping mechanism [186]. Gregg at al. [187] have demonstrated a reversible self-doping mechanism of a water dispersible PDI with conductivities up to 10^{-3} S cm^{-1}. The relation between electrical conductivity and the tether length has been also investigated: increasing the length of the alkyl tether (from two to six methylene groups), the electrical conductivity increases hundred times, reaching 0.5 S cm^{-1} and power factor of 1.4 x 10^{-6} $Wm^{-1}K^{-2}$ (Figure 45, [188])

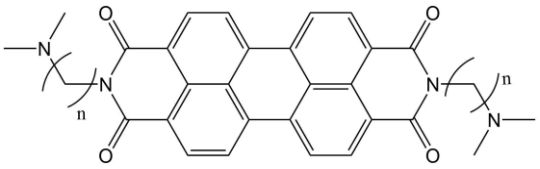

Figure 45. PDI functionalized with tertiary amine tethered with linear alkyl chains.

Bao et al. [189] have studied perylene diimide-based polymers doped with $(2\text{-Cyc-DMBI})_2$. The authors have used different linkers such as bithiophene (T2), ethylene (A), ethynylene (E) and diethynylbenzothiadiazole (DEBT) to connect the perylene diimide units. Then they have studied regioregularity and polaron delocalization of the doped polymer (Figure 46). (Table 5). The authors concluded that doped polymers do not need to follow the same design guidelines of pristine materials for OTFTs, where backbone regioregularity and crystallinity are required for the positive effect on charge carrier mobility. On the contrary, design of doped polymers aimed at giving extended polaron delocalization.

Polymer	Mn [kDa]	PDI	μ [cm^2/Vs]	Σ [S/cm]	Dopant %	LUMO [eV]
P(PDI2OD-A)	24.9	3.76	1.8 x 10^{-3}	0.27	0.75	-4.19
P(PDI2OD-DEBT)	7.5	9.12	6.5 x 10^{-3}	0.06	0.55	-4.06
P(PDI2OD-T2)	20.2	1.40	2.0 x 10^{-3}	0.0006	0.54	-3.91
P(PDI2OD-E)	6.6	1.58	0.3 x 10^{-3}	0.002	0.48	-3.98

Table 5 Summary of material characterization and electrical measurements performed in [189]. The samples were doped with $(2\text{-Cyc-DMBI})_2$. Dopant concentration is expressed as molar ratio.

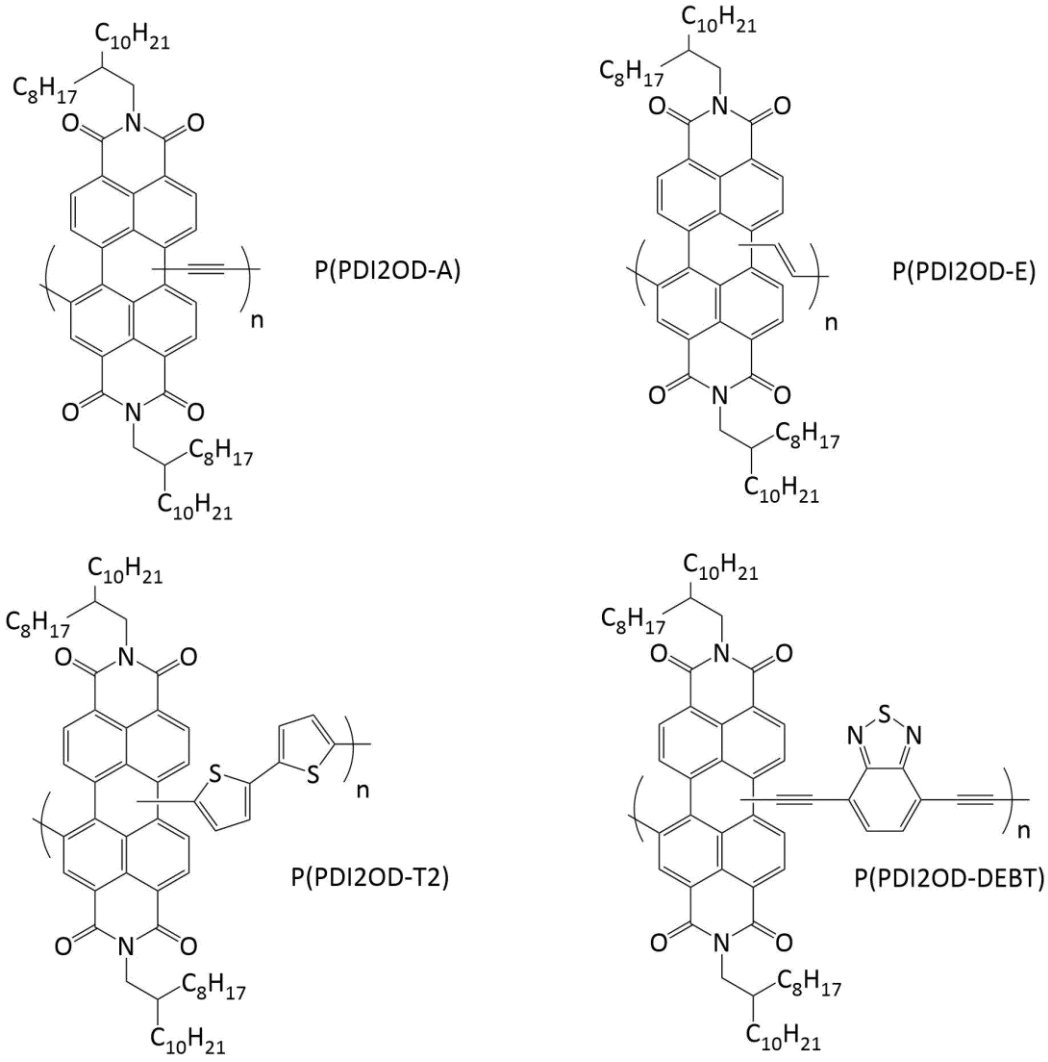

Figure 46. polymers based on perylene diimide with different conjugated linkers.

6. P(NDI2OD-T2)

Among all n-type conductive polymers, the most famous one is poly{[*N*,*N*'-bis(2-octyldodecyl)-naphthalene-1,4,5,8-bis(dicarboximide)-2,6-diyl]-*alt*-5,5'-(2,2'-bithiophene)} P(NDI2OD-T2) (Figure 47), which is the copolymer of naphtalenediimide (NDI, Figure 44 D) and bithiophene (T2). Thanks to its commercial availability, its high solubility (around 60g/L in $CHCl_3$) and its relatively high charge carrier mobility (up to 0.85 $cm^2\ V^{-1}\ s^{-1}$ [86], [185] P(NDI2OD-T2), P(NDI2OD-T2) has attracted a lot of interest for TE applications [86], [190].

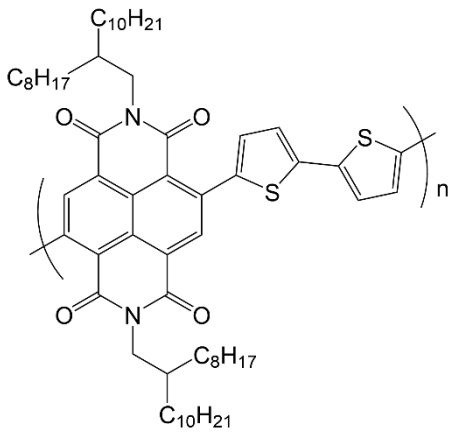

Figure 47. Chemical structure of poly{[*N*,*N*'-bis(2-octyldodecyl)-naphthalene-1,4,5,8-bis(dicarboximide)-2,6-diyl]-*alt*-5,5'-(2,2'-bithiophene)}, (P(NDI2OD-T2)).

6.1 SYNTHESIS

The synthesis of P(NDI2OD-T2) consists in the co-polimerisation of the naphthalene-based monomer (NDI2OD-Br_2) with the commercially available bithiophene monomer.

6.1.1 NDA-Br_2

The first step is the bromination of 1,4,5,8-naphthalenetetracarboxylic dianhydride (NDA) to obtain 2,6-dibromonaphthalene-1,4,5,8-tetracarboxydianhydride (NDA-Br_2). Dibromoisocyanuric acid [190] or tribromoisocyanuric acid [191] are used as brominating agents, in oleum (Figure 48). Unfortunately, the bromination is not selective, and the synthesis also leads to both the mono-brominated (NDA-Br) and the tri-brominated (NDA-Br_3) side products, which cannot be removed at this stage because of their low solubility in common organic solvents that prevents the use of common purification techniques.

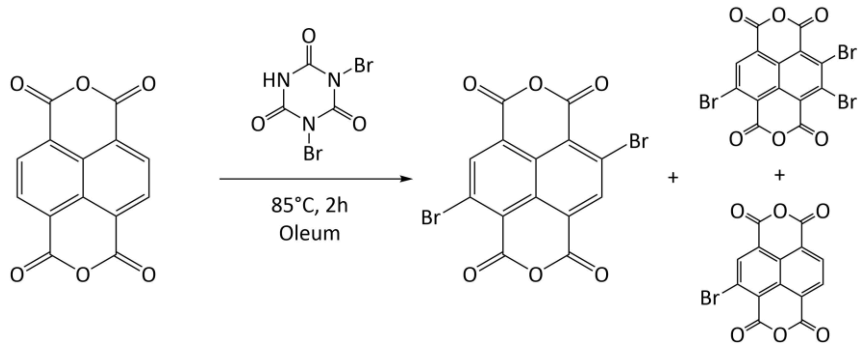

Figure 48 bromination of NDA with dibromoisocyanuric acid to obtain NDA-Br_2 **[190]**.

6.1.2 NDI2OD-Br_2

The second step is the functionalization of the NDA-Br2 with 2- octyldodecylamine to obtain NDI2OD-Br_2 (Figure 49). Since after the functionalization, the crude product is soluble in chloroform, after this step the undesired products (NDA-Br and NDA-Br_3) are removed by column chromatography using a mixture of chloroform and hexane (1:1) as eluent. It is crucial to remove NDA-Br because it acts as chain terminating group during the polymerization, strongly reducing the polymer molecular weight.

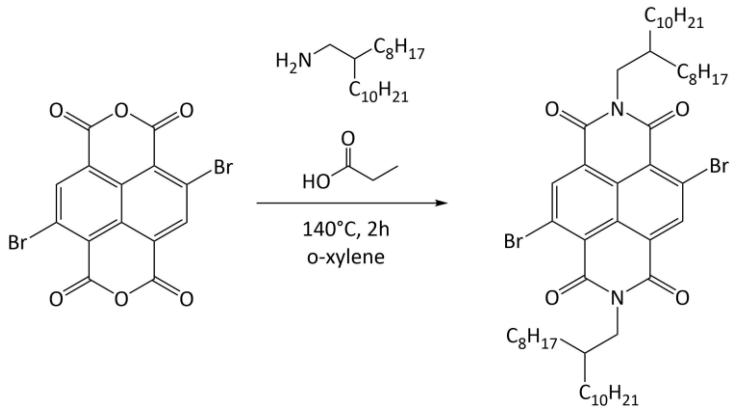

Figure 49 synthesis of NDI2OD-Br_2.

6.1.3 POLYMERYZATION

P(NDI2OD-T2) was initially synthetized by Stille polycondensation as reported by Facchetti et al. [190]. Unfortunately, such reaction route involves organo-stannanes that are highly neurotoxic compounds. [192] Kiriy et al. [193] have proposed a radical anion polymerization, that requires a symmetrical monomer and a Riekez zinc suspension. However, this last method resulted less versatile and more challenging. Recently,

direct arylation polycondensation (DOP) has gained interest for the versatile synthesis of n-type copolymers. [194] Indeed, DOP synthesis does not require toxic organo-metallic monomers, and it results faster and less expensive. The synthesis of P(NDI2OD-T2) through DOP has been firstly proposed by Sommer et al. [195] (Figure 50).

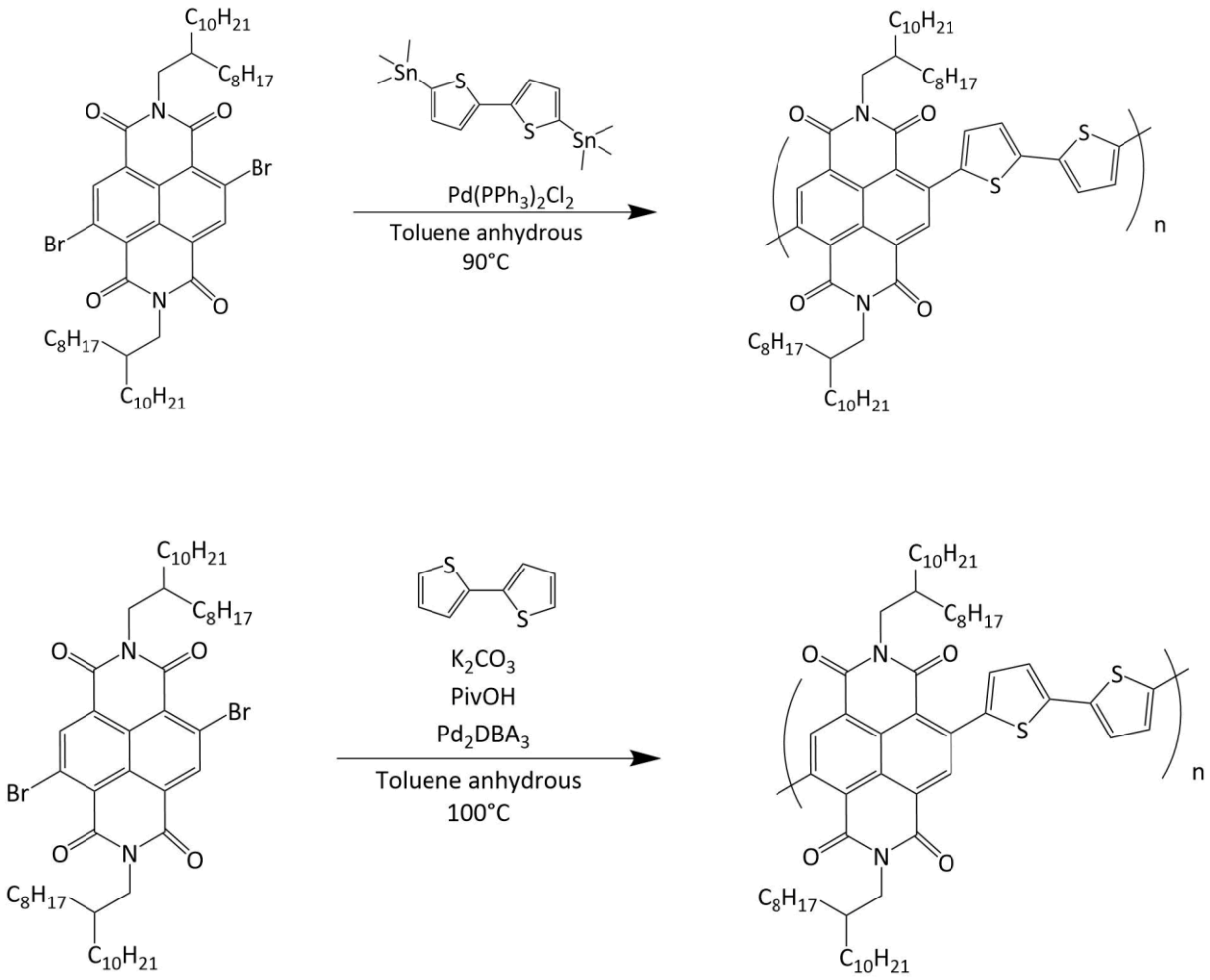

Figure 50. Synthesis of P(NDI2OD-T2). On the top: Stille reaction route, the palladium catalyst is bis(triphenylphosphine)palladium(II) dichloride ($Pd(PPh_3)_2Cl_2$) [190]. On the bottom direct arylation route. The palladium catalyst is tris(dibenzylideneacetone)dipalladium(0) (Pd_2DBA_3) [195].

6.2 STRUCTURE

Although P(NDI2OD-T2) consists of two almost planar building blocks (T2 and NDI), its structure is overall distorted, indeed there is a high torsion dihedral angle between NDI and T2 units (Figure 51, [196]). As underlined by Fabiano et al. [197], such torsion together with the donor-acceptor character of the building blocks cause a strong charge localization and causes the polaron to be strongly localized on the NDI moiety (Figure 52). Therefore, charge transport is related to inter-chain polaron hopping from two NDI units rather than intra chain polaron delocalization.

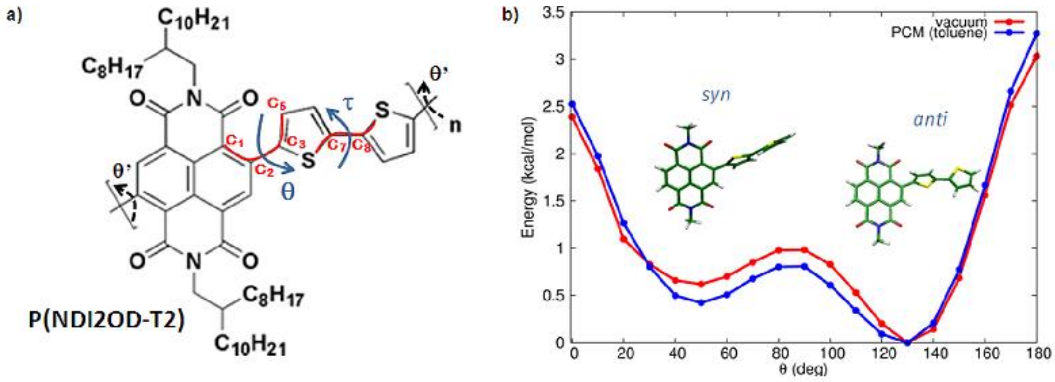

Figure 51. (a) P(NDI2OD-T2) chemical structure with indication of σ and τ dihedral angles. (b) Potential energy expressed at the variation of σ (B3LYP/6-311G**), the red line is referred to vacuum case and the blue line is referred to IEF-PCM in toluene, in both cases the polymer features methyl groups instead of alkyl chains. The authors considered τ = +148° (taken from in vacuo calculations). The polymer has two possible conformations: anti (σ = 138°) and syn (σ = 42°). Image adapted from [196].

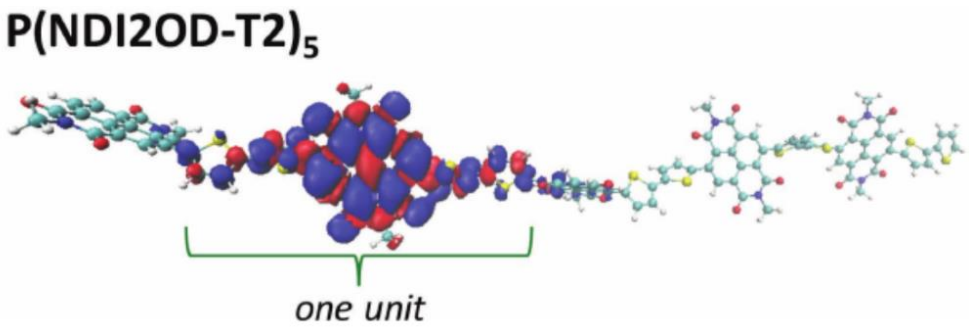

Figure 52. spin density distribution in $P(NDI2OD\text{-}T2)_5$ pentamer calculated at the UDFT level (ωB97X-D3/6-31G*). Image adapted from [197].

Initially, P(NDI2OD-T2) was supposed to lack long-range crystalline order and to likely be amorphous [86]. However, the presence of a melting-like transition in differential scanning calorimetry (DSC) suggests the presence of a crystalline phase. Heeger et al. demonstrated that P(NDI2OD-T2) morphology is rather ordered at a 10 nm scale, and it keeps a long-range relation for distances up to 1 µm [198]. The structure and molecular packing of P(NDI2OD-T2) was investigated by Salleo et al. [199]. According to X-ray scattering measures, P(NDI2OD-T2) shows a remarkable degree of in-plane order and adopts a face-on packing (i.e the π-stacking direction between NDI units is perpendicular to the substrate, Figure 53, on the left). Salleo et al. [200] have studied P(NDI2OD-T2) films annealed at 150-180°C (below melting point) and at 300-320°C (above melting point) and slowly cooled, demonstrating that melt-annealed films show an edge-on packing (i.e. the π-stacking direction between NDI units is parallel to the substrate, Figure 53 on the right).

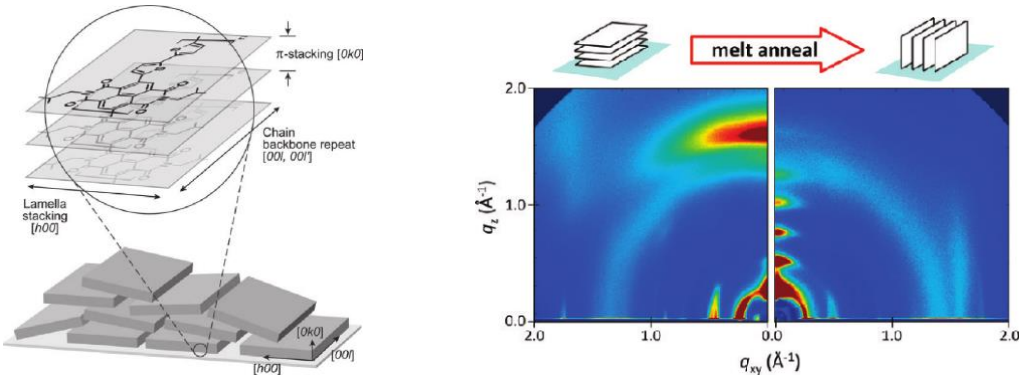

Figure 53. On the left: schematic representation of molecular packing of P(NDI2OD-T2), reporting the three directions referenced and microstructural arrangement of P(NDI2OD-T2) crystallites. On the right: 2D grazing incidence X-ray scattering of a P(NDI2OD-T2) film before and after melt-annealing and a slow cooling. Images adapted from **[199]** and **[200]**, respectively.

The optical properties of pristine P(NDI2OD-T2) have been studied by Brinkmann et al. [201]. The authors demonstrated that the transition between face-on and edge-on geometries is accompanied by a change in the absorption spectra of the polymer (Figure 54). P(NDI2OD-T2) edge-on structure have also been obtained with Langmuir-Schäfer deposition [202].

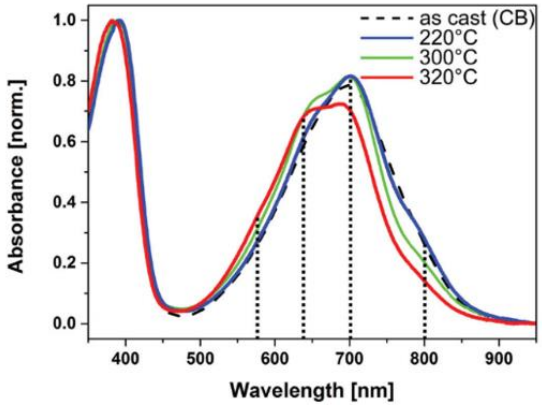

Figure 54. Absorption spectra of spin coated P(NDI2OD-T2) annealed at different temperatures. The samples have been heated for 1 min followed by cooling at a 0.5°C/min rate. Image adapted from [201].

Sommer et al. [203] used different epitaxial crystallization processes to obtain highly oriented crystals in two different polymorphs that feature either segregated or mixed interchain stacks of NDI and T2 (form I and form II, respectively, Figure 55). P(NDI2OD-T2) shows a different morphology depending on processing: at low temperatures (ca. 150°C), the π-stacking direction is face-on, whereas the direction is edge-on at high temperatures (ca. 300°C). It is important to notice that spin coated P(NDI2OD-T2) films have a face-on arrangement, but they differ from epitaxially grown form I films for a different orientation of NDI and T2 local planes with respect to the substrate. Face on P(NDI2OD-T2) spin coated films exhibit T2 units parallel to the substrate and NDI units tilted by around 42°, while epitaxially grown form I films are characterized by NDI units parallel to the substrate and T2 units tilted (Figure 56, [204]).

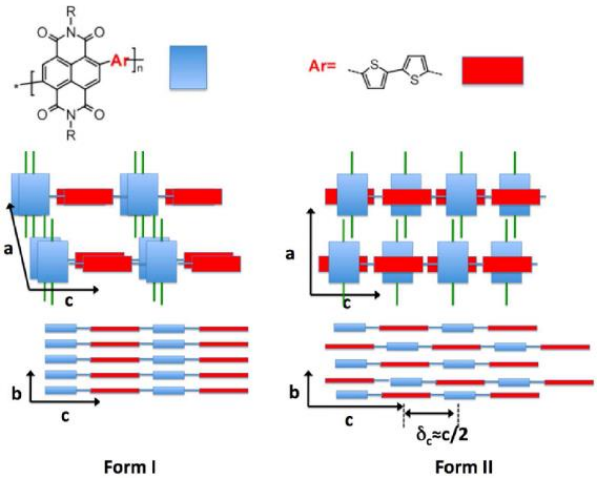

Figure 55. differences in the stacking of NDI and T2 units in form I and form II of epitaxially grown P(NDI2OD-T2) films. Form I is characterized by NDI and T2 segregated columns, while form II is characterized by the alternating π-stacking of the two moieties. Image adapted from [203].

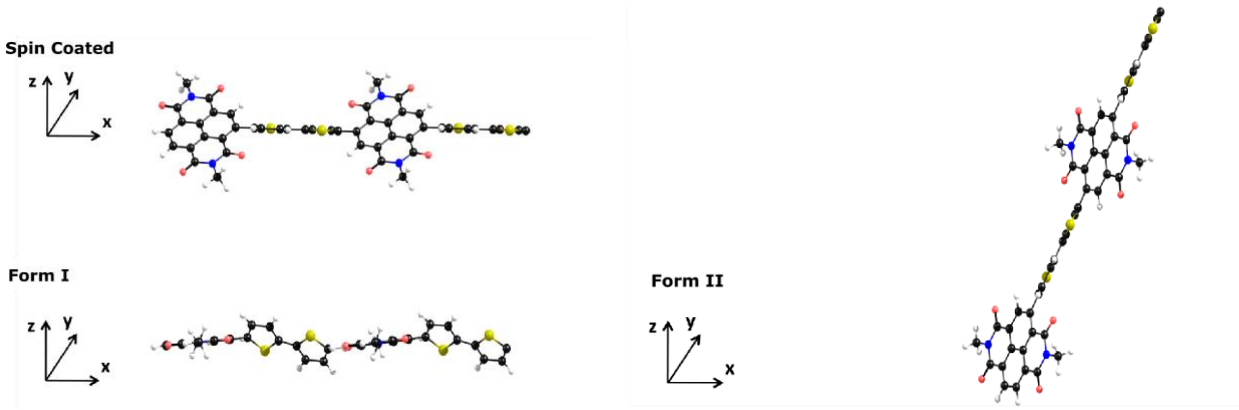

Figure 56. structure of spin coated P(NDI2OD-T2) film compared with polymorph I and II of epitaxially grown highly oriented crystalline P(NDI2OD-T2) films. Cartesian coordinate system refers to substrate surface (XY plane). Image adapted from [204].

Caironi et al. [205] have studied the relation between film morphology and charge transport, demonstrating that charge carrier mobility can be increase up to 2 orders of magnitude by controlling the size of oriented domains through the solvent selection and deposition process. Specifically, solvents that favour the formation of pre-aggregates leads to the formation of ordered domain at the solid state, hence carrier mobility.

6.3 DOPING

Kahn et al. doped P(NDI2OD-T2) with rhodocene dimers such as $(RhCp_2)_2$ (Figure 57). [206] According to the ^{1}H-NMR spectrum, $(RhCp_2)_2$ dopant does not degrade when it is exposed to air for a few hours. [169] Spin coated 50nm thick P(NDI2OD-T2) films doped at 2% (weight) with $(RhCp_2)_2$ demonstrated an increase of six orders of magnitude of electrical conductivity compared to the pristine polymer. During doping, rhodocene dimer is converted to the monomeric cation $RhCp_2^+$.

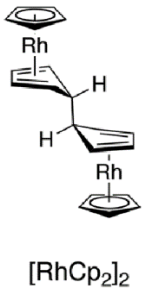

Figure 57. on the left: chemical structure of $(RhCp_2)_2$ dopant.

Crispin et al. investigated the effect of volatile polyethylenimine (PEI) impurities (low molecular weight amines, PEI vapor) on P(NDI2OD-T2). [207] In particular, the authors analysed the dependency between the electrical conductivity of the polymer and the duration of exposure to PEI vapor (Figure 58). Within 1h of exposure to PEI vapor, P(NDI2OD-T2) increases its electrical conductivity of 3-4 orders of magnitude. As expected, such rapid saturation of electrical conductivity is strong evidence that the doping effect is limited to the surface of the polymer, and the dopant cannot penetrate through the bulk.

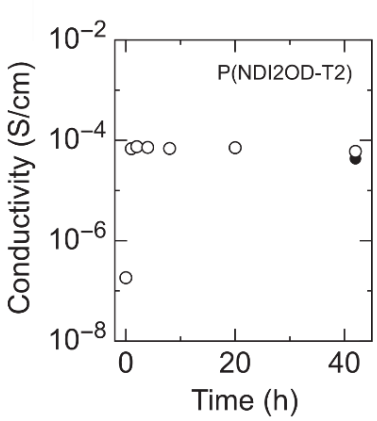

Figure 58. time-dependent electrical conductivity of P(NDI2OD-T2) exposed to PEI vapor. The black circle represents the conductivity after storing the sample in vacuum (10^{-7} mbar). Image adapted from [207].

Chabinyc et al. [208] used benzimidazole derivatives to n-dope P(NDI2OD-T2), namely the 4-(1,3-dimethyl-2,3-dihydro-1H-benzimidazol-2-yl)-N,N-dimethylaniline (DMBI, Figure 39) and the 4-(1,3-dimethyl-2,3-dihydro-1H-benzimidazol-2-yl)-N,N-diphenylaniline (DPhBI, Figure 59). In their work, the authors spin cast a 50 nm thick film and they measured the conductivity of P(NDI2OD-T2) at different dopant concentrations (3%, 9% and 25%, which correspond to a ratio between polymer repeating unit and dopant molecules of 30:1, 10:1 and 3.3:1). Electrical conductivity initially increases with the increase of the extrinsic doping molecule; however, it reaches a maximum (5×10^{-4} S cm^{-1}), then it starts to decrease (Figure 59). The decrease in electrical conductivity above the threshold concentration value was ascribed to a polymer-dopant miscibility limit which causes dopant solid-state segregation.

Figure 59. On the left: chemical structure of 4-(1,3-dimethyl-2,3-dihydro-1H-1,3-benzodiazol-2-yl)-N,N-diphenylaniline (DPhBI). On the right: electrical conductivity of a spin casted 50nm thick film of P(NDI2OD-T2) doped with either DMBI (red diamonds) or DPBI (blue diamonds) in function of doping amount (mol %). Filled diamonds refer to measures taken immediately after film fabrication; empty diamonds refer to measures taken after one month. Image adapted from [208].

Bao et al. [209] doped P(NDI2OD-T2) using neutral benzimidazoline-dimers ($DMBI_2$ Figure 60), which is relatively stable in air: after 3 weeks of storage in air it does not show any sign of degradation, and only after 3 months 1H-NMR evidences around 5% (mol) of decomposition product. Electrical conductivities obtained by doping P(NDI2OD-T2) with DMBI dimers are reported in Table 6.

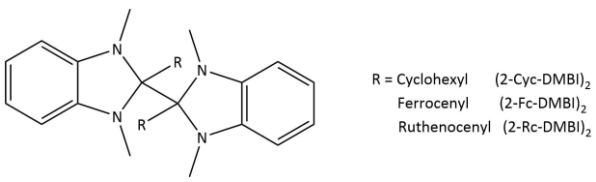

Figure 60. Chemical structure of benzimidazoline-radical dimers $DMBI_2$.

Dopant	σ	Mol%
$(2\text{-Cyc-DMBI})_2$	2.8×10^{-3} S cm^{-1}	11
$(2\text{-Fc-DMBI})_2$	7.6×10^{-3} S cm^{-1}	26
$(2\text{-Rc-DMBI})_2$	3.0×10^{-3} S cm^{-1}	12

Table 6 electrical conductivity of P(NDI2OD-T2) doped with different DMBI dimers reported in **[209]**.

Bertarelli et al. [210] further investigated the relation between dopant structure, phase segregation and doped P(NDI2OD-T2) electrical conductivity: in their work they functionalized DMBI with different side chains (Figure 61) and demonstrated that a tailored functionalization of the dopant toward bulkier and longer alkyl substituents produces a strong effect on dopant-polymer-miscibility, thus increasing doping efficiency. Conductivity reaches values as high as 7×10^{-3} S cm^{-1} in the case of DiPrBI (Figure 62). According to the structural analysis, doping causes a decrease in the lamellar stacking distance compared to pristine P(NDI2OD-T2), due to the intercalation of the dopant.

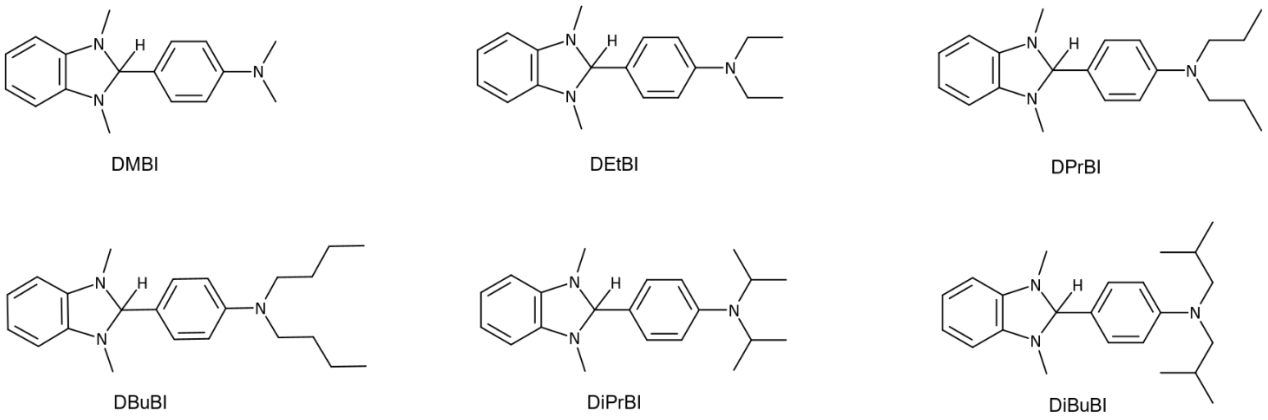

Figure 61. Chemical structure of benzimidazole dopants used in [210]. 4-(1,3-dimethyl-2,3-dihydro-1H-1,3-benzodiazol-2-yl)-N,N-diethylaniline (DEtBI);4-(1,3-dimethyl-2,3-dihydro-1H-1,3-benzodiazol-2-yl)-N,N-dipropylaniline (DPrBI); N,N-dibutyl-4-(1,3-dimethyl-2,3-dihydro-1H-1,3-benzodiazol-2-yl)aniline (DBuBI); 4-(1,3-dimethyl-2,3-dihydro-1H-1,3-benzodiazol-2-yl)-N,N-bis(propan-2-yl)aniline (DiPrBI); 4-(1,3-dimethyl-2,3-dihydro-1H-1,3-benzodiazol-2-yl)-N,N-bis(2-methylpropyl)aniline (DiBuBI).

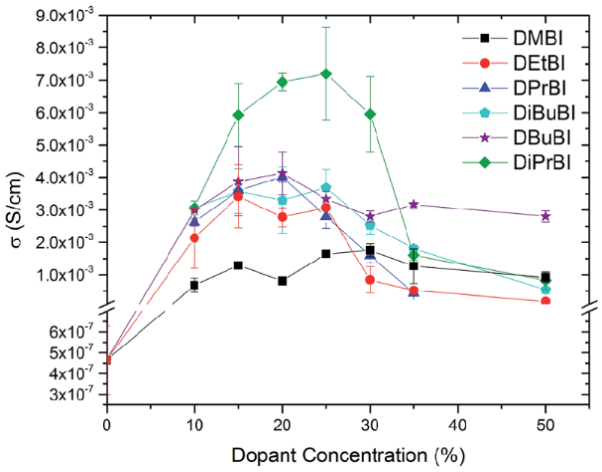

Figure 62. electrical conductivity of doped P(NDI2OD-T2) vs dopant concentration (from 10% to 50%) for all the alkyl substituted benzimidazole based dopants of Figure 61. Image adapted from [210].

It worth to notice that 1H-benzimidazoles and specifically the commercially available DMBI have become one of the most common n-type dopants. Nevertheless, its doping mechanism is still subject of debate, and it has not been completely explained. There are three main possible mechanisms, either thermally or optically activated (Figure 63), as follows:

- Hydride (H^-) transfer from the dopant to the polymer, involving the formation of a new covalent bond between the hydride and the polymer.
- Homolytic C-H bond break in DMBI with the release of a hydrogen radical atom ($H^\bullet$), followed by an electron transfer from the newly generated radical $DMBI^\bullet$ singly occupied molecular orbital (SOMO) to the polymer LUMO.
- Direct electron transfer from dopant HOMO to the polymer LUMO.

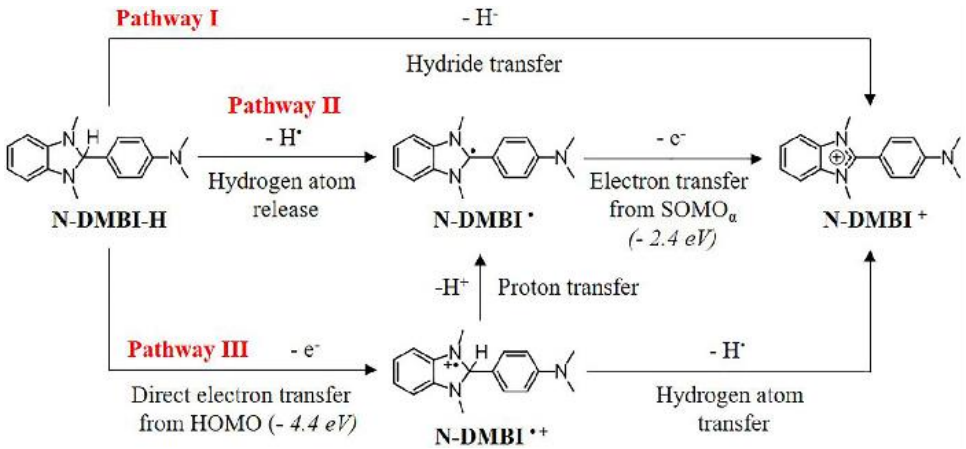

Figure 63. Different n-doping paths reported for DMBI. Image adapted from **[211]**.

The doping mechanism strongly depends on the nature of the host polymer and on the dielectric constant of the medium. [212], [211] Fabiano et al. [213] hypothesized that the DMBI n-doping of P(NDI2OD-T2) involves the thermally activated formation of an intermediate radical DMBI• followed by a direct electron transfer from the radical SOMO to the polymer LUMO. The authors studied the relationship between the benzimidazole-dopant SOMO energy and the dopant efficiency, concluding that a decrease of the radical SOMO energy increases the electrical conductivity of around 10 times (Figure 64).

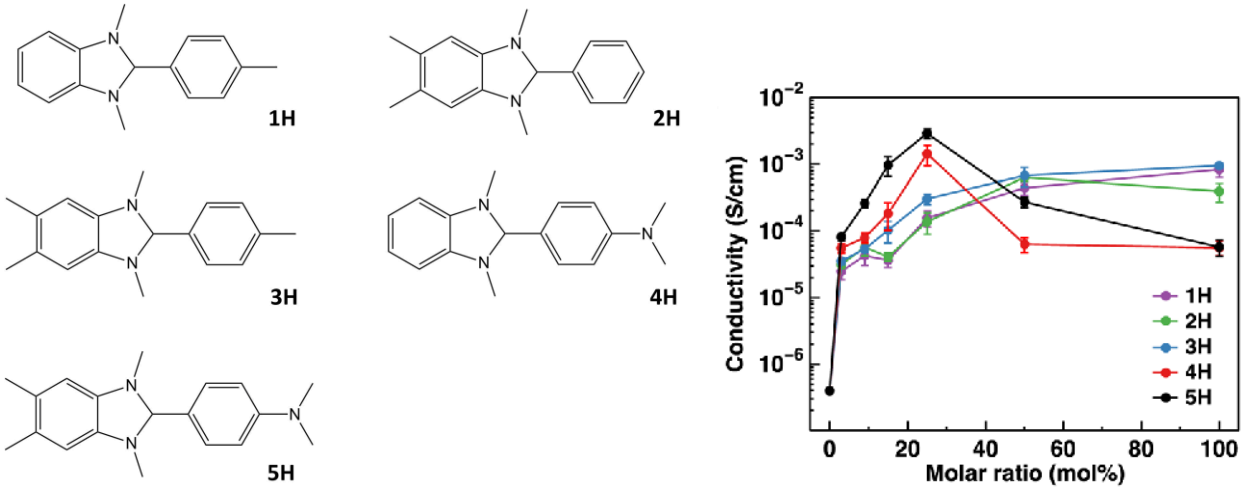

Figure 64. Chemical structure of different benzimidazole derived dopants: 1,3-dimethyl-2-(4-methylphenyl)-2,3-dihydro-1H-1,3-benzodiazole (1H, HOMO: -4.68eV, SOMO -3.02eV); 1,3,5,6-tetramethyl-2-phenyl-2,3-dihydro-1H-1,3-benzodiazole (2H, HOMO: -4.55eV, SOMO: -2.99eV); 1,3,5,6-tetramethyl-2-(4-methylphenyl)-2,3-dihydro-1H-1,3-benzodiazole (3H, HOMO: -4.54eV, SOMO: -2.91eV); DMBI (4H, HOMO: -4.62eV, SOMO: -2.82 eV); N,N-dimethyl-4-(1,3,5,6-tetramethyl-2,3-dihydro-1H-1,3-benzodiazol-2-yl)aniline (5H, HOMO: -4.49eV, SOMO: -2.73eV). On the right: electrical conductivity of P(NDI2OD-T2) doped at different concentrations. Image adapted from **[213]**.

6.4 P(NDI2OD-T2) DERIVED MATERIALS

Beyond the attempts to improve P(NDI2OD-T2) electrical conductivity through dopant optimization [208], [209], [210], several studies have been performed to develop new P(NDI2OD-T2) inspired copolymers by tailoring either the polymer backbone or the polymer side chains. Highly planarized polymers, such as BBL (poly benzo bisimidazobenzophenanthroline, Figure 65 on the left), are more conjugated than P(NDI2OD-T2), and they can achieve electrical conductivities up to three orders of magnitude more than P(NDI2OD-T2). [197] However, their main drawback is their lack of solubility in common organic solvents, which limits their processability. In order to improve electrical conductivity of P(NDI2OD-T2) while keeping its excellent solubility, Facchetti et al. [214] have synthetized a P(NDI2OD-T2) inspired polymer where the T2 moiety is replaced by a 5,5'-di(1,3-thiazolyl) unit (Tz2, Figure 66 on the left). NDI-Tz2 shows less internal steric repulsion than NDI-T2, promoting a more planar chain structure. According to DFT, P(NDI2OD-Tz2) has a greater conformational freedom than P(NDI2OD-T2): at room temperature, P(NDI2OD-Tz2) all quasi planar conformations ($-20° < \theta < +20°$) are populated (Figure 66 on the right). Upon doping with tetrakis(dimethylamino)ethylene (TDAE), an electrical conductivity of 0.06 Scm^{-1} (3 min TDAE vapor exposure) and a PF of 1.5 $\mu Wm^{-1}K^{-2}$ (around 5 times greater than the value obtained doping P(NDI2OD-T2) with TDAE) were obtained.

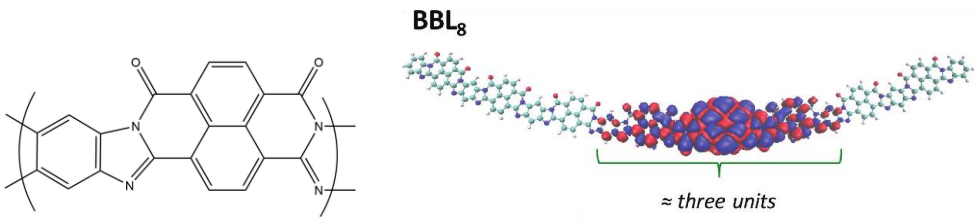

Figure 65. On the left: chemical structure of poly (benzo bisimidazobenzophenanthroline) (BBL). On the right: spin density distribution in $(BBL)_8$ octamer calculated at the UDFT-BS level (ωB97X-D3/6-31G*). Image adapted from [197].

Koster et al. [215] synthetized a P(NDI2OD-T2)-inspired polymer replacing alkyl chains with polar triethylene glycol side chains (P(NDI2TEG-T2), obtaining a strong increase of electrical conductivity after doping the polymer with DMBI (0.17 Scm^{-1}) (Figure 67). According to the authors, the 200-fold increase of electrical conductivity is due to the presence of TEG chains that greatly reduce the dopant segregation and that increase the dopant dispersion into the polymer matrix. Furthermore, the presence of polar side chains potentially increases the application of aqueous electrolytes. [216]

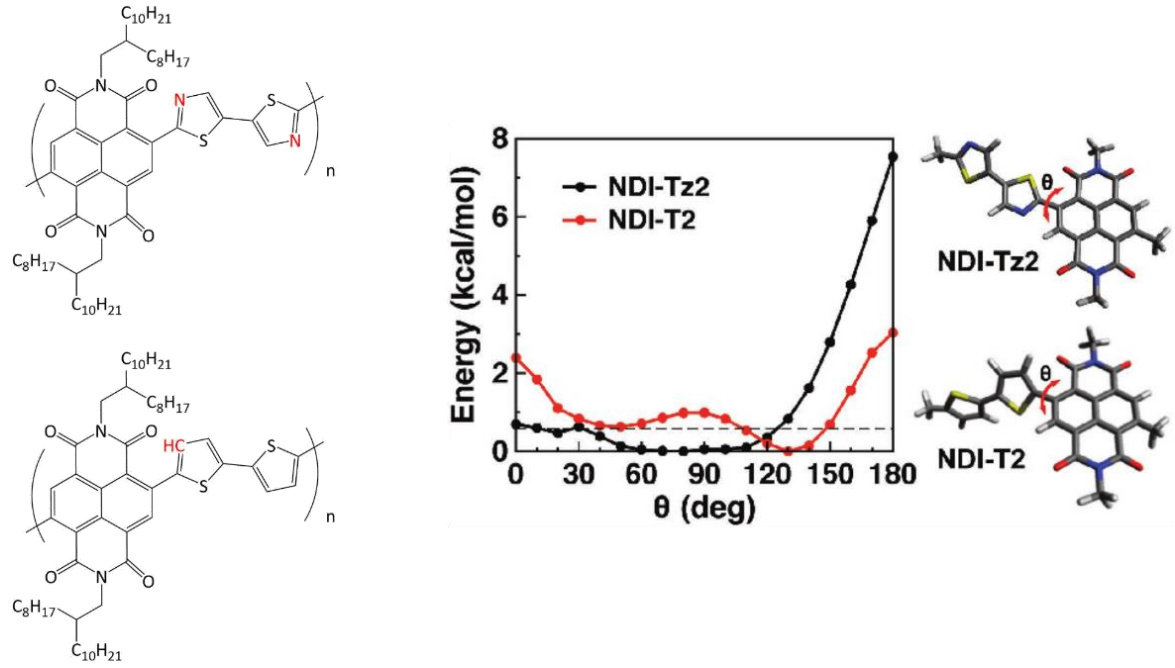

Figure 66. on the left: comparison between chemical structure of P(NDI2OD-T2) and chemical structure of P(NDI2OD-Tz2). On the right: comparison between P(NDI2OD-Tz2) (black line) and P(NDI2OD-Tz2) (red line) potential energy expressed at the variation of torsion dihedral angle σ (ωB97X-D/6-311G**). The horizontal dashed line represents the energy available to the system at room temperature (around 0.6 kcal/mol at 298K). Image adapted from [214].

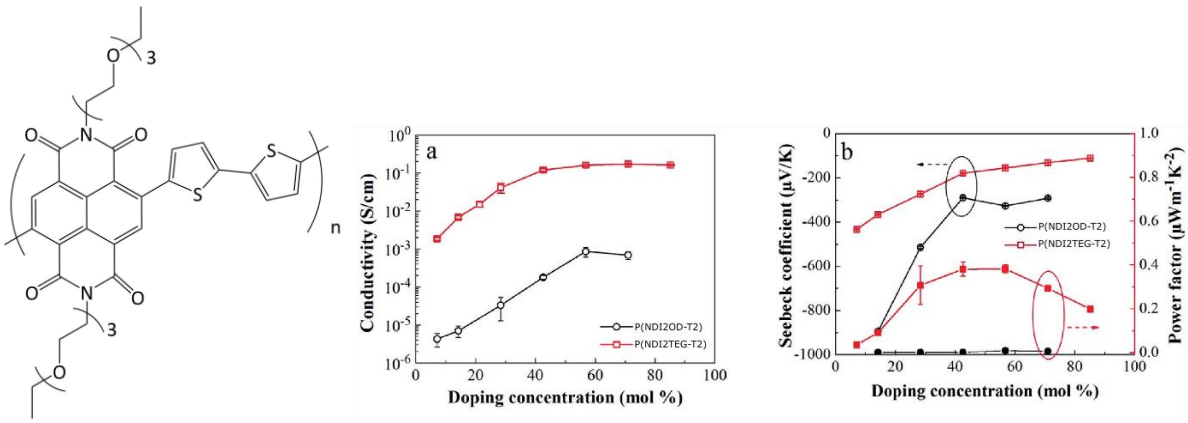

Figure 67. on the left: chemical structure of P(NDI2TEG-T2). On the right: electrical conductivities (on the left) and Seebeck coefficient and power factor (on the right) of doped P(NDI2OD-T2) (black line) and P(NDI2TEG-T2) (red line) at different doping levels. Image adapted from [215].

Given the positive effect that glycol side chains have on the dopant-polymer miscibility, Müller et al. [217] have synthetized P(gNDI-gT2) (Figure 68), a P(NDI2OD-T2)-inspired polymer that carries glycol-based side chains both on the NDI and on the T2 moieties. A film of P(gNDI-gT2) 20% doped with DMBI exhibits an electrical conductivity of over 10^{-1} Scm^{-1} and a PF up to 0.4 $\mu WK^{-2}m^{-1}$. Furthermore, it maintains its electrical conductivity for about 20 minutes even if exposed to air.

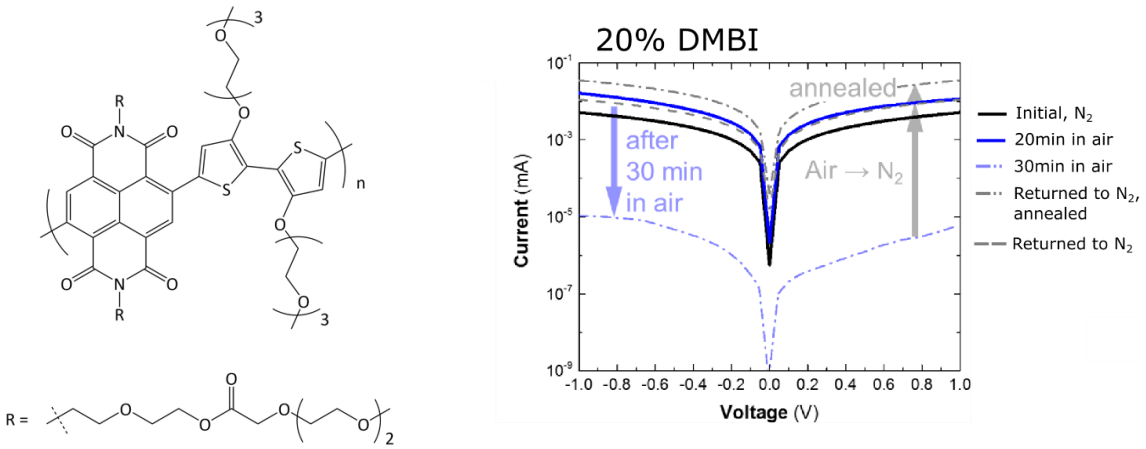

Figure 68. chemical structure of P(gNDI-gT2). On the right, electrical current vs voltage of P(gNDI-gT2) doped with 20% (mol) of DMBI. Image adapted from [217].

Koster et al. [218], have further modified the structure of P(NDI2OD-Tz2) by adding glycol side chains to the thiazole unit (P(NDI2TEG-2Tz, Figure 69). The resulting material, when 21% doped with DMBI exhibits an electrical conductivity of 1.8 Scm^{-1} and PF of 4.5 $\mu WK^{-2}m^{-1}$.

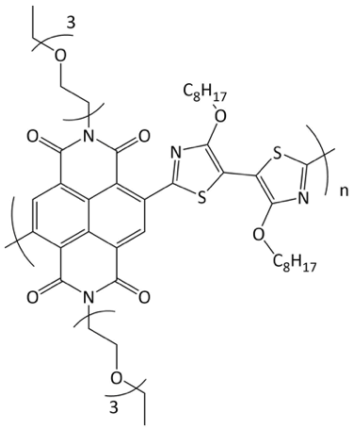

Figure 69. chemical structure of P(NDI2TEG-2Tz).

Finally, Caironi et al. [219] have substituted two imide oxygen atoms with a sulphur atom (Figure 70). This modification lowers the LUMO level, of the resulting 2S-trans-PNDI2OD-T2 polymer, which remains stable over 16h of air exposure after doping. Pristine 2S-trans-PNDI2OD-T2 has an electrical conductivity of 4 x 10^{-6} Scm^{-1}. When DPBI-doped (15% w/w), 2S-trans-PNDI2OD-T2 reaches an electrical conductivity of 6 x 10^{-3} Scm^{-1}

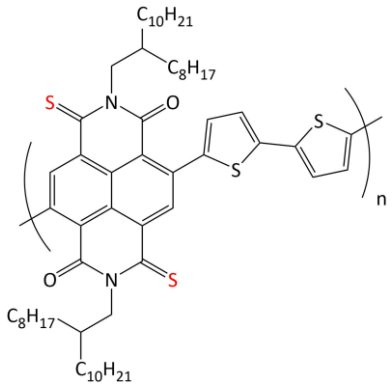

Figure 70. chemical structure of 2S-trans-PNDI2OD-T2.

7. DOPING OF P(NDI2OD-T2) WITH DiPrBI: THE ANNEALING

Despite the high number of studies on 1H-benzimidazole-doped P(NDI2OD-T2), until today, there is a lack of a standard procedure for sample preparation. Despite variations among the specific experimental methods, doping procedure often involves similar steps, namely i) P(NDI2OD-T2) is dissolved in an organic solvent, ii) the dopant is added to the P(NDI2OD-T2) solution, iii) the resulting mixture is spin coated under inert atmosphere and iv) the deposited films are annealed for several hours. Often annealing is carried at 150°C for 6 hours under N_2 atmosphere [208], [220], but there are several cases where milder conditions (from 80 to 120°C) [215], [221] have been adopted from few minutes up to a few hours [209], [222].

Given the supposed thermal-activation nature of benzimidazole-derived dopants, [213], [220] our first aim was to better understand the optimal timing and steps for the doping. Initially, we have focussed on DiPrBI dopant (reported as one of the most effective benzimidazole-derived dopants [210]) and we have studied the effect of annealing time and temperature on its interactions with P(NDI2OD-T2).

7.1 ELECTRICAL CHARACTERIZATION

To provide a benchmark for doped samples, we firstly measured the electrical conductivity of pristine P(NDI2OD-T2) films annealed at 70 °C, 110 °C and 150 °C for different amounts of time. Additional details regarding the electrical characterization measurements can be found in the Experimental chapter.

The annealing temperatures were chosen considering the wide range of values reported in literature, which spans from rather mild conditions [221] up to 150 °C [208]. Regardless the annealing time and temperature, the electrical conductivity remains constant around 4.0×10^{-7} Scm^{-1} for all the pristine P(NDI2OD-T2) samples (Figure 71 A). This result agrees with literature, which reports significant changes of P(NDI2OD-T2) morphology, thus of electrical conductivity, only in the case of either annealing assisted by rubbing or at very high annealing temperatures (over 300°C). [200], [201]

Two different dopant concentrations (molar ratios) were selected to dope P(NDI2OD-T2) films, namely 76% and 100%; the first one corresponds to the optimal dopant concentration for the P(NDI2OD-T2)-DiPrBI pair, while the second is above the dopant segregation threshold (Figure 71 B, [210]).

One of the most interesting results was obtained measuring the electrical conductivity of the doped *as-spun* films: at room temperature, without any annealing process, the electrical conductivity is in the order of 10^{-3} Scm^{-1}, which is around four orders of magnitude higher than the pristine polymer. Furthermore, regardless the specific dopant concentration, all the samples exhibit a similar electrical conductivity, with a mean value of $1.8 \pm 0.4 \times 10^{-3}$ Scm^{-1} (Figure 71 C). These experimental results clearly prove that the 1H-benzimidazole dopant is already active at room temperature and that, contrary of what it is often reported in literature, a thermally activated doping mechanism is not strictly needed for the P(NDI2OD-T2)-DiPrBI pair.

Nevertheless, the doped P(NDI2OD-T2) samples exhibit a further increase in electrical conductivity once the films are annealed; in this case, different result are achieved depending on both the annealing temperature and the dopant concentration.

For all the annealing temperatures, an excessive dopant concentration (i.e. dopant molar ratio of 100%) leads to a lower electrical conductivity with respect to the case of the optimal 76% DiPrBI:P(NDI2OD-T2) molar ratio, despite the annealing time (Figure 71 C). This result further confirms what was previously reported by Chabinyc et al. [208] and by Bertarelli et al. [210] regarding the decrease of the doping efficiency at high dopant concentration, due to the phase segregation that hinders dopant-polymer interaction. As a consequence, no further measures were carried out on 100% DiPrBI doped P(NDI2OD-T2) samples.

In the case of annealing performed at high temperatures (i.e. 150°C and 110°C), the electrical conductivity of the 76% doped samples exhibits an interesting trend: it almost constantly increases in the first 15-30 minutes, than it reaches a plateau for a longer annealing time (Figure 71 D). Accordingly, it is possible to speculate that the doping mechanism is composed of multiple stages.

The first one occurs at room temperature and causes a dramatic increase (more than 3.5 orders of magnitude) of electrical conductivity. Furthermore, since it was infeasible to isolate a doped, yet not-annealed film with an electrical conductivity comparable to the one of a pristine sample, it is possible to conclude that the first stage progresses very rapidly. Namely, it occurs within 1 minute from film deposition, or it might even occur during the actual spin coating process.

The second stage is triggered by the annealing process, which occurs within the first 15-30 minutes of thermal treatment, and it is responsible of an increase of electrical conductivity of around 50-100%.

Finally, a much slower third stage, which requires up to 5 hours and produces a further 20-30% increase of electrical conductivity.

To sum up, the total contribution of the two annealing stages to the electrical conductivity amounts to an increase of 2-3 times only, way below the astonishing 5000 times increase that already occurs at room temperature during the first stage.

Surprisingly, in the case of annealing performed at low temperatures (70°C), the electrical conductivity of the doped films decreases over time, indicating that a too low annealing temperature is detrimental (Figure 71 C). This suggests that different competitive mechanisms are responsible for the electrical conductivity changes and that the thermal post-process is ruled by the annealing temperature.

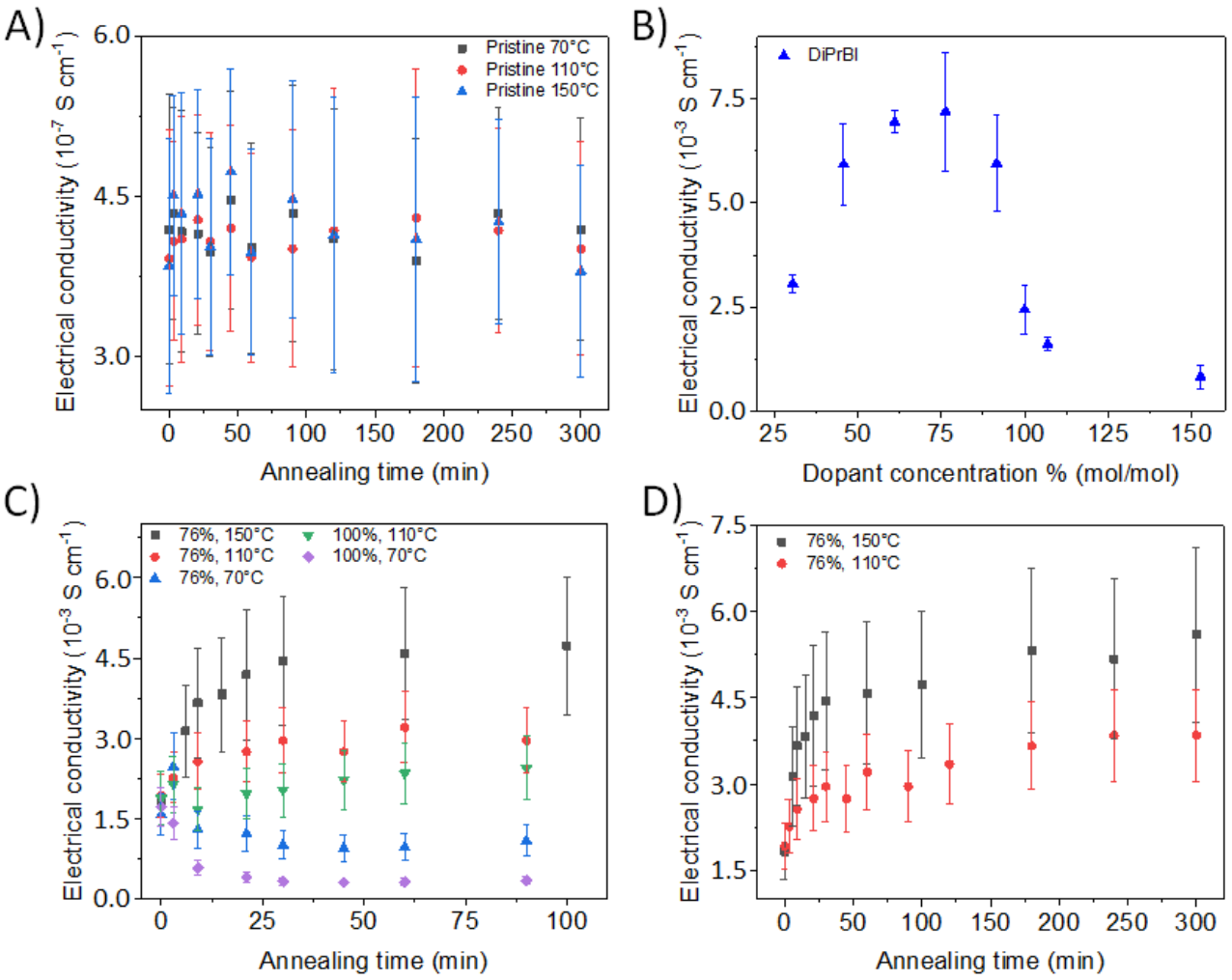

Figure 71. A) electrical conductivity of pristine P(NDI2OD-T2) films annealed at 150°C, 110°C and 70°C over time. B) electrical conductivity of P(NDI2OD-T2) films doped at different concentration with DiPrBI after a 5h annealing at 150°C. C) electrical conductivity of DiPrBI-doped P(NDI2OD-T2) spin coated films annealed at different temperatures over time. Blue, red and black series refer to P(NDI2OD-T2) films 76% doped with DiPrBI annealed at 70°C, 110°C and 150°C, respectively. Violet and green series refer to P(NDI2OD-T2) films 100% doped with DiPrBI annealed at 70 °C and 110 °C, respectively. D) electrical conductivity of P(NDI2OD-T2) films 76% doped with DiPrBI annealed for a longer duration (up to 5h).

7.2 IR CHARACTERIZATION

To identify characteristic spectroscopic signatures of the doping mechanism, we initially investigated films of P(NDI2OD-T2) doped with DiPrBI at different doping molar ratios before and after the annealing process. All the samples were prepared as described in the experimental chapter.

First, the IR spectra of a film of pristine P(NDI2OD-T2) does not change during the annealing process (Figure 72). This result further confirms what was reported in Figure 71 A. Similarly, the pristine DiPrBI film does not exhibit any appreciable modification.

Interestingly, the IR spectra of the doped, not annealed films do not differ from the sum of the spectra of the two pristine compounds weighted over the dopant amount. Indeed, it is possible to notice, an increase of intensity of the characteristic DiPrBI IR bands with the increase of dopant molar ratio (Figure 72 A, black dashed vertical lines).

After the annealing process, the situation is completely different: the intensity of the IR band of the dopant at 1120 cm^{-1} is much weaker than in the case of not annealed samples (Figure 72 B, green dashed vertical line). Moreover, the characteristic bands of pristine P(NDI2OD-T2) weaken while the doping molar ratio increases. The most noticeable signal reductions are the C=C stretching (1570 cm^{-1}) and the symmetric and anti-symmetric C=O stretching (1706 cm^{-1} and 1666cm^{-1}, respectively). Finally, new absorption features arise with the increase of dopant concentration, namely the new band at 1638 cm^{-1} which cannot be ascribed neither to the unreacted dopant nor to the pristine polymer (Figure 72 B). These bands can be ascribed to the polaron formation and can be exploited to monitor the doping evolution through vibrational spectroscopy. More details regarding Raman spectroscopy results, computational details and other dopants (such as DPhBI) can be found in ref. [220].

Worth to notice, the time passed between the drop casting of Figure 72 samples and the actual IR measure is around 5 minutes. According to the electrical characterization, the first stage of the doping mechanism occurs remarkably fast at room temperature (Figure 71). Therefore, it would be reasonable to conclude that the doped samples whose spectra is showed in Figure 72A have already undergone the first stage of doping. Nevertheless, their IR spectra is equal to the IR spectra of pristine P(NDI2OD-T2).

However, it is important to consider, that the measures were carried out in air and that the presence of oxygen and humidity partially hindered the effect of doping mechanism. This aspect will be further discussed in the next paragraph.

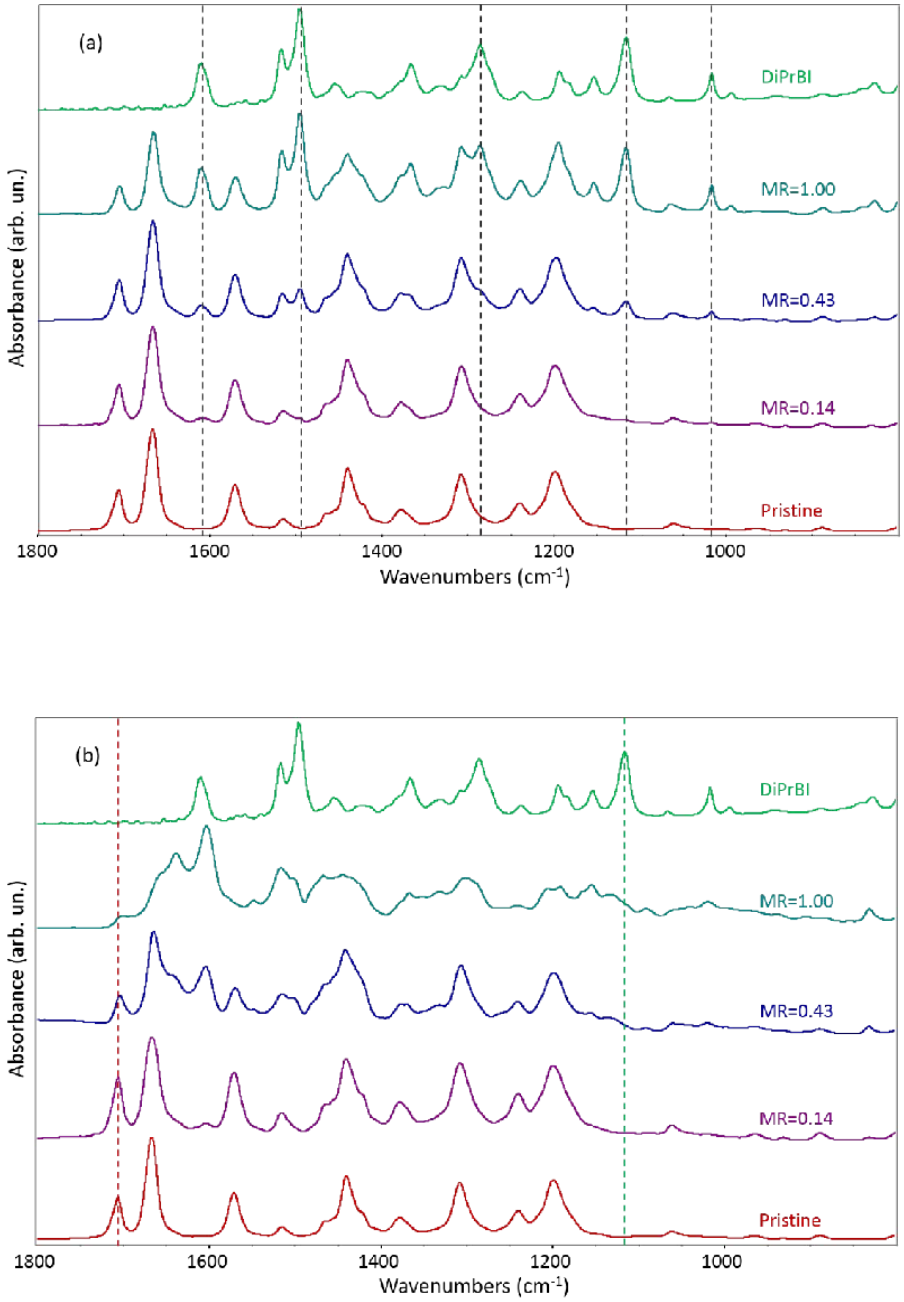

Figure 72. IR spectra of drop casted films from chloroform of pristine P(NDI2OD-T2) (in red), pristine DiPrBI (in green) and P(NDI2OD-T2) doped at 100%, 43% and 14% molar ratios with DiPrBI (in light blue, dark blue and violet, respectively). The spectra on the top (a) are recorded before annealing, the spectra on the bottom (b) are recorded on the same samples after 6h annealing at 150°C in N_2. The black dashed lines mark the strong absorption features of DiPrBI, the red dashed line shows the trend of the symmetric C=O stretching of P(NDI2OD-T2) varying the dopant concentration.

As an improvement to the previous measure, after film deposition, the samples were quickly introduced inside a Schlenk tube and were treated with three vacuum-argon cycles. Furthermore, FT-IR transmission spectra of the drop-casted films were acquired inside a sealed heating chamber under a copious N_2 flux.

We have initially prepared a 100% doped P(NDI2OD-T2) sample and, without annealing it, we have recorded the evolution of the IR spectra over a 120-minute interval. During the 2-hour period, the intensity of the C=O symmetric stretching band (at 1706cm^{-1}) decreases, while the new IR band at 1638cm^{-1} rises over time (Figure 73, red dashed line).

Worth to notice that this time, since the IR spectra were measured in an oxygen and humidity free chamber, even at t = 0 min, the intensity of the IR band at 1638cm^{-1} is nonzero. This agrees with the result of the electrical characterization, and it is another strong evidence of the presence of a doping mechanism stage that occurs at room temperature.

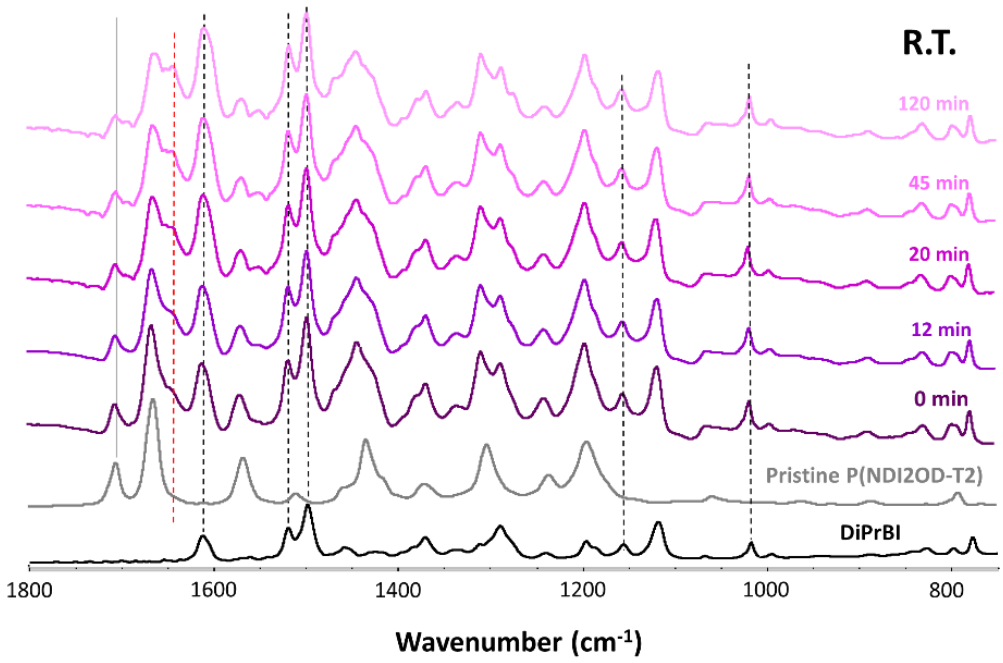

Figure 73: IR spectra of P(NDI2OD-T2) 100% doped with DiPrBI. The sample was left under N_2 atmosphere at room temperature and IR spectra were recorded over time. IR spectra of pristine P(NDI2OD-T2) (grey) and DiPrBI (black) are reported for comparison. Dashed black lines correspond to intense absorption features of DiPrBI. The grey solid line (1706 cm^{-1}) corresponds to the CO symmetric stretching of the polymer. The red continue line (1638 cm^{-1}) corresponds to new IR transition ascribed to polaron formation.

To further investigate the results obtained during the electrical characterization, we have repeated the previous measure while annealing the samples at 110°C and at 70°C, under N_2 atmosphere. In both cases, the IR band at 1638 cm^{-1} rises over time while the band at 1706cm^{-1} decreases in intensity (Figure 74).

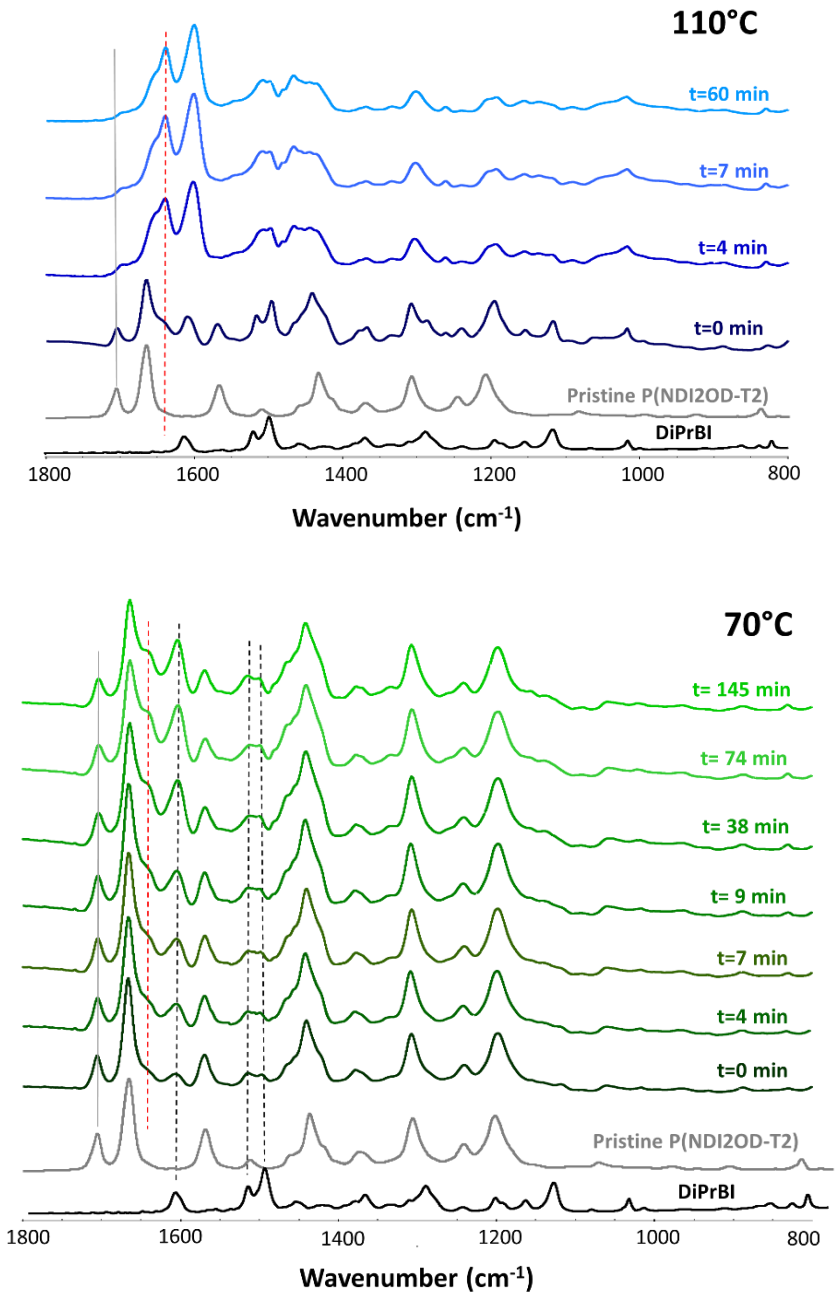

Figure 74: IR spectra of P(NDI2OD-T2) 100% doped with DiPrBI annealed under N_2 atmosphere at 110°C (on the top) and at 70°C (on the bottom) for different amounts of time. IR spectra of pristine P(NDI2OD-T2) (grey) and DiPrBI (black) are reported for comparison. The grey solid line corresponds to the CO symmetric stretching of the polymer. The red continue line corresponds to new IR transition ascribed to polaron formation.

In the case of 110°C annealing, the increase of intensity of the IR band at 1638 cm^{-1} is much faster than the other samples. Indeed, the intensity reaches a plateau within the first 7 min of annealing. Such plateau is of a higher intensity with respect to the case of both the sample left at room temperature after 120 min; and the case of the sample annealed at 70°C for 145 min. Furthermore, the intensity drop of the C=O symmetric stretching band (1706 cm^{-1}) is more pronounced than the other two samples.

In the case of 70°C annealing, the increase of the 1638 cm^{-1} band reaches a plateau after around 40 min and its intensity never achieves the value of the sample annealed at 110°C despite the annealing time. On the contrary, after 120 minutes, even the unannealed sample of Figure 73 exhibits a higher 1638 cm^{-1} band intensity (Figure 75). Although the IR measurements were performed on drop-cast thick films from a chloroform solution and the electrical measurements were carried out with spin-coated thin films from dicholorobenzene, the results of IR analysis are perfectly in agreement with the electrical characterization (Figure 71 C). Namely, a slow decrease in electrical conductivity of both samples annealed at 70°C occurs, and it suggests that annealing process could be detrimental to electrical conductivity if not performed at a sufficiently high temperature. This seems to be a general behaviour of the DiPrBI-P(NDI2OD-T2) system, unaffected by film thickness or solvent nature. Further details will be produced in the following section.

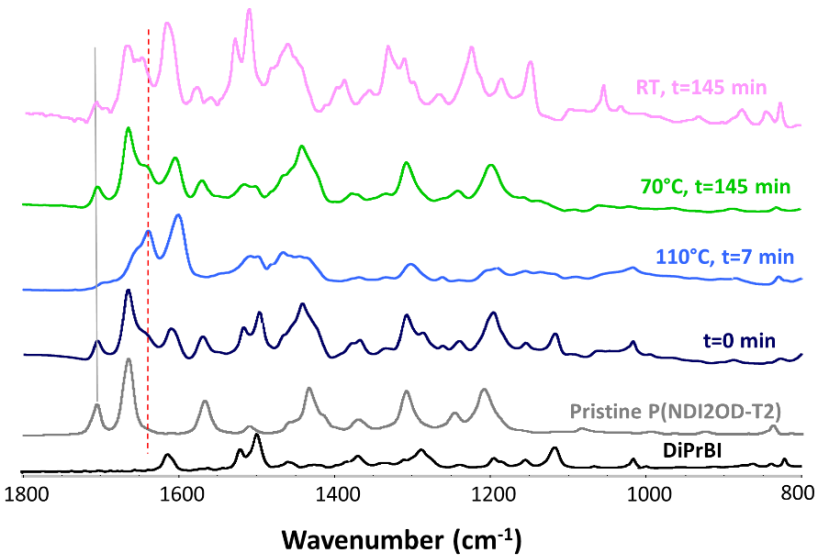

Figure 75: comparison between the IR spectra of P(NDI2OD-T2) 100% doped with DiPrBI. The sample have been annealed at 70°C for 145 min (green), annealed at 110°C for 7 min (light blue), unannealed and measured just after film deposition (dark blue) and unannealed and stored for 145 min under N_2 atmosphere (purple). The grey solid line corresponds to the CO symmetric stretching of the polymer. The red continue line corresponds to new IR transition ascribed to polaron formation.

Considering that the intensity of the IR band at 1638 cm^{-1} is proportional to the number of polarons [220], hence to the charge carrier density, it is clearly demonstrated in Figure 73, the dopant is actually able to donate charge carriers to the polymer at room temperature. However, given the rate of increase of the intensity of the IR band at 1638 cm^{-1}, it is possible to speculate that such room temperature process not only is rather slow, but it also does not occur quantitatively. Only at a sufficiently high annealing temperature the dopant is consumed, and charge carrier density further increases (Figure 74).

This seems in contrast with the electrical characterization that clearly demonstrates that the greatest increase of electrical conductivity occurs at room temperature just after film deposition (Stage I), when the IR band at 1638 cm^{-1} generally exhibits a low intensity absorption and hence when the charge carrier density is relatively low (Figure 73). During the first minutes of annealing, the remaining dopant is thermally activated, and it further increases the charge carrier density, causing the increasing of the electrical conductivity (stage II and III).

7.3 X-RAY CHARACTERIZATION

To determine the effects of the presence of the dopant and the different annealing processes on the film structure, we performed grazing incidence wide-angle X-ray scattering (GIWAXS) on both pristine and doped P(NDI2OD-T2) samples, under different annealing temperatures and times. Additional details regarding the GIWAXS characterization can be found in the Experimental chapter.

As a control, the GIWAXS measure of pristine P(NDI2OD-T2) both annealed at 110°C and not annealed was performed. The reduced 1D line profiles shown in Figure 76, are taken along the horizontal (in plane, q_{xy}) and the vertical scattering (out of plane, q_z) directions. The structure of the two pristine samples does not differ remarkably, regardless the annealing. Indeed, annealing temperature applied is too low to modify P(NDI2OD-T2) structure from a face-on to an edge-on conformation [200] - [201], further confirming the measurements of electrical conductivity displayed in Figure 71A. It is possible to notice, however, a slight decrease in the intensity of q_z (010) signal relative to the q_{xy} (100) and to the q_z (100)' signal that might be attributed to a structural relaxation or to an almost neglectable face-on to edge-on transition, which is too weak to affect electrical conductivity.

On the contrary, the as deposited 76% (mol) DiPrBI/ P(NDI2OD-T2) film exhibits a relevant morphology change. The mere presence of the dopant dramatically perturbs the P(NDI2OD-T2) structure. We observe a shift of both q_z (100)' and q_{xy} (100) peaks towards higher q values than in the case of the pristine polymer. Furthermore, the q_z (010) peak (at ≈ 1.6 $Å^{-1}$) associated with the π-stacking direction undergoes an intensity drop and a wide broadening. The decrease of the intensity of the q_z (010) peak was already reported in literature for P(NDI2OD-T2) doped with DMBI [210], [221] and it is ascribed to the orientation change of the crystallites with respect to the film substrate, from face-on to edge-on. Furthermore, the peak broadening suggests that the dopant intercalation modifies the π-stacking direction.

The measurements were then repeated for 76% DiPrBI doped P(NDI2OD-T2) annealed at 70°C and 110°C for 5, 30 and 90 minutes. In all the samples, the (001) backbone peak does not change either in intensity or in position, indicating that the doping does not influence the repeating distance along the polymer backbone axis. The (100) lamellar peak drifts toward higher q_{xy} values with the increase of annealing time and temperature. Worth to notice that after 5 minutes, the sample annealed at 110°C exhibits a (100) peak with a higher q value than the sample annealed at 70°C for 90 minutes (Figure 76). Both the 70°C and the 110°C samples are characterized by a decrease of coherence length, as indicated by the broadening and the decrease of intensity of the q_z (010) peak with respect to the q_z (100)' peak, with a more pronounced drop in the case of the 110°C annealed samples. Moreover, the 70°C annealed sample shows a sharper q_z (010) peak and with a higher intensity with respect to both the unannealed doped sample and the 110°C annealed doped sample. This behaviour suggests that at low annealing temperatures, the face-on arrangement is favoured

and further confirms the results of electrical characterization, which exhibits a reduction of electrical conductivity for the samples annealed at 70°C (Figure 71).

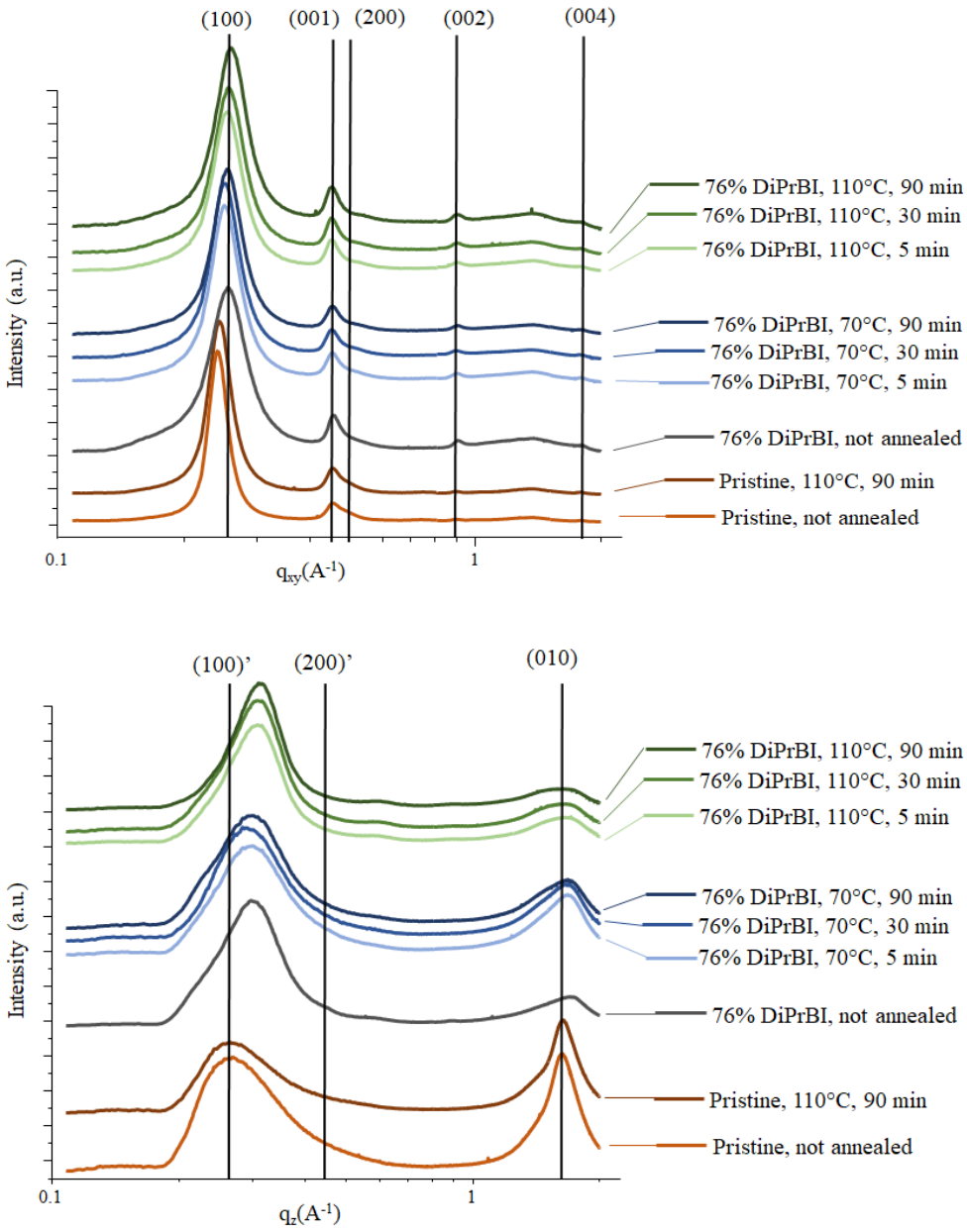

Figure 76. 1D patterns for pristine P(NDI2OD-T2) both annealed at 110°C for 90 minutes (brown) and not annealed (orange); 76% doped P(NDI2OD-T2) not annealed (grey); 76% doped P(NDI2OD-T2) annealed for increasing amount of time at 70°C (blue series); 76% doped P(NDI2OD-T2) annealed for increasing amount of time at 110°C (green series). On the top is reported the 1D q_{xy} (in plane) axis and on the right is reported the 1D q_z (out of plane axis). Data are normalized considering sample thickness and detector counts.

To sum up, these measurements demonstrate that the dopant causes a change in the crystallites orientation: from face-on to edge-on with respect to the film substrate. Furthermore, it causes the widening of the peak associated to π-stacking direction indicating a higher crystallites disorder than in the pristine samples. It is possible to speculate that DiPrBI intercalates between the quasi-planar NDI units, modifying the π-stacking distance, causing the polymer chains to rearrange and to pack in an edge-on fashion during film deposition.

All the recorded GIWAX (2D) patterns are shown in Figure 77.

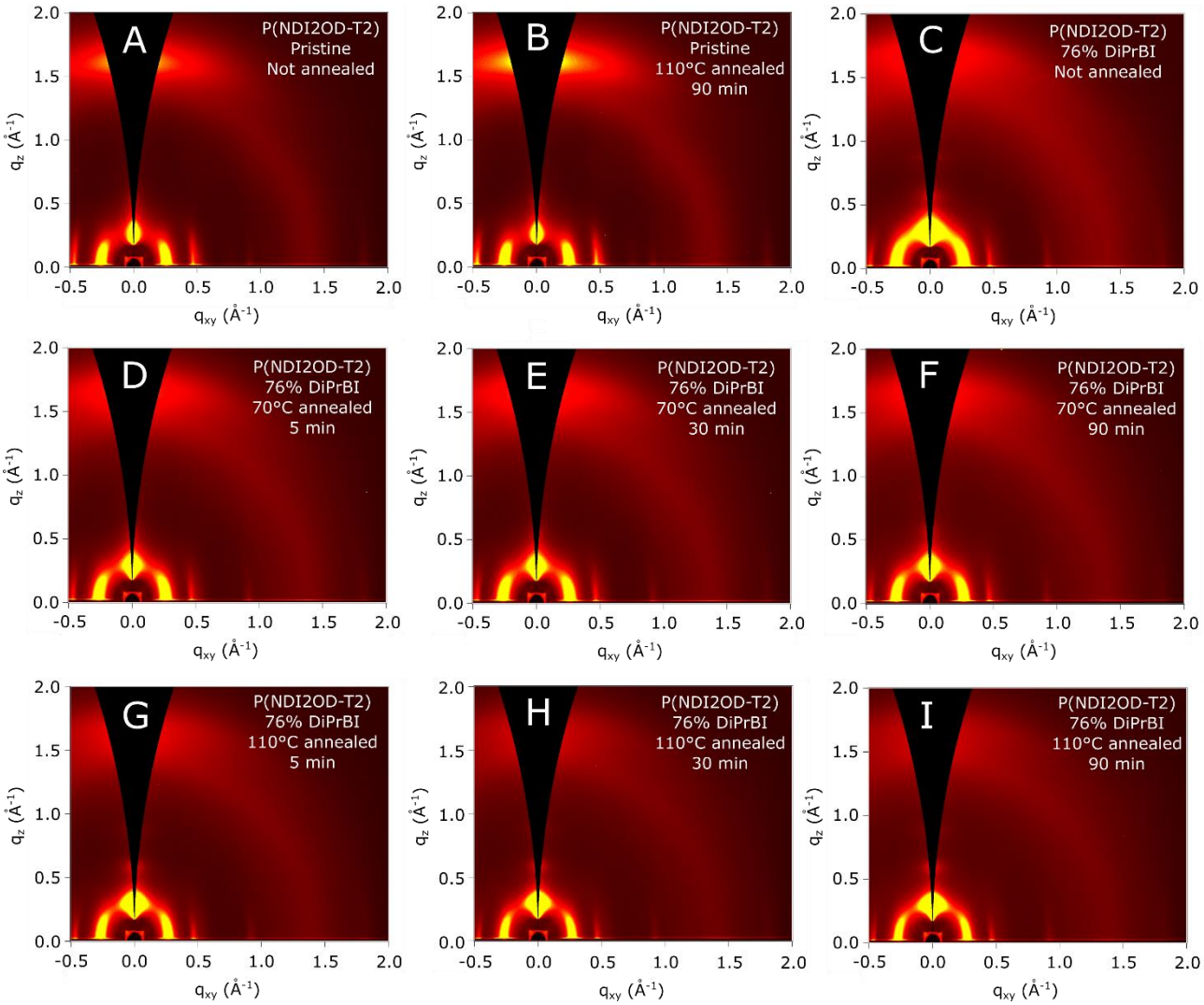

Figure 77 GIWAXS data for A) not annealed pristine P(NDI2OD-T2); B) pristine P(NDI2OD-T2) annealed at 110°C for 90 min; C) not annealed 76% DiPrBI doped P(NDI2OD-T2); D-F) 76% DiPrBI doped P(NDI2OD-T2) annealed at 70°C for 5, 30 and 90 min, respectively; G-I) 76% DiPrBI doped P(NDI2OD-T2) annealed at 110°C for 5, 30 and 90 min, respectively.

7.4 A NEW DOPING MECHANISM

According to our measurements, DiPrBI produces a strong effect on P(NDI2OD-T2) already at room temperature, nevertheless annealing is strictly necessary to reach the highest conductivity values. Therefore, the traditional concept of an exclusive thermal activation of DiPrBI should be ruled out. Here we present a new possible doping mechanism, which does not require the thermal activation of the dopant.

The change of the q_z (010) peak in the GIWAXS analysis, which is associated to the order along the π-stacking direction, suggests the presence of DiPrBI molecules between the NDI units. Both the X-ray and IR spectroscopy provide indication that significant intermolecular interactions between dopant and the polymer are established through this intercalation. We hypothesized a conformation change of the dopant while it intercalates between the narrow polymer lamellae, accompanied by a perturbation of the dopant electronic structure

According to DFT calculations (Figure 78), DiPrBI in its absolute minimum conformation (single point energy around -615849 kcal/mol) is not planar. For reference, the plane passing through the phenyl ring composed of atoms from 1 to 6 is set to be of equation Z = 0 Å. Nitrogen atoms 13 and 14 do not lay on the same horizontal plane but are close and can be considered coplanar to ease modelling. The dihedral angle between the Z = 0 Å plane and the plane passing through atoms 13, 14 and 15 is 29.3°. The dihedral angle between the plane passing through atoms from 7 to 12 and the Z=0 Å plane is 72°. The nitrogen atom 18 lays on a horizontal plane of equation Z = -4,52 Å. The Z axis is defined positive in the semi-space where the H atom of carbon atom 15 points.

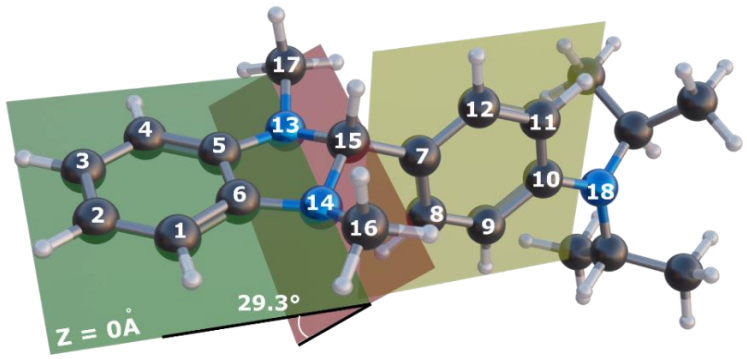

Figure 78. structure of DiPrBI in the vacuum without any geometrical constriction. Carbon atoms from 1 to 6 lay on the Z=0 Å horizontal plane, nitrogen atoms 13 and 14 are almost coplanar. The carbon atoms from 7 to 12 lay on a tilted plane whose intersection with the Z=0 Å plane generates a dihedral angle of around 72°. The angle between the Z=0 Å plane and the plane passing through atoms 13, 14 and 15 is 29.3°. The single point energy of DiPrBI is -615849 kcal/mol.

The 13 and 14 nitrogen atoms of DiPrBI are sp3 hybridized and are stereogenic centres. Figure 78 shows the sin stereoisomer that has a symmetry plane perpendicular to the Z=0 Å plane. The anti stereoisomer is chiral. The single point energy of such compound is around 9kcal/mol higher than the other isomer (Figure 79).

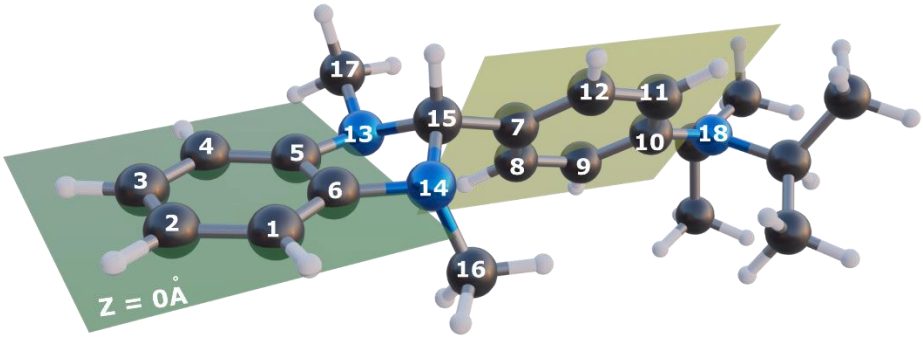

Figure 79. structure of the DiPrBI anti stereoisomer. Carbon atoms 16 and 17 were forced to lay on different sides of the Z=0 Å plane. The DFT calculated single point energy is -615840 kcal/mol, 9kcal/mol above the single point energy of sin-isomer. The calculated HOMO energy level of the anti-stereoisomer is -4.7eV, around 0.3eV deeper than the other stereoisomer.

The calculated HOMO level of DiPrBI in its minimum energy conformation (Figure **78**) is -4.4eV, which is lower than the LUMO of P(NDI2OD-T2) [189], [223], [224]. Therefore, the energy barrier to transfer an electron from dopant HOMO to polymer LUMO is around 0.5 eV (Figure 80).

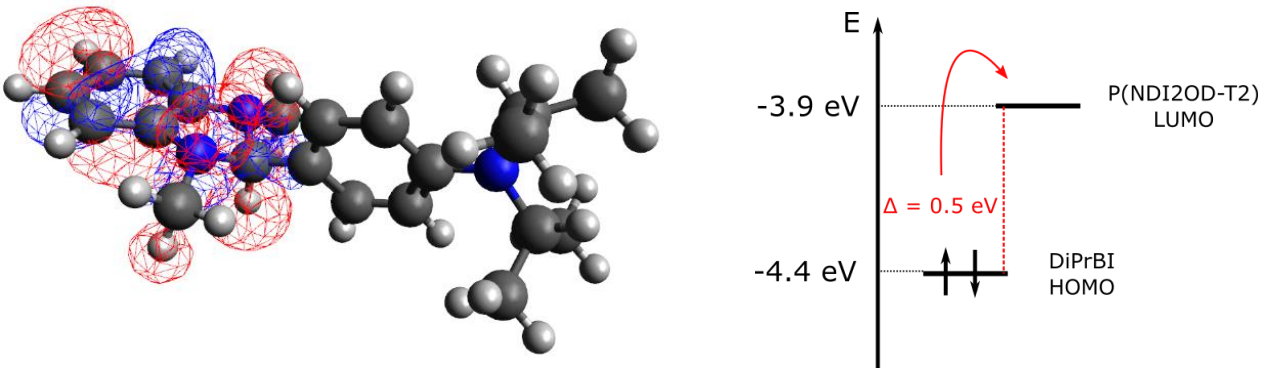

Figure 80: spatial representation of DiPrBI HOMO and comparison with P(NDI2OD-T2) LUMO according to the integer charge transfer model (Figure 24). DFT calculations performed with Orca, using B3LYP functional and 6-31G** basis set.

The 0.5eV HOMO-LUMO gap corresponds to an energy barrier of around 23kcal/mol, this value should not be easily overcome by simply mixing the dopant and the polymer. Nevertheless, according to our results, the dopant does not need thermal energy to overcome the energy barrier to donate e^- to the polymer. Therefore, we have performed DFT calculations to evaluate the amount of energy involved in the dopant-polymer interaction.

To maintain a good accuracy and an acceptable computational cost, we performed the geometry optimizations on a simplified model consisting of a single DiPrBI molecule sandwiched between two repeating units of the polymer. Furthermore, the branched octyl-dodecyl alkyl chains on the NDI moiety have been replaced with branched iso-butyl chains (Figure 81, Figure 82, Figure 83).

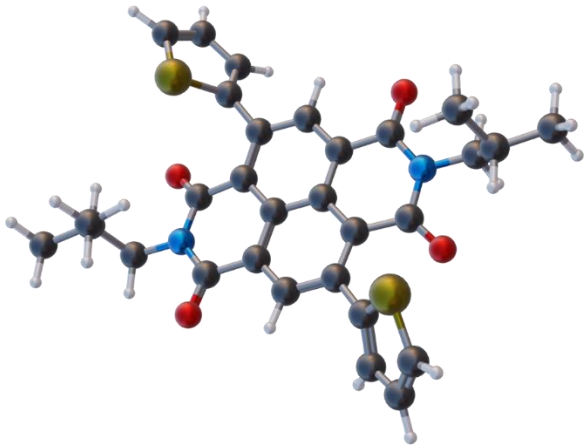

Figure 81: structure of a T-NDI2Bu-T unit. The structure was optimized using Orca with B3LYP functional and 6-31G* basis set and finally, the orbital and the energy levels have been obtained with a single point energy calculation using B3LYP functional and 6-31G** basis set. The single point energy of a single T-NDI2Bu-T unit is -1483928 kcal/mol.

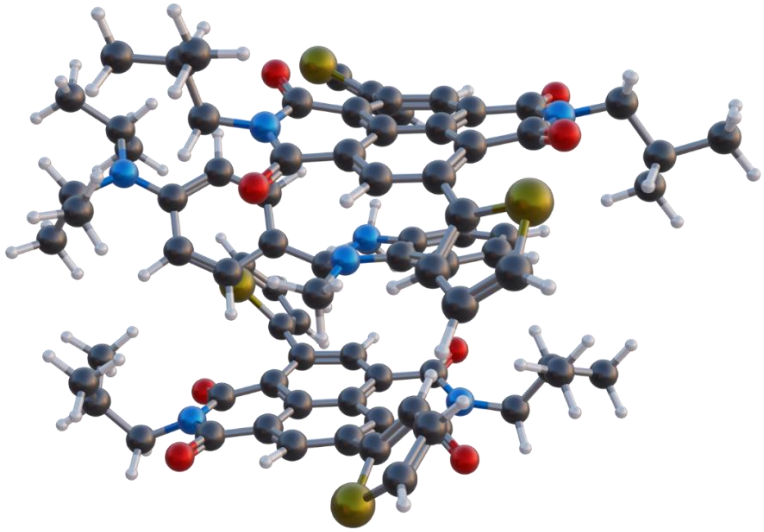

Figure 82: optimized structure of DiPrBI sandwiched between two T-NDI2Bu-T units. According to calculations, single point energy of this structure is -3583759 kcal/mol. The structure was drawn with Avogadro and was initially optimized using Orca with B3LYP functional and 6-31G* basis set and finally, the orbital and the energy levels have been obtained with a single point energy calculation using B3LYP functional and 6-31G** basis set.

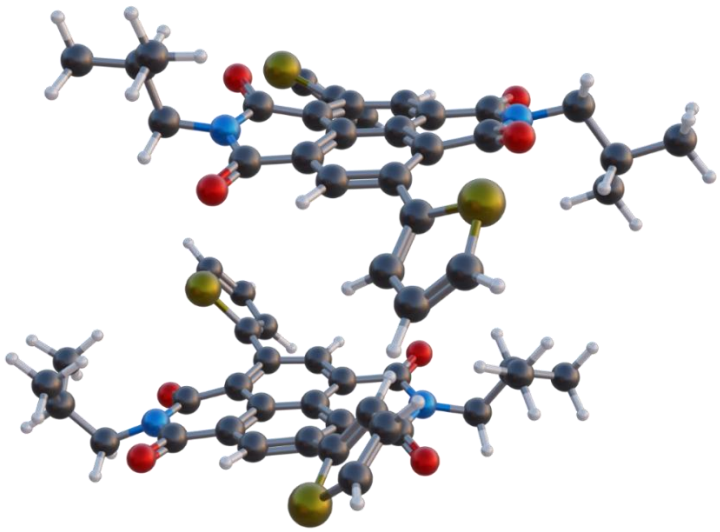

Figure 83: structure of two T-NDI2Bu-T units obtained by removing the dopant molecule from the geometry of Figure 82. The single point energy of this structure is -2.967855 kcal/mol, around twice the energy of a single T-NDI2Bu-T unit.

The interaction energy between DiPrBI and T-NDI2Bu-T can be evaluated as (Equation 59):

Equation 59 $$\boldsymbol{E_{(Interaction)} = E_{(T-NDI2Bu-T\ /DiPrBI/T-NDI2Bu-T)} - E_{(DiPrBI)} - E_{(2\ x\ T-NDI2Bu-T)}}$$

According to our calculation, the interaction energy is around -57 kcal/mol. Given the planar nature of NDI units (Figure 81), here we investigated the possibility that intercalation of the dopant between the narrow polymer lamella involves the planarization of the DiPrBI molecule.

Different planarization mechanisms have been investigated, and results are presented in the following pages.

7.4.1 Planarization A (A-DiPrBI)

The horizontal plane of equation Z = 0 Å is defined as the plane passing through the phenyl ring composed of carbon atoms from 1 to 6. Nitrogen atoms 13 and 14 and carbon atoms 16 and 17 are also coplanar. Carbon atoms from 7 to 12 are constricted on a horizontal plane of equation Z = k, where k spans from 0.477 Å to –0.954 Å. This set of structures will be referred as A-DiPrBI. For each k value, the structure was optimized using Orca with B3LYP functional and 6-31G** basis set. The dopant structures, the HOMO energy as a function of both the structure conformation, $E_{HOMO}(k)$ and the planarization energy costs, $E_{HOMO}(E_{planarization})$ are reported in Figure 84.

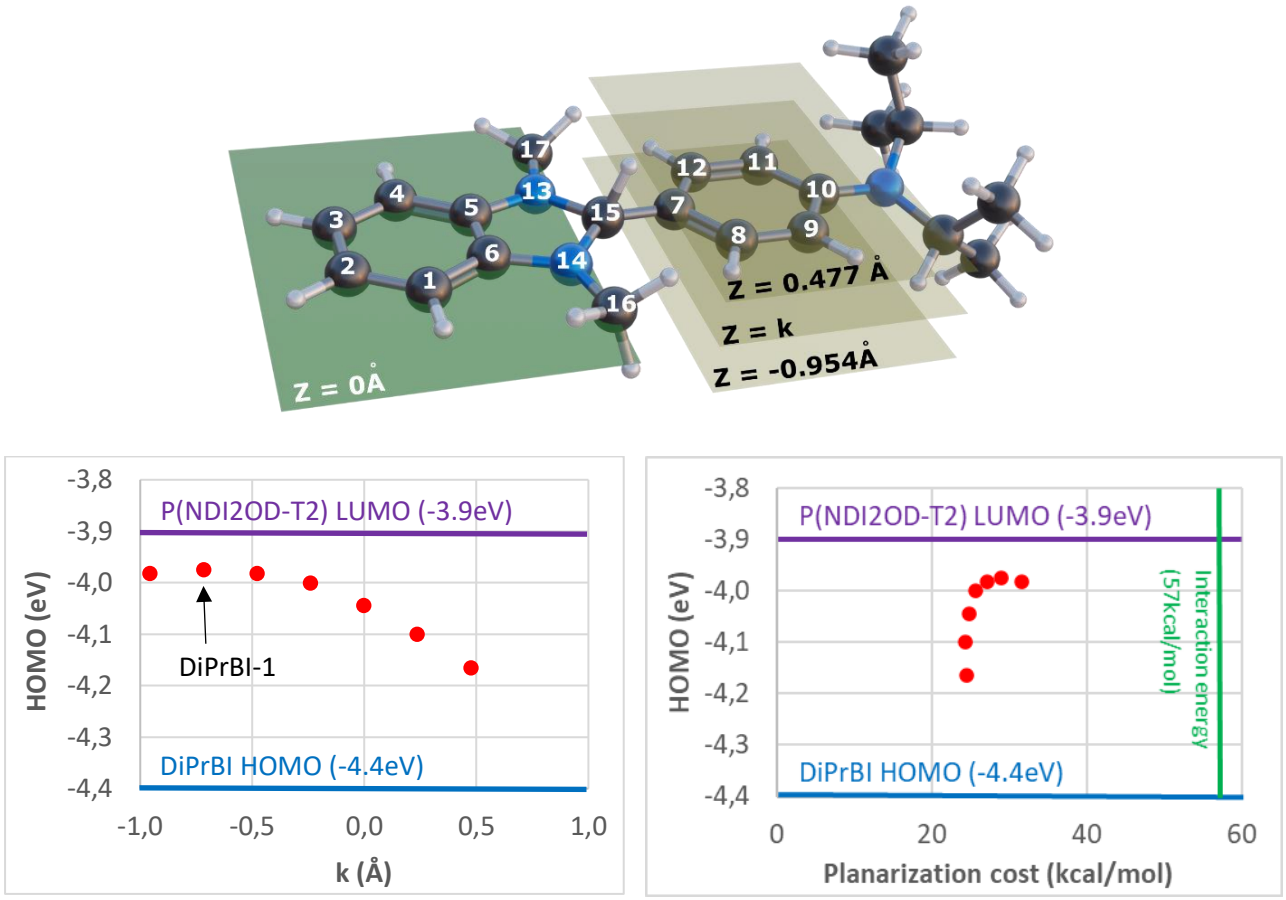

Figure 84: On the top: scheme of A-DiPrBI. Carbon atoms from 1 to 6, 16-17 and nitrogen atoms 13 and 14 lay on the horizontal plane Z=0 Å; carbon atoms from 7 to 12 lay on the horizontal plane Z=k (-0.954 Å < k < 0.477 Å). For each geometry, the structure has been optimized with Orca using B3LYP functional and 6-31G** basis set. On the bottom: HOMO level for different k values and HOMO level as a function of the planarization energy cost. For reference DiPrBI HOMO level, P(NDI2OD-T2) LUMO and interaction energy are reported in blue, violet, and green, respectively.

Among all the geometries of Figure 84, the highest HOMO is reached in the case of Z = -0.716 Å (DiPrBI-1). The calculated HOMO level of this conformation is -4.0 eV, which is 0.4 eV higher than DiPrBI HOMO but still 0.1 eV lower than P(NDI2OD-T2) LUMO. The single point energy of DiPrBI-1 is around 615816 kcal/mol, therefore, the energy required to planarize DiPrBI to DiPrBI-1 is 29 kcal/mol, which is lower than the interaction energy available (57kcal/mol) (Figure 85), indicating that the DiPrBI-1 conformation is accessible to the dopant while it is sandwiched between the NDI units.

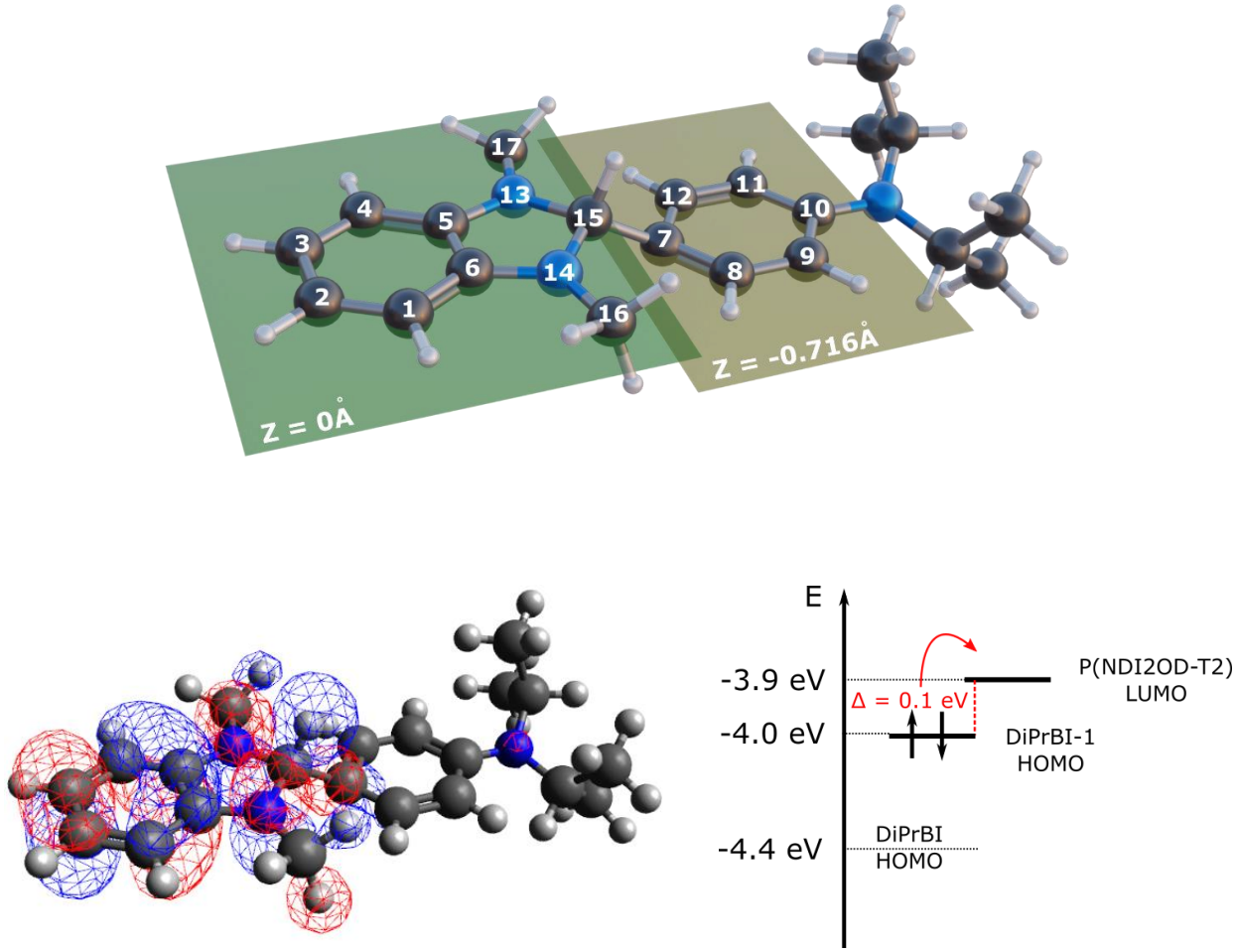

Figure 85: On the top: geometric structure of DiPrBI-1: carbon atoms from 1 to 6, 16-17 and nitrogen atoms 13 and 14 lay on the Z=0 Å horizontal plane, while carbon atoms from 7 to 12 lay on the parallel plane of equation Z = -0.716 Å. On the bottom: spatial representation of DiPrBI-1 HOMO (-4.0 eV) and comparison between DiPrBI, DiPrBI-1 and P(NDI2OD-T2) energy levels according to the integer charge transfer model (Figure 24). The single point energy is -615816 kcal/mol. The structure with geometrical constraints has been drawn with Avogadro, then optimized with Orca using B3LYP functional and 6-31G** basis set.

7.4.2 Planarization B (B-DiPrBI)

The horizontal plane of equation Z = 0 Å is defined as the plane passing through the phenyl ring composed of carbon atoms from 1 to 6. Nitrogen atoms 13 and 14 and carbon atoms 16 and 17 are also coplanar. Carbon atoms from 7 to 12 and 15 are constricted on a horizontal plane of equation Z = k, where k spans from 0.477 Å to – 0.477 Å. This set of geometries is slightly more restrictive than A-DIPrBI set, that does not impose any condition on carbon atom 15, and it will be referred as B-DiPrBI. For each k value, the structure was optimized using Orca with B3LYP functional and 6-31G** basis set. The dopant structures, the HOMO energy as a function of both the structure conformation, $E_{HOMO}(k)$ and the planarization energy costs, $E_{HOMO}(E_{planarization})$ are reported in Figure 86.

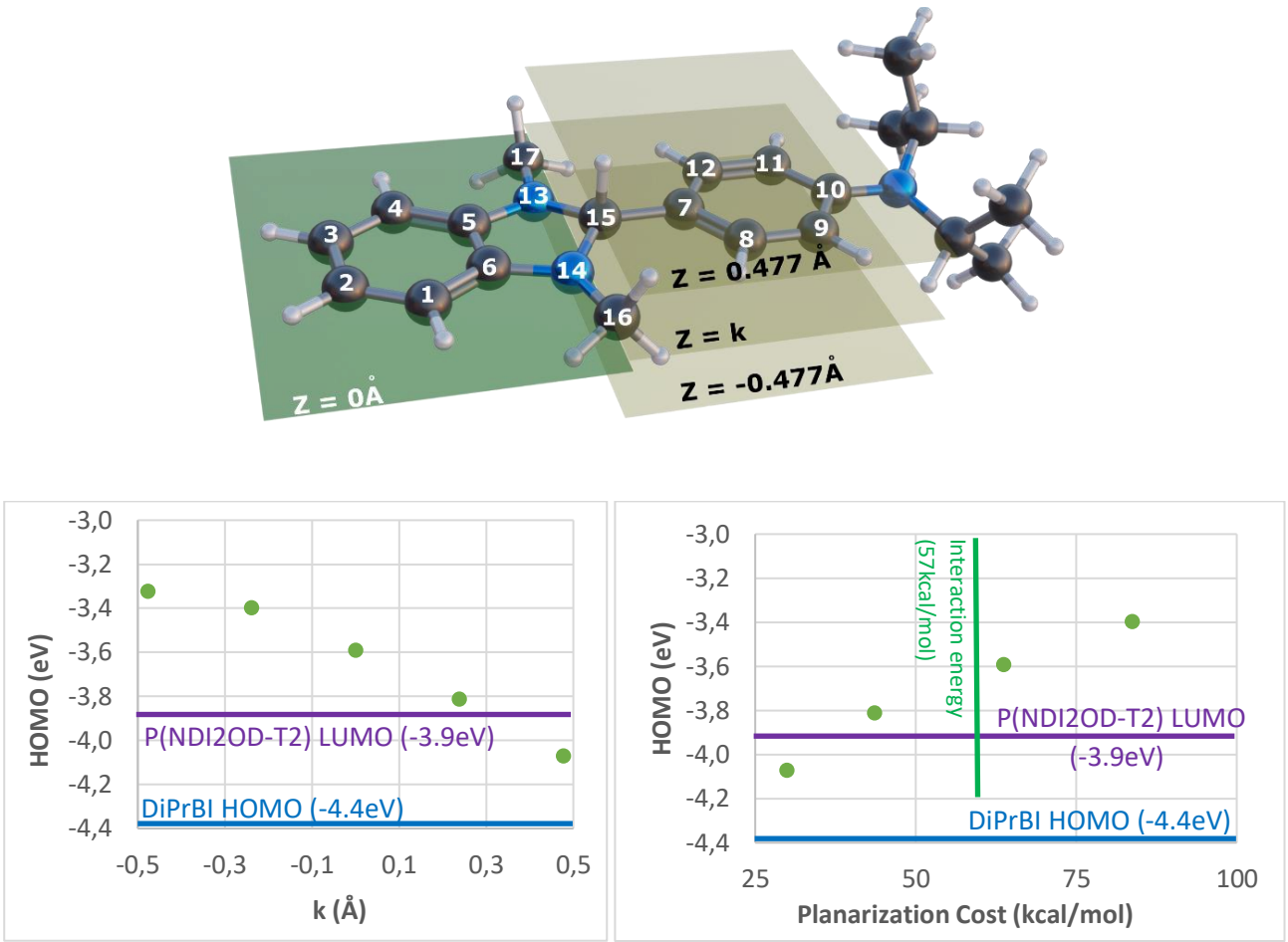

Figure 86: On the top: scheme of B-DiPrBI structures. Carbon atoms from 1 to 6, 16-17 and nitrogen atoms 13 and 14 lay on the horizontal plane Z=0 Å; carbon atoms from 7 to 12 and 15 lay on the horizontal plane Z=k (-0.477 Å < k < 0.477 Å). For each geometry, the structure has been optimized with Orca using B3LYP functional and 6-31G** basis set. On the bottom: HOMO level for different k values and HOMO level of as a function of the planarization energy cost. For reference DiPrBI HOMO level, P(NDI2OD-T2) LUMO and interaction energy are reported in blue, violet and green, respectively.

Among all the geometries calculated, the most interesting is obtained for k = 0.239 Å (DiPrBI-2, Figure 87): the other structures either have a too low HOMO level or a too high planarization cost. The calculated HOMO of DiPrBI-2 is -3.8 eV, which is 0.6 eV higher than DiPrBI HOMO and 0.1 eV higher than P(NDI2OD-T2) LUMO. The single point energy of DiPrBI-2 is around -615802 kcal/mol, therefore, the energy required to planarize DiPrBI to DiPrBI-2 is 44 kcal/mol, which is lower than the interaction energy available (57kcal/mol), indicating that the DiPrBI-2 conformation is accessible to the dopant while it is sandwiched between the NDI units.

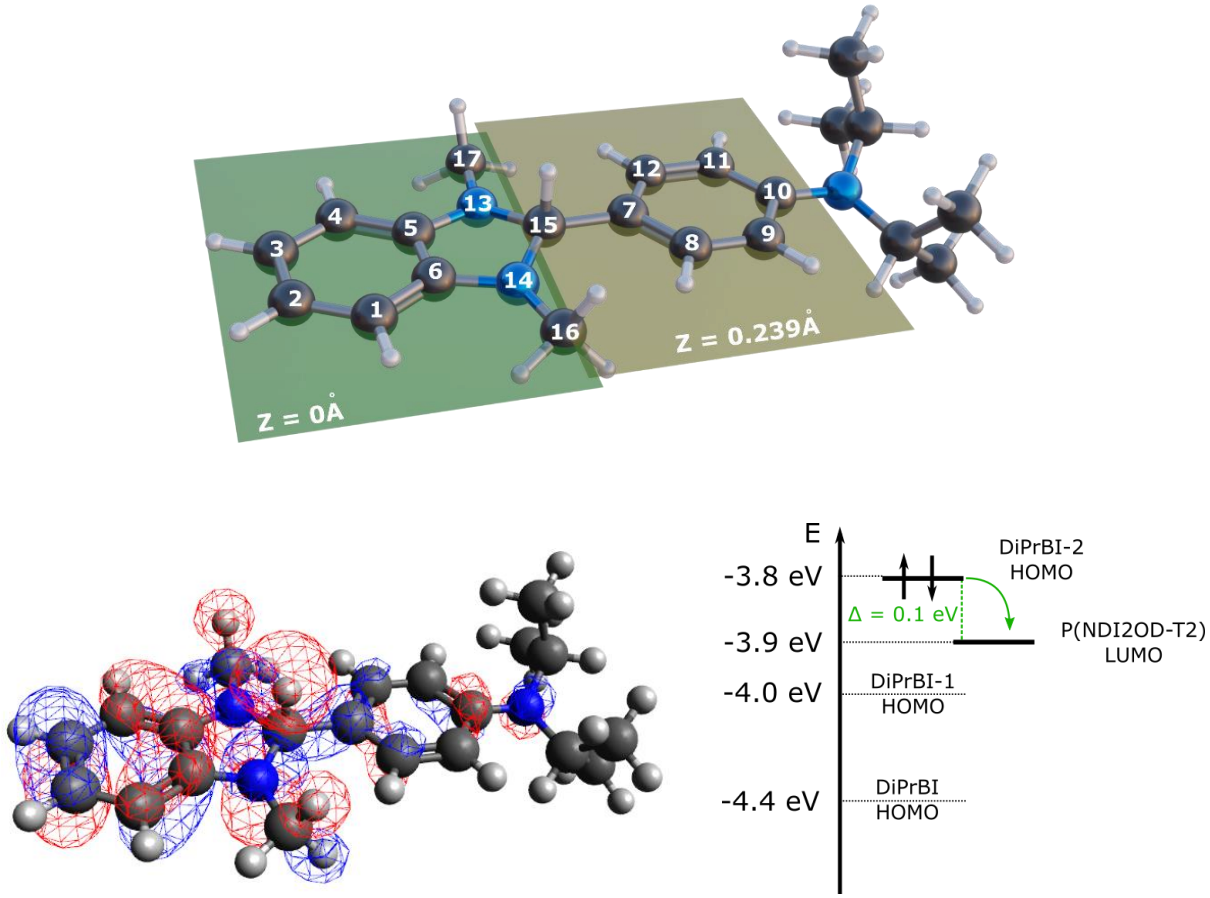

Figure 87: On the top: geometric structure of DiPrBI-2: carbon atoms from 1 to 6, 16-17 and nitrogen atoms 13 and 14 lay on the Z=0 Å horizontal plane, while carbon atoms from 7 to 12 and 15 lay on the parallel plane of equation Z = 0.239 Å. On the bottom: spatial representation of DiPrBI-2 HOMO (-3,8 eV) and comparison between DiPrBI, DiPrBI-1, DiPrBI-2 and P(NDI2OD-T2) energy levels according to the integer charge transfer model (Figure 24). The single point energy is -615802 kcal/mol. The structure with geometrical constraints has been drawn with Avogadro, then optimized with Orca using B3LYP functional and 6-31G** basis set.

7.4.3 Planarization C (C-DiPrBI)

The horizontal plane of equation Z = 0 Å is defined as the plane passing through the phenyl ring composed of carbon atoms from 1 to 6 and 16-17. Nitrogen atoms 13 and 14 are also coplanar. The dihedral angle defined by atoms 13, 15, 7 and 12 is α. This set of structures will be referred as C-DiPrBI. For each fixed α value between 0° and 120° the structure was optimized using Orca with B3LYP functional and 6-31G** basis set (Figure 88:Figure 88). It worth to notice that C-DiPrBI has no geometrical restrictions neither on the carbon atoms from 7 to 12 nor on the nitrogen atom 18, therefore, while α varies, the entire structure of the molecule bends. For this reason, the value of the dihedral α is not an intuitive indication of either the torsion or the planarization of the structure. Indeed, C-DiPrBI cannot be considered a proper planarization and in fact, the HOMO level of the dopant remains around -4.1eV regardless the value of α. For this reason, no further analysis of C-DiPrBI is performed and D-DiPrBI is carried out instead (see next paragraph).

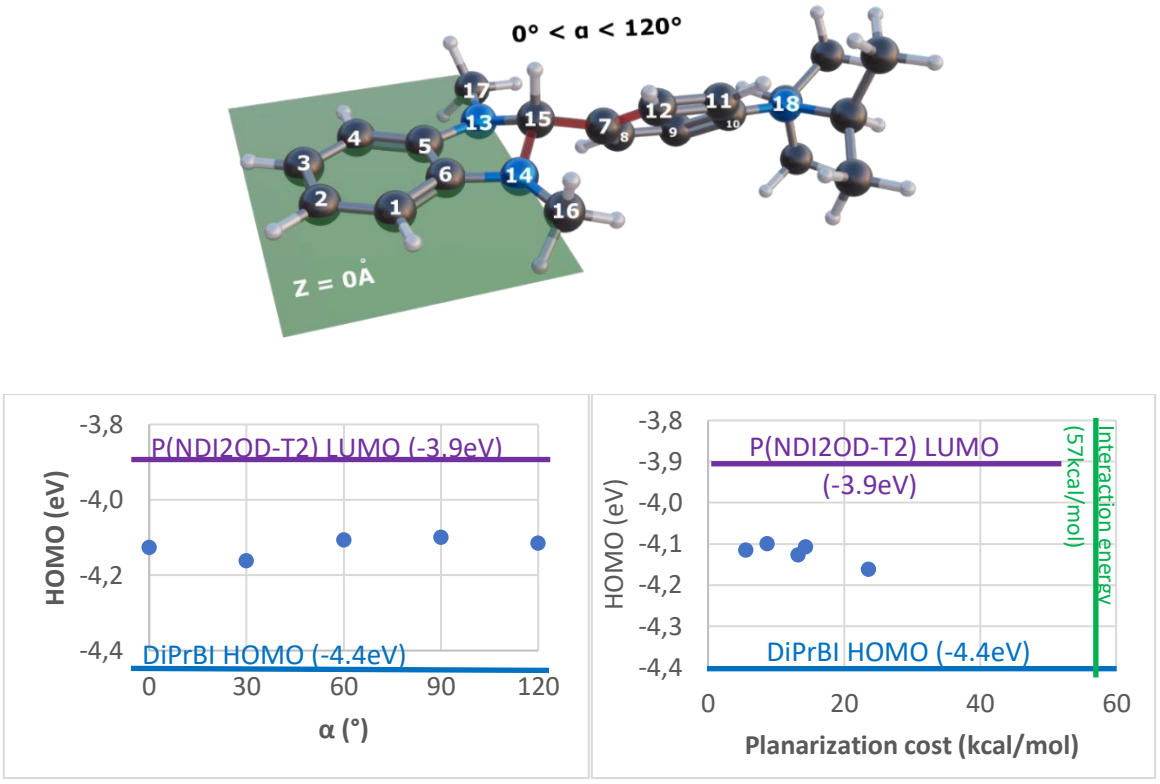

Figure 88: On the top: scheme of C-DiPrBI structures. Carbon atoms from 1 to 6, 16-17 and nitrogen atoms 13 and 14 lay on the horizontal plane Z=0 Å. The dihedral angle α (highlighted in red) defined by atoms 14, 15, 7 and 12 is systematically varied between 0° and 120°. For each geometry, the structure has been optimized with Orca using B3LYP functional and 6-31G** basis set. On the bottom: HOMO level for different α values and HOMO level of as a function of the planarization energy cost. For reference DiPrBI HOMO level, P(NDI2OD-T2) LUMO and interaction energy are reported in blue, violet and green, respectively.

7.4.4 Planarization D (D-DiPrBI)

The horizontal plane of equation Z = 0 Å is defined as the plane passing through the phenyl ring composed of carbon atoms from 1 to 6 and 16-17. Nitrogen atoms 13, 14 and 18 are also coplanar (this set of structures differs from C-DiPrBI because of the geometrical constriction imposed to nitrogen atom 18). The dihedral angle defined by atoms 13, 15, 7 and 12 is α. This set of geometries are referred as D-DiPrBI. For each fixed α value between 0° and 90° the structure was optimized using Orca with B3LYP functional and 6-31G** basis set. The dopant structures, the HOMO energy as a function of both the structure conformation, $E_{HOMO}(\alpha)$ and the planarization energy costs, $E_{HOMO}(E_{planarization})$ are reported in Figure 89.

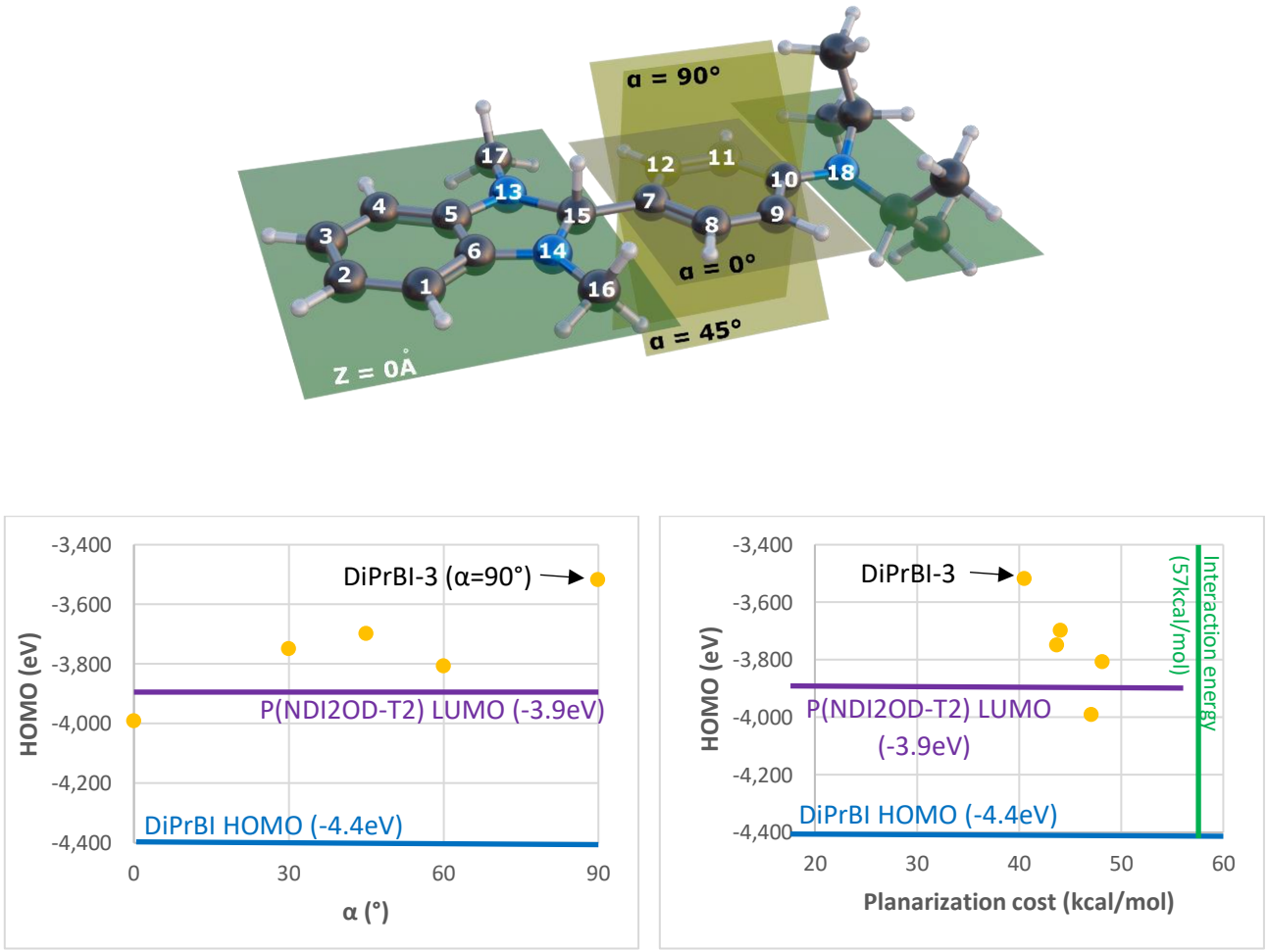

Figure 89: On the top: scheme of D-DiPrBI structures. Carbon atoms from 1 to 6, 16-17 and nitrogen atoms 13, 14 and 18 lay on the horizontal plane Z=0 Å. The dihedral angle α defined by atoms 13, 15, 7 and 12 is systematically changed from 0° to 90°. For each geometry, the structure has been optimized with Orca using B3LYP functional and 6-31G** basis set. On the bottom: HOMO level for different α values and HOMO level of as a function of the planarization energy cost. For reference DiPrBI HOMO level, P(NDI2OD-T2) LUMO and interaction energy are reported in blue, violet and green, respectively.

It is interesting to notice that the HOMO level decreases with decreasing the torsion angle α. Such stabilization is probably due to the increased aromaticity of D-DiPrBI when α = 0°. In the case of α = 90° (DiPrBI-3, which corresponds to the highest HOMO and also to the lowest planarization energy cost, Figure 90) DiPrBI-3 is less planar than in the case of α = 0°, but in its entirety, due to the geometrical constriction of nitrogen atom 18, all D-DiPrBI geometries are more planar than both C-DiPrBI and DiPrBI in its absolute minimum geometry for every value of α.

The calculated HOMO of DiPrBI-3 is -3.5 eV, which is 0.9 eV higher than DiPrBI HOMO and 0.4 eV higher than P(NDI2OD-T2) LUMO. The single point energy of DiPrBI-3 is around -615805 kcal/mol, therefore, the energy required to planarize DiPrBI to DiPrBI-3 is 41 kcal/mol, which is lower than the interaction energy available (57kcal/mol), indicating that DiPrBI-3 conformation is accessible to the intercalated dopant.

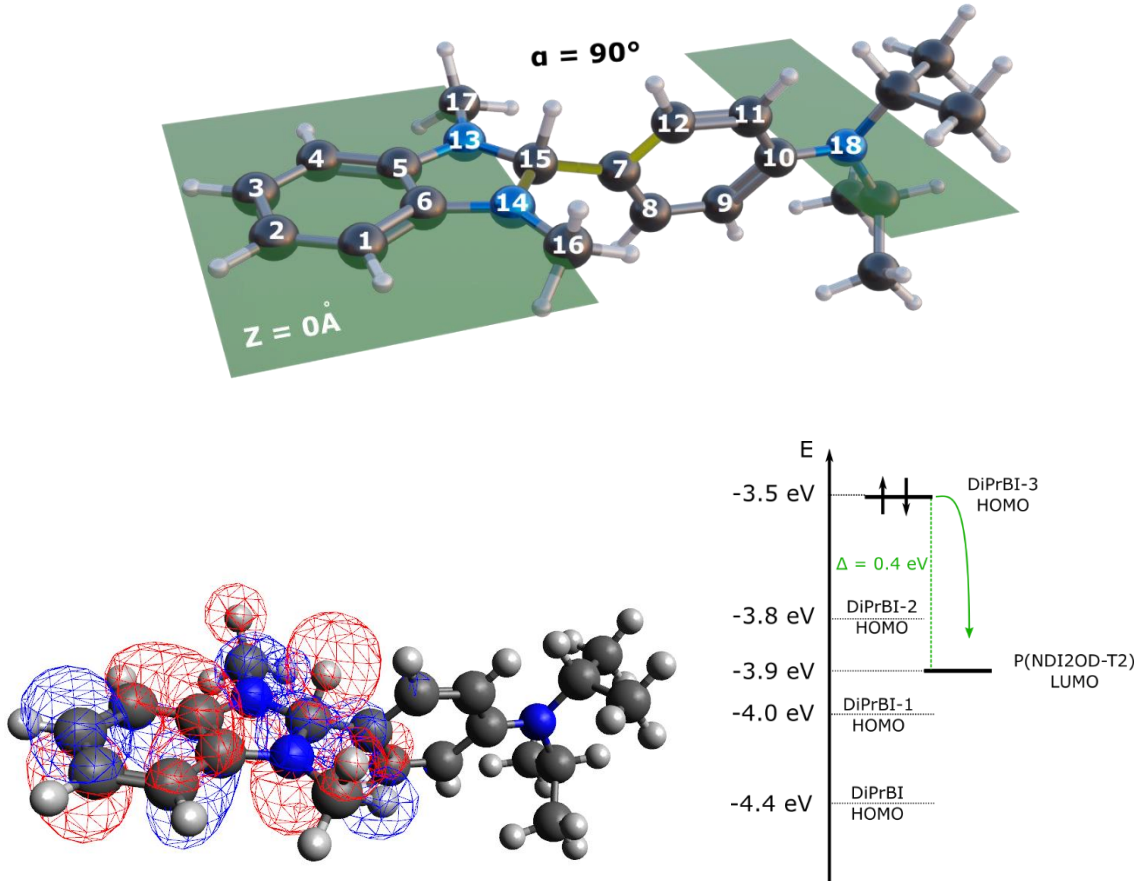

Figure 90: On the top: geometric structure of DiPrBI-3: carbon atoms from 1 to 6, 16, 17 and nitrogen atoms 13, 14 and 18 lay on the Z=0 Å horizontal plane. The dihedral angle defined by atoms 14, 15, 7 and 12 is set at 90°. On the bottom: spatial representation of DiPrBI-3 HOMO (-3.5 eV) and comparison between DiPrBI, DiPrBI-1, DiPrBI-2, DiPrBI-3 and P(NDI2OD-T2) energy levels according to the integer charge transfer model (Figure 24). The single point energy is -615805 kcal/mol. The structure with geometrical constraints has been drawn with Avogadro, then optimized with Orca using B3LYP functional and 6-31G** basis set.

7.4.5 Planarization E (E-DiPrBI)

According to planarization mechanism D, constricting the nitrogen atom 18 on the plane of equation Z=0 Å produces a dramatic effect on the molecule. Indeed, regardless the value of the dihedral angle α, the overall structure of the molecule is more planar with comparison with DiPrBI in vacuum and the HOMO value is higher (Figure 78). Here, we study how the molecule overall planarity affects its energy levels.

The horizontal plane of equation Z = 0 Å is defined as the plane passing through the phenyl ring composed of carbon atoms from 1 to 6 and 15-17. Nitrogen atoms 13, 14 are also coplanar. The nitrogen atom 18 is constricted on a horizontal plane of equation Z = k, where k spans from 4.52 Å to – 4.52 Å.

This set of geometries will be referred as E-DiPrBI. The dopant structures, the HOMO energy as a function of both the structure conformation, $E_{HOMO}(k)$ and the planarization energy costs, $E_{HOMO}(E_{planarization})$ are reported in Figure 91.

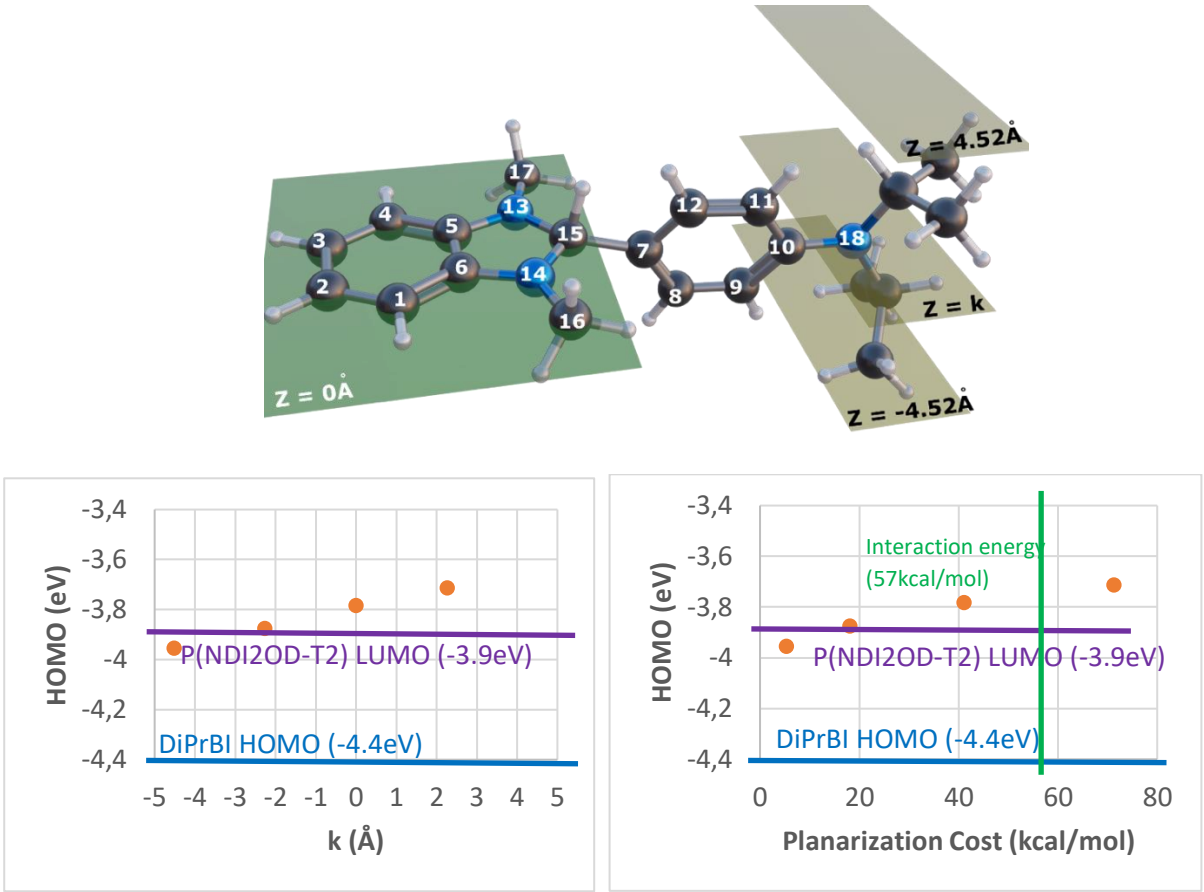

Figure 91. On the top: scheme of E-DiPrBI structures. Carbon atoms from 1 to 6, 16-17 and nitrogen atoms 13 and 14 lay on the horizontal plane Z=0 Å. The nitrogen atom 18 is set on a plane of equation Z=k. For each geometry, the structure was optimized with Orca using B3LYP functional and 6-31G** basis set. On the bottom: HOMO level for different k values and HOMO level of as a function of the planarization energy cost. For reference DiPrBI HOMO level, P(NDI2OD-T2) LUMO and interaction energy are reported in blue, violet, and green, respectively.

Worth to notice that the E planarization does not apply any condition neither on the phenyl ring composed of carbon atoms 7-12, nor on the dihedral angle α. Indeed, the D-DiPrBI family is a particular case of E-DiPrBI (when k=0 Å). Furthermore, since less constriction are imposed on the molecule, the overall internal energy and the HOMO energy are generally lower with respect to the case of D-DiPrBI.

Worth to notice that in DiPrBI minimum energy conformation, the nitrogen atom 18 lays on the horizontal plane Z = -4.52Å, and the HOMO of the molecule is -4.4eV (Figure 78). In the case of E-DiPrBI, when K= -4.52Å, the HOMO energy is -4.0eV. This indicates that forcing carbon atoms 15-17 on the horizontal plane Z = 0 Å causes a HOMO increase of around 0.4eV and it has an energy cost of 5.35kcal/mol (Figure 91).

Among the different configurations tested in Figure 91, the case of k = -2.26 Å (DiPrBI-4, Figure 92) is likely interesting: the calculated HOMO of such conformation is -3.9eV, equal to P(NDI2OD-T2) LUMO and the planarization energy cost is 18 kcal/mol, less than a third of the available interaction energy.

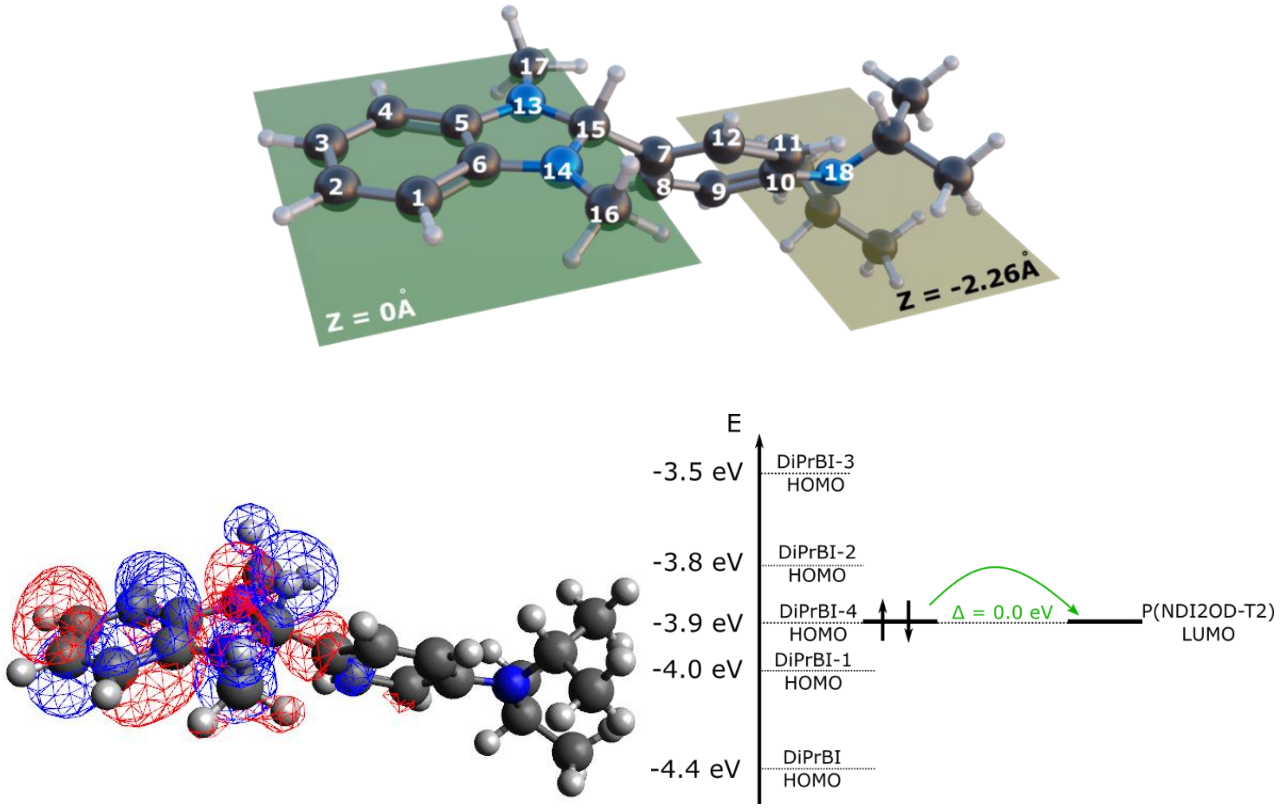

Figure 92. On the top: geometric structure of DiPrBI-4: carbon atoms from 1 to 6, 16, 17 and nitrogen atoms 13 and 14 lay on the Z=0 Å horizontal plane. The nitrogen atom 18 lays on the plane Z=-2.26 Å. On the bottom: spatial representation of DiPrBI-4 HOMO (-3.9 eV). The single point energy is -615827kcal/mol. The structure with geometrical constraints has been drawn with Avogadro, then optimized with Orca using B3LYP functional and 6-31G** basis set.

According to these finding, a significant increase of the HOMO accompanies the planarization, hence the dopant thermal activation is not necessary and DiPrBI has a strong effect on P(NDI2OD-T2) already at room temperature.

Indeed, the GIWAXS measurements indicates that the doped not annealed sample has a more pronounced edge-on structure with respect to the pristine polymer, which is face-on (Figure 76). Moreover, the FT-IR spectra demonstrated that, at room temperature, a doped not annealed sample exhibits a nonzero intensity of the IR polaronic band at 1638 cm^{-1} which continues to increase over time (Figure 73). Finally, the electrical conductivity measurements demonstrated that the doped not annealed sample has an electrical conductivity 5000 times greater than the pristine polymer (Figure 71).

According to DFT calculations it is possible to hypothesize that since the dopant intercalates between the narrow quasi-planar NDI units, it modifies its conformation from a bent geometry to a more planar structure. This causes a perturbation of the dopant electronic structure that increases the HOMO energy, and it makes accessible new electronic transitions to the dopant electrons, eventually allowing direct electron transfer from DiPrBI to P(NDI2OD-T2).

Five different planarization mechanisms have been investigated with DFT, and in all cases the planarization process increases the dopant HOMO level, reducing the energy barrier against direct electron transfer from the dopant to the polymer.

In particular, the D-DiPrBI planarization mechanism causes a dramatic increase of the dopant HOMO energy with a relatively high, yet affordable dopant planarization cost (Figure 89). Among all the calculated geometries, the top performing is DiPrBI-3 (Figure 90), which is characterized by an overall planar structure (carbon atoms 1-6 and nitrogen atoms 13,14 and 18 are coplanar) and the dihedral angle $\alpha = 90°$, reducing aromatic stabilization. The planarization energy cost of DiPrBI-3 is around 44kcal/mol, and it produces a HOMO increase of 0.7eV.

On the contrary, the E-DiPrBI series has less strict conditions, and it requires generally lower planarization energy costs. Among all the structures, DiPrBI-4 conformation (Figure 92) exhibit a less pronounced HOMO increase (0.5eV), which is barely sufficient to overcome P(NDI2OD-T2) LUMO, however it requires a contained energy cost of 18kcal/mol.

Worth to consider that all the planarization mechanisms studied in this work require different amounts of energy to be triggered: indeed, while B-DiPrBI and E-DiPrBI span a large range of planarization energies, A-DiPrBI and D-DiPrBI are more localized around 30 kcal/mol and 43 kcal/mol, respectively. Therefore, it is important to consider that A-E planarizations are only theoretical models and that the real mechanism might

result from their combination. The differences between all the studied planarization mechanisms are reported in Figure 93.

Furthermore, the slow increase of the IR polaronic band at 1638 cm^{-1} in doped not-annealed P(NDI2OD-T2) samples (Figure 73) suggests that the electron transfer caused by dopant planarization might be an out-of-equilibrium mechanism, eventually triggered by fluctuations of the dopant structure.

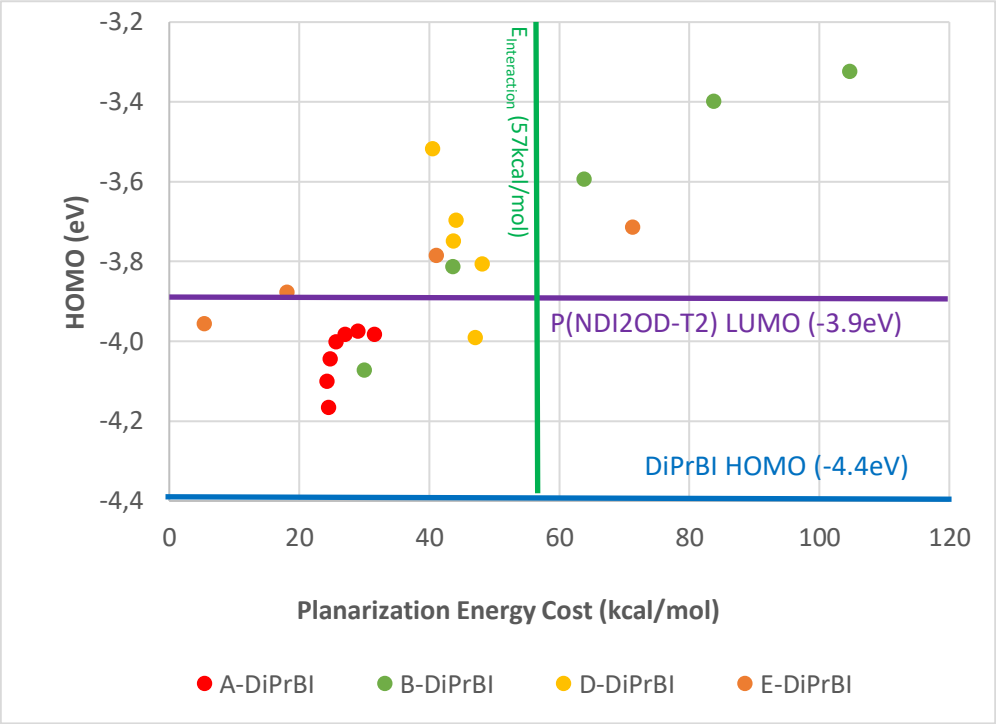

Figure 93. Comparison between the different planarization mechanisms reported in this work. For reference DiPrBI HOMO level in its absolute minimum conformation, P(NDI2OD-T2) LUMO and interaction energy are reported in blue, violet, and green, respectively.

Finally, in the case of annealing, the temperature is an important parameter: if it is high enough (i.e., over 110°C), it has positive effects on the electrical conductivity, while if it is too low, it is detrimental. All the analyses performed suggests that 70°C heating temperature is too low and such annealing process is detrimental for the electrical conductivity of the doped sample. Indeed, the electrical conductivity of the 70°C annealed sample decreases over time (Figure 71 C); the intensity of the IR polaronic band at 1638 cm^{-1} rises less than the same feature in the unannealed sample, over time (Figure 75); the broadening of the

GIWAX q_z (010) signal in the 70°C annealed sample is less pronounced compared to both the case of the unannealed doped sample and the 110°C annealed doped sample (Figure 76).

Therefore, the doping mechanism of the DiPrBI-P(NDI2OD-T2) can be summarized in a multi-step process:

Step 1A) The dopant forces the polymer to pack in a more edge-on fashion with respect to the pristine polymer which is face-on (Figure 76). The edge-on structure is characterized by a higher charge carrier mobility.

Step 1B) During film deposition the dopant, driven by π- π interactions, intercalates within the quasi-planar NDI units. The dopant constricted within such a narrow space eventually planarize its structure. Such deformation is accompanied by an increase of the HOMO level of the dopant that reduces the energy gap that hinders electron transfer to polymer LUMO. Subsequently to dopant intercalation, new electronic transitions could be available to the dopant electrons, eventually allowing a direct electron transfer from the dopant to the polymer (Figure 89). Mechanism 1B might be triggered by out-of-equilibrium fluctuations of the dopant structure, that begin immediately after film deposition, but that require a long time to go to completion (Figure 73). The combination of 1A and 1B mechanisms affects both charge carrier mobility and density, respectively. This causes a fast increase of around 3.5 orders of magnitude of the electrical conductivity of the system (Figure 71), at room temperature.

Step 2) Annealing process, through classical doping mechanism, activates the remaining unreacted dopant, further increasing charge carrier density. This process lasts around 15 minutes and causes the doubling of the electrical conductivity (Figure 71, Figure 74, Figure 76). The annealing temperature must be high enough to activate the dopant, otherwise it is detrimental. The annealing process also triggers a polymer structure rearrangement that affects charge carrier mobility.

Step 3) A high temperature annealing causes a relaxation of the structure that further increases the electrical conductivity. A low temperature annealing favours a more face-on structure that lowers electrical conductivity (Figure 71, Figure 74, Figure 76)

8. DOPING OF P(EO-NDIT2) WITH DiPrBI

As reported in the section 6.4, P(NDI2OD-T2) derived polymers have been recently developed, and the presence of polar glycol side chains attributes to the polymer interesting features such as solubility in polar less-toxic solvents, improved compatibility with aqueous electrolytes and increased polymer-dopant miscibility.

As previously discussed, both the NDI and the T2 units have been functionalized with linear glycol chains, often carrying mixed ester/ether groups. [217] Sommer et al. [225] synthetized P(EO-NDIT2), a polymer derived from P(NDI2OD-T2) by replacing the branched alkyl side chains with branched oligoethylene glycol chains purely based on ethylene oxide (EO) (Figure 94). The absence of ester functionalities makes the polymer more stable under basic conditions, expanding the range of possible polymerizations to polycondensation pathways.

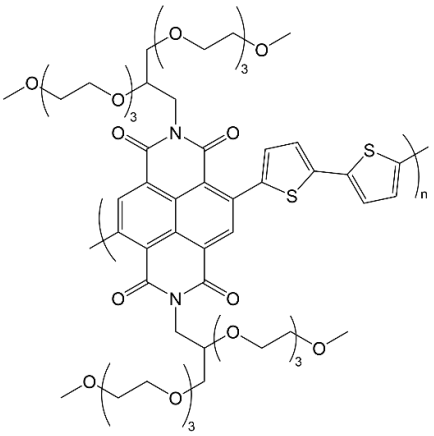

Figure 94: Chemical structure of P(EO-NDIT2).

Due to the amphiphilic nature of P(EO-NDIT2), it should exhibit a generally good solubility in common organic solvents, but it might also generate solution aggregates, depending on the solvent.

First, to test the effect of the polar side chains, the polymer was dissolved in different deuterated solvents at the fixed concentration of 4.2mg/mL. Then the solvent-dependent aggregation of P(EO-NDIT2) was investigated with ^{1}H NMR spectroscopy at 30°C. Worth to notice that NDI derived polymers generally have only two centre-symmetric hydrogen atoms on the NDI unit, which produce a well distinguishable singlet in the aromatic region, whose intensity and broadening can be easily monitored (Figure **95**).

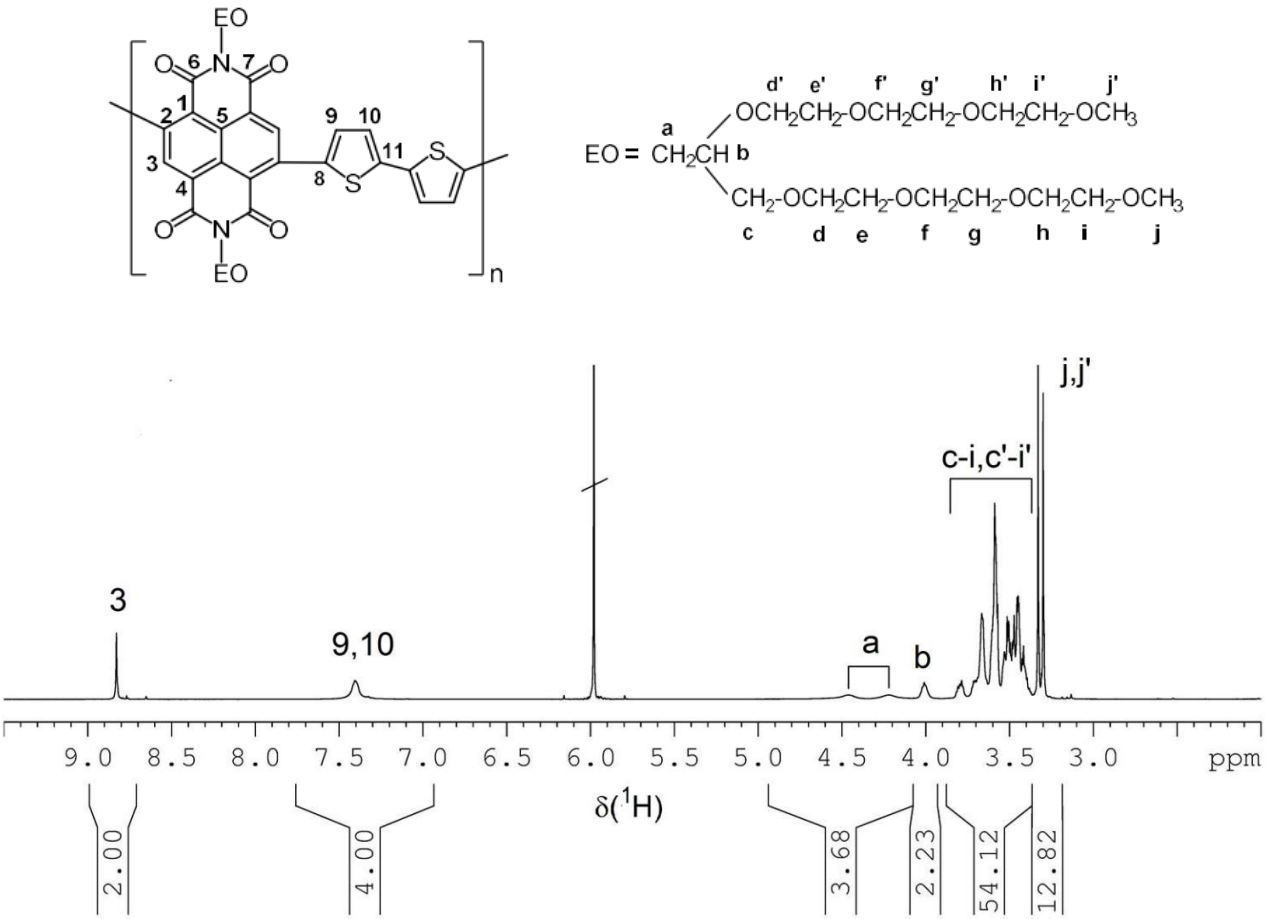

Figure 95. 1H NMR spectra (500MHz) of P(EO-NDIT2) in $C_2D_2Cl_4$ at 30°C. Image adapted from **[225]**.

The spectra recorded in dimethylformammide and tetrahydrofuran exhibit significant broadening of the H-NDI signal, indicating poor solubilization and unsuppressed π-π aggregation. In contrast, chloroform and ortho-dichlorobenzene exhibit narrow signals, indicating a complete polymer dissolution. The solvatation increases, as follows: tetrahydrofuran < dimethylformammide < dioxane < ortho-dichlorobenzene < chloroform (Figure 96 left).

The solvent quality was also studied with UV-vis spectroscopy (Figure 96 right): with the decrease of solventation ability, a new band at around 750nm rises, which is characteristic of the solution aggregates. Worth to notice, THF is such a poor solvent that it was not possible to record the UV-vis spectrum of P(EO-NDIT2), despite increased temperature and decreased concentration.

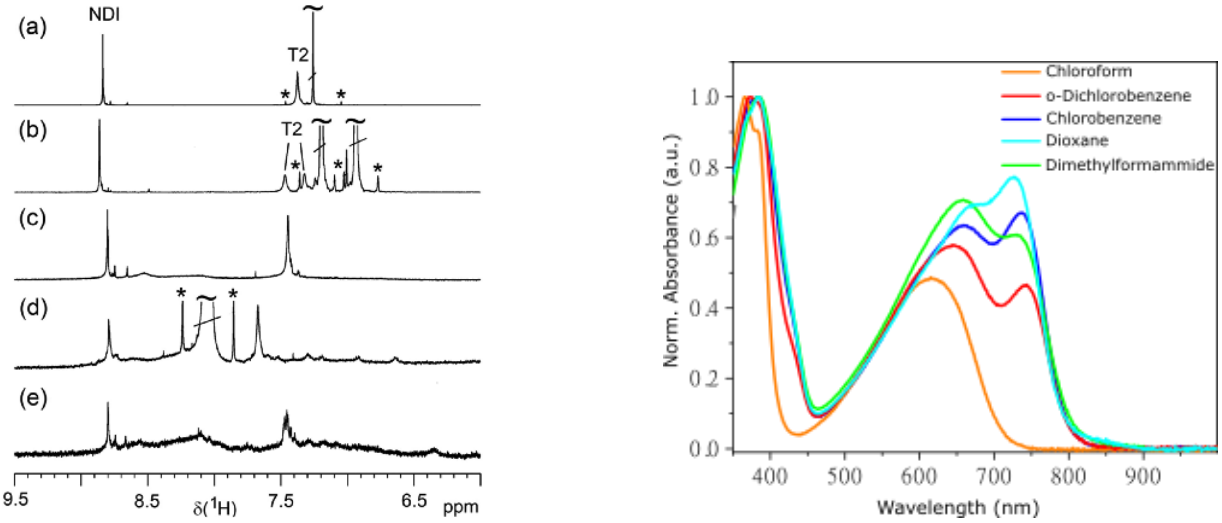

Figure 96. On the left: ^{1}H NMR spectra of P(EO-NDIT2) dissolved in different deuterated solvents with a concentration of 4.2mg/mL. a) $CDCl_3$; b) o-DCB-d4; c) dioxane-d8; d) DMF-d7 and e) THF-d4. The symbol "*" marks satellites of the solvent signal. On the right: UV-vis spectra of solutions of P(EO-NDIT2) in different solvents.

Increasing temperature yields to further dissolution and different temperatures are required for each solvent to fully dissolve the aggregates. The temperature dependency dissolution in the two high-boiling-point solvents DMF and o-DCB was probed with temperature dependent 1H NMR between 30 and 120°C (Figure **97**). At 30°C the two solvents exhibit a different behaviour: DMF has a rather high degree of aggregation while o-DCM has a rather low aggregation. Molecularly dissolved signals are reached only at temperatures between 90-120°C. DMF appears to be a good solvent at high temperatures, but a poor one at low temperatures, on the contrary, o-DCB appears to have a rather constant performance across the entire temperature range.

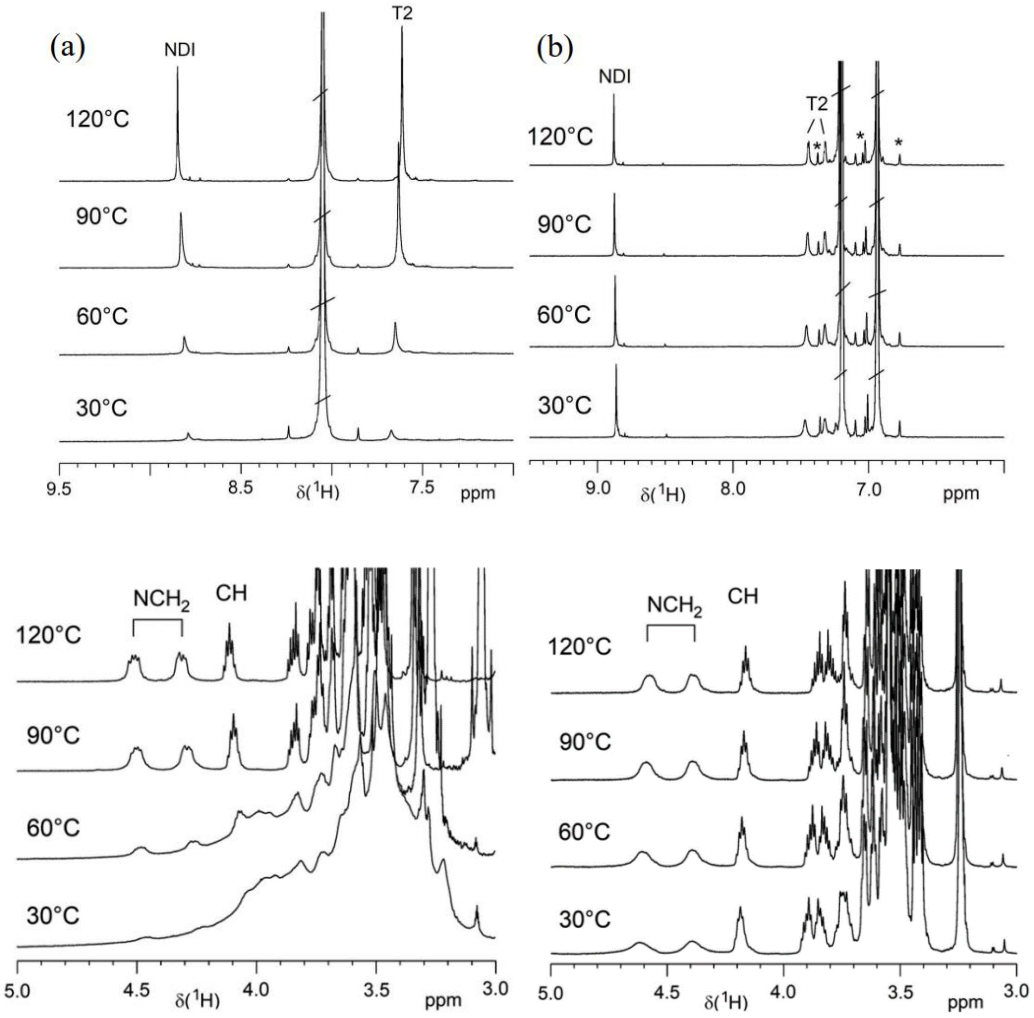

Figure 97. Temperature dependent aggregation 1H NMR of P(EO-NDIT2) in (a) DMF-d7 and (b) o-DCB-d4. Only the aromatic region of the spectra is shown on the top, the alchilic region is shown on the bottom.

The aggregation temperature dependency was also investigated for o-dichlorobenzene (DCB) and chlorobenzene (CB) with UV-vis spectroscopy at different temperatures (from 20°C to 100°C, at 20°C increments) during a heating cycle and a cooling cycle.

o-Dichlorobenzene: during the heating cycle, the intensity of the 750nm band, characteristic of aggregates in solution, starts to decrease between 20 and 40°C and vanishes at 60°C (Figure 98 a). Furthermore, during the cooling cycle, such feature is not restored, and the UV-vis spectrum of the solution remains constant even after 14 days at 20°C. This clearly indicates that once the initial energy barrier against polymer dissolution is overcome by increasing temperature, the polymer keeps stably dissolved in a condition of a thermodynamic minimum (Figure 98 b).

Chlorobenzene: similarly, during the heating cycle the intensity of the 750nm band gradually decreases with the increase of temperature, although a higher temperature (up to 80°C) was needed to fully dissolve aggregates (Figure 98 c). Furthermore, during the cooling cycle, the intensity of the 750 nm band increases as the of temperature decreases, hence indicating a re-formation of solution aggregates (Figure 98 d).

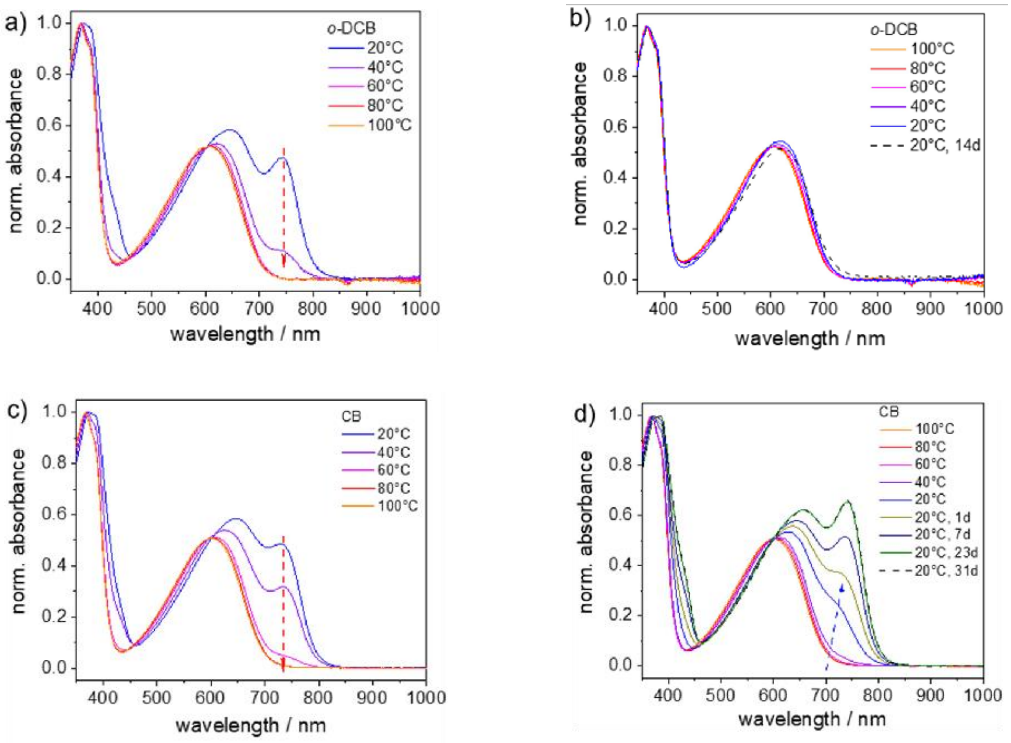

Figure 98: UV-vis spectra of P(EO-NDIT2) upon a heating cycle from 20 to 100°C (a, c) and then a cooling cycle from 100 to 20°C (b, d). The solvent is 1,2-diclorobenzene (a, b) and chlorobenzene (c, d).

Spin-cast thin films of P(EO-NDIT2) from CB and DCB were studied using GIWAXS. Both films exhibit characteristic backbone, lamellar and π-π stacking features (Figure 99). The intensity of signals is stronger in the case of the spin-cast film from CB. This agrees with the UV-vis measurements and suggest that CB is more capable to form ordered aggregates. Furthermore, the use of CB increases the size of crystallites along all three crystallographic directions: from 12.6 nm to 17.9 nm (42%) along the backbone direction, from 9.8 nm to 17.4 nm (77%) along the lamellar stacking direction, and from 2.2 to 3.4 nm (54%) along the π-π stacking direction. Worth to notice, CB is an interesting solvent, because it induces and tailors P(EO-NDIT2) backbone aggregation allowing to obtain larger crystal and a higher degree of order of the polymer film.

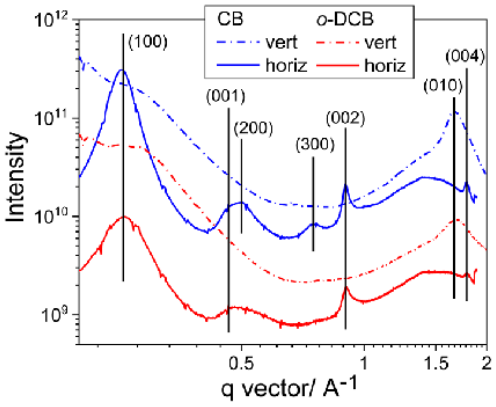

Figure 99: 1D GIWAXS profile along the horizontal (in plane) and vertical (out of plane) scattering directions.

The electrical conductivity of P(EO-NDIT2) doped with different 1H-benzimidazole dopants, such as DMBI, DPhBI and DiPrBI was measured (Figure 100). DiPrBI demonstrated to be the best performing dopant at low concentrations, and it was selected to carry out an analysis of dopant-polymer interaction in CB and DCB.

DCB solutions were heated to 90°C to dissolve aggregates, then the dopant was added, and the film spin coated. The thickness of the films ware evaluated with a profilometer to be within 40±5nm. In the case of CB, a set of samples was prepared by heating the solution to 80°C to dissolve aggregates before the addition of the dopant, while another set was prepared by adding the dopant at room temperature, while aggregates are present. The highest electrical conductivity, in the order of 10^{-2} S/cm, was reached in the case of the 20% doped sample from heated CB.

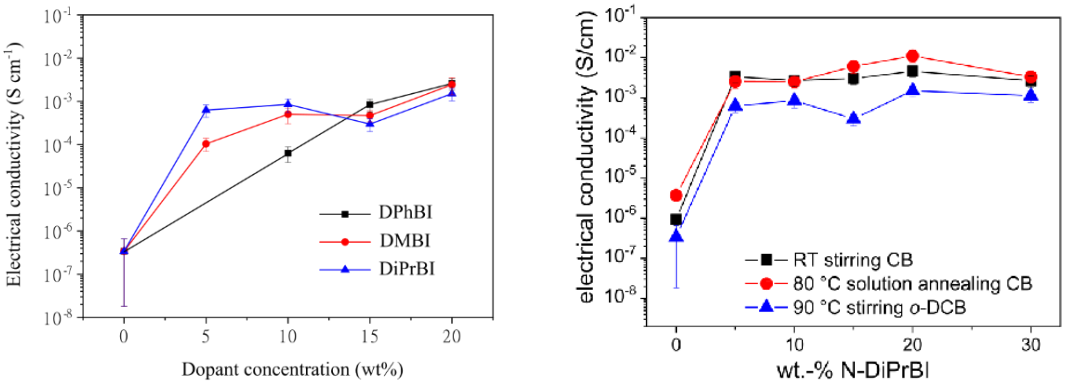

Figure 100: On the left: electrical conductivity of P(EO-NDIT2) doped with different benzimidazole derived dopants (DMBI, DPhBI and DiPrBI). Film cast from CB. On the right: electrical conductivity of P(EO-NDIT2) doped with DiPrBI under different conditions.

To conclude, as previously reported in literature, the presence of EO groups greatly improves the polymer solubility and TE performances. [215], [218] P(EO-NDIT2) exhibits an excellent solubility thanks to its the

amphiphilic nature and also a tunable backbone aggregation in solution depending on the solvent. This feature can be exploited to favour the formation of large crystal with a high order degree.

The highest power factor obtained with P(EO-NDIT2) doped with DiPrBI is 0.11 µW/mK^2 (Figure 101). This result is obtained at relatively low doping levels, around 1-2 wt% (6-12% mol). For comparison, the highest PFs obtained doping P(NDI2TEG-T2) and P(gNDI-gT2) with DMBI have been obtained with a doping level around 90% mol (0.9 µW/mK^2) [215] and 20% mol (0.4 µW/mK^2) [217], respectively.

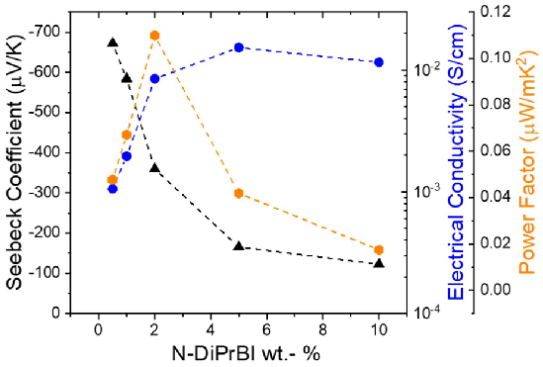

Figure 101: Electrical conductivity, Seebeck coefficient and Power Factor of a spin coated thin film of P(EO-NDIT2) (molecular weight around 116kg/mol) doped with DiPrBI from a solution of chlorobenzene annealed at 80°C before dopant addition.

9. NEW DOPANTS

In the previous chapter it was discussed how the increase of the 1H-benzimidazole HOMO caused by the planarization of the molecule is beneficial to the doping of P(NDI2OD-T2). In this chapter, increasing the dopant HOMO through chemical functionalization of the molecule is discussed and same preliminary experimental results are reported.

9.1 FUNCTIONALIZATION ON THE BENZIMIDAZOLE

Alkyl side chains on the aniline of 1H-benzimidazoles allows to improve the miscibility between dopant and naphtelenediimide copolymers, as widely discussed in literature [210]. Instead, they do not affect the frontiers energy levels of the dopant, as the HOMO of the dopant mostly lies on the benzimidazole portion of the molecule (Figure 102). Here the idea was to modify the electron density of the 1H-benzimidazoles by introducing donor or acceptor substituents (Figure 104 - Figure 113). Some of the benzimidazole dopants here studied, their characteristics, and a reference to the synthesis processes are listed in Table 7.

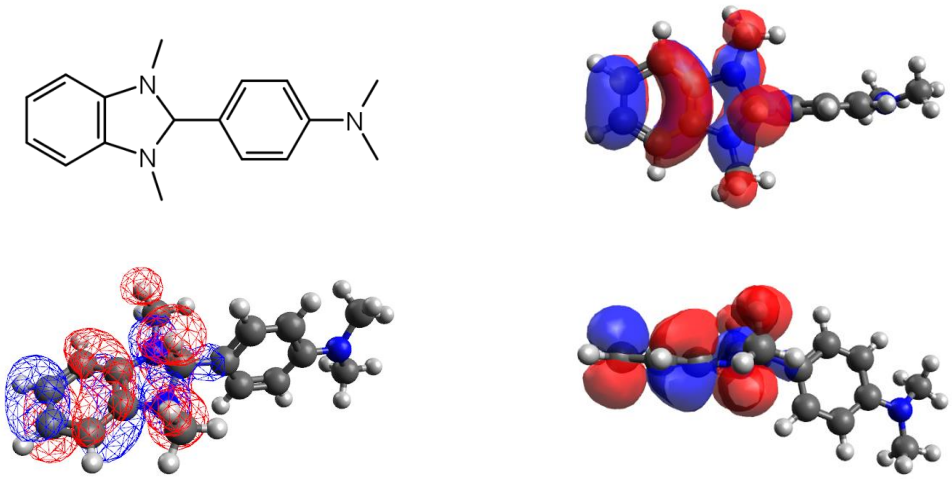

Figure 102: chemical structure of 4-(1,3-dimethyl-2,3-dihydro-1H-1,3-benzodiazol-2-yl)-N,N-dimethylaniline (DMBI) and spatial representation of its HOMO (-4.4 eV). DFT calculations have been performed with Orca (B3LYP 6-31G**).

Name		Synthesis	Calculated HOMO (eV)	Figure
4-(1,3-dimethyl-2,3-dihydro-1H-1,3-benzodiazol-2-yl)-N,N-bis(propan-2-yl)aniline	DiPrBI	Synthesis B	-4.4	Figure 80
4-(1,3-dimethyl-2,3-dihydro-1H-1,3-benzodiazol-2-yl)-N,N-dimethylaniline	DMBI	Synthesis C	-4.4	Figure 102
4-(1,3-dimethyl-2,3-dihydro-1H-1,3-benzodiazol-2-yl)-N,N-diphenylaniline	DPhBI	Synthesis D	-4.5	Figure 103
N,N-dimethyl-4-(1,3,5-trimethyl-2,3-dihydro-1H-1,3-benzodiazol-2-yl)aniline	Me-DMBI	Synthesis I	-4.3	Figure 104
N,N-dimethyl-4-(1,3,5,6-tetramethyl-2,3-dihydro-1H-1,3-benzodiazol-2-yl)aniline	Me_2-DMBI	Synthesis M	-4.2	Figure 105
2-[4-(dimethylamino)phenyl]-1,3-dimethyl-2,3-dihydro-1H-1,3-benzodiazol-5-amine	NH_2-DMBI	-	-4.0	Figure 106
2-[4-(dimethylamino)phenyl]-N,1,3-trimethyl-2,3-dihydro-1H-1,3-benzodiazol-5-amine	MeNH-DMBI	-	-3.9	Figure 107
2-[4-(dimethylamino)phenyl]-N,N,1,3-tetramethyl-2,3-dihydro-1H-1,3-benzodiazol-5-amine	Me_2N-DMBI	-	-4.1	Figure 108
4-(1,3-dimethyl-5-nitro-2,3-dihydro-1H-1,3-benzodiazol-2-yl)-N,N-dimethylaniline	NO_2-DMBI	-	-4.3	Figure 109
2-[4-(dimethylamino)phenyl]-1,3-dimethyl-2,3-dihydro-1H-1,3-benzodiazole-5-carbonitrile	NC-DMBI	-	-4.9	Figure 110
1,2,3-trimethyl-2,3-dihydro-1H-1,3-benzodiazol-4-ol	OH-TMBI	Synthesis O	-4.4	Figure 111
2-[4-(dimethylamino)phenyl]-1,3-dimethyl-2,3-dihydro-1H-1,3-benzodiazol-4-ol	OH-DMBI	-	-4.3	Figure 112
4-(4-methoxy-1,3-dimethyl-2,3-dihydro-1H-1,3-benzodiazol-2-yl)-N,N-dimethylaniline	MeO-DMBI	-	-4.3	Figure 113

Table 7: benzimidazole-derived dopants discussed in this work and their HOMO level. DFT calculations have been performed with Orca (B3LYP 6-31G**).

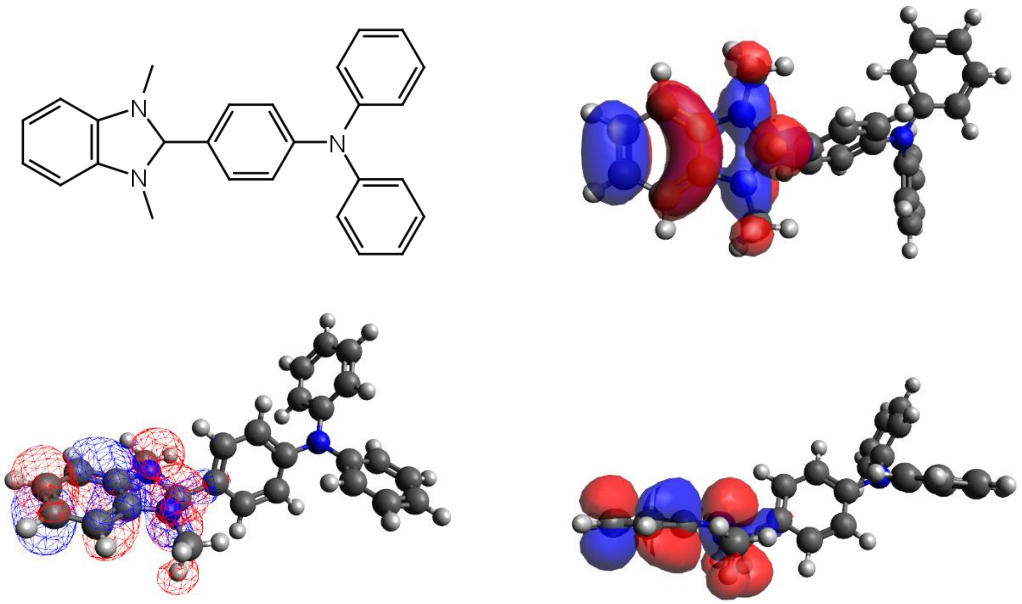

Figure 103: chemical structure of 4-(1,3-dimethyl-2,3-dihydro-1H-1,3-benzodiazol-2-yl)-N,N-diphenylaniline (DPhBI) and spatial representation of its HOMO (-4.5 eV). DFT calculations have been performed with Orca (B3LYP 6-31G**).

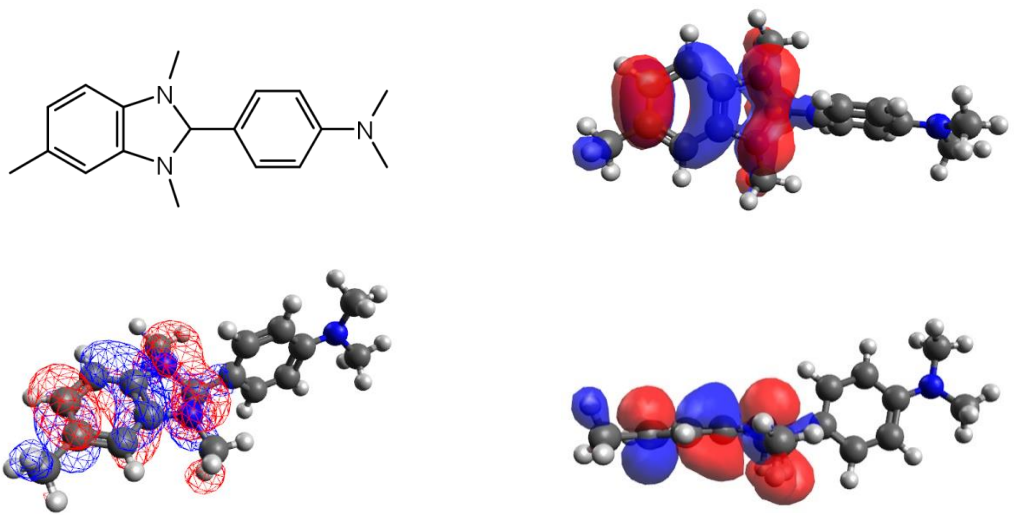

Figure 104: chemical structure of N,N-dimethyl-4-(1,3,5-trimethyl-2,3-dihydro-1H-1,3-benzodiazol-2-yl)aniline (Me-DMBI) and spatial representation of its HOMO (-4.3 eV). DFT calculations have been performed with Orca (B3LYP 6-31G**).

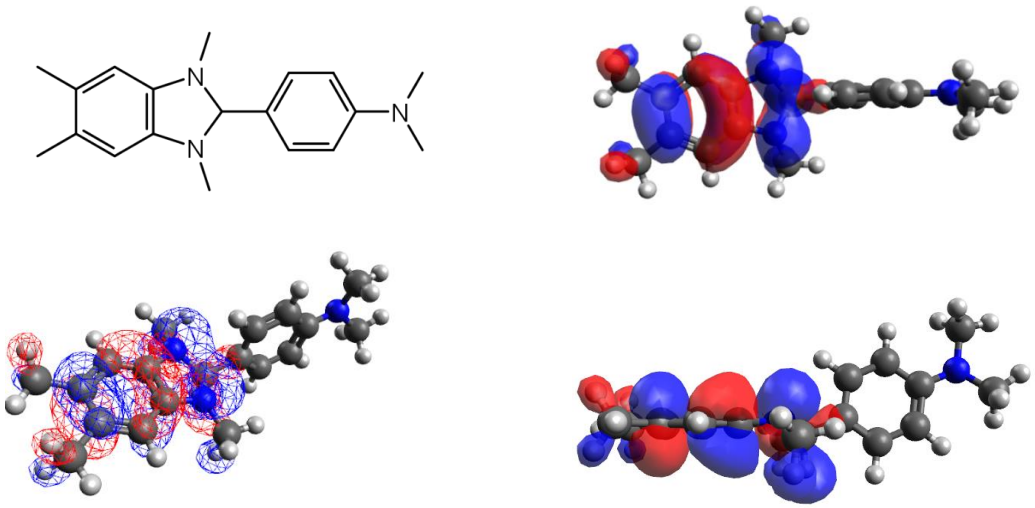

Figure 105: chemical structure of N,N-dimethyl-4-(1,3,5,6-tetramethyl-2,3-dihydro-1H-1,3-benzodiazol-2-yl)aniline (Me_2-DMBI) and spatial representation of its HOMO (-4.2 eV). DFT calculations have been performed with Orca (B3LYP 6-31G**).

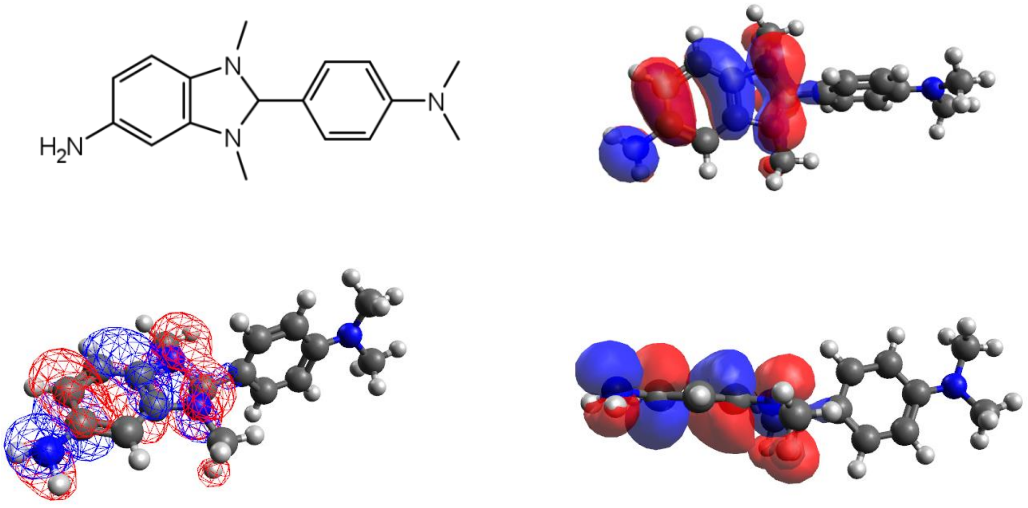

Figure 106: chemical structure of 2-[4-(dimethylamino)phenyl]-1,3-dimethyl-2,3-dihydro-1H-1,3-benzodiazol-5-amine (NH_2-DMBI) and spatial representation of its HOMO (-4.0eV). DFT calculations have been performed with Orca (B3LYP 6-31G**).

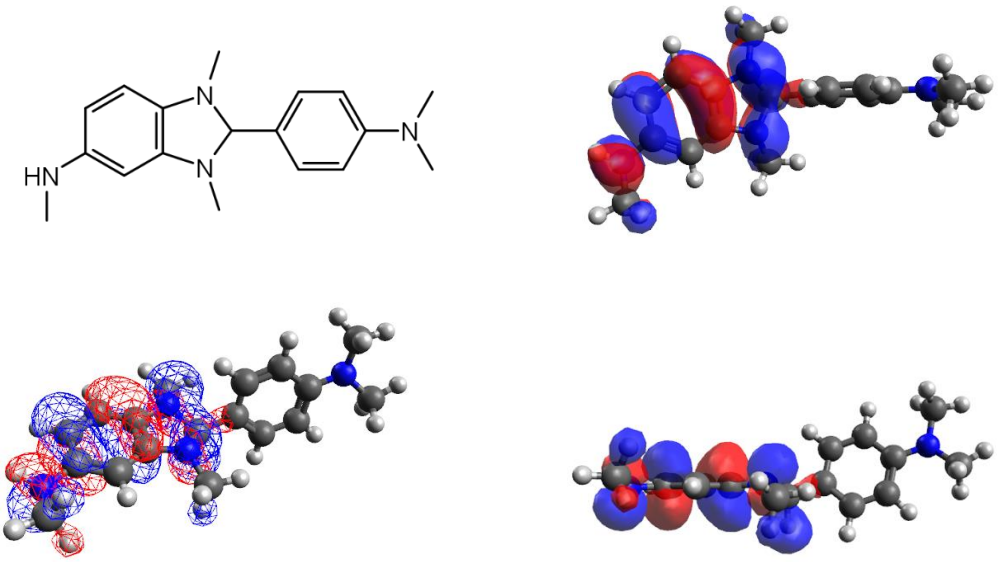

Figure 107: chemical structure of 2-[4-(dimethylamino)phenyl]-N,1,3-trimethyl-2,3-dihydro-1H-1,3-benzodiazol-5-amine (MeNH-DMBI) and spatial representation of its HOMO (-3.9Ev).). DFT calculations have been performed with Orca (B3LYP 6-31G**).

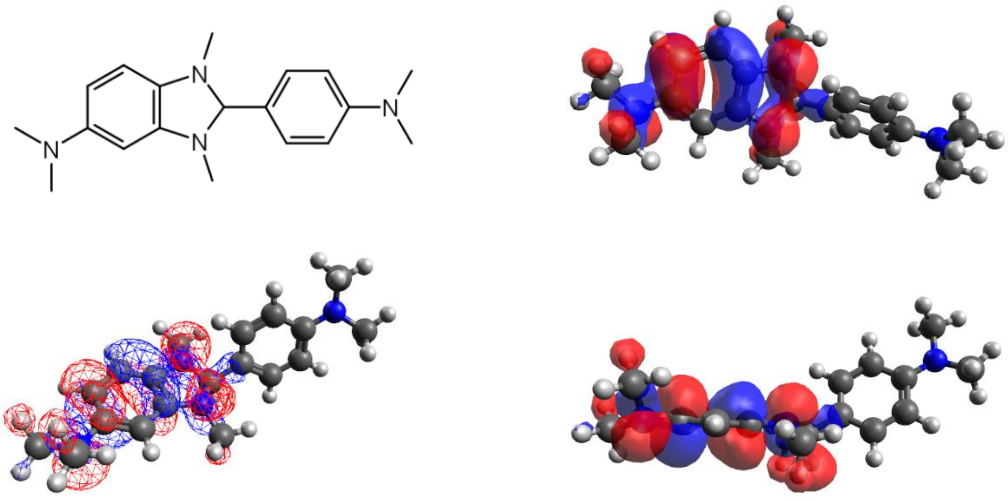

Figure 108: chemical structure of 2-[4-(dimethylamino)phenyl]-N,N,1,3-tetramethyl-2,3-dihydro-1H-1,3-benzodiazol-5-amine (Me_2N-DMBI) and spatial representation of its HOMO (-4.1eV). DFT calculations have been performed with Orca (B3LYP 6-31G**).

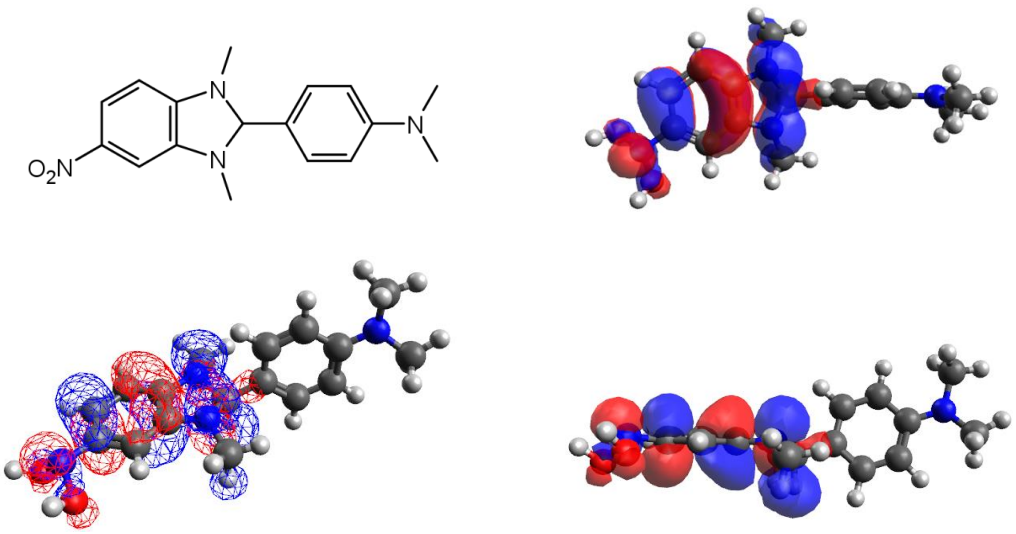

Figure 109 : chemical structure of 4-(1,3-dimethyl-5-nitro-2,3-dihydro-1H-1,3-benzodiazol-2-yl)-N,N-dimethylaniline (NO_2-DMBI) and spatial representation of its HOMO (-4.3 eV). DFT calculations have been performed with Orca (B3LYP 6-31G**).

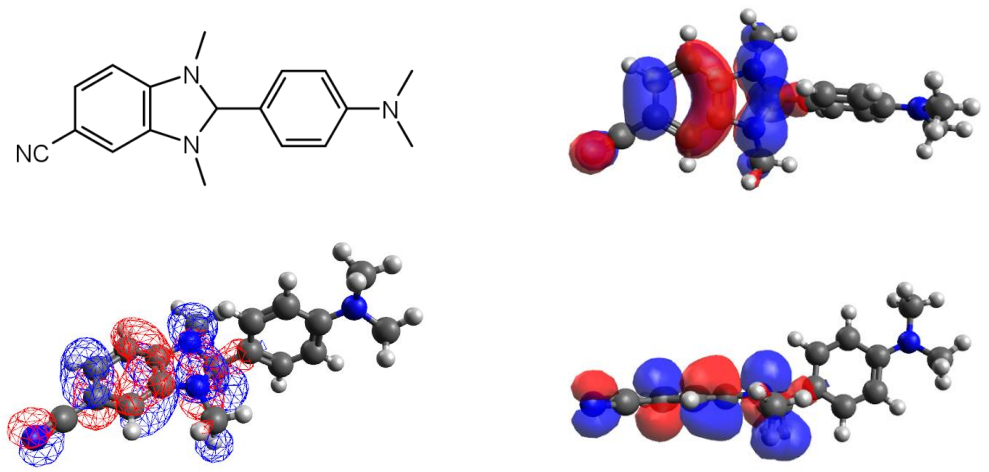

Figure 110: chemical structure of 2-[4-(dimethylamino)phenyl]-1,3-dimethyl-2,3-dihydro-1H-1,3-benzodiazole-5-carbonitrile (NC-DMBI) and spatial representation of its HOMO (-4.9 eV). DFT calculations have been performed with Orca (B3LYP 6-31G**).

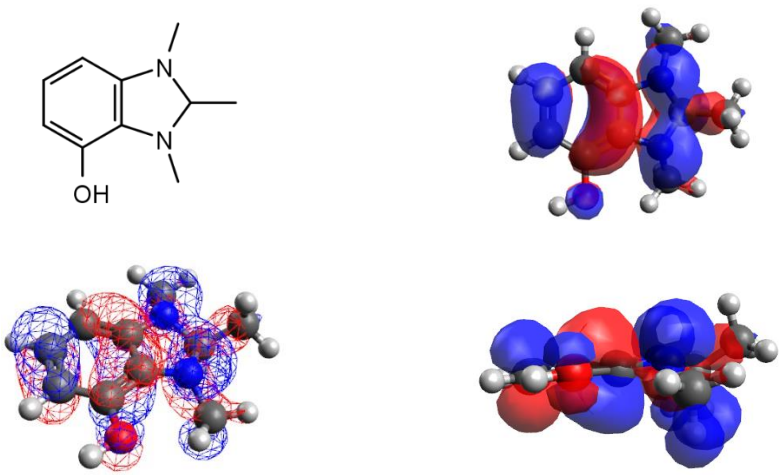

Figure 111: chemical structure of (1,2,3-trimethyl-2,3-dihydro-1H-1,3-benzodiazol-4-ol (OH-TMBI) and spatial representation of its HOMO (-4.4eV). DFT calculations have been performed with Orca (B3LYP 6-31G**).

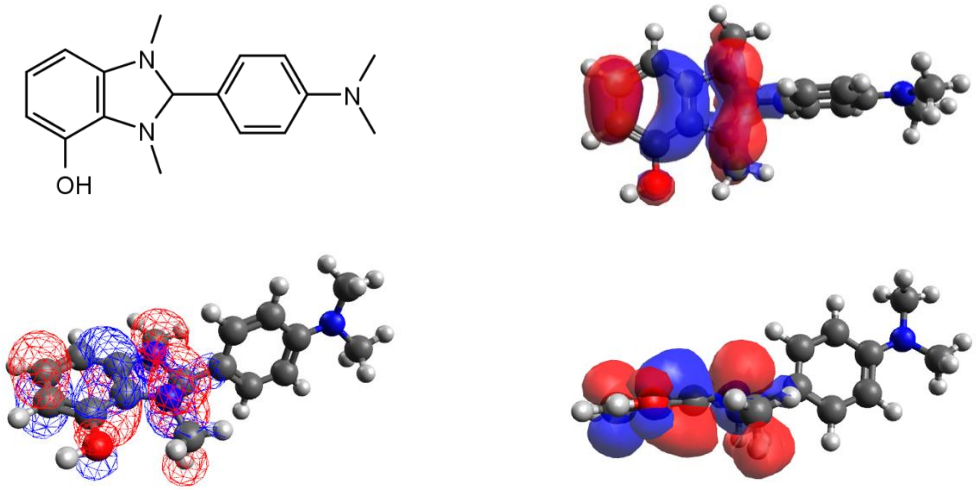

Figure 112: chemical structure of 2-[4-(dimethylamino)phenyl]-1,3-dimethyl-2,3-dihydro-1H-1,3-benzodiazol-4-ol (OH-DMBI) and spatial representation of its HOMO (-4.3eV). DFT calculations have been performed with Orca (B3LYP 6-31G**).

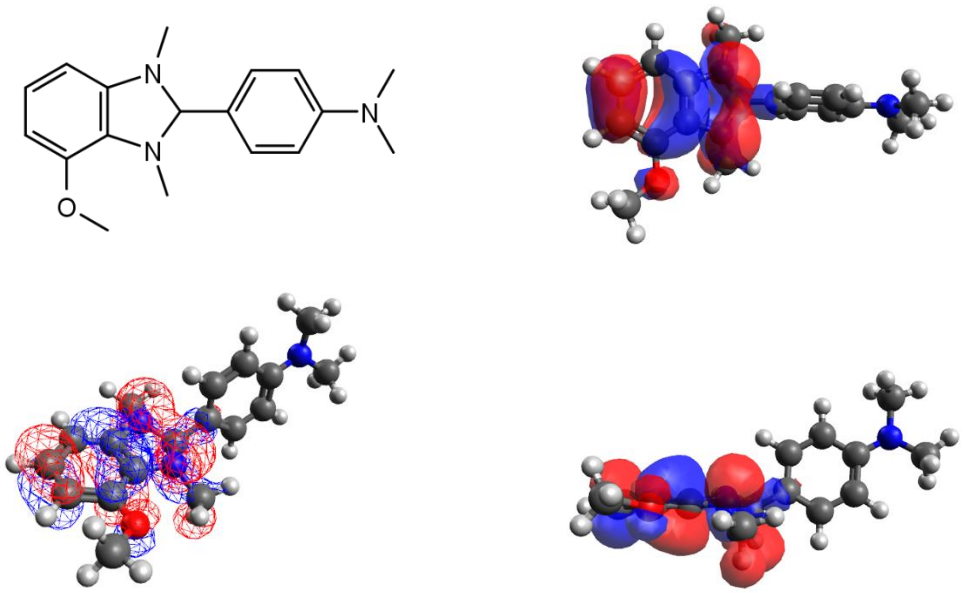

Figure 113 chemical structure of 4-(4-methoxy-1,3-dimethyl-2,3-dihydro-1H-1,3-benzodiazol-2-yl)-N,N-dimethylaniline (MeO-DMBI) and spatial representation of its HOMO (-4.3eV). DFT calculations have been performed with Orca (B3LYP 6-31G**).

Worth to mention that in the case of DiPrBI and DMBI, the HOMO level was also calculated from cyclic voltammograms against ferrocene (Figure 114). Experimentally, the HOMO energies of DMBI and DiPrBI are -4.67eV and -4.59eV, respectively. These values are within the 6% of the calculated values listed in Table 7. Additional details regarding the cyclic voltammograms can be found in the experimental chapter.

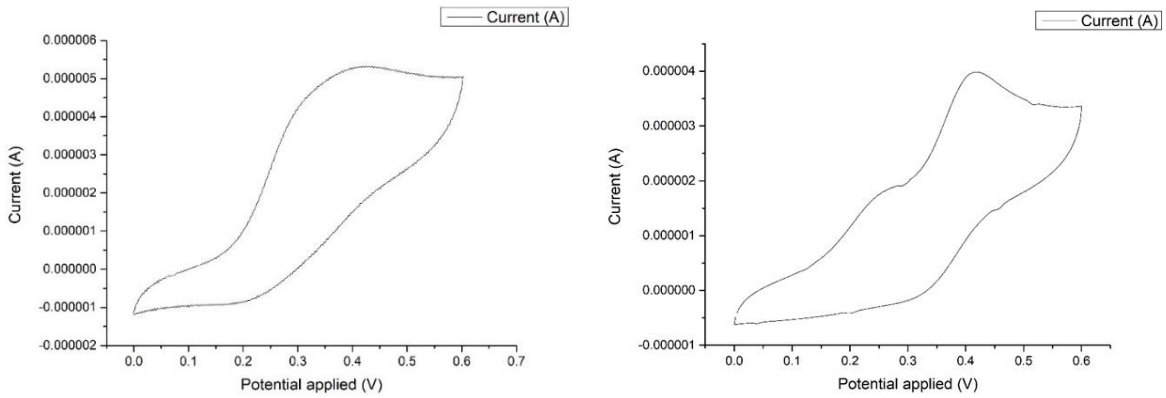

Figure 114. On the right: cyclic voltammograms of DMBI. In the middle: cyclic voltammograms of DiPrBI.

The synthesis of DMBI is relatively simple and it consists of a single reaction step. Indeed, it requires N1,N2-dimethylbenzene-1,2-diamine and 4-(dimethylamino)benzaldehyde as reagents which are both commercially available (Figure 115, Synthesis C).

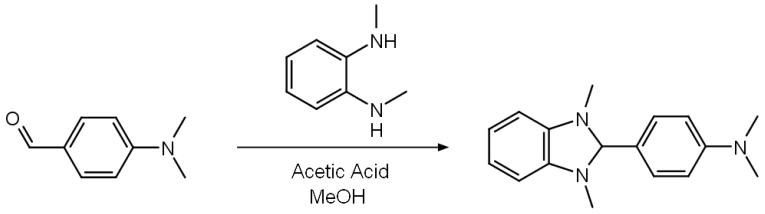

Figure 115. Synthesis of DMBI from N1,N2-dimethylbenzene-1,2-diamine and 4-(dimethylamino) benzaldehyde. Additional details can be found in the experimental chapter, Synthesis C.

To synthetize Me-DMBI and Me2-DMBI, it is not possible to follow the same synthetic path because N1,N2,4-trimethylbenzene-1,2-diamine and N1,N2,4,5-tetramethylbenzene-1,2-diamine are not commercially available. Therefore, it is necessary to begin the synthetic path starting from primary aryldiamines (namely 4-methylbenzene-1,2-diamine and 4,5-dimethylbenzene-1,2-diamine, Figure 116).

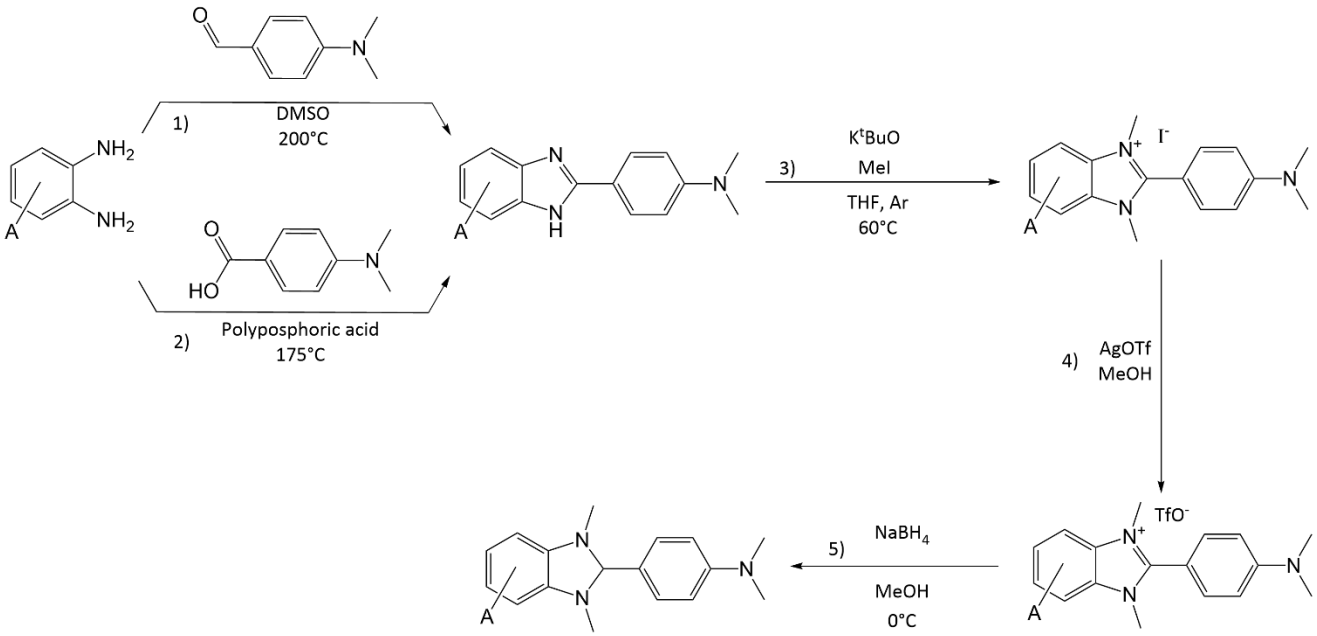

Figure 116. Synthetic path for the synthesis of Me-DMBI and Me2-DMBI. Additional details can be found in the experimental chapter. 1) Synthesis E, Synthesis J. 2) Synthesis F. 3) Synthesis G, Synthesis K. 4) Synthesis H, Synthesis L. 5) Synthesis I, Synthesis M

The first step consists in the cyclocondensation of the aryldiamine and either 4-(dimethylamino)benzaldehyde (Synthesis E, Synthesis J) or 4-(dimethylamino)benzoic (Synthesis F). Although the synthesis involving benzaldehyde leads to a lower yield, it is less time-consuming, and it requires less purification efforts. Therefore, it was selected for further reactions. The second step is the one-pot alkylation of the benzimidazole with an excess of methyl iodide which leads to the methylated benzimidazolium iodide salt (Synthesis G, Synthesis K). To enhance product purity, and ease the purification of the final step, it is possible to replace the iodide counterion of the benzimidazoline salt with triflate, conducting a ion exchange reaction at room temperature with trifluoromethanesulfonate (Synthesis H, Synthesis L, [213]). The final step is the reduction of the benzimidazolium salt with an excess of sodium borohydride which leads to the desired product (Synthesis I, Synthesis M).

OH-TMBI was also synthetized as a side product (Figure 117). Indeed, the original aim was to synthetize OH-DMBI starting from the commercially available 2,3-diaminophenol. However, after the alkylation of 2,3-diaminophenol with a light excess of methyl iodide (Synthesis N), the one-pot reaction of 3-methoxy-N1,N2-dimethylbenzene-1,2-diamine with 4-(dimethylamino)benzaldehyde previously described in Figure 115 failed to yield the desired OH-DMBI. Instead, the ciclocondensation took place between 3-methoxy-N1,N2-dimethylbenzene-1,2-diamine and the traces of acetic acid. The methoxy group was finally removed by acid hydrolysis (Synthesis O).

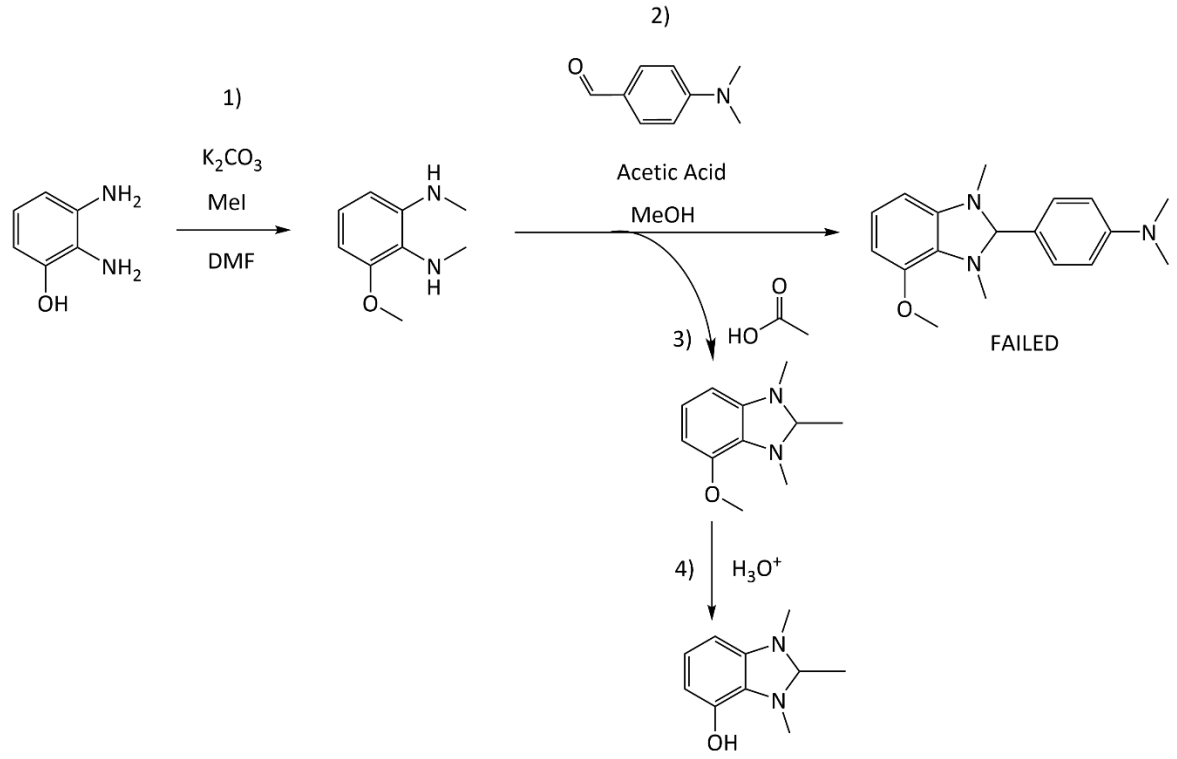

Figure 117 synthesis of OH-TMBI. Additional details can be found in the experimental chapter. 1) Synthesis N. 2-4) Synthesis O.

Unfortunately, due to the extremely low yield of the synthesis, we were able to prepare only one sample of P(NDI2OD-T2) doped at 76%; furthermore, during the measurements, such sample got degraded. Here, we present only one single data relative to OH-TMBI dopant, namely the not annealed 76% doped P(NDI2OD-T2), which shows an electrical conductivity of $2.7 \times 10^{-3} \pm 4 \times 10^{-4}$ Scm^{-1}. This result, although interesting, deserves further investigation.

9.2 ELECTRICAL CHARACTERIZATION

Concerning Me-DMBI and Me2-DMB, first determined the critical concentration above which dopant segregation occurs: doped P(NDI2OD-T2) samples were prepared at different dopant concentrations, namely 20%, 40% 60%, 76%, 100%, 115%, 130%, 145% and 200%, for each molecule. Every sample was then annealed at 150°C for 6 hours under N_2 atmosphere. Finally, the electrical conductivity was measured as previously described, at room temperature under N_2 atmosphere (Figure 118).

Dopants exhibit a different critical concentration, indicating that the introduced functionalization affects the polymer-dopant miscibility. Moreover, at such optimal dopant concentration, all the samples achieved, after 5 hours annealing at 150°C, a significantly higher electrical conductivity with respect to what previously reported for DiPrBI. Worth noting, the doping efficiency of Me2-DMBI is much higher than DiPrBI. Indeed, the sample 40% doped with Me2-DMBI reaches 1.56 x 10^{-2} Scm^{-1}, while the sample 76% doped with DiPrBI (almost twice as much the amount of dopant) reaches only 7.20 x 10^{-3} Scm^{-1}.

As a matter of fact, the top performing dopant Me_2-DMBI, has been published while this project was performing. However, we have obtained a higher conductivity than what was previously reported [213].

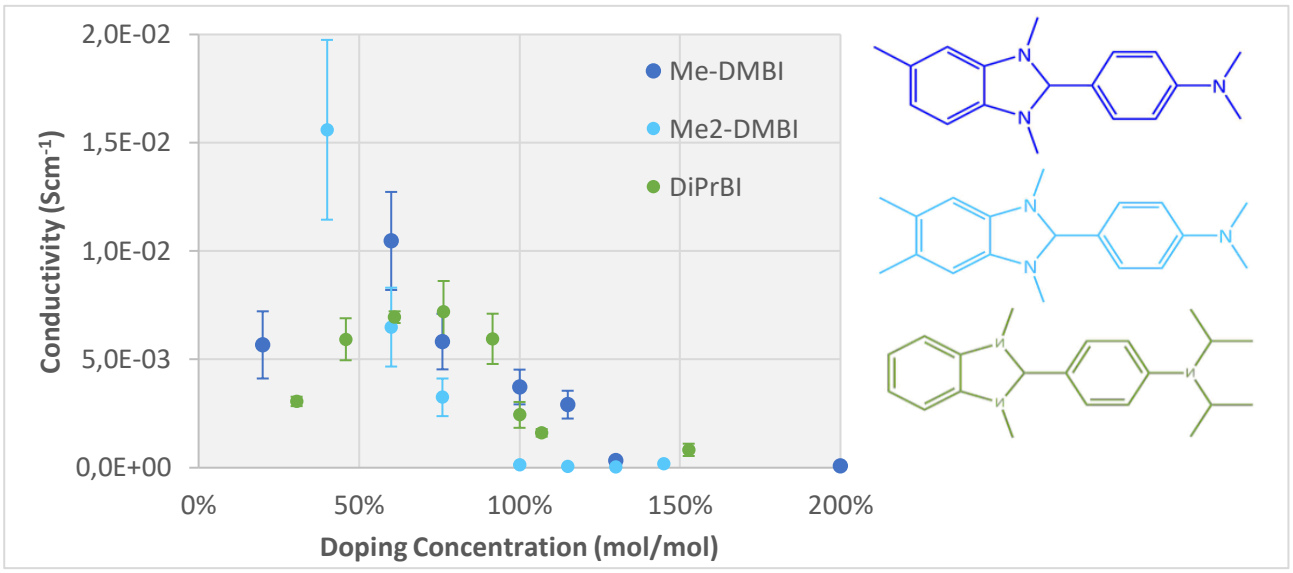

Figure 118. On the left: electrical conductivity of doped P(NDI2OD-T2) with different dopants at different concentrations. Each sample was annealed at 150°C in N_2 atmosphere for 6 hours and electrical conductivity measurements were conducted under N_2 atmosphere at room temperature. On the right: chemical structure of the dopants.

Once the critical concentration of each new dopant was determined (Figure 118), for each molecule, new samples of P(NDI2OD-T2) doped at the optimal concentration were prepared and their electrical conductivity was measured before annealing and then at increasing annealing time. Each sample was annealed under N_2 atmosphere at 150°C (Figure 119), as previously described.

Similarly, to what already reported in Figure 71, before the annealing process, the electrical conductivity of all the doped samples is more than 3 orders of magnitude higher than pristine polymer. In this case, however, the electrical conductivity of samples doped with different dopants is significantly different, suggesting that dopant HOMO level is involved in the doping mechanism before annealing process takes place. In fact, DiPrBI and Me-DMBI have similar HOMO (within 0.04 eV) and they show similar initial electrical conductivity (around 1.69 x 10^{-3} Scm^{-1}), while Me2-DMBI has a shallower HOMO (0.1eV more than DiPrBI) and exhibits a significantly higher initial electrical conductivity (2.76 x 10^{-3} Scm^{-1}).

Finally, for each annealing time, the higher the HOMO of the dopant, the higher the electrical conductivity.

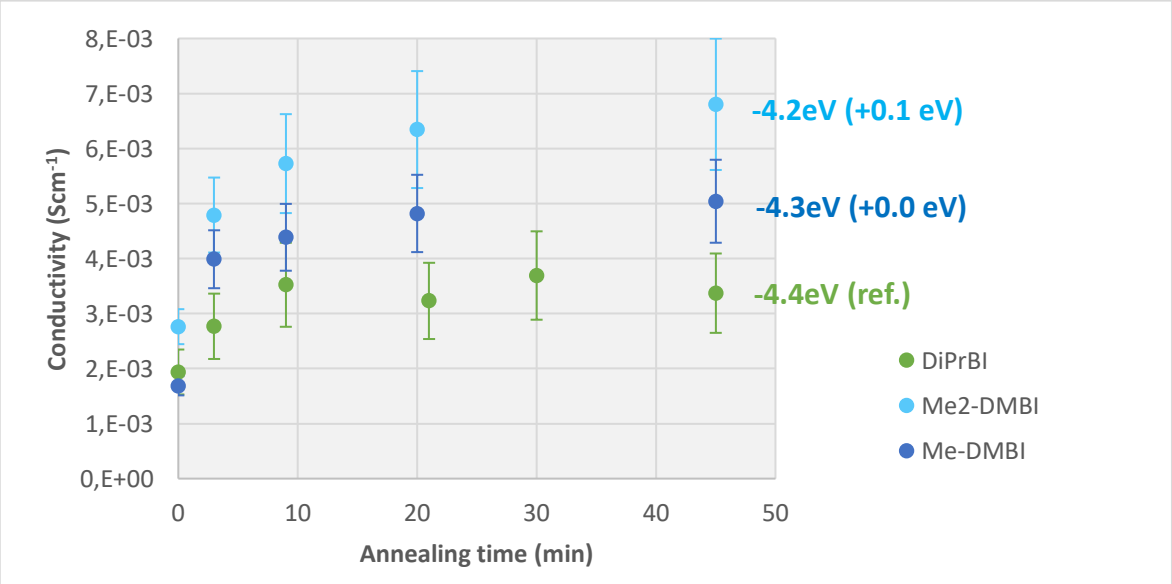

Figure 119: electrical conductivity of P(NDI2OD-T2) doped with different dopants each at the critical concentration determined in Figure 118 before the annealing (t = 0 min) and in the first 45 minutes of annealing. The dopant HOMO energy in its absolute minimum conformation is also reported. Within the brackets is the difference of HOMO energy between any given dopant and DiPrBI, used as reference.

9.3 PLANARIZATION

Although Me-DMBI and Me_2-DMBI exhibit a higher HOMO than DiPrBI when they are in their minimum energy conformation, the direct electron transfer mechanism from dopant HOMO to polymer LUMO is still hindered by an energy barrier of around 0.42 eV and 0.29 eV, respectively.

As discussed in the previous chapter, dopant planarization caused by the intercalation of the molecule between the NDI units might perturbate the electronic structure of the benzimidazole, increasing its HOMO energy and eventually allowing for new electronic transitions. Among the different planarization mechanisms discussed in the previous chapter, we have selected planarization D and E and we have studied Me-DMBI and Me_2-DMBI undergoing those planarization mechanisms. Finally, we have compared the results with D-DiPrBI and E-DiPrBI (Figure 120 and Figure 121, respectively).

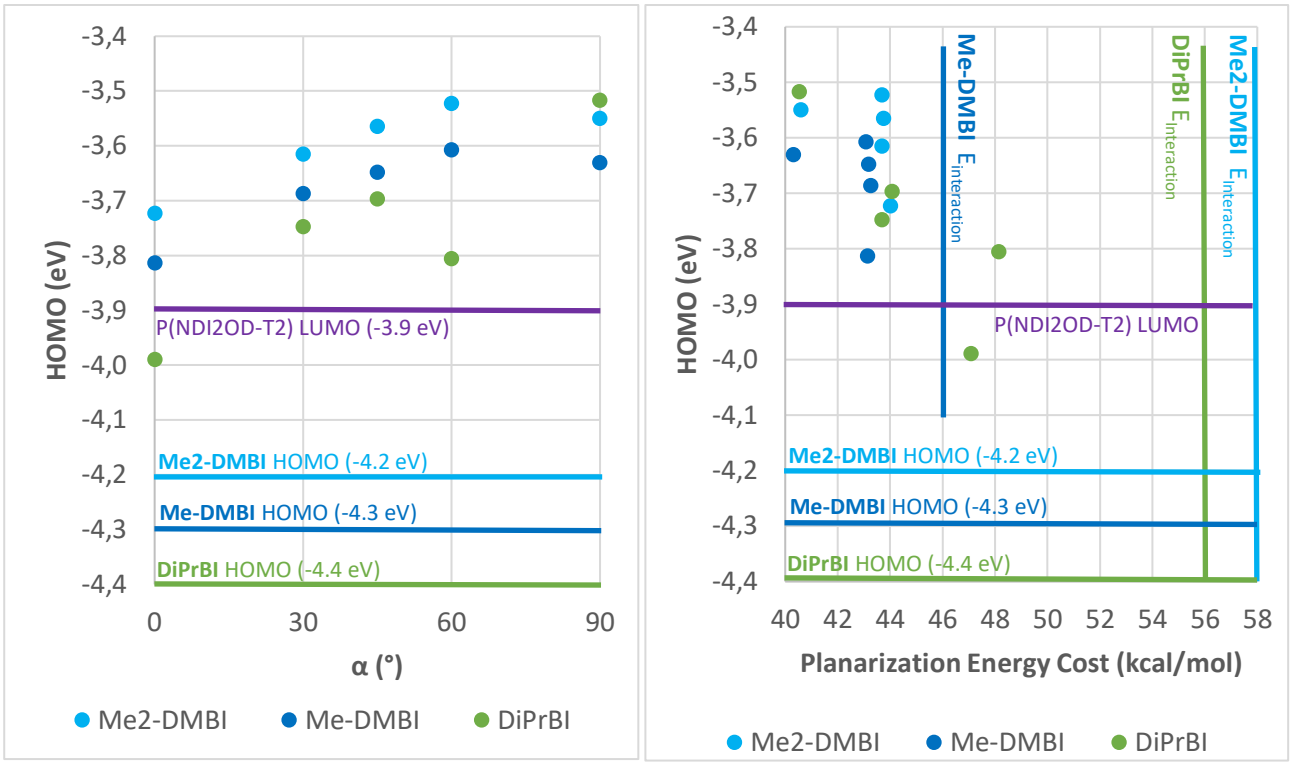

Figure 120. Me_2-DMBI, Me-DMBI and DiPrBI undergoing planarization mechanism D (Figure 89). On the left, HOMO level for different α values. On the right, HOMO level as a function of the planarization energy cost. For each geometry, the structure has been optimized with Orca using B3LYP functional and 6-31G** basis set. For reference the HOMO level of each dopant in its absolute minimum conformation, P(NDI2OD-T2) LUMO and dopant-polymer interaction energies are also reported.

According to Figure 120, every dopant exhibits a dramatic increase of the HOMO energy caused by the planarization mechanism D, overcoming the P(NDI2OD-T2) LUMO. Most of the times, the planarization energy cost is around 43kcal/mol regardless the dihedral angle value α. This is a strong indication that the dramatic increase of the HOMO energy is given by the nitrogen atom 18 laying on the Z = 0 Å plane and not by the variation of α. Furthermore, the dopants significantly differ in the value of their interaction energy with the polymer: DiPrBI and Me_2-DMBI gain around 56 kcal/mol and 58 kcal/mol, respectively, while Me-DMBI only gains 48 kcal/mol. The best performing dopant is DiPrBI since it reaches the highest HOMO with the lowest required planarization energy cost. This contradicts the electrical conductivity measures of Figure 119, however, it is possible to notice that Me-DMBI and Me2-DMBI exhibit many isoenergetic conformations, regardless the value of the dihedral angle α, while DiPrBI does not. It is possible to speculate that the higher doping efficiency of Me-DMBI and Me2-DMBI might be related to a structure with a higher conformational freedom that favours out-of-equilibrium fluctuations of the dopant structure.

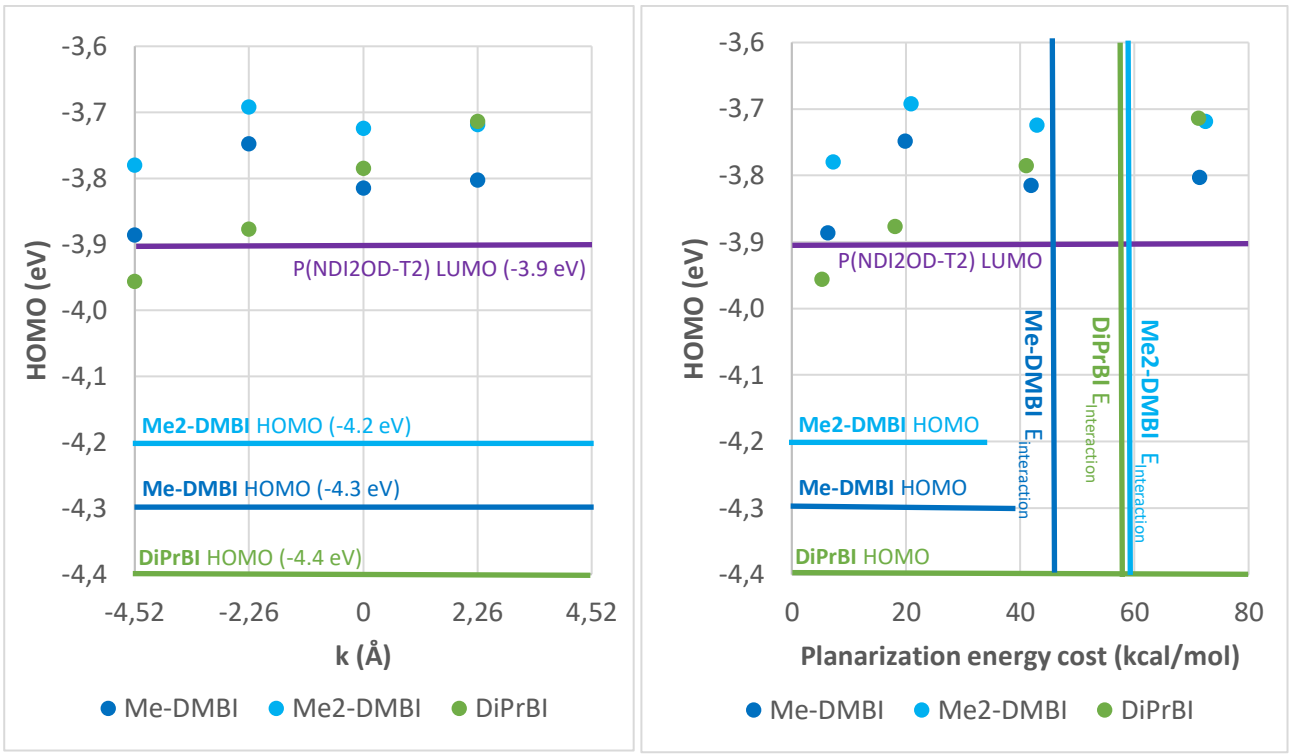

Figure 121. Me_2-DMBI, Me-DMBI and DiPrBI undergoing planarization mechanism E (Figure 91). On the left, HOMO level for different α values. On the right, HOMO level as a function of the planarization energy cost. For each geometry, the structure has been optimized with Orca using B3LYP functional and 6-31G** basis set. For reference the HOMO level of each dopant in its absolute minimum conformation, P(NDI2OD-T2) LUMO and dopant-polymer interaction energies are also reported.

The results showed in Figure 121 agree with the electrical conductivity characterization of Figure 119. Indeed, at planarization energies below 21kcal/mol, Me_2-DMBI exhibits a HOMO higher than Me-DMBI, which in turn exhibits a HOMO higher than DiPrBI. The first discrepancy from this trend occurs over 40 kcal/mol (k > 0 Å), confirming what it was reported in Figure 120.

10. CONCLUSIONS

A collection of experimental evidence interestingly showed that, contrary to the traditional concept of thermally activated doping mechanism, the n-type doping of P(NDI2OD-T2) by 1H- benzimidazoles is already active at room temperature. We have demonstrated that before the thermal treatment takes place, the electrical conductivity of P(NDI2OD-T2):DiPrBI thin films increases more than three orders of magnitude with respect to the pristine polymer. IR spectroscopy further confirms such evidence, showing in doped-not annealed samples the rise of new absorption features that can be ascribed by the formation of the polaron. This is a clear indication that DiPrBI is already active at room temperature, while annealing has only a minor effect, causing a further tripling of the electrical conductivity. GIWAXS measurements have revealed that the morphology of pristine non-doped films is remarkably different from the morphology of the doped polymer films, regardless the annealing process, whose contribution is relatively marginal. The results are compatible with a dopant intercalation between the polymer NDI units. Based on density functional theory calculations we have proposed a new doping mechanism that does not require thermal energy to be triggered. The introduced mechanism involves the conformational modification of the dopant molecule that, while intercalating between the narrow planar NDI unit, planarizes. Such flattening is accompanied by a perturbation of the dopant electron density and by an increase of the dopant HOMO energy. A systematic study on many different planarization mechanisms has been reported, demonstrating that new electronic transitions are available to the electrons of the planarized dopant, whose HOMO energy can increase enough to reach polymer LUMO, and eventually allowing direct electron transfer towards the polymer.

Finally, according to all the performed density functional theory simulations, the spatial localization of the dopant HOMO is always localized on the benzimidazole moiety. Therefore, we have investigated the possibility of fine-tuning the HOMO energy level of the dopant by adding electron-donor or electron-withdrawing functional groups to the benzimidazole moiety. New dopants were designed, simulated, and synthetized, showing a highly improved dopant efficiency with respect to the DMBI benchmark.

Overall, our work demonstrated that although it is possible to improve doping efficiency by increasing the dopant HOMO level or by increasing the polymer-dopant miscibility, it is important to always consider the morphological interactions between the two chemical species that might generate new conformational geometries characterized by new sets of possible electronic transitions.

These results set guidelines for the molecular design of the next generation of 1H benzimidazole derived n-type dopants.

11. EXPERIMENTAL

10.1 SYNTHESIS

All the chemicals were purchased from Sigma-Aldrich, TCI-chemicals and Fluorochem and used as received. NMR spectra were acquired using a Bruker ARX400 instrument.

Most of the synthetic paths reported in the following pages are not new and are already well described in literature. [210],[223]

In particular, DiPrBI, the most important dopant for this work, was fully characterized in [210] including NMR and DSC measures. The synthesis is known to afford a high purity product with a low yield. For these reasons it was decided to use NMR to confirm the identity of synthesized DiPrBI without further purity characterization.

On the contrary, Me-DMBI, the only original compound of this work, would deserve further characterization, however, Covid-19 pandemic severely reduced the working time, the laboratory, and the instruments availability, therefore electrical measures were performed without further dopant purity characterization.

Synthesis A **4-[bis(propan-2-yl)amino]benzaldehyde**

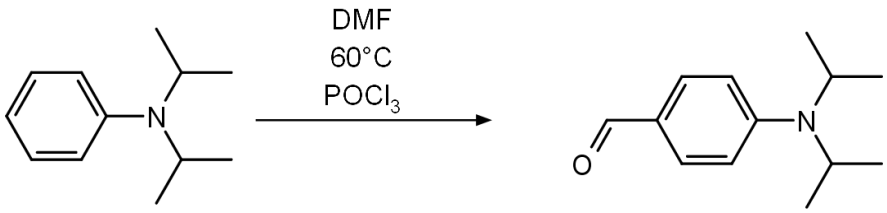

The procedure was adapted from [226]. 0.8mL of $POCl_3$ (1.300g, 8.480mmol) were added to a solution of N,N-bis(propan-2-yl)aniline (1.000g, 5.640mmol) in anhydrous DMF (2mL). The solution was stirred at 60°C overnight. After cooling to room temperature, 50mL of H_2O and 100mL of ethyl acetate were added. The organic fraction was washed with water and then dried over Na_2SO_4. Finally, the organic solvent was removed under reduced pressure. The crude product was purified with column chromatography on silica gel using a solution of n-hexane : ethyl acetate (1:2) as eluent. 0.350 g (1.704mmol) of white product were obtained at the end of the process. The calculated reaction yield is 30%.

^{1}H NMR (400MHz, $CDCl_3$) δ: 9.705 (s, 1H, ●); 7.671 (d, J = 9.05 Hz, 2H, ●); 6.837 (d, J = 9.05 Hz, 2H, ●); 3.995 (hept, J = 6.90 Hz, 2H, ●); 2.008 (d, J = 6.90 Hz, 12H, ●)

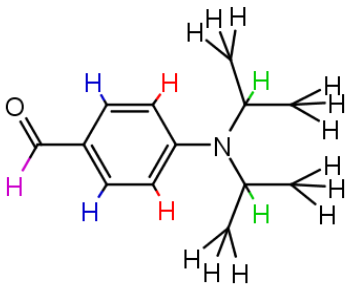

Synthesis B **DiPrBI: 4-(1,3-dimethyl-2,3-dihydro-1H-1,3-benzodiazol-2-yl)-N,N-bis(propan-2-yl)aniline**

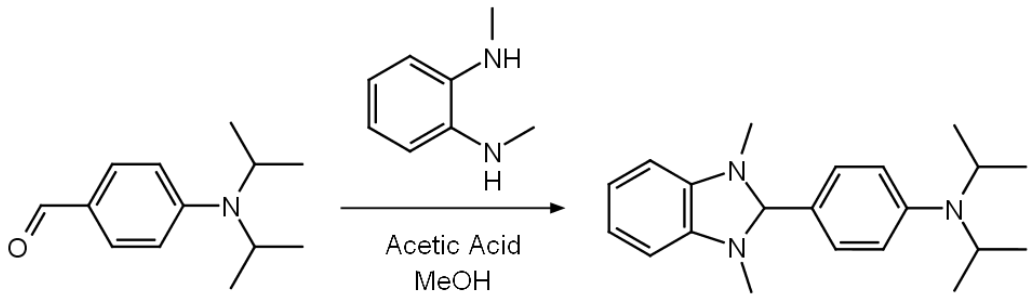

N1,N2-dimethylbenzene-1,2-diamine (0.100g, 0.735mmol) was dissolved in methanol (1.5mL). 0.151g (0.735mmol) of 4-[bis(propan-2-yl)amino]benzaldehyde and 2 drops of glacial acetic acid were subsequently added. The resulting mixture was sonicated overnight. The solution was then cooled to -12°C for 24h. The precipitate was filtered and washed with cold methanol. The product was finally dried under reduced pressure to afford 0.080g (0.247mmol) of pure product as a white powder. The calculated reaction yield is 34%.

^{1}H NMR (400MHz, $CDCl_3$) δ: 7.34 (d, J = 6.68 Hz, 2H, ●); 6.87 (d, J = 6.68 Hz, 2H, ●); 6.72 – 6.67 (m, 2H, ●); 6.43 – 6.39 (m, 2H, ●); 4.76 (s, 1H, ●); 3.84 (hept; J = 6.73 Hz= 2H, ●); 2.56 (s, 6H, ●); 1.26 (d, J = 6.73 Hz, 12H, ●).

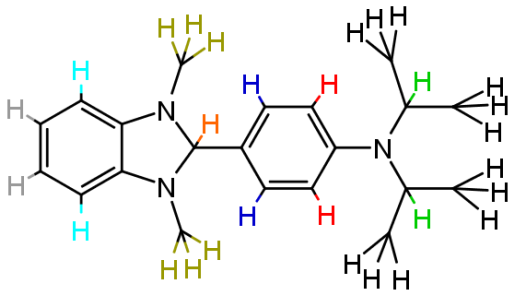

For comparison the ^{1}H NMR (400MHz, $CDCl_3$) spectrum of N1,N2-dimethylbenzene-1,2-diamine is also reported. δ: 6.86 – 6.83 (m, 2H, ●); 6.72 – 6.68 (m, 2H, ●); 2.87 (s, 6H, ●)

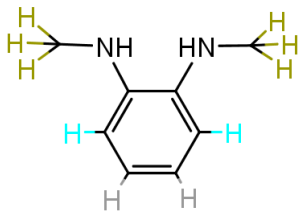

Synthesis C **DMBI: 4-(1,3-dimethyl-2,3-dihydro-1H-1,3-benzodiazol-2-yl)-N,N-dimethylaniline**

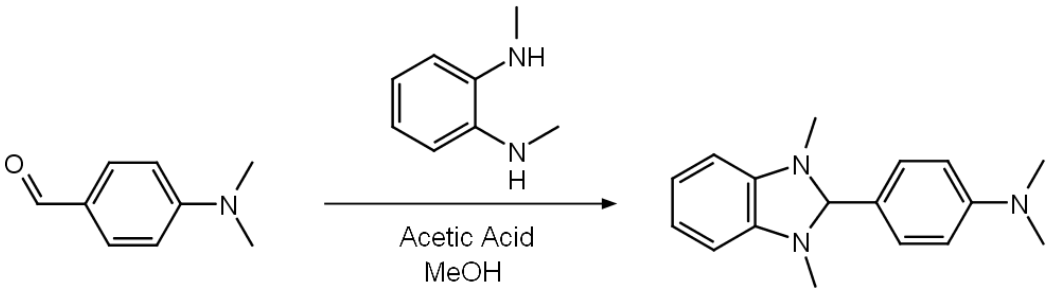

N1,N2-dimethylbenzene-1,2-diamine (0.100g, 0.735mmol) was dissolved in methanol (1.5mL). 0.109g (0.735mmol) of 4-(dimethylamino)benzaldehyde and 2 drops of glacial acetic acid were added. The resulting mixture was sonicated overnight. The solution was then cooled to -12°C for 24h. The precipitate was filtered and washed with cold methanol. The product was then dried under reduced pressure and it was purified with short column chromatography using a solution of n-hexane : diethyl ether (1:1) as eluent to afford 0.057g (0.213 mmol) of pure product as a brown crystals. The calculated reaction yield is 29%.

^{1}H NMR (400MHz, $CDCl_3$) δ: 7.43 (d, J = 8.80 Hz, 2H, ●); 6.75 (d, J = 8.80 Hz, 2H, ●); 6.72 – 6.67 (m, 2H, ●); 6.43 – 6.39 (m, 2H, ●); 4.78 (s, 1H, ●); 2.99 (s, 6H, ●); 2.55 (s, 6H, ●).

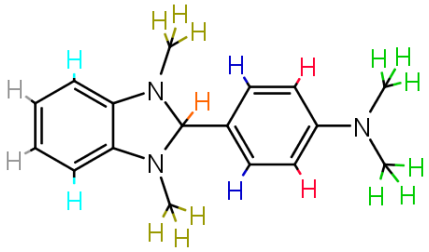

For comparison, the ^{1}H NMR (400MHz, $CDCl_3$) spectrum of 4-(dimethylamino)benzaldehyde is also reported. δ: 9.76 (s, 1H,●); 7.76 (d, J = 8.93 Hz; 2H, ●); 6.79 (d, J = 8.93 Hz; 2H, ●); 3.09 (s, 6H, ●)

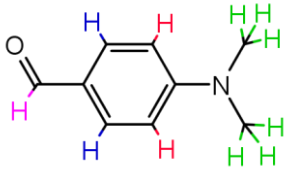

Synthesis D **DPhBI: 4-(1,3-dimethyl-2,3-dihydro-1H-1,3-benzodiazol-2-yl)-N,N-diphenylaniline**

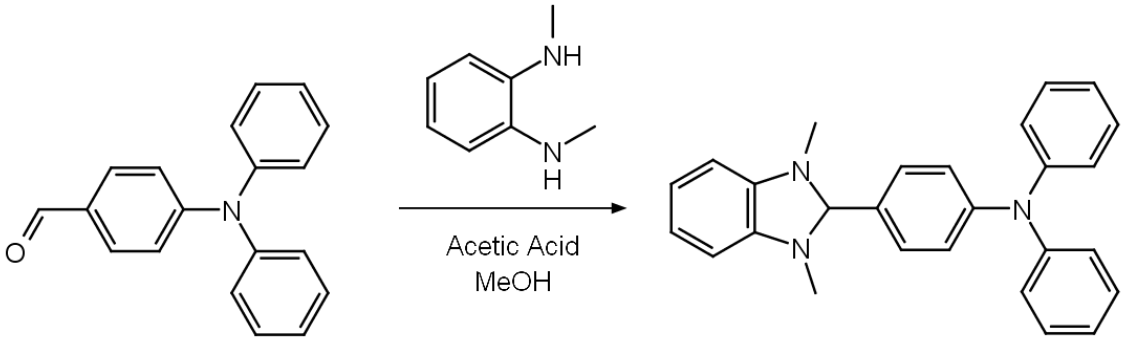

N1,N2-dimethylbenzene-1,2-diamine (0.100g, 0.735mmol) was dissolved in methanol (1.5mL). 0.201g (0.735mmol) of 4-(diphenylamino)benzaldehyde and 2 drops of glacial acetic acid were added. The resulting mixture was sonicated overnight. The solution was then cooled to -12°C for 24h. The precipitate was filtered and washed with cold methanol. The product was finally dried under reduced pressure to afford 0.258g (0.662mmol) of pure product as a white powder. The calculated reaction yield is 90%.

^{1}H NMR (400MHz, $CDCl_3$) δ: 7.41 (d, J = 8.56 Hz, 2H, ●); 7.25 (dd, J1 = J2= 7.34 Hz, 4H, ●); 7.12 (d, J= 7.4 Hz, 4H, ●); 7.09 (d, J = 8.56 Hz, 2H, ●); 7.04 (dd, J1 = J2 = 7.34 Hz, 2H, ●); 6.72 - 6.69 (m, 2H, ●); 6.46 – 6.42 (m, 2H, ●); 4.82 (s, 1H, ●); 2.60 (s, 6H, ●).

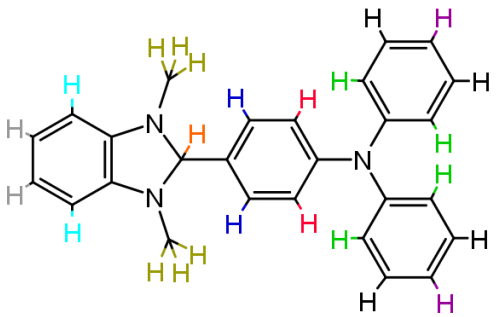

For comparison, the ^{1}H NMR (400MHz, $CDCl_3$) spectrum of 4-(diphenylamino)benzaldehyde is also reported. δ: 9.82 (s, 1H, ●); 7.68 (d, J = 8.80 Hz, 2H, ●); 7.36-7.32 (m, 4H, ●); 7.18 – 7.15 (m, 6H, ●); 7.01 (d, J= 8.80 Hz, 2H, ●).

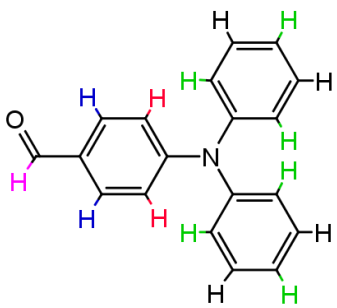

Synthesis E **N,N-dimethyl-4-(6-methyl-1H-1,3-benzodiazol-2-yl)aniline**

(starting from 4-(dimethylamino)benzaldehyde)

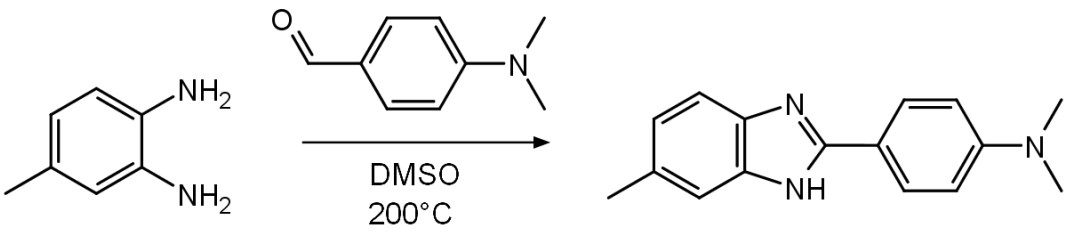

0.500g (4.10mmol) of 4-methylbenzene-1,2-diamine and 0.610g (4.10mmol) of 4-(dimethylamino)benzaldehyde were dissolved in 8mL of dimethyl sulfoxide. The solution was heated at 200°C in a sealed tube for 30min. Then the flask was cooled to room temperature and 70mL of ice were added to the solution. The mixture was sonicated for 1h. The bright yellow precipitate was filtered and dried under reduced pressure. At the end of the process, 0.7751g (3.088mmol) of beige powder were obtained. The calculated reaction yield is 75%.

^{1}H NMR (400MHz, $CDCl_3$) δ: 8.08 (d, J = 8.90 Hz, 2H, ●); 7.61 (d, J = 8.19 Hz, 1H, ●); 7.52 (s, 1H, ●); 7.07 (d, J = 8.19 Hz, 1H, ●); 6.25 (d, J = 8.90 Hz, 1H, ●); 2.75 (s, 6H, ●); 2.40 (s, 3H, ●).

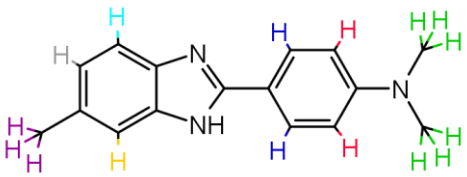

For comparison, the ^{1}H NMR (89.56MHz, $CDCl_3$) spectrum of 4-methylbenzene-1,2-diamine is also reported. [227] δ: 6.57 (d, 1H, ●); 6.49 (d, 1H, ●); 6.49 (s, 1H, ●); 3.28 (s, 4H, ●); 2.19 (s, 3H, ●).

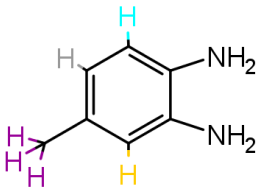

Synthesis F **N,N-dimethyl-4-(6-methyl-1H-1,3-benzodiazol-2-yl)aniline**

(starting from 4-(dimethylamino)benzoic acid)

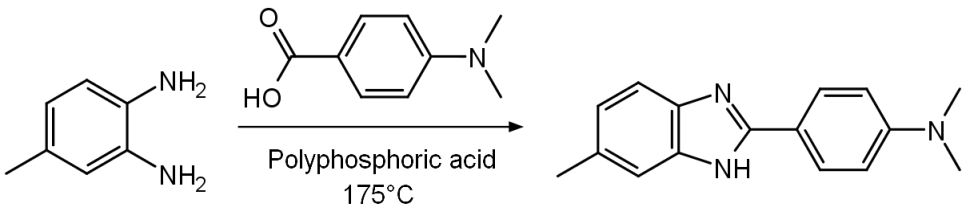

4g of polyphosphoric acid are added to a mixture of 0.500g (4.10mmol) of 4-methylbenzene-1,2-diamine and 0.792g (4.79mmol) of 4-(dimethylamino)benzoic acid. The mixture is heated at 175°C for 48h under stirring. Then a solution of NH_4OH (7%) is added to reach pH 7, the mixture is sonicated 1h. The pink precipitate is filtered and washed with H_2O multiple times. The crude product is partially dried under reduced pressure and then it is dissolved in THF and dried over Na_2SO_4. The organic solvent is then evaporated under reduced pressure. At the end of the process, 0.9427g (3.755mmol) of brown product are collected. The calculated reaction yield is 91%. Worth to notice that although reaction yield is higher than in the case of Synthesis E, the synthesis is more time consuming, and the purification requires much more effort and yield a less pure product. For this reason, the synthetic route described in Synthesis E is preferable for future reactions.

^{1}H NMR (400MHz, $CDCl_3$) δ: 8.08 (d, J = 8.90 Hz, 2H, ●); 7.61 (d, J = 8.19 Hz, 1H, ●); 7.52 (s, 1H, ●); 7.07 (d, J = 8.19 Hz, 1H, ●); 6.25 (d, J = 8.90 Hz, 1H, ●); 2.75 (s, 6H, ●); 2.40 (s, 3H, ●).

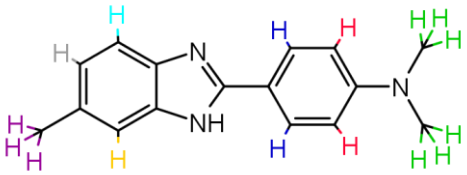

For comparison, the ^{1}H NMR (89.56MHz, DMSO) spectrum of 4-(dimethylamino)benzoic acid is also reported. [227] δ: 7.71 (d, 2H, ●); 6.71 (d, 2H, ●); 2.98 (s, 1H, ●).

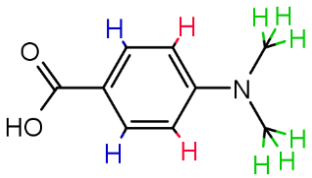

Synthesis G **2-[4-(dimethylamino)phenyl]-1,3,6-trimethyl-1H-1,3-benzodiazol-3-ium iodide**

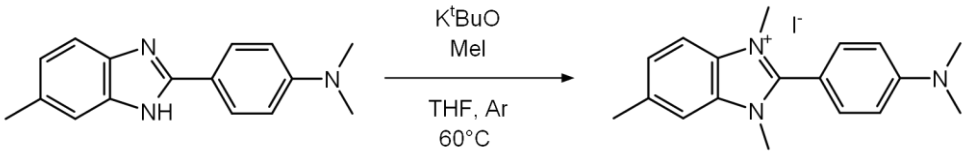

0.775g (3.08mmol) of N,N-dimethyl-4-(6-methyl-1H-1,3-benzodiazol-2-yl)aniline (obtained either *via* Synthesis E or *via* Synthesis F) and 0.379g (3.38mmol) of potassium tert-butoxide were dissolved in 12mL of anhydrous THF in a sealed tube. The mixture was left under stirring in Ar atmosphere for 30min. Then 0.958mL (2.185g, 15.40mmol) of iodomethane were added to the solution. The reaction was left at 60°C for 4 days. Then the reaction was cooled to room temperature, the solvent was removed under reduced pressure, 50mL of H_2O were added to the flask and the solution was extracted 3 times with 50mL of chloroform. The organic fractions were collected and dried over Na_2SO_4. At the end of the process, 0.435g (1.069mmol) of pale-yellow product were obtained. The calculated reaction yield is 32%.

Synthesis H **2-[4-(dimethylamino)phenyl]-1,3,6-trimethyl-1H-1,3-benzodiazol-3-ium triflate**

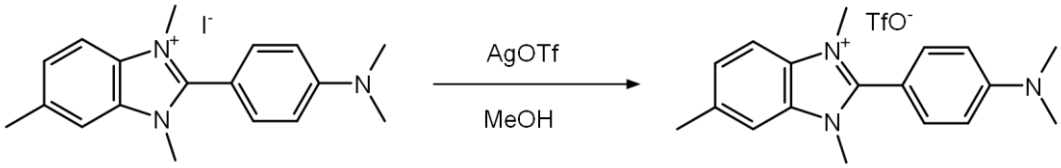

Synthesis adapted from **[213]**. 0.232g (0.570mmol) of 2-[4-(dimethylamino)phenyl]-1,3,6-trimethyl-1H-1,3-benzodiazol-3-ium iodide (Synthesis G) were dissolved in 5mL of methanol. A solution of silver trifluoromethanesulfonate (0.146g, 0.570mmol) in 7mL of methanol was added dropwise. The mixture was left 1h at room temperature, under stirring in the dark. The precipitate was filtered over celite and it was washed with methanol. The solvent was removed under reduced pressure and the crude product was triturated with 1mL of ethyl acetate at 0°C. The precipitate was filtered and washed with more cold ethyl acetate to afford 0.096g (0.223mmol) of pure product as a white powder. The reaction yield is 39%.

^{1}H NMR (400MHz, $CDCl_3$) δ: 7.72 (d, J = 9.00 Hz, 2H, ●); 7.65 (d, J = 8.44 Hz, 1H, ●); 7.55 (s, 1H, ●); 7.46 (d, J = 8.44 Hz, 1H, ●); 6.92 (d, J = 9.00Hz, 2H, ●); 4.04 (s, 3H, ●); 4.03 (s, 3H, ●); 3.13 (s, 6H, ●); 2.60 (s, 3H, ●).

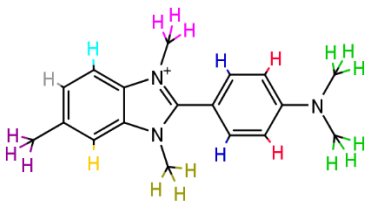

Synthesis I **Me-DMBI: N,N-dimethyl-4-(1,3,5-trimethyl-2,3-dihydro-1H-1,3-benzodiazol-2-yl)aniline**

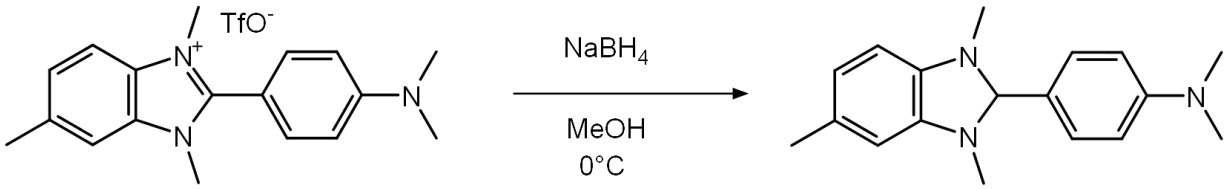

0.096g (0.224mmol) of 2-[4-(dimethylamino)phenyl]-1,3,6-trimethyl-1H-1,3-benzodiazol-3-ium triflate (Synthesis H) were dissolved in 5mL of methanol. The solution was cooled to 0°C. 0.025g (0.669mmol) of $NaBH_4$ were added slowly under stirring. The mixture was left for 2h at room temperature under stirring in the dark. 70mL of H_2O were added and the mixture was extracted 3 times with 70mL of n-hexane. The organic fractions were collected, dried over Na_2SO_4 and the solvent was evaporated under reduced pressure. At the end of the process 0.022g (0.078mmol) of pure white product were obtained. The calculated reaction yield is 35%.

^{1}H NMR (400MHz, acetonitrile-d3) δ: 7.36 (d, J = 8.68 Hz, 2H, ●); 6.78 (d, J = 8.68 Hz, 2H, ●); 6.44 (d, J = 7.46 Hz, 1H, ●); 6.30 (d, J = 7.46 Hz, 1H, ●); 6.27 (s, 1H, ●); 4.63 (s, 1H, ●); 2.95 (s, 6H, ●); 2.45 (s, 3H, ●); 2.44 (s, 3H, ●); 2.21 (s, 3H, ●).

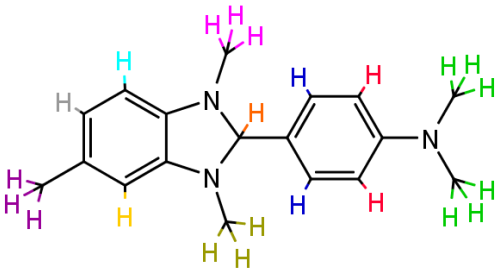

Synthesis J **4-(5,6-dimethyl-1H-1,3-benzodiazol-2-yl)-N,N-dimethylaniline**

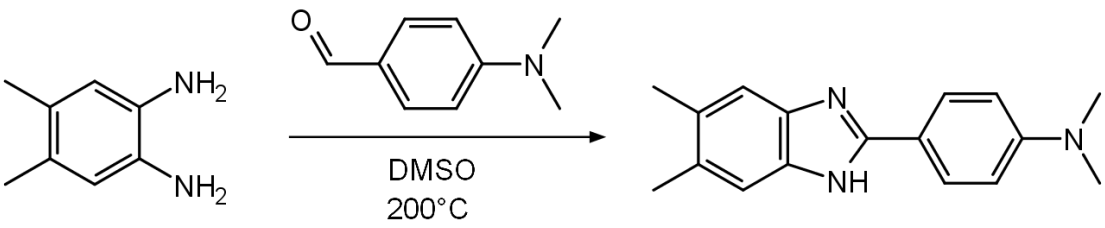

0.545g (4.001mmol) of 4,5-dimethylbenzene-1,2-diamine and 0.597g (4.001mmol) of 4-(dimethylamino)benzaldehyde were dissolved in 8mL of dimethyl sulfoxide. The solution was heated at 200°C for 30min. Then the flask was cooled to room temperature and 70mL of ice were added to the solution. The mixture was sonicated for 1h. The bright yellow precipitate was filtered and dried under reduced pressure. At the end of the process, 0.786g (2.966mmol) of beige product were obtained. The calculated reaction yield is 74%.

As previously discussed in the description of Synthesis F, it is probably possible to obtain the same product with a higher yield starting with 4-(dimethylamino)benzoic acid and using polyphosphoric acid as reaction solvent. However, the synthetic path followed in Synthesis J requires less steps and it was selected as less time consuming.

^{1}H NMR (400MHz, $CDCl_3$) δ: 7.96 (d, J = 8.56 Hz, 2H, ●), 7.39 (s, 2H, ●); 6.56 (d, J = 8.56 Hz, 2H, ●); 2.92 (s, 6H, ●); 2.32 (s, 6H, ●)

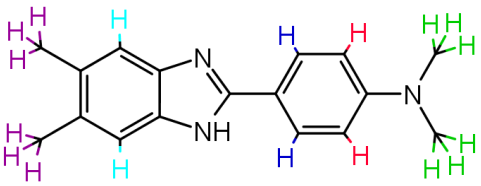

For comparison, the ^{1}H NMR (89.56MHz, $CDCl_3$) spectrum of 4,5-dimethylbenzene-1,2-diamine is also reported [227]. δ 6.46 (s, 2H, ●); 3.19 (s, 4H, ●); 2.10 (s, 6H, ●).

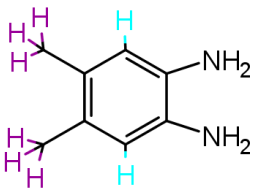

Synthesis K **2-[4-(dimethylamino)phenyl]-1,3,5,6-tetramethyl-1H-1,3-benzodiazol-3-ium iodide**

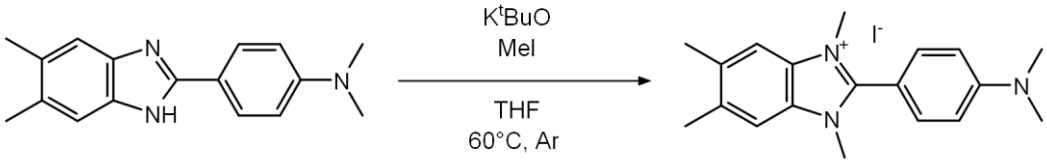

0.786g (2.968mmol) of 4-(5,6-dimethyl-1H-1,3-benzodiazol-2-yl)-N,N-dimethylaniline (Synthesis J) and 0.365g (3.265mmol) of potassium tert-butoxide were dissolved in 45mL of anhydrous THF. The mixture was left under stirring in Ar atmosphere for 30min. Then 0.924mL (2.106g, 14.84mmol) of iodomethane were added to the solution. The reaction was left at 60°C for 4 days. Then the reaction was cooled to room temperature, the solvent was removed under reduced pressure, 50mL of H_2O were added to the flask and the solution was extracted 6 times with 50mL of dichloromethane. The organic fractions were collected and dried over Na_2SO_4. At the end of the process, 0.858g (2.043mmol) of beige product were obtained. The calculated reaction yield is 69%.

Synthesis L **2-[4-(dimethylamino)phenyl]-1,3,5,6-tetramethyl-1H-1,3-benzodiazol-3-ium triflate**

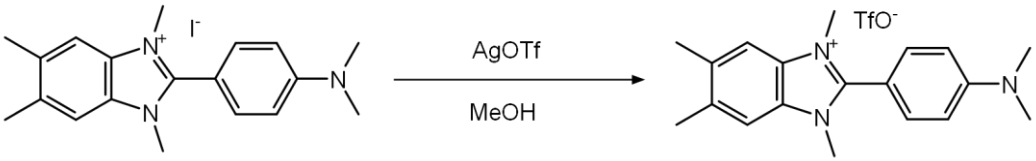

Synthesis adapted from [213]. 0.859g (2.045mmol) of 2-[4-(dimethylamino)phenyl]-1,3,5,6-tetramethyl-1H-1,3-benzodiazol-3-ium iodide (Synthesis K) were dissolved in 15mL of methanol. A solution of silver trifluoromethanesulfonate (0.526g, 2.045mmol) in 19mL of methanol was added dropwise. The mixture was left 1h at room temperature, under stirring in the dark. The precipitate was filtered over celite and it was washed with methanol. The solvent was removed under reduced pressure and the crude product was triturated with 3mL of ethyl acetate at 0°C. The precipitate was filtered and washed with more cold ethyl acetate to afford 0.550g (1.242mmol) of pure product as a white powder. The reaction yield is 61%.

^{1}H NMR (400MHz, $CDCl_3$) δ: 7.68 (d, J = 8.93 Hz, 2H, ●); 7.51 (s, 2H, ●); 6.90 (d, J = 8.93 Hz, 2H, ●); 4.00 (s, 6H, ●); 3.12 (s, 6H, ●); 2.47 (s, 6H, ●).

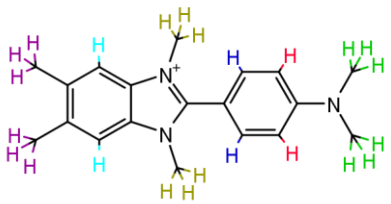

Synthesis M **Me_2-DMBI: N,N-dimethyl-4-(1,3,5,6-tetramethyl-2,3-dihydro-1H-1,3-benzodiazol-2-yl)aniline**

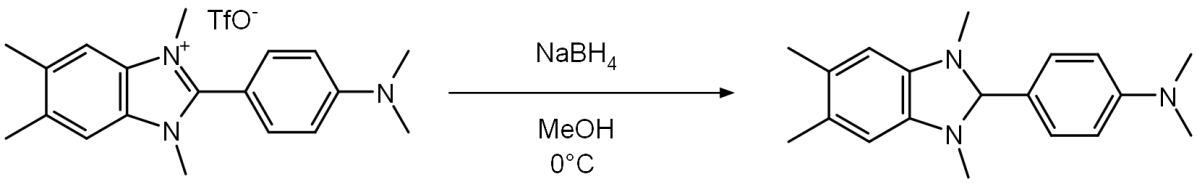

0.550g (1.241mmol) of 2-[4-(dimethylamino)phenyl]-1,3,5,6-tetramethyl-1H-1,3-benzodiazol-3-ium triflate (Synthesis L) were dissolved in 30mL of methanol. The solution was cooled to 0°C. 0.141g (3.724mmol) of $NaBH_4$ were added slowly under stirring. The mixture was left for 2h at room temperature, under stirring in the dark. 100mL of H_2O were added and the mixture was extracted 3 times with 100mL of n-hexane. The organic fractions were collected, dried over Na_2SO_4 and the solvent was evaporated under reduced pressure. At the end of the process 0.158g (0.535mmol) of pure pale-yellow product were obtained. The calculated reaction yield is 43%

^{1}H NMR (400MHz, DMSO) δ: 7.32 (d, J = 8.68 Hz, 2H, ●); 6.75 (d, J = 8.68 Hz, 2H, ●); 6.25 (s, 2H, ●); 4.52 (s, 1H, ●); 2.93 (s, 6H, ●); 2.40 (s, 6H, ●); 2.10 (s, 6H, ●).

^{1}H NMR (400MHz, acetonitrile-d3) δ: 7.35 (d, J = 8.80 Hz, 2H, ●); 6.78 (d, J = 8.80 Hz, 2H, ●); 6.25 (s, 2H, ●); 4.51 (s, 1H, ●); 2.95 (s, 6H, ●); 2.43 (s, 6H, ●); 2.13 (s, 6H, partially covered by H_2O signal, ●).

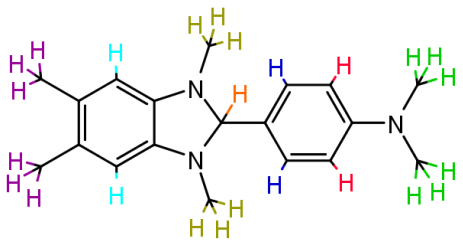

Synthesis N **3-methoxy-N1,N2-dimethylbenzene-1,2-diamine**

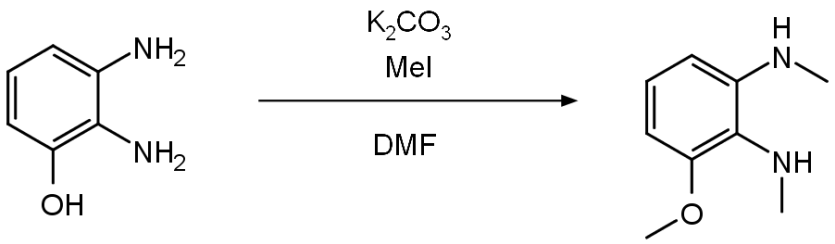

Synthesis adapted from [228]. 3.000g (24.166mmol) of 2,3-diaminophenol and 10.019g (72.499mmol) of K_2CO_3 were dissolved in 60mL of anhydrous dimethylformamide. The mixture was left under stirring at room temperature for 1h. Then 4.513mL (10.290g, 72.499mmol) of iodomethane were added, under stirring. The mixture was then heated at 30°C for 2h. 360mL of H_2O were added and the product was extracted multiple times with diethylether. The organic fractions were collected and dried over Na_2SO_4. The solvent was evaporated under reduced pressure and the crude product was purified with silica chromatography using a solution of petroleum ether : ethyl acetate (3:1) as eluent. The desired product was the first fraction recovered. At the end of the process, 0.944g (5.686mmol) of white crystals (thin needles around 3-5mm long) were obtained. The calculated reaction yield is 24%.

^{1}H NMR (400MHz, $CDCl_3$) δ: 6.97 (dd, J1 = J2 = 8.1 Hz, 1H, ●); 6.31 (d, J = 8.1 Hz, 1H, ●); 6.17 (d, J = 8.1 Hz, 1H, ●); 2.87 (s, 3H, ●); 2.83 (s, 6H, ●).

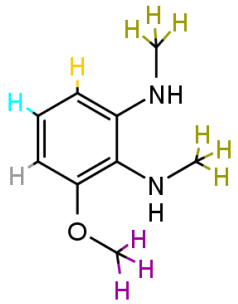

Synthesis O **OH-TMBI: 1,2,3-trimethyl-2,3-dihydro-1H-1,3-benzodiazol-4-ol**

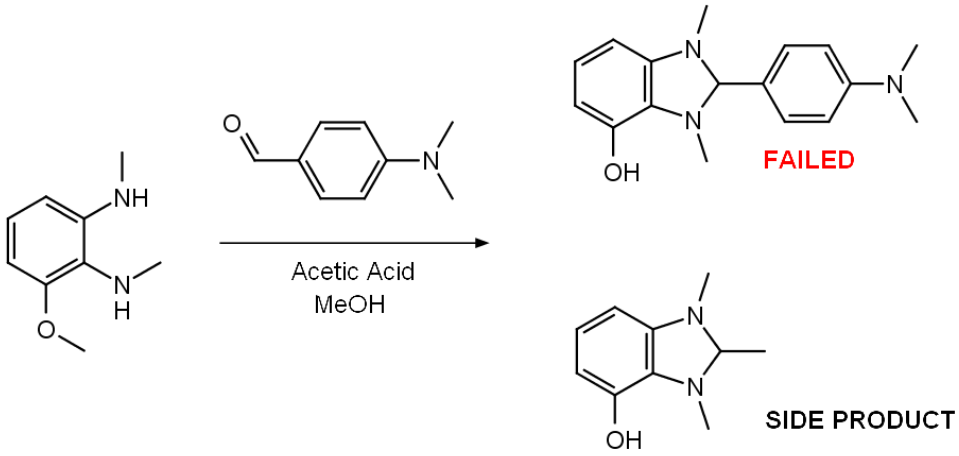

4-(dimethylamino)benzaldehyde (0.149g, 1.000mmol) was dissolved in methanol (1mL). 0.166g (1.000mmol) of 3-methoxy-N1,N2-dimethylbenzene-1,2-diamine (Synthesis N) and 2 drops of glacial acetic acid were added. The resulting mixture was sonicated overnight. The solution was then cooled to -12°C for 24h. The precipitate was filtered and washed with cold methanol. The product was then dried under reduced pressure to afford 0.004g (0.022 mmol) of pure product as white crystals. The calculated reaction yield is 2%.

It is interesting to notice that although the desired product was 2-[4-(dimethylamino)phenyl]-1,3-dimethyl-2,3-dihydro-1H-1,3-benzodiazol-4-ol, as expected from literature [210], TLC analysis does not show any evidence of such compound, on the contrary, it indicates that the major amount of the two reagents did not react. Only few crystals (needles around 2mm in length) of 1,2,3-trimethyl-2,3-dihydro-1H-1,3-benzodiazol-4-ol have been recovered. This product is probably obtained from the side reaction of 3-methoxy-N1,N2-dimethylbenzene-1,2-diamine and acetic acid, with the removal of the methyl group caused by acid hydrolysis.

^{1}H NMR (400MHz, DMSO) δ: 8.81 (s, 1H, ●); 6.73 (dd, J1 = J2 = 8.07 Hz, 1H, ●); 6.04 (d, J = 8.07 Hz, 1H, ●); 5.94 (d, J = 8.07 Hz, 1H, ●); 5.28 (q, J = 5.3 Hz, 1H, ●); 2.68 (d, J = 5.3 Hz, 3H, ●); 2.64 (s, 6H, ●).

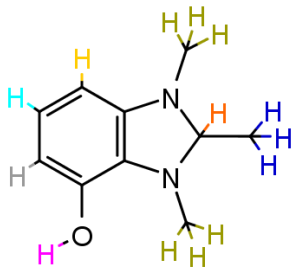

10.2 MATERIALS

P(NDI2OD-T2) (Polyera ActivInk N2200) was purchased from Ossila Lim (M_n = 150 kDa), and the same batch was used for every sample. Dopants were synthetized as described in the previous paragraph and stored under Ar atmosphere at 4 °C. Before sample preparation, dopants were dissolved in dichloromethane or other low-boiling point solvents (20 mM concentration), aliquots of the resulting solutions were distributed in separate vials and the solvent was finally evaporated under reduced pressure overnight. All the dopant concentrations expressed in this work refer to the molar ratio (MR) between the dopant and the number of repeating units of P(NDI2OD-T2).

10.3 ELECTRICAL CHARACTERIZATION

Electrical conductivity measures have been performed using low-alkali 1737F Corning glass as substrate. Initially, the substrates were cleaned through three ultrasonic baths in water, isopropanol and acetone of a 10 minutes duration each. Then the glasses were exposed for 10 minutes to an O_2 plasma at 100 W. Finally, contacts were thermally evaporated using a shadow mask, obtaining two parallel contact lines (6mm distant from each other) made of 1.5 nm thick Cr adhesion layer and 25 nm thick Au layer (2 mm wide, 15 mm long). The film preparation was performed inside a glovebox in N_2 atmosphere. P(NDI2OD-T2) was dissolved in 1,2-diclorobenzene (concentration 10mg/mL), and the polymer solution was stirred at 80 °C for 1 hour. The mixture was loaded into a syringe and filtered using a 0.45 µm pore-size polytetrafluoroethylene (PTFE) filter. Aliquots of 50 µL of the filtered solution were added to vials containing the desired amount of dopant. Meanwhile, the previously described glass substrates were cleaned with two ultrasonic baths in isopropanol and acetone (5 minutes each), then treated with an oxygen plasma for 10 minutes and finally introduced inside the glovebox. P(NDI2OD-T2) films were spin coated at 1000 rpm for 60 s and then at 3000 rpm for 10 s. The thickness of the films was measured after the electrical characterization using a profilometer, every film was within 40±5nm. If required, the resulting films were annealed inside the glovebox on a hot plate. All the electrical characterizations were performed at room temperature in N_2 atmosphere using a Wentworth Laboratories probe station with a semiconductor device analyser (Agilent B1500A). Electrical conductivity was calculated through the linear fit of the I−V curves as follows.

Equation 60

$$\sigma = \frac{x}{R\,z\,y}$$

Where x is the distance between the gold contact lines, z is the thickness of the film, y is the length of the film, and R is the film resistance.

10.4 IR CHARACTERIZATION

The samples were prepared from a chloroform solution of P(NDI2OD-T2) (10 gL^{-1}) heated at 60°C, under stirring, for 1h in air and filtered on a 0.45µm PTFE filter. Then, 200µL of the polymer solution were injected in four different vials. Finally, aliquots of a 20.2mM DiPrBI solution in chloroform were added to three vials, achieving s dopant molar ratios of 0%, 14%, 43% and 100%, respectively. The solutions were sonicated for 5 min and then the solutions were drop casted on KRS5 (thallium bromoiodide) substrates, in air. Using a Nicolet Nexus spectrometer (256 scans, 2cm^{-1} resolution), FT-IR spectra of the drop-casted films were acquired before and after annealing the samples at 150°C for 6h in Ar. IR spectra were analysed with OMNIC software.

10.5 GIWAXS CHARACTERIZATION

The entire process of film preparation was carried inside a N_2 glovebox (<1 ppm of O_2). A solution (10 mg/mL) of P(NDI2OD-T2) in 1,2-diclorobenzene is heated at 80°C for 2 hours under stirring. The solution was filtered with a 0.45µm pore-size polytetrafluoroethylene filter and added to a vial containing the desired amount of dopant. Native oxide p+ Si substrate were cleaned with acetone, isopropanol, and ethanol. Films were spin-coated at 1000rpm for 60s and then at 3000rpm for 10s. GIWAXS measurements were performed at the Stanford Synchrotron Radiation Lightsource (SSRL) on beamline 11-3 equipped with an area detector (Rayonix MAR-225), with an incident energy of 12.73 keV. To minimize air scattering and damages to the sample, all the measurements were performed in a chamber under a helium flux. The sample-detector distance (321 mm) was calibrated through a LaB6 polycrystalline standard and the incident angle was selected at 0.1°. Data analysis was performed with the Igor Pro software packages Nika 1D SAXS29 and WAXStools.

10.6 CYCLIC VOLTAMMETRY CHARACTERIZATION

For the test a 15mL electrochemical cell was used with a working glassy carbon electrode, a platinum counter electrode and a reference electrode composed of an aqueous saturated calomel electrode (Figure 122). All the electrodes were cleaned as described in [229]. Each dopant was dissolved in DCM (0.50 mM) and the

solutions were sonicated for 5 min while N_2 was bubbled through a needle. TBAP (tetrabutylammonium perchlorate, 0.1000M in DCM) was used as supporting electrolyte. Ferrocene 0.50 mM was used as an internal standard. The electrodes were connected to a PGSTAT302N potentiostat set with a scan range between 0.0V and 0.6V scanned with a 0.05 V/s scan rate. All the HOMO levels were calculated with Fc+/Fc couple as potential reference as follows:

$$E_{HOMO/LUMO} = [-(E_{onset} - E_{onset\ (Fc/Fc+)})] - 4.8\ eV$$

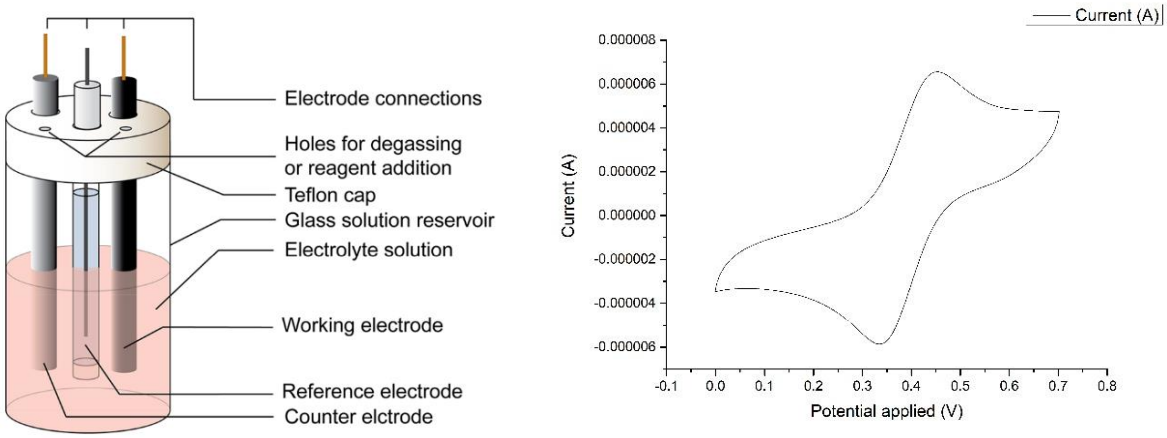

Figure 122. On the left: experimental setup. Image adapted from **[229]**. On the right: ferrocene reference measured in the same conditions of the dopants.

12. APPENDIX 1: OTHER DOPANTS

Although most of the dopants studied in this work were functionalized with a substituent on the benzimidazole ring, namely where the dopant HOMO lies, we have also simulated few DMBI derived dopants by replacing the dimethyl aniline moiety with other aromatic groups. The list of these dopants and their characteristics are listed in

Table **8**. Although the one-pot synthesis of these compounds was attempted as described in Figure 115, given their relatively low calculated HOMO level, they were not further investigated.

Name		HOMO (eV)	Figure
2-(3,4-dimethoxyphenyl)-1,3-dimethyl-2,3-dihydro-1H-1,3-benzodiazole	DMBI-$(OMe)_2$	-4.6	Figure 123
1,3-dimethyl-2-(pyridin-4-yl)-2,3-dihydro-1H-1,3-benzodiazole	DMBI-Pyr	-4.8	Figure 124
1,3-dimethyl-2-(1,3-thiazol-2-yl)-2,3-dihydro-1H-1,3-benzodiazole	DMBI-TA	-4.7	Figure 125

Table 8. Additional benzimidazole-derived dopants discussed in this work and their HOMO level. DFT calculations have been performed with Orca (B3LYP 6-31G**).

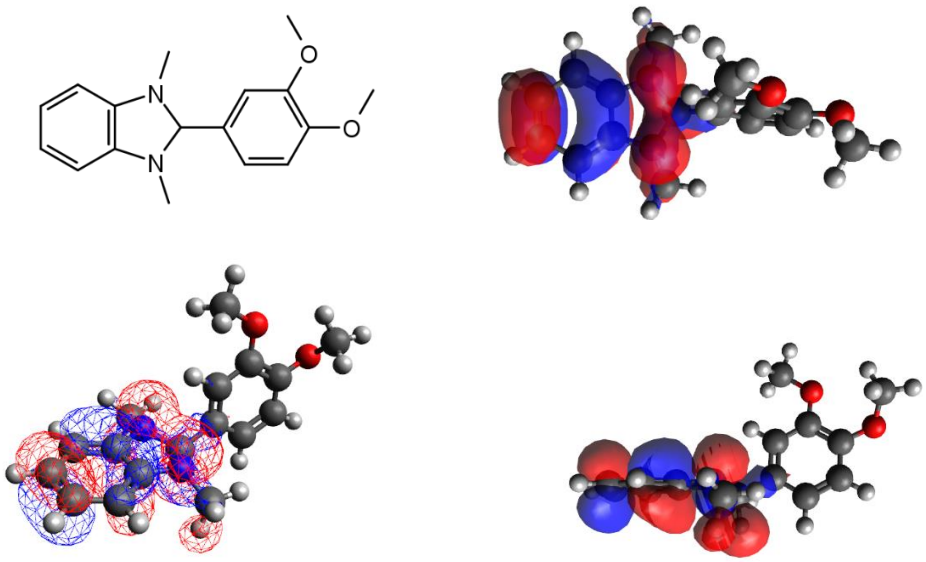

Figure 123: chemical structure of 1,3-dimethyl-2-(pyridin-4-yl)-2,3-dihydro-1H-1,3-benzodiazole DMBI-$(MeO)_2$) and spatial representation of its HOMO (-4.6eV). DFT calculations have been performed with Orca (B3LYP 6-31G**).

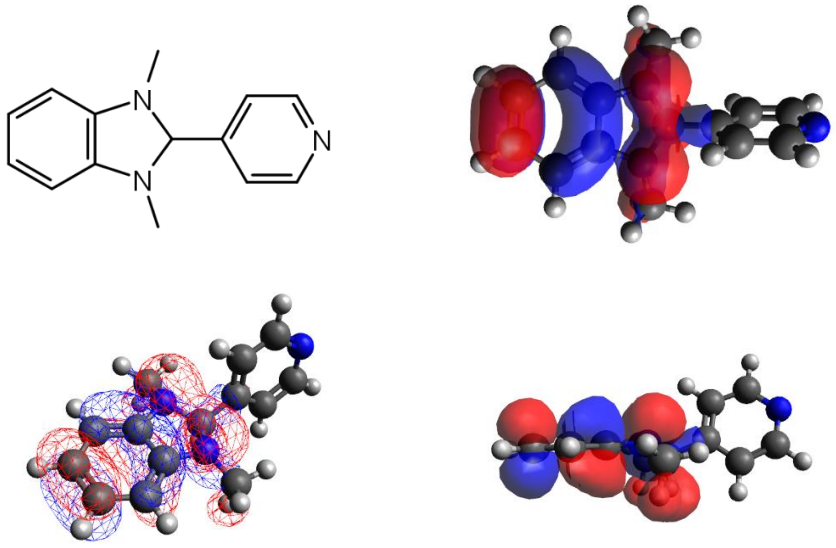

Figure 124: chemical structure of 1,3-dimethyl-2-(pyridin-4-yl)-2,3-dihydro-1H-1,3-benzodiazole (DMBI-Pyr) and spatial representation of its HOMO (-4.8eV). DFT calculations have been performed with Orca (B3LYP 6-31G**).

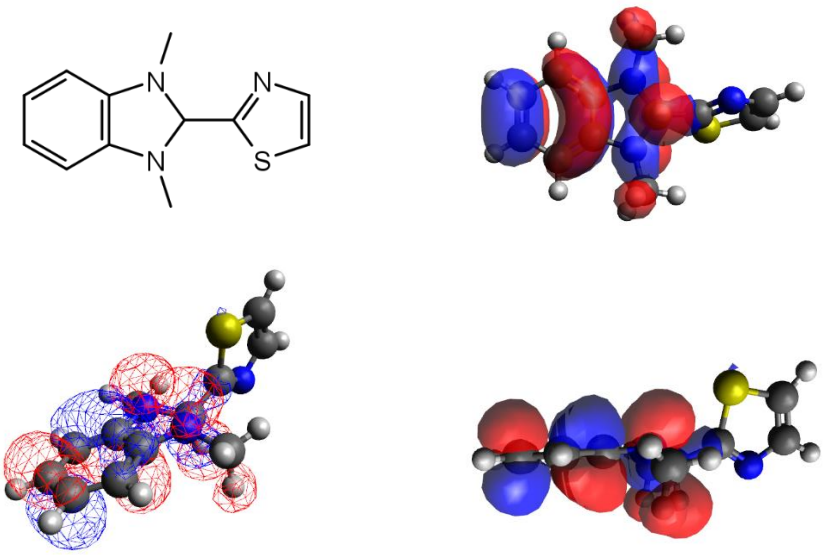

Figure 125: chemical structure of 1,3-dimethyl-2-(1,3-thiazol-2-yl)-2,3-dihydro-1H-1,3-benzodiazole (DMBI-TA) and spatial representation of its HOMO (-4.7eV). DFT calculations have been performed with Orca (B3LYP 6-31G**).

Synthesis P **DMBI-(OMe)$_2$: 2-(3,4-dimethoxyphenyl)-1,3-dimethyl-2,3-dihydro-1H-1,3-benzodiazole**

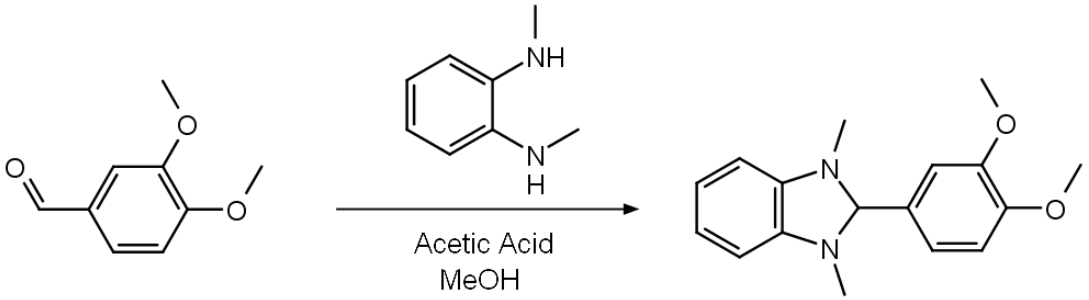

N1,N2-dimethylbenzene-1,2-diamine (0.100g, 0.735mmol) was dissolved in methanol (1.5mL). 0.121g (0.735mmol) of 3,4-dimethoxybenzaldehyde and 2 drops of glacial acetic acid are added. The resulting mixture was sonicated overnight. The solution was then cooled to -12°C for 24h. The precipitate was filtered and washed with cold methanol. The product was then dried under reduced pressure and further purified with a short column chromatography using a solution of n-hexane : diethyl ether (1:1) as eluent. At the end of the process, 0.050g (0.176 mmol) of pink needle-like crystals were obtained. The calculated reaction yield is 24%.

^{1}H NMR (400MHz, $CDCl_3$) δ: 7.24 (s, 1H, ●); 7.02 (d, J = 8.07 Hz, 1H, ●); 6.88 (d, J = 8.07 Hz, 1H, ●); 6.75 – 6.71 (m, 2H, ●); 6.47 – 6. 43 (m, 2H, ●); 4.82 (s, 1H, ●); 3.92 (s, 3H, ●); 3.90 (s, 3H, ●); 2.57 (s, 6H, ●).

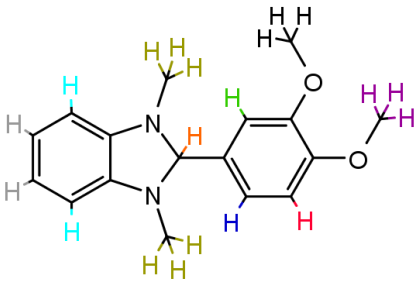

For comparison the ^{1}H NMR (89.56MHz, $CDCl_3$) spectrum of 3,4-dimethoxybenzaldehyde is also reported. [227] δ: 9.85 (s, 1H, ●); 7.47 (d, 1H, ●); 7.41 (s, 1H, ●); 6.99 (d, 1H, ●); 3.97 (s, 3H, ●); 3.94 (s, 3H, ●)

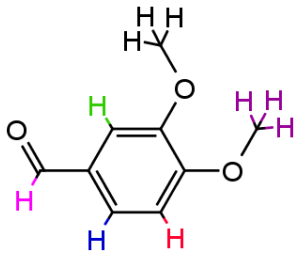

Synthesis Q **DMBI-Pyr: 1,3-dimethyl-2-(pyridin-4-yl)-2,3-dihydro-1H-1,3-benzodiazole**

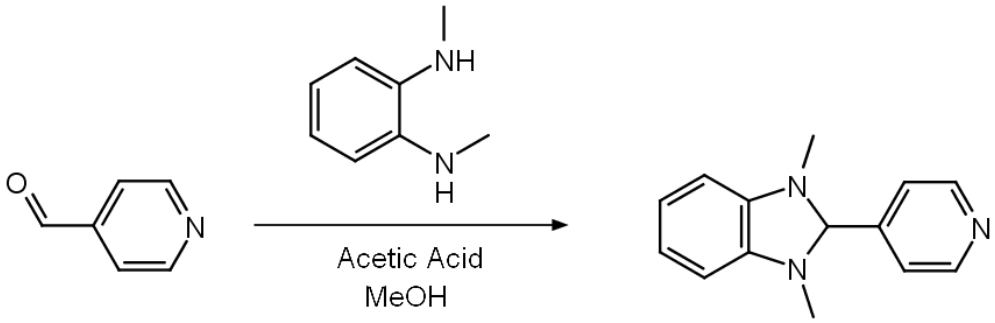

N1,N2-dimethylbenzene-1,2-diamine (0.100g, 0.735mmol) was dissolved in methanol (1.5mL). 0.079g (0.735mmol, 69.3 µL) of pyridine-4-carbaldehyde and 2 drops of glacial acetic acid were added. The resulting mixture was sonicated overnight. The solution was then cooled to -12°C for 24h. The precipitate was filtered and washed with cold methanol. The product was then dried under reduced pressure to afford 0.042g (0.139 mmol) of pure product as a beige powder. The calculated reaction yield is 19%.

^{1}H NMR (400MHz, $CDCl_3$) δ: 8.70 (d, J = 6.00 Hz, 2H, ●); 7.56 (d, J = 6.00 Hz, 2H, ●); 6.77 – 6.73 (m, 2H, ●); 6.49 – 6.44 (m, 2H, ●); 4.91 (s, 1H, ●); 2.59 (s, 6H, ●).

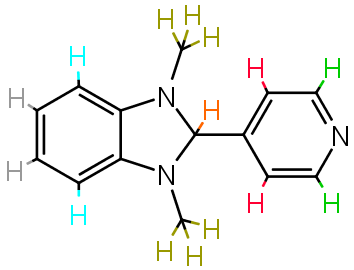

For comparison, the ^{1}H NMR (89.56MHz, $CDCl_3$) spectrum of pyridine-4-carbaldehyde is also reported. [227] δ: 10.11 (s, 1H, ●); 8.90 (d, 2H, ●); 7.72 (d, 2H, ●).

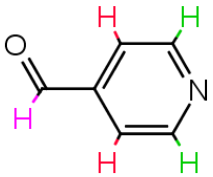

Synthesis R **DMBI-TA: 1,3-dimethyl-2-(1,3-thiazol-2-yl)-2,3-dihydro-1H-1,3-benzodiazole**

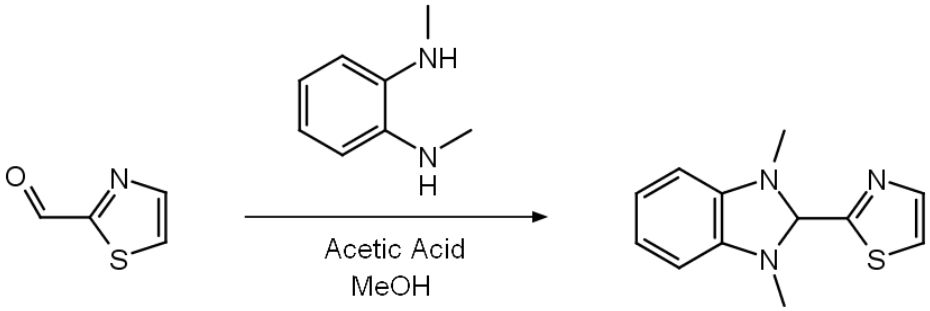

N1,N2-dimethylbenzene-1,2-diamine (0.100g, 0.735mmol) was dissolved in methanol (1.5mL). 0.083g (0.735mmol) of 1,3-thiazole-2-carbaldehyde and 2 drops of glacial acetic acid were added. The resulting mixture was sonicated overnight. The solution was then cooled to -12°C for 24h. The precipitate was filtered and washed with cold methanol. The product was then dried under reduced pressure to afford 0.044g (0.190 mmol) of pure product as a light brown powder. The calculated reaction yield is 26%.

^{1}H NMR (400MHz, $CDCl_3$) δ: 7.81 (d, J = 3.18 Hz, 1H, ●); 7.48 (d, J = 3.18, 1H, ●); 6.78 – 6.74 (m, 2H, ●); 6.50 – 6.46 (m, 2H, ●); 5.35 (s, 1H, ●); 2.75 (s, 6H, ●).

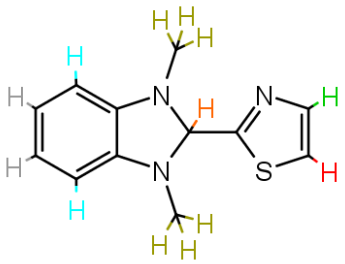

For comparison, the ^{1}H NMR (300MHz) spectrum of thiazole is also reported. [227] δ: 8.68 (s, 1H, ●); 7.83 (d, J = 3.2 Hz, 1H, ●); 7.19 (d, J = 3.2, 1H, ●)

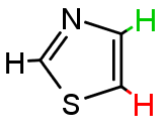

13. APPENDIX 2: AZOBENZENES

The second part of this work refers to a side project, which was carried mostly during the first PhD year. This project aims at developing chromophore compounds to solve retinal degeneration diseases.

A chromophore is a molecule able to change its conformation upon photo isomerization. In all mammalians, the chromophore function is often carried by 11-cis-retinaldehyde which is a molecule covalently bound to photoreceptor proteins. The absorption of a photon isomerizes the chromophore, changing its structure from cis-retinaldehyde to trans-retinaldehyde (Figure 126). This induces a change in the conformation of the photoreceptor and triggers a process that generates the visual signal. [230].

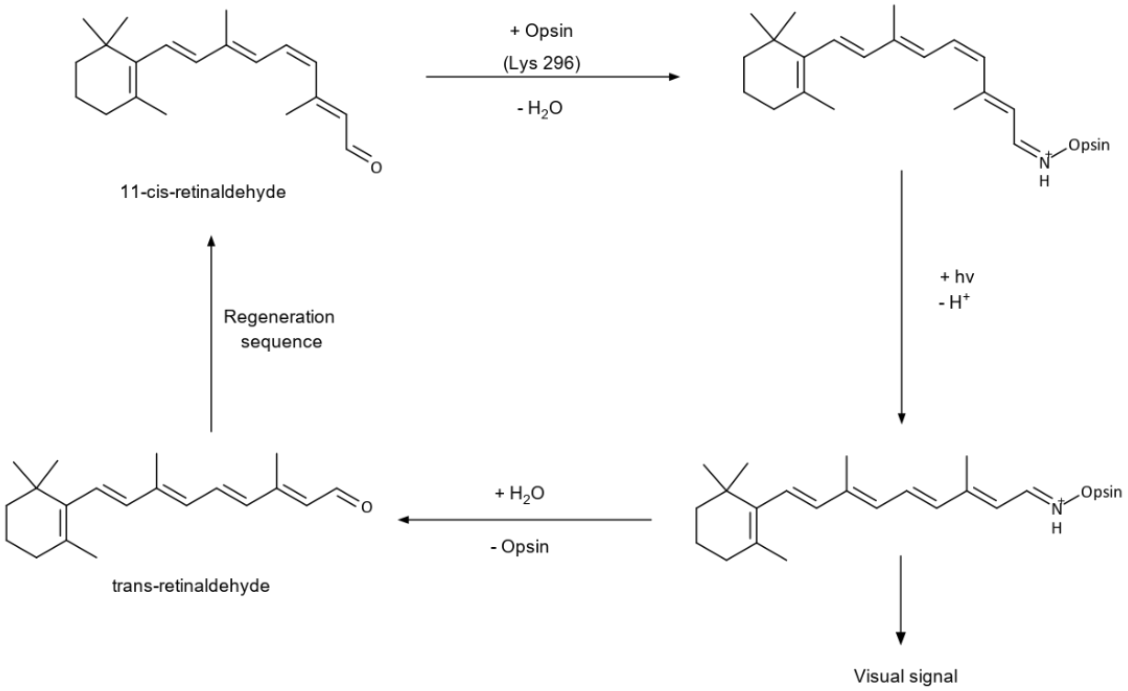

Figure 126: visual retinoid cycle.

To be suitable for biological applications, artificial photochromic materials must have water solubility, low toxicity, and stability to the biological environment, finally, synthetic tractability is a key factor to tune the molecular properties such as light absorption spectra and solubility [231]. Since azobenzenes (AB) possess all these desired characteristics, they are the most frequently employed photo switches for biological applications. To be applied in vision restoration processes, a photo-switch should be triggered by visible light (400-700nm). AB usually need UV light to undergo a *trans* → *cis* isomerization, however, by inserting side

groups to the AB core, it is possible to red shift the absorption band of the *trans*-isomer to the visible range [232].

We have synthetized azobenzenes (AB) where the 4- and the 4'- positions of the two phenyl rings are substituted with an azepane group and/or with one or more hydrophobic linear chains carrying a polar group (such as pyridinium or ammonium bromide) at the extremity. This general structure mimics the cellular membrane phospholipids and provides an amphiphilic character to ABs making them able to dwell inside cell membrane (Figure 127). In the following pages are reported two articles published on the topic.

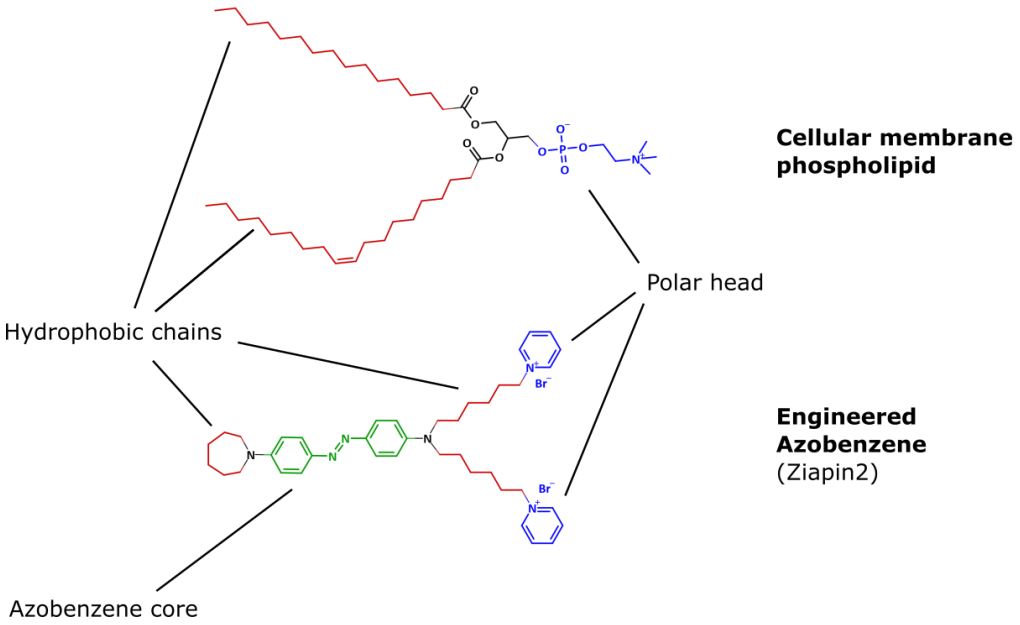

Figure 127 : the structure of the ziapin compounds has been engineered to mimic phospholipid amphiphilic behaviour.

ARTICLES
https://doi.org/10.1038/s41565-019-0632-6
nature nanotechnology

Neuronal firing modulation by a membrane-targeted photoswitch

Mattia Lorenzo DiFrancesco[1,2,13], Francesco Lodola[3,13], Elisabetta Colombo[1,2,13], Luca Maragliano[1,2], Mattia Bramini[1,2,10], Giuseppe Maria Paternò[3], Pietro Baldelli[2,4], Mauro Dalla Serra[5,6], Lorenzo Lunelli[5,6], Marta Marchioretto[5,6], Giorgio Grasselli[1,2], Simone Cimò[3,7], Letizia Colella[7], Daniele Fazzi[8], Fausto Ortica[9], Vito Vurro[3], Cyril Giles Eleftheriou[1,2,11], Dmytro Shmal[1,2], José Fernando Maya-Vetencourt[1,2,12], Chiara Bertarelli[3,7,13], Guglielmo Lanzani[3,13]* and Fabio Benfenati[1,2,13]*

Optical technologies allowing modulation of neuronal activity at high spatio-temporal resolution are becoming paramount in neuroscience. In this respect, azobenzene-based photoswitches are promising nanoscale tools for neuronal photostimulation. Here we engineered a light-sensitive azobenzene compound (Ziapin2) that stably partitions into the plasma membrane and causes its thinning through *trans*-dimerization in the dark, resulting in an increased membrane capacitance at steady state. We demonstrated that in neurons loaded with the compound, millisecond pulses of visible light induce a transient hyperpolarization followed by a delayed depolarization that triggers action potential firing. These effects are persistent and can be evoked in vivo up to 7 days, proving the potential of Ziapin2 for the modulation of membrane capacitance in the millisecond timescale, without directly affecting ion channels or local temperature.

Optical technologies for the modulation of neuronal activity are becoming increasingly important in cell biology and neuroscience[1,2]. Indeed, the possibility to obtain neuronal excitation or inhibition on demand not only has allowed an unprecedented power in interrogating and dissecting out the function of specific brain circuits, but also has opened new perspectives for treating neurological and psychiatric diseases[3].

Optogenetics is the pioneering technique in neuro-optical technologies[3,4]. Similar to optogenetics, the generation of tethered azobenzene photoswitches targeted to membrane bilayers[5–10] or linked to ion channels[11–16] allowed modulating ion channel dynamics and/or the electrical properties of the membrane in a light-dependent fashion.

Extracellular photostimulation by light-sensitive interfaces represents an alternative strategy. Extended planar organic interfaces were used to achieve light-dependent modulation of the electrical state of neurons[17–21] that, at high light intensities, also involved a thermal effect[19,22,23]. Similar results were obtained by increasing the local temperature with infrared illumination of absorbers in contact with cells[24,25], thus increasing the membrane capacitance and in turn depolarizing the target cell. However, temperature rises of several degrees can be harmful to neurons, particularly if administered repeatedly.

In this work, we engineered an amphiphilic azobenzene-based photoswitch to obtain an intramembrane actuator for inducing heatless membrane stress/perturbation upon irradiation with visible light. Our photochromic actuator, named Ziapin2, contains two ionic-terminated alkyl chains that align with the phospholipid headgroups and the azobenzene moiety end-capped with a hydrophobic azepane that can be folded/unfolded in a light-dependent manner. Incubation of the compounds with primary neurons showed that the molecules spontaneously partition into the membrane, where they preferentially distribute to membrane rafts and induce membrane thinning and increased capacitance through *trans*-dimerization. *Trans*→*cis* isomerization triggered by millisecond pulses of visible light displaces the hydrophobic end group from the membrane core and causes a sharp and transient decrease in capacitance due to membrane relaxation that generates a transient hyperpolarization. In neurons, the fast return of capacitance to the steady-state level is followed by action potential (AP) firing. Persistent light-evoked stimulation of Ziapin2-labelled mouse somatosensory cortex activity is also observed in vivo.

Synthesis and characterization of Ziapin2

Amphiphilic azobenzenes have been previously reported for different applications[5]. Herein, we were inspired by the initial work of Fujiwara and Yonezawa, who showed that an aliphatic amphiphilic azobenzene derivative was able to change the capacitance of black lipid membranes in response to prolonged ultraviolet (UV)

[1]Center for Synaptic Neuroscience, Istituto Italiano di Tecnologia, Genoa, Italy. [2]IRCCS Ospedale Policlinico San Martino, Genoa, Italy. [3]Center for Nano Science and Technology, Istituto Italiano di Tecnologia, Milan, Italy. [4]Department of Experimental Medicine, University of Genova, Genoa, Italy. [5]Istituto di Biofisica, Consiglio Nazionale delle Ricerche, Trento, Italy. [6]Laboratory of Biomarker Studies and Structure Analysis for Health, Fondazione Bruno Kessler, Trento, Italy. [7]Dipartimento di Chimica, Materiali e Ingegneria Chimica 'Giulio Natta', Politecnico di Milano, Milan, Italy. [8]Department of Chemistry, Institut für Physikalische Chemie, University of Cologne, Cologne, Germany. [9]Department of Chemistry, Biology and Biotechnology, Università degli Studi di Perugia, Perugia, Italy. [10]Present address: Mattia Bramini, Department of Applied Physics, Faculty of Sciences, University of Granada, Granada, Spain. [11]Present address: Cyril Giles Eleftheriou, Departments of Ophtalmology and Neurology, Burke Medical Research Institute, Weil Medical College of Cornell University, White Plains, NY, USA. [12]Present address: José Fernando Maya-Vetencourt, Department of Biology, University of Pisa, Pisa, Italy. [13]These authors contributed equally: Mattia Lorenzo DiFrancesco, Francesco Lodola, Elisabetta Colombo, Chiara Bertarelli, Guglielmo Lanzani, Fabio Benfenati. *e-mail: guglielmo.lanzani@iit.it; fabio.benfenati@iit.it

illumination[6–8], and by the subsequent work of Bazan and collaborators, who reported that non-photochromic water-soluble distyrylstilbene oligoelectrolytes (DSSN+), capped at each end with nitrogen-bound terminally charged pendant groups, effectively localized to the membrane, modifying its optical and electronic properties[9,10]. Here, we combined a hydrophobic backbone containing the photoactive 4-4′ diaminoazobenzene substituted on one side with an azepane and on the opposite side with alkyl chains that are ω-substituted with cationic groups, that is, pyridinium salts. The combination of the alkyl-substituted azobenzenes with a capping cation leads to amphiphilic species able to dwell inside the cell membrane (Ziapin2; Supplementary Fig. 1 and Methods).

Azobenzene molecules undergo *trans*→*cis* isomerization upon illumination with visible radiation (Fig. 1a), with the reverse *cis*→*trans* isomerization driven by either light or thermal excitation[26–28]. Ziapin2 shows the typical UV–visible (Vis) absorption features of para amino-substituted azobenzenes, with a strong absorption peak centred at 470 nm (Fig. 1b), attributed to the $\pi \rightarrow \pi^*$ transitions of the *trans* isomer[28]. Irradiation with blue light leads to *trans*→*cis* isomerization as seen from the concomitant bleaching of the *trans* isomer absorption and increase of the *cis* conformer absorption. A well-defined and relatively fast collective photoswitching dynamics of Ziapin2 in dimethyl sulphoxide (DMSO) was detected by measuring the decrease of absorbance at 470 nm versus irradiation time (Fig. 1c). The steep time-dependent decrease in Ziapin2 photoluminescence (PL) at 540 nm in DMSO upon blue light exposure (Fig. 1d,e) can also be related to the photoisomerization-induced reduction in the *trans* population due to the negligible PL quantum yield of the *cis* isomer. Indeed, the excitation profile of the normalized change in PL (Supplementary Fig. 2a,b) follows the absorption profile of the *trans* isomer, confirming its relation to the isomerization process. We estimated a *trans*→*cis* photoisomerization coefficient $k\tau = 16.9\ \mathrm{cm^2\,J^{-1}}$ and a *cis*→*trans* thermal rate $y = 0.06\ \mathrm{s^{-1}}$ (red line in Fig. 1e; see Methods). A complete suppression of the Ziapin2 photoswitching was observed in water as compared with DMSO (Fig. 1f), likely caused by strong aggregation of Ziapin2[29]. The formation of aggregates was also corroborated by the redshift of Ziapin2 PL (82 nm, Supplementary Fig. 2c,d) and absorption (22 nm, Supplementary Fig. 2e) in water. To disentangle a possible fast relaxation behaviour from a complete isomerization suppression of Ziapin2 in water, we carried out time-resolved PL measurements in the picosecond (ps) time regime (Supplementary Fig. 2f). These data indicate a strong difference in the deactivation path for Ziapin2 in the two solvents, with a relatively fast emission lifetime in DMSO (8 ps), consistent with the photoisomerization reaction, and a marked slowdown of the lifetime in water (26 ps) due to the formation of molecular aggregates. Interestingly, in sodium dodecyl sulphate (SDS) we observed a 25% decrease of the lifetime when compared with water, an effect that can be attributed to the partially recovered isomerization ability of membrane-embedded Ziapin2. Aggregation was also investigated by UV–Vis and PL spectra as a function of concentration (Supplementary Fig. 3a–c) and on water addition (Supplementary Fig. 3d–f). While normalized absorption spectra of Ziapin2 show little dependence on concentration, PL exhibits a linear redshift, suggesting the occurrence of an excited state interaction. Absorption/PL spectra for Ziapin2 at fixed concentration (25 μM) and different DMSO/water ratios show a growing a redshift upon water addition alongside an increase of PL intensity (Supplementary Fig. 3d–f). The broad, featureless and Stokes-shifted emission suggests the formation of aggregates with an excimeric-like deactivation, similarly to that observed for confined azobenzene derivatives in nanostructured silica[30].

Interestingly, the PL spectra of Ziapin2 in SDS micelles, mimicking the bilayer environment[31], and in cell membranes essentially coincide, lying between DMSO and water spectra (Supplementary Fig. 2c). Total internal reflection fluorescence microscopy on model bilayers composed of either phosphatidylcholine (PC) or a mixture of PC, cholesterol and sphingomyelin (SM), mimicking the composition of lipid rafts, confirmed the spectral overlap among Ziapin2 PL in SDS micelles, model membranes and raft-like membranes (Supplementary Fig. 4). Similarly, the photoswitching dynamics in either SDS micelles (Supplementary Fig. 2d) or cell membranes (Fig. 1f) were intermediate between the fast photoswitching behaviour in DMSO and the frozen photodynamics observed in aqueous media. The non-exponential PL decay in the cell membrane (Fig. 1g) reflects the relaxation time distribution in disordered environments, such as lipid rafts or local phase/thickness changes. Although the molecular event of photoisomerization occurs in the sub-ps time scale, the sizable change observed in the time evolution of the isomeric populations in the ensemble is associated with a macroscopic fraction of isomerized molecules. All these findings suggest that the partition of the molecule in lipid membranes avoids the aggregation of Ziapin2, enabling effective isomerization and light-controlled photoswitching.

Ziapin2 increases membrane capacitance

We performed molecular dynamics (MD) simulations placing one molecule of Ziapin2 in *trans* conformation in the water region, parallel to a PC membrane and in different orientations. In three simulations, the molecule entered the bilayer within 100 ns and remained in the membrane for the rest of the trajectory (Fig. 2a,b). In all cases, Ziapin2 entered the membrane by first piercing it with the azobenzene side and then moving towards the centre of the bilayer by keeping the elongated axis almost parallel to the bilayer normal (Fig. 2a; I–IV). The insertion stopped when the positively charged pyridine rings were at the level of the lipid heads, coordinated by phosphate groups. Interestingly, in a different simulation, one Ziapin2 molecule placed at the centre of the bilayer and parallel to it reached very rapidly (<5 ns) the same equilibrium position. The insertion process was quantitatively studied by calculating the associated free-energy profile (Fig. 2c). We found essentially no barrier for Ziapin2 adsorption in the membrane, a pronounced minimum at the equilibrium position spontaneously obtained before and a barrier for membrane desorption to water of ~12 kcal mol^{-1} (0.52 eV).

Before studying the cellular distribution and effects of Ziapin2 in neurons, we demonstrated that Ziapin2 did not elicit any toxic or inflammatory reaction in neurons (Supplementary Figs. 5 and 6).

Next, primary hippocampal neurons loaded with Ziapin2 were live-stained with the plasma membrane reporter CellMask and subjected to three-dimensional confocal imaging (Fig. 2d). The quantification revealed that more than 70% of Ziapin2 was localized to the neuronal surface, with a coverage of ~15% of the total membrane surface (Fig. 2d–f) that progressively decreased over time ($t_{1/2} = 36.4$ h, Supplementary Fig. 7a). The occurrence of fluorescence resonance energy transfer between Ziapin2 and CellMask further demonstrates that Ziapin2 is strictly localized to the membrane bilayer (Supplementary Fig. 7b,c).

Given the punctate distribution of Ziapin2 fluorescence on the plasma membrane, we evaluated the colocalization of Ziapin2 with lipid rafts[32] by live labelling with cholera toxin β-subunit and high-resolution fluorescence microscopy with structured light (SIM; Fig. 2e). Interestingly, the percentage of Ziapin2 colocalizing with lipid rafts (~60%) was only slightly smaller than that observed with CellMask and covered a substantially higher proportion (~25%) of the total raft surface with respect to CellMask (Fig. 2e,f). To unambiguously demonstrate the propensity of Ziapin2 for lipid rafts, we treated primary neurons with methyl-β-cyclodextrin (MβCD) to partially deplete membrane cholesterol and decrease the density of lipid rafts (~50% decrease based on Filipin staining; Supplementary Fig. 8a; Fig. 2g). Strikingly, MβCD markedly altered the punctate distribution of Ziapin2 in the membrane by decreasing the density of Ziapin2-positive puncta and increasing the Ziapin2-positive

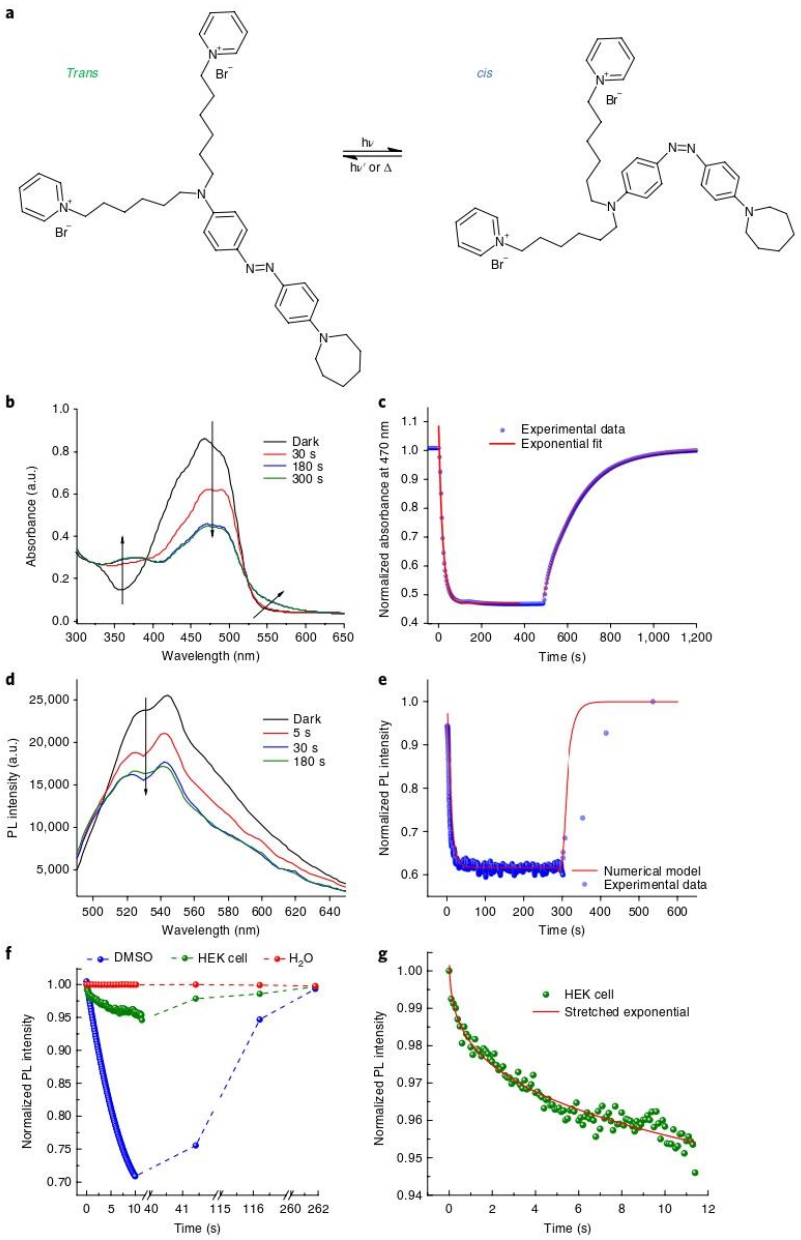

Fig. 1 | *Trans*→*cis* isomerization of Ziapin2 in various environments. a, Schematic of the isomerization process in Ziapin2. **b**,**c**, Changes in the Ziapin2 absorbance spectrum (25 μM in DMSO) as a function of time (**b**) and time course of absorbance at 450 nm upon illumination with a diode laser (**c**). The collective photoswitching dynamics upon light exposure reveals a well-defined and relatively fast photoreaction dynamics of Ziapin2 in DMSO, reaching a photostationary population after about 100 s of illumination and achieving a complete recovery with a t_{V2} of 108 s in the dark at room temperature. While the photoisomerization process occurs typically in the picosecond range, the population dynamics towards the photostationary state takes much longer, depending on the conformer thermodynamic stability and molecular environment. **d**,**e**, Changes in the Ziapin2 PL spectrum (25 μM in DMSO) as a function of time (**d**) and time course of the emission at 540 nm upon excitation at 450 nm with a Xenon lamp (**e**). The red line is the numerical model employed to describe the time evolution of the fluorescence signal. **f**, Photoswitching/relaxation dynamics of Ziapin2 in DMSO, human embryonic kidney 239 (Hek293) cells and water acquired by exciting at 450 nm and collecting the emission at 540, 580 and 620 nm, respectively. **g**, Zoom on the PL dynamics in Hek293 cells, highlighting the stretched exponential decay. Such function considers the distribution of relaxation times occurring in disordered environments. a.u., arbitrary units.

areas, indicative of release of the probe from the rafts and its dispersion within the membrane (Fig. 2g,h).

Spatially resolved membrane thickness maps calculated from simulations of multiple Ziapin2 molecules in *trans* or *cis* conformations revealed the presence of thinner bilayer regions in the *trans* case (Fig. 3a and Supplementary Fig. 9). Indeed, *trans* Ziapin2 molecules anchored to the opposite leaflets of the membrane form dimers via backbone interaction, pulling lipid heads towards the centre of the bilayer and resulting in a local depression of the membrane (Fig. 3a, left panels). Conversely, when Ziapin2 is in *cis* conformation, the hydrophobic tails of opposed molecules are too far from each other to dimerize, leaving the membrane thickness unperturbed (Fig. 3a, right panels). A similar bilayer depression, associated with *trans* Ziapin2 dimerization, was observed in a lipid raft model (Fig. 3b).

We then investigated by atomic force microscopy (AFM) whether insertion of Ziapin2 in artificial membranes affects bilayer thickness. According to MD predictions, incorporation of *trans* Ziapin2 in unilamellar liposomes composed of either PC or a raft-like mixture induced a significant reduction in membrane thickness that was more extended and pronounced in the raft-mimicking environment (Fig. 3c,d and Supplementary Fig. 10).

Given the inverse proportionality between capacitance and thickness, we measured the capacitance of stably preformed planar membranes of PC or raft-like composition after addition of *trans* Ziapin2 to one or both sides of the bilayer. Unilateral addition of Ziapin2 increased the bilayer capacitance in both types of membrane, an effect that became significantly larger when Ziapin2 was added on both sides (Fig. 3e and Supplementary Fig. 11a).

We then checked whether Ziapin2 in the dark had any effect on capacitance in a simple cell model (Hek293; Fig. 3f). The addition of Ziapin2 induced a significant increase in capacitance (32.1 ± 1.7 pF), probably attributable to the bilayer thinning caused by Ziapin2 *trans*-dimerization, while the DMSO vehicle was ineffective (26.4 ± 1.4 pF; see Supplementary Materials and Supplementary Fig. 11b–d).

Light-induced neuronal activity by Ziapin2 in vitro

MD simulations predict that light-induced *trans*→*cis* photoconversion of Ziapin2 would relax the membrane towards its native thickness (Supplementary Fig. 12), thereby reversing the effect on membrane capacitance. When light stimuli were administered to Ziapin2-loaded Hek293 cells, the increased capacitance returned towards basal levels (mean decrease ± s.e.m.: 4.4 ± 0.5 pF) while vehicle-loaded cells did not respond to light (Supplementary Fig. 13a; cf. Fig. 3f). Such effect was associated with membrane hyperpolarization, peaking ~13 ms after light onset and followed by a delayed depolarization (Supplementary Fig. 13b,c), as reproduced by a numerical simulation of the membrane equivalent circuit (Supplementary Fig. 13d). We next tested the physiological effects of Ziapin2 in primary hippocampal neurons (Fig. 4a). In the dark, a significant capacitance increase was observed (from 32.4 ± 1.7 pF to 53.3 ± 6.0 pF; Fig. 4b), without significant changes in other passive membrane properties (Supplementary Figs. 11e–g and 14a). When Ziapin2-loaded neurons were photostimulated, a fast and significant capacitance drop (mean decrease ± s.e.m.: 6.5 ± 1.1 pF) was observed, followed by a slow return to the pre-illumination level (Fig. 4b). The change in capacitance peaked a few ms after light onset and was not significantly different between 20 and 200 ms of light stimulation. Notably, a significant correlation was observed between the *trans* Ziapin2 capacitance increase and the light-induced capacitance drop (Fig. 4b).

Ziapin2-labelled neurons showed a biphasic modulation of the membrane potential characterized by an early hyperpolarization, with a time course overlapping with the capacitance change, followed by a delayed depolarization of similar amplitude (Fig. 4c,d). While the hyperpolarization peak occurred with similar latency with 20 or 200 ms, the peak depolarization was delayed with 200 ms stimuli (Fig. 4e). To distinguish intrinsic effects from the effects of the reverberant network of synaptic connections, we employed blockers of excitatory and inhibitory synaptic transmission. Under these conditions, the magnitude and timing of hyperpolarization were unaffected (Fig. 4c,d; $P = 0.79$ and $P = 0.69$, Mann–Whitney U test), while the amplitude of the depolarization was significantly decreased (Fig. 4c,d; $P < 0.01$ for both 20 and 200 ms stimuli, Mann–Whitney U test), similarly to that observed in Hek293 cells (Supplementary Fig. 13b,c). These data indicate that light-induced hyperpolarization is an intrinsic effect resulting from the drop in capacitance, while the late depolarization response of neurons is amplified by the network synaptic transmission.

We then ran voltage-clamp experiments in Ziapin2-loaded neurons to build I/V plots of the light-induced transient capacitive current. Light stimulation (20 ms) elicited outward and inward currents at negative and positive potentials, respectively, with an inversion at approximately 0 mV, as expected by a pure capacitive current.

Fig. 2 | Ziapin2 distributes to the plasma membrane and lipid rafts in neurons. a, Snapshots extracted from an MD simulation showing Ziapin2 (*trans*) spontaneously entering the membrane (PC lipid model) at consecutive time frames (I–IV); lipid phosphate atoms are shown as orange spheres and acyl chains as grey lines; water molecules are not reported for clarity. **b**, Time dependence of the distance between the centre of mass (COM) of Ziapin2 and the bilayer centre in three independent simulations; the dashed line indicates the interface between water and lipid head groups. **c**, Free-energy profile for Ziapin2 (*trans*) entering the membrane bilayer, calculated versus the distance between the bilayer centre and the centre of mass of the two pyridinic nitrogens of Ziapin2. **d**, Primary neurons pulse exposed to Ziapin2 for 7 min were stained with the specific plasma membrane reporter CellMask (red) to evaluate the membrane incorporation of Ziapin2 (green). Scale bars: 10 and 20 µm for large and small panels, respectively. **e**, Primary neurons pulse exposed to Ziapin2 (green) for 7 min were stained with the specific lipid raft marker Vybrant Alexa Fluor 555 (red) with or without pretreatment with methyl-β-cyclodextrin (MβCD) to deplete cholesterol and imaged by structured illumination microscopy (SIM). Scale bars: 5 and 2 µm for large and small panels, respectively. **f**, Analysis of z-stack confocal images of CellMask/Ziapin2 and Vybrant/Ziapin2 double-stained neurons. Upper panel: Partitioning of Ziapin2 to the plasma membrane and lipid rafts was evaluated as the percentage of total cell Ziapin2 fluorescence colocalizing with the respective marker 7 min after loading and subsequent washout. Means ± standard error of the mean (s.e.m.) with individual experimental points are shown. Lower panel: Percentage of the total plasma membrane (CellMask staining) or lipid raft domains (Vybrant staining) that were positive for Ziapin2 7 min after loading. Means ± s.e.m. with individual experimental points are shown. The Vibrant/CellMask surface ratio, determined in parallel samples double labelled with the two probes, was 71 ± 2%. ***$P < 0.001$, unpaired Student's t test ($n = 26$ and 39 for CellMask and Vybrant staining, respectively, from three independent primary neuronal preparations). **g**, Effects of cholesterol depletion on the membrane distribution of Ziapin2. Representative images of Ziapin2 clusters acquired by SIM imaging in control neurons and neurons pretreated with MβCD. Scale bars: 2 µm. The line-scan fluorescence intensity plots reveal a dot-pattern profile for untreated (Ctrl) samples (black traces) and a more diffuse signal for MβCD-treated cells (red traces). **h**, The density of Ziapin2 clusters and of Vybrant-labelled rafts (puncta µm^{-2}) and their average size were evaluated washout in Ctrl and MβCD-treated neurons after 7 min of Ziapin2 labelling and subsequent live staining with Vybrant to label lipid rafts. Means ± s.e.m. with individual experimental points are shown. **$P < 0.01$; ***$P < 0.001$, Kruskal-Wallis/Dunn's test ($n = 20$ for Ctrl and MβCD, respectively, from three independent neuronal preparations).

Consistently, no changes were observed in the I/V plots when choline replaced extracellular Na^+ or a cocktail of ion channel blockers for passive and active conductances was used (Supplementary Fig. 15a,b and Methods). These treatments also left unaltered the hyperpolarization response to light when the recording was switched to current-clamp (Supplementary Fig. 15c,d).

The hyperpolarization response to light of neurons that had been partially depleted of membrane cholesterol by MβCD (see

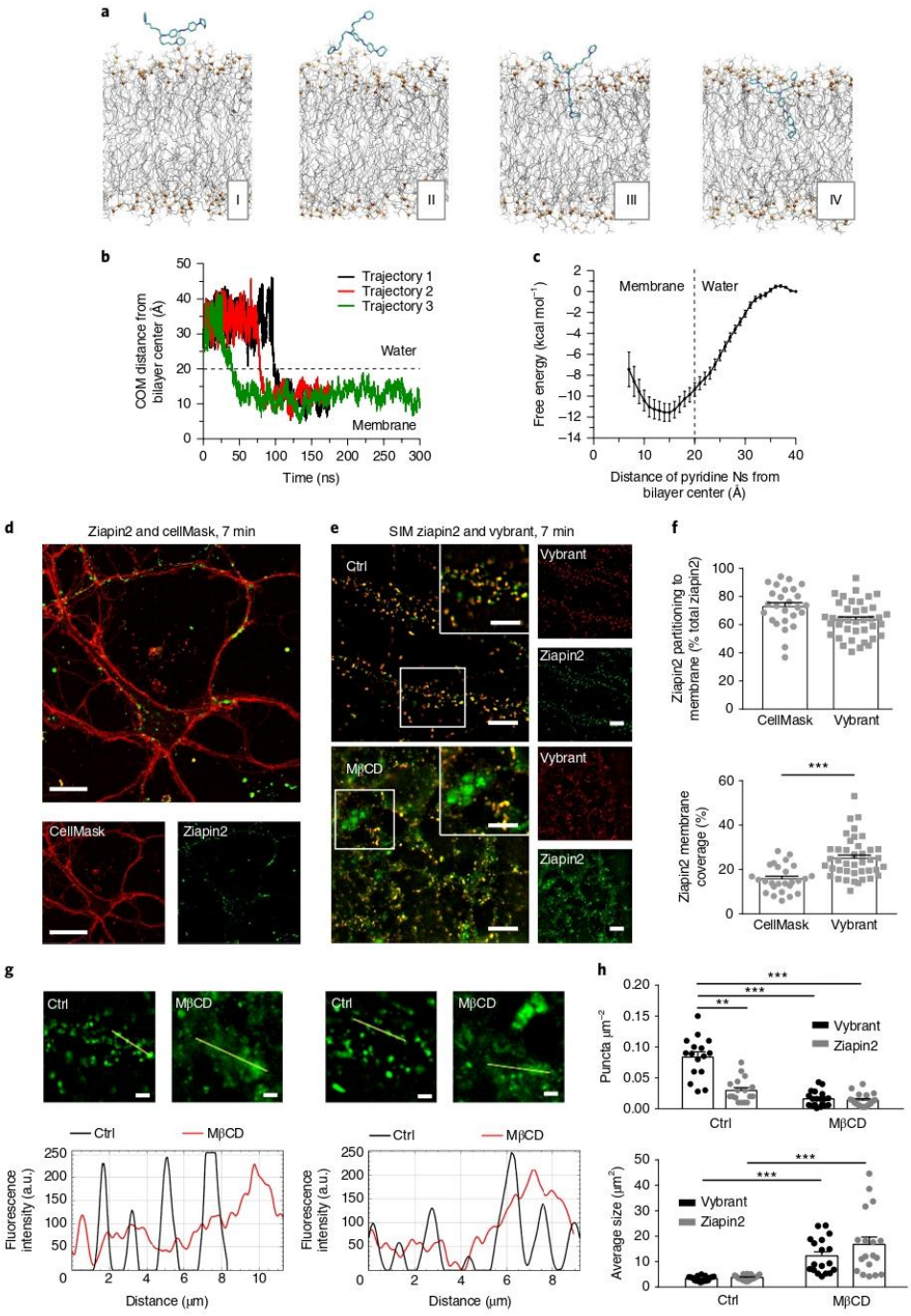

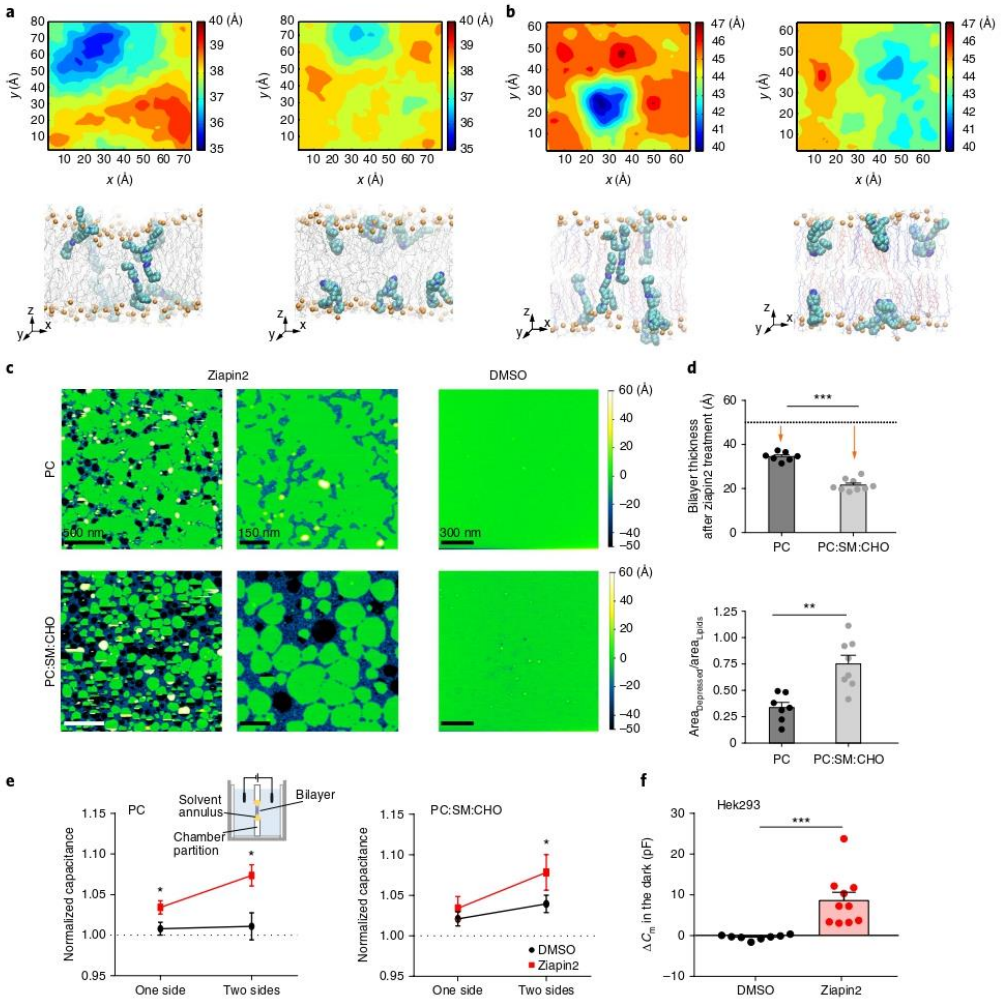

Fig. 3 | Ziapin2 reversibly modifies membrane thickness in artificial membranes, cell lines and neurons. a, Upper panels: Average membrane thickness maps, shown perpendicular to the bilayer plane, for the simulations of Ziapin2 (eight molecules) in *trans* (left) and *cis* (right) conformations, respectively. Ziapin2 molecules were embedded in PC model membranes. For the two Ziapin2 conformations, simulations (200 ns trajectory^{-1}) were started with the molecule in the equilibrium position. In both cases, the position along the bilayer normal was stationary over the whole trajectory, while the orientation fluctuated between a parallel and a perpendicular state. Axis and thickness values are in Å. Lower panels: Snapshots from simulations of Ziapin2 (eight molecules) in *trans* (left) and *cis* (right) conformations, respectively. **b**, Upper panels: Average thickness maps of a raft membrane model (simulations with eight Ziapin2 molecules in *trans* (left) and *cis* (right) conformations, respectively). The raft membrane model is composed of a mixture of PC, SM and cholesterol (CHO) (1:1:1). Axis and thickness values are in Å. Lower panels: Snapshots from the simulations of eight Ziapin2 molecules in *trans* (left) and *cis* (right) conformations. PC lipid molecules are shown as grey lines, and phosphate atoms as orange spheres; cholesterol and SM molecules are shown as red and blue lines, respectively; water molecules and ions are not reported for clarity. **c**, AFM maps realized in liquid environment on lipid bilayers formed either by PC (top) or by PC:SM:CHO (bottom) on mica and exposed to Ziapin2 or DMSO. Maps of Ziapin2-containing bilayers show the spatial distribution of depressed areas and the fine structure of the roughness modulation (left and middle panels at different magnification), while DMSO-containing bilayers show a very well-preserved uniformity (right). **d**, Top: Bilayer thickness after Ziapin2 incorporation in the dark with respect to the untreated nominal value (broken line). Bottom: Ratio between the area of depressed membrane and the total lipid-covered area. Raft-like bilayers show a higher decrease in thickness (top) and a more extended area of depression (bottom) when exposed to Ziapin2 if compared with single PC bilayers. The effects of Ziapin2 on thickness and depressed area are statistically significant for both types of bilayer ($P<0.05$ for both PC and PC:SM:CHO, one sample Student *t* test) and significantly more pronounced in raft-like than in pure PC membranes (***$P<0.001$, Mann–Whitney *U* test, $n=7$ and 9 for PC and PC:SM:CHO, respectively). **e**, Planar lipid membrane experiments realized with PC (left) or PC:SM:CHO (right) show a systematic increase of capacitance measured across the bilayers when Ziapin2 was present in both recording chambers with respect to the sole insertion in one of the two sides. *$P<0.05$, Mann–Whitney *U* test ($n=6$ and 5 for Ziapin2 and DMSO, respectively, for each type of bilayer). **f**, Evaluation of cell capacitance changes (means ± s.e.m.) by patch-clamp recordings after exposure of Hek293 cells to either DMSO (0.25% v/v; black) or Ziapin2 (5 μM in DMSO; red) in the dark. °°°$P<0.001$, Mann–Whitney *U* test ($n=8$ and 9 for DMSO and Ziapin2, respectively).

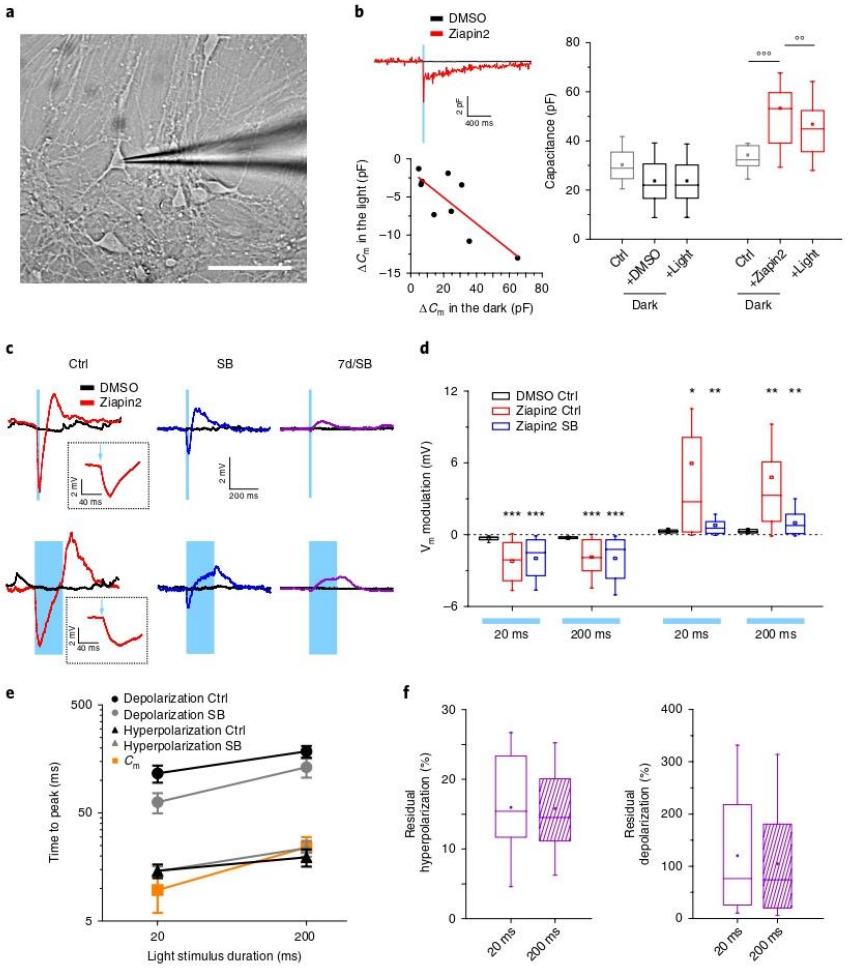

Fig. 4 | Light-evoked membrane voltage modulation by Ziapin2 in primary neurons. a, Primary hippocampal neurons at 14 days in vitro were incubated with Ziapin2 for 7 min, washed and recorded by whole-cell patch-clamp either immediately after pulse labelling or 7 d after. Scale bar: 20 µm. **b**, Left: Representative averaged capacitance traces of neurons pulse labelled with either DMSO (0.25% v/v; black traces) or Ziapin2 (5 µM in DMSO; red traces), washed and recorded in current-clamp configuration in the presence of SB before and after light stimulation (470 nm; 18 mW mm^{-2}; cyan-shaded areas). In the bottom panel, single-cell correlation between the capacitance increase in the dark upon Ziapin2 addition (*x* axis) and the phasic capacitance drop induced by light (*y* axis). Pearson's correlation coefficient −0.801, $P<0.05$. Right: Box plots of the peak capacitance changes after exposure of neurons to either DMSO (0.25% v/v; black) or Ziapin2 (5 µM in DMSO; red) in the dark (DMSO, $n=11$; Ziapin2, $n=13$) and subsequent illumination in the presence of the compound and of SB. The same neurons were recorded under basal conditions, added with either DMSO or Ziapin2 and finally stimulated with light. $^{**}P<0.01$; $^{***}P<0.001$; Ziapin2 versus DMSO, Friedman/Dunn's tests. **c**, Representative whole-cell current-clamp traces recorded from neurons incubated with either 0.25% (v/v) DMSO (black traces) or 5 µM Ziapin2 in DMSO (red traces) in the absence (Ctrl) or presence of SB (Methods) and after 7 d of incubation in the presence of SB (7d/SB). The duration of the light stimulation (20 and 200 ms) is shown as a cyan-shaded area (470 nm; 18 mW mm^{-2}). In the insets, traces are shown in an expanded timescale. **d**, Box plots of the peak hyperpolarization (left) and peak depolarization (right) changes in primary neurons exposed to DMSO/Ziapin2 and subjected to 20/200 ms light stimulation in the absence (Ctrl) or presence of SB. Hyperpolarization and depolarization were measured as the minimum and maximum voltage, respectively, reached within 350 ms from light onset. The box plots show that the peak hyperpolarization response generated by the presence of Ziapin2 is an intrinsic response of the neuron and is not affected by the presence of blockers of synaptic transmission, while depolarization, already present in synaptically isolated neurons, is enhanced by active synaptic transmission. **e**, Time-to-peak hyperpolarization, depolarization and capacitance changes as a function of the light stimulus duration under Ctrl and synaptic block conditions. Data (means ± s.e.m.) represent the time necessary to reach the minimum and maximum membrane voltages in the above-mentioned time windows. **f**, Persistence of the light response over time. The residual light-induced hyperpolarization (left) and depolarization (right) effects observed 7 d after the initial Ziapin2 loading in the presence of SB are expressed in percentage of the corresponding effects measured acutely after Ziapin2 loading. Box plots are shown for both 20 and 200 ms light stimuli. All experiments with neurons were carried out at 24 ± 1 °C. $^{*}P<0.05$; $^{**}P<0.01$; $^{***}P<0.001$ DMSO versus Ziapin2, Mann–Whitney *U* test. Ziapin2-treated neurons: $n=19$, 20, 15 (20 ms) and $n=20$, 19, 14 (200 ms) for Ctrl, SB and 7d/SB, respectively; DMSO-treated neurons: Ctrl, SB, 7d/SB: $n=10$, 7, 10 for both 20 and 200 ms.

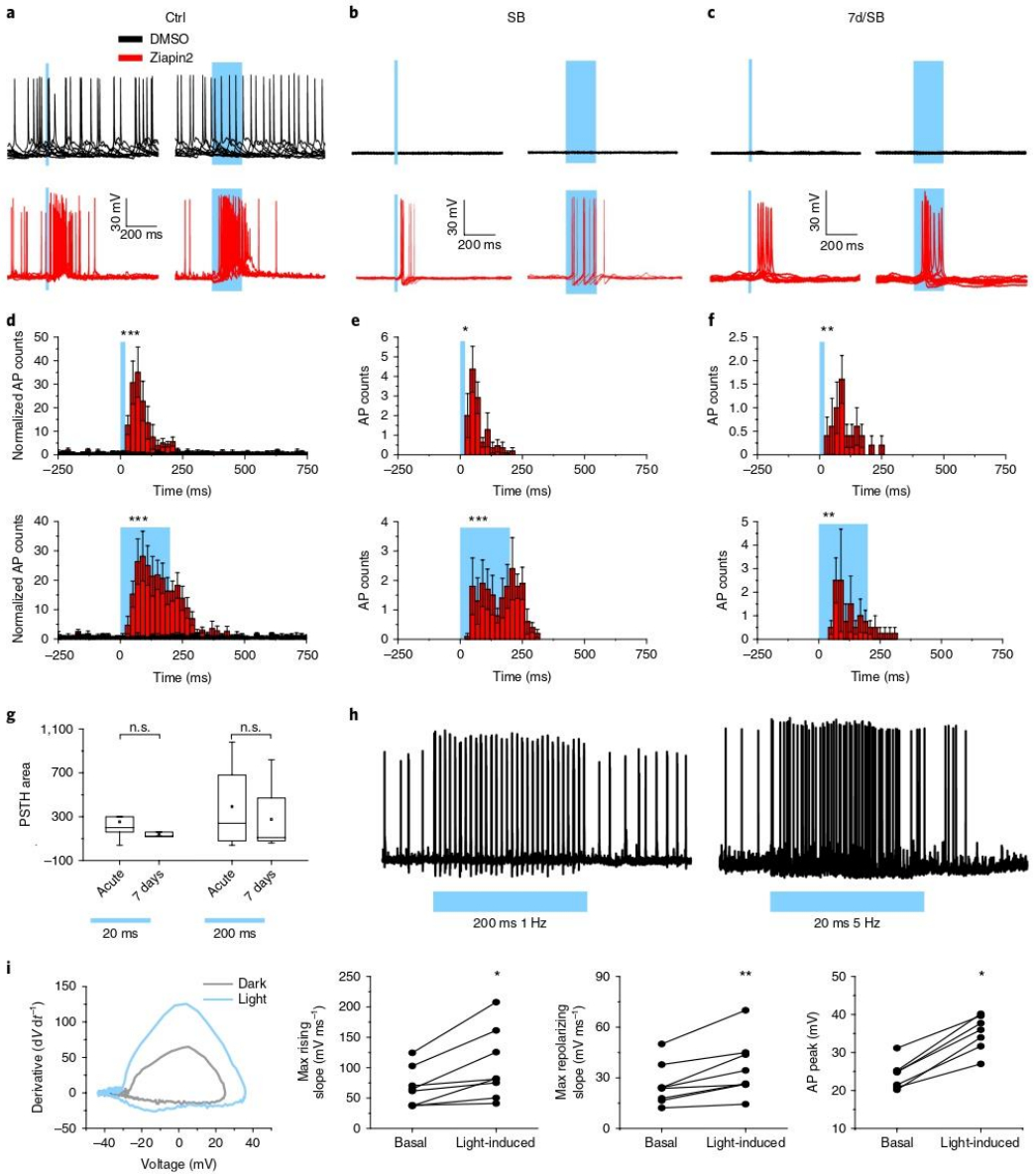

Fig. 5 | Light-evoked firing activity in primary neurons loaded with Ziapin2. a–c, Representative averaged traces recorded in current-clamp configuration from neurons incubated with either DMSO (0.25% v/v, black traces) or Ziapin2 (5 μM in DMSO, red traces) in the absence (**a**; Ctrl) or presence (**b**) of SB. In **c**, recordings were performed 7 d after Ziapin2 labelling with SB. Light stimulation (470 nm; 18 mW mm^{-2}) is shown as a cyan-shaded area. **d–f**, Peristimulus time histograms (PSTHs) (bin = 20 ms) reconstructed from the firing rate of neurons recorded in the absence (**d**) or presence of SB 7 min (**e**) and 7 d (**f**) after DMSO/Ziapin2 labelling, respectively, and subjected to either 20 ms (upper panel) or 200 ms (lower panel) light stimulation. Ziapin2-treated neurons: $n = 7, 11, 5$ (20 ms) and $n = 6, 10, 4$ (200 ms) for Ctrl, SB, 7d/SB, respectively; DMSO-treated neurons: $n = 4, 7, 10$ (20 and 200 ms) for Ctrl, SB, 7d/SB, respectively. $^*P < 0.05$; $^{**}P < 0.01$; $^{***}P < 0.001$ DMSO versus Ziapin2, Mann–Whitney *U* test on 160 ms bins (20 ms stimulation) and 240 ms bins (200 ms stimulation). **g**, PSTH areas of AP firing in response to 20/200 ms light stimulation in the presence of SB recorded either acutely or 7 d after Ziapin2 exposure. $N = 10$ (acute); $N = 5$ (7 d); n.s., not significant, Mann–Whitney *U* test. **h**, Representative AP firing activities recorded from neurons incubated with Ziapin2 (5 μM) in the absence of SB and stimulated with 200 ms light pulses administered at 1 Hz (upper traces) or with 20 ms light pulses administered at 5 Hz (lower traces). **i**, Left: Representative phase plane plot analysis of AP waveforms generated in the same Ziapin2-loaded neuron before (grey trace) and after (blue trace) light stimulation (470 nm; 20 ms pulses @ 20 mW mm^{-2}). Right: Quantification of the maximal rising and repolarizing slopes and of the AP peak amplitude before and after illumination. $^*P < 0.05$; $^{**}P < 0.01$, paired Student's *t* test ($n = 7$ neurons).

above; Supplementary Fig. 8a,b) was then investigated. Cholesterol depletion reduced the amplitude of light-evoked hyperpolarization in Ziapin2-labelled neurons, suggesting that clustering of Ziapin2 molecules at cholesterol-enriched membrane domains is essential for enhancing the light-dependent effects on membrane thickness (Supplementary Fig. 8b,c).

Morphological studies indicated that ~30% of the initial Ziapin2 labelling was present on the plasma membrane 7 d after loading, with a parallel reduction of light-evoked hyperpolarization with respect to acute Ziapin2 (Fig. 4f and Supplementary Fig. 7). However, the delayed depolarization was only slightly decreased (Fig. 4f), suggesting that the reduced membrane Ziapin2 concentration decreases the extent of light-evoked capacitance drop, leaving the return to basal capacitance relatively unaffected.

The steady increase in membrane capacitance induced by Ziapin2 in the dark significantly increased the rheobase and slowed AP's spontaneous frequency. Analysis of the AP waveform by phase plane plot revealed a slowdown of the rising and repolarizing slopes and an increased AP half-width in the absence of changes in AP amplitude (Supplementary Fig. 14b,c). We then examined the ability of light stimulation to elicit APs in Ziapin2-loaded neurons acutely and 7 d after membrane labelling (Fig. 5a–c). Light stimulation elicited a significant increase of AP frequency (Fig. 5a). Such result was even more striking in the presence of synaptic blockers (SB) that abolished spontaneous light-independent firing (Fig. 5b). Light-evoked firing was persistent over time, as shown 7 d after Ziapin2 labelling in the presence of SB (Fig. 5c). Peristimulus time histogram analysis showed that light reliably induced AP firing activity. AP firing peaked after light offset for short stimuli and during the light phase for long stimuli (Fig. 5d–g). Interestingly, repetitive firing was obtained with light pulse trains of 200 ms at 1 Hz or 20 ms at 5 Hz, with only occasional failures (Fig. 5h). Phase plane plot analysis of AP waveforms (Fig. 5i) revealed that light-evoked APs were characterized by increased rising/repolarization slopes and peak amplitudes, consistent with the light-induced drop in membrane capacitance.

Comparable light-evoked physiological effects of Ziapin2 described in murine neurons were also observed in human neurons differentiated from induced pluripotent stem cell (iPSC) clones generated from skin fibroblasts of healthy volunteers (Supplementary Fig. 16 and ref. [33]). We also compared the Ziapin2 effects with the photostimulation of primary neurons transduced with the ultrafast microbial opsin ChETA, a light-dependent cationic channel[34] (Supplementary Fig. 17). As expected from a light-gated ion channel, ChETA induced a larger V_m modulation than Ziapin2 at all stimulus durations, although the peak-to-peak difference reached significance only in the presence of SB (Supplementary Fig. 17a). Notably, no significant differences were observed in the latency to the peak V_m change in the absence of APs (Supplementary Fig. 17a), as well as in the light-induced firing probability measured both at the resting membrane potential (-53.6 ± 0.9 mV) and with neurons depolarized near threshold (−35 mV; Supplementary Fig. 17c). However, ChETA was faster in the latency to the first light-induced AP (Supplementary Fig. 17d). Waveform analysis of light-evoked APs failed to detect differences between ChETA- and Ziapin2-labelled neurons, indicating that the light-induced decrease in capacitance in Ziapin2-loaded neurons normalized the AP dynamics (Supplementary Fig. 17e).

Light-induced cortical activity by Ziapin2 in vivo

Ziapin2 or vehicle was injected in the somatosensory cortex of mice subsequently implanted with a multielectrode array coupled with an optical fibre (Fig. 6a). Cortical responses to light stimuli were measured shortly after surgery (30–60 min) and 1, 4 and 7 d after the Ziapin2 injection. Ziapin2 fluorescence analysed in brain slices showed a diffusion diameter in the range of 1 mm and persisted up to 7 d from injection (Fig. 6b). Immunohistochemistry in cortical slices at the injection site performed 7 d after the injection demonstrated that Ziapin2 did not alter the inflammatory reaction to the surgery, as evaluated by the expression of GFAP and Iba1, specific markers for astrocytes and microglia, respectively (Supplementary Fig. 18). Optical stimulation at various power densities induced activation of cortical activity evaluated as extracellular local field potentials (LFPs) that peaked at about 200 ms after light onset (Fig. 6c). Ziapin2 induced a significant dose-dependent increase in the LFP amplitude with respect to vehicle-injected animals that was more pronounced for 200 ms stimuli (Fig. 6d). Analysis of the time course of the light-evoked LFP responses revealed that the optical stimulation of cortical activity persisted up to 7 d after injection (Fig. 6e,f).

Conclusions

We report here on an opto-mechanical effect driven by intramembrane molecular machines composed of clustered photochromic molecules. The predictions by MD simulations, confirmed by experimental observations on artificial membranes, are consistent with a model in which the hydrophobic azepane-substituted aniline in the amphiphilic azobenzenes on the two sides of the membrane interact when in *trans* configuration, retracting to *cis* after photoconversion. This brings about shrinkage of the membrane on *trans* Ziapin2 loading that eventually relaxes to the natural thickness following light-induced Ziapin2 dissociation. The evoked relaxation increases membrane thickness, thus transiently decreasing its capacitance.

Ziapin2 differentiates from previously reported capacitance-changing azobenzene-cored amphiphilic probes containing long alkyl chains[6–8,35,36] for distinctive functional groups and features: (1) the two hexyl chains ω-terminated with pyridinium bromide that target the membrane;[35,36] (2) the presence of an amine on both azobenzene sides that, as strong electron-donor group, redshifts azobenzene absorption to the visible; (3) the azepane moiety that mediates the formation of *trans*-Ziapin2 dimers through the interaction between two facing Ziapin2 molecules on opposite bilayer leaflets. Thanks to these features, Ziapin2 responds to millisecond-range visible light stimuli by deforming the membrane and causing the fast physiological effects.

The light-induced capacitance drop generates a pure capacitive current responsible for a hyperpolarizing shift that depends on membrane coverage and rate of capacitance change. These effects do not involve ion channels, being recapitulated by Hek293 cells and neurons subjected to intra/extracellular blockade of membrane conductances. Thus, we are exploiting a novel membrane nanomachine with a mechanical effect at the molecular scale.

Although the existence of lipid rafts is a matter of controversy[37], photochromic molecules have already been targeted to lipid rafts[38]. The propensity of Ziapin2 to localize to cholesterol and sphingolipid-enriched membrane microdomains is functionally important. Indeed, the membrane-thinning effect, evaluated by AFM, was amplified in raft-like bilayers, and disruption of lipid rafts caused disappearance of Ziapin2 clusters and decrease of light-induced hyperpolarization.

Several papers reported a link between temperature-dependent decrease in membrane thickness, increased capacitance and depolarization[22–25], demonstrating that membrane capacitance is effective in modulating neuronal activity. In the dark, Ziapin2-induced increase in capacitance renders neurons less excitable and more refractory to membrane-voltage changes. This stabilization of neuronal activity is a potentially exploitable effect in the regulation of network excitability and in demarcating the discharge areas in neuronal networks. In response to light stimulation, Ziapin2 controls AP firing through two cooperating mechanisms: (1) the fast light-induced C_m decrease, generating hyperpolarization, followed by a slower C_m increase at the light offset, associated with rebound depolarization, as predicted by the equivalent circuit simulation; (2) membrane hyperpolarization may cause an 'anode break excita-

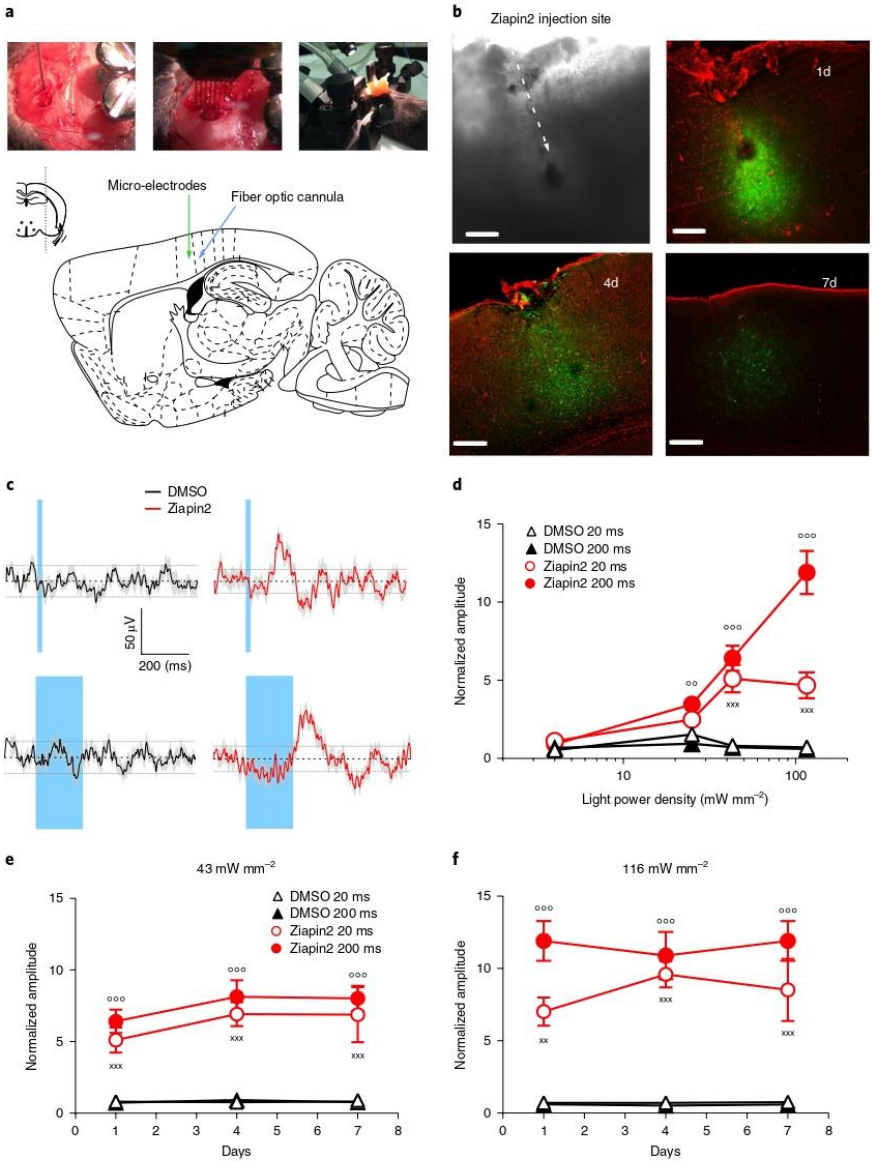

Fig. 6 | Light-evoked cortical responses invivo in mice loaded with Ziapin2 in the somatosensory cortex. a, Schematic representation of the stereotaxic injection of Ziapin2 (200 µM in 1µl 10% DMSO) in the somatosensory cortex (S1ShNc, 2 mm anterior to lambda, 2 mm lateral to midline, and −723 µm ventral to brain surface) and of the 16-microelectrode array implant for LFP recordings coupled with optical fibre for photostimulation. **b**, Bright field image (left) and endogenous LC339 fluorescence micrograph (right) of unfixed slices from the injected somatosensory cortex taken 1, 4 and 7 d after Ziapin2 administration. The injection site and the diffusion of the compound are visible. Scale bar: 150 µm. **c**, Representative recordings of LFPs evoked in the somatosensory cortex by 20 and 200 ms light stimulation (43 mW mm^{-2}) in mice injected with either DMSO (black trace) or Ziapin2 (red trace) 1 day before. The cyan-shaded areas represent the light stimulation. Potentials were considered significant above twofold the standard deviation range (broken horizontal lines). **d**, Dose-response analysis of LFP responses in DMSO- (black) or Ziapin2- (red) injected mice as a function of power and duration of the light stimulus (20 and 200 ms; open and closed symbols, respectively). The peak amplitude of light-evoked LFPs was normalized by the averaged noise amplitude calculated from the non-responding channels over the same epoch. Photostimulation at increasing power from 4 to 116 mW mm^{-2} triggered significant responses in Ziapin2-injected animals that were already significant at 25 mW mm^{-2} (200 ms stimulus). No significant responses were recorded in DMSO-treated animals. **e**,**f**, Time course of the normalized LFP amplitude recorded in the somatosensory cortex 1, 4 and 7 d after intracortical injection of either DMSO (black) or Ziapin2 (red). LFPs were evoked by 20 (open symbols) and 200 (closed symbols) ms light stimuli at 43 (**e**) and 116 (**f**) mW mm^{-2}. 20 ms: $^{xx}P<0.01$, $^{xxx}P<0.001$; 200 ms: $^{oo}P<0.01$; $^{ooo}P<0.001$; repeated measure ANOVA/Tuckey's tests versus DMSO-injected control ($n=3$ mice for each experimental group).

tion' at the light offset, decreasing outward K^+ current and removing Na^+ channel inactivation[39]. The rebound post-hyperpolarization AP firing depends on the duration of membrane hyperpolarization[40], explaining the limitation in the maximal stimulation frequency that can be achieved.

Neurons display larger depolarization, with respect to Hek293 cells, that is sensitive to synaptic transmission, which instead does not affect hyperpolarization. Depolarization may contribute to the light-evoked firing through a positive feedback within the network mediated by excitatory synaptic transmission. In this respect, using conjugated polymer interfaces, we previously showed that light-induced inhibition is followed by a rebound depolarization and firing[19,23], indicating that the fast return of capacitance and voltage to basal levels is responsible for neuronal activation.

With respect to optogenetic light-gated ion channels such as ChETA, Ziapin2 does not interfere with ionic fluxes or reversal potential of membrane conductances but directly targets passive membrane properties. Although the Ziapin2 effect is slower than that of a light-driven ion channel, it has a comparable ability in eliciting of APs.

Ziapin2 is not harmful to primary neurons, and neuronal activation by Ziapin2 is persistent in vitro despite the slow decrease of the plasma membrane concentration due to membrane turnover. Moreover, Ziapin2 is effective in inducing a light-dependent electrical activation of the cortical networks after in vivo injection in the somatosensory cortex of the mouse, with a sustained effect of photostimulation and a complete absence of inflammatory responses to the compound, paving the way to their potential future in vivo applications.

In conclusion, our new amphiphilic photochromic molecules have several characteristics that differentiate them from previous compounds: (1) marked affinity for the hydrophobic environment of the membrane; (2) high tolerability and sensitivity to the visible spectrum; (3) reversible photoinduction of local membrane deformations altering membrane capacitance, potential and firing in the absence of heat generation; (4) effectiveness and prolonged effects in vivo. In view of these features, these molecules display a high potential for future applications in neurosciences and biomedicine.

Online content

Any methods, additional references, Nature Research reporting summaries, source data, extended data, supplementary information, acknowledgements, peer review information; details of author contributions and competing interests; and statements of data and code availability are available at https://doi.org/10.1038/s41565-019-0632-6.

Received: 4 September 2018; Accepted: 18 December 2019;
Published online: 3 February 2020

References

1. Paoletti, P., Ellis-Davies, G. C. R. & Mourot, A. Optical control of neuronal ion channels and receptors. *Nat. Rev. Neurosci.* **20**, 514–532 (2019).
2. Rivnay, J., Wang, H., Fenno, L., Deisseroth, K. & Malliaras, G. Next-generation probes, particles, and proteins for neural interfacing. *Sci. Adv.* **3**, e1601649 (2017).
3. Tønnesen, J. Optogenetic cell control in experimental models of neurological disorders. *Behav. Brain Res.* **255**, 35–43 (2013).
4. Deisseroth, K. Optogenetics: 10 years of microbial opsins in neuroscience. *Nat. Neurosci.* **18**, 1213–1225 (2015).
5. Zhang, J. J., Wang, J. X. & Tia, H. Taking orders from light: progress in photochromic bio-materials. *Mater. Horiz.* **1**, 169–184 (2014).
6. Fujiwara, H. & Yonezawa, Y. Photoelectric response of a black lipid membrane containing an amphiphilic azobenzene derivative. *Nature* **351**, 724–726 (1991).
7. Yonezawa, Y., Fujiwara, H. & Sato, T. Photoelectric response of black lipid membranes incorporating an amphiphilic azobenzene derivative. *Thin Solid Films* **210/211**, 736–738 (1992).
8. Tanaka, M. & Yonezawa, Y. Photochemical regulation of ion transport through "quasi-channels" embedded in black lipid membrane. *Mat. Sci. Eng. C.* **4**, 297–301 (1997).
9. Garner, L. E. et al. Modification of the optoelectronic properties of membranes via insertion of amphiphilic phenylenevinylene oligoelectrolytes. *JACS* **132**, 10042–10052 (2010).
10. Hinks, J. et al. Modeling cell membrane perturbation by molecules designed for transmembrane electron transfer. *Langmuir* **30**, 2429–2440 (2014).
11. Gorostiza, P. & Isacoff, E. Optical switches and triggers for the manipulation of ion channels and pores. *Mol. Biosyst.* **3**, 686–704 (2007).
12. Fortin, D. L. et al. Photochemical control of endogenous ion channels and cellular excitability. *Nat. Methods* **5**, 331–338 (2008).
13. Kramer, R. H., Mourot, A. & Adesnik, H. Optogenetic pharmacology for control of native neuronal signaling proteins. *Nat. Neurosci.* **16**, 816–823 (2013).
14. Tochitsky, I., Kienzler, M. A., Isacoff, E. & Kramer, R. H. Restoring vision to the blind with chemical photoswitches. *Chem. Rev.* **118**, 10748–10773 (2018).
15. Laprell, L. et al. Restoring light sensitivity in blind retinae using a photochromic AMPA receptor agonist. *ACS Chem. Neurosci.* **7**, 15–20 (2016).
16. Laprell, L. et al. Photopharmacological control of bipolar cells restores visual function in blind mice. *J. Clin. Invest.* **127**, 2598–2611 (2017).
17. Ghezzi, D. et al. A hybrid bioorganic interface for neuronal photoactivation. *Nat. Commun.* **2**, 166 (2011).
18. Ghezzi, D. et al. A polymer optoelectronic interface restores light sensitivity in blind rat retinas. *Nat. Photonics* **7**, 400–406 (2013).
19. Feyen, P. et al. Light-evoked hyperpolarization and silencing of neurons by conjugated polymers. *Sci. Rep.* **6**, 22718 (2016).
20. Rand, D. et al. Direct electrical neurostimulation with organic pigment photocapacitors. *Adv. Mater.* **30**, e1707292 (2018).
21. Maya-Vetencourt, J. F. et al. A fully organic retinal prosthesis restores vision in a rat model of degenerative blindness. *Nat. Mater.* **16**, 681–689 (2017).
22. Martino, N. et al. Photothermal cellular stimulation in functional bio-polymer interfaces. *Sci. Rep.* **5**, 8911 (2015).
23. Lodola, F., Martino, N., Tullii, G., Lanzani, G. & Antognazza, M. R. Conjugated polymers mediate effective activation of the mammalian ion channel transient receptor potential vanilloid 1. *Sci. Rep.* **7**, 8477 (2017).
24. Shapiro, M. G., Homma, K., Villarreal, S., Richter, C. P. & Bezanilla, F. Infrared light excites cells by changing their electrical capacitance. *Nat. Commun.* **3**, 736 (2012).
25. Carvalho-de-Souza, J. L. et al. Photosensitivity of neurons enabled by cell-targeted gold nanoparticles. *Neuron* **86**, 207–217 (2015).
26. Bandara, H. M. & Burdette, S. C. Photoisomerization in different classes of azobenzene. *Chem. Soc. Rev.* **41**, 1809–1825 (2012).
27. Hartley, G. S. The *Cis*-form of azobenzene. *Nature* **140**, 281–281 (1937).
28. Rau, H. Spectroscopic properties of organic azo compounds. *Angew. Chem.* **12**, 224–235 (1973).
29. Tang B. Z. & Qin A. *Aggregation-Induced Emission: Fundamentals* (Wiley, 2013).
30. Sierocki, P. et al. Photoisomerization of azobenzene derivatives in nanostructured silica. *J. Phys. Chem. B* **110**, 24390–24398 (2006).
31. Fendler, J. H. Surfactant vesicles as membrane mimetic agents: characterization and utilization. *Acc. Chem. Res.* **13**, 7–13 (1980).
32. Head, B. P., Patel, H. H. & Insel, P. A. Interaction of membrane/lipid rafts with the cytoskeleton: impact on signaling and function: membrane/lipid rafts, mediators of cytoskeletal arrangement and cell signaling. *Biochim. Biophys. Acta* **1838**, 532–545 (2014).
33. Fruscione, F. et al. PRRT2 controls neuronal excitability by negatively modulating Na^+ channel 1.2/1.6 activity. *Brain* **141**, 1000–1016 (2018).
34. Thalhammer, A. et al. Alternative splicing of P/Q-type Ca^{2+} channels shapes presynaptic plasticity. *Cell Rep.* **20**, 333–343 (2017).
35. Zhang, Q. & Bazuin, C. G. Liquid crystallinity and other properties in complexes of cationic azo-containing surfactomesogens with poly(styrenesulfonate). *Macromolecules* **42**, 4775–4786 (2009).
36. Peddie, V., Anderson, J., Harvey, J. E., Smith, G. J. & Kay, A. Synthesis and solution aggregation studies of a suite of mixed neutral and zwitterionic chromophores for second-order nonlinear optics. *J. Org. Chem.* **79**, 10153–10169 (2014).
37. Allen, J. A., Halverson-Tamboli, R. A. & Rasenick, M. M. Lipid raft microdomains and neurotransmitter signalling. *Nat. Rev. Neurosci.* **8**, 128–140 (2007).
38. Frank, J. A., Franquelim, H. G., Schwille, P. & Trauner, D. Optical control of lipid rafts with photoswitchable ceramides. *J. Am. Chem. Soc.* **138**, 12981–12986 (2016).
39. Hodgkin, Al & Huxley, A. F. A quantitative description of membrane current and its application to conduction and excitation in nerve. *J. Physiol.* **117**, 500–544 (1952).
40. Tremere, L. A., Pinaud, R., Irwin, R. P. & Allen, C. N. Postinhibitory rebound spikes are modulated by the history of membrane hyperpolarization in the SCN. *Eur. J. Neurosci.* **28**, 1127–1135 (2008).

Methods

Synthesis and characterization of Ziapin2. The synthetic route consists of the reduction of the nitro group of the Disperse Orange 3 dye in amine, which is then alkylated with α,ω-dibromohexane and finally treated with pyridine to yield the terminated pyridinium bromide.

Unless otherwise stated, all chemicals and solvent were commercially available and used without further purification. Thin-layer chromatography was performed using silica gel on aluminium foil (Sigma Aldrich); ^{1}H and ^{13}C NMR spectra were collected with a Bruker ARX400. Mass spectroscopy was carried out with a Bruker Esquire 3000 plus.

4-[2-(4-aminophenyl)diazen-1-yl]aniline (1). A mixture of Disperse Orange 3 (Sigma Aldrich, 1.21 g, 5.0 mmol) and $Na_2S{\cdot}9H_2O$ (3.60 g 15.0 mmol) dissolved in 100 mL of MeOH is refluxed overnight under stirring. Then the mixture is cooled to room temperature and the solvent is removed under reduced pressure. The resulting red powder is washed with DCM and Et_2O, the combined organic layers are collected and the solvent is evaporated under reduced pressure to give 540 mg of the desired product **1** as an orange powder in 51% yield.

^{1}H NMR: (400 MHz, DMSO) δ 7.56 (d, J = 8.82 Hz, 2H), 6.62 (d, J = 8.82 Hz, 2H), 5.70 (s, 4H)

4,4′-Bis-(N,N-di-ω-bromohexyl)diaminoazobenzene (Azo-Br4), Azo-Br1, Azo-Br2. 537 mg of product **1** (2.53 mmol) is stirred in 10 ml of previously degassed acetonitrile, then 2.20 g of K_2CO_3 (15.9 mmol) and 1.6 ml of 1,6-dibromohexane (10.4 mmol) are added dropwise to the reaction mixture and refluxed for 72 h while monitored by thin-layer chromatography. The reaction mixture is filtered, and the solid is washed three times with diethyl ether, ethylacetate and dichloromethane. The excess of dibromohexane is removed under reduced pressure (3×10^{-1} mbar) at 70 °C. The raw material is purified by flash chromatography with silica gel using hexane/Et_2O 3/1 as eluent to give 52 mg of 4,4′-Bis-(N,N-di-ω-bromohexyl) diaminoazobenzene (Azo-Br4, 2.4% yield); 32 mg of Azo-Br1 (2.8% yield) and 33 mg of Azo-Br2 (2.1% yield) are also recovered.

Azo-Br4. ^{1}H NMR: (400 MHz, DMSO) δ (ppm) 7.62 (d, J = 8.80 Hz, 4H), 6.72 (d, J = 8.80 Hz, 4H), 3.53 (t, 16H), 1.82 (m, 8H), 1.56 (m, -CH_2-,8H), 1.44 (m, -CH_2-,8H), 1.35 (m, -CH_2-, 8H); MS: 865 (M + H)$^+$, 887 (M + Na)$^+$

Azo-Br1. ^{1}H NMR: (400 MHz, DMSO) δ (ppm) 7.63 (d, J = 8.80 Hz, 2H), 7.58 (d, J = 8.80 Hz, 2H), 6.77 (d, J = 8.80 Hz, 2H), 6.64 (d, J = 8.80 Hz, 2H), 6.21 (t, -NH, 1H), 3.54 (t, -N-CH_2-, 6H), 3.09 (m, CH_2-NH, 2H), 1.83-1.42 (m, 1 CH_2-, 6H); MS: 458 (M + H)$^+$

Azo-Br2. ^{1}H NMR: (400 MHz, DMSO) δ (ppm) 7.63 (d, J = 8.80 Hz, 4H), 6.77 (d, J = 8.80 Hz, 2H), 6.72 (d, J = 8.80 Hz, 2H), 3.53 (t, -N-CH_2-, 8H), 3.35 (t, -CH_2-Br), 1.82-1.35 (m, -CH_2-, 24H); MS: 621 (M + H)$^+$

1-{6-[(4-{2-[4-(azepan-1-yl) phenyl]diazen-1-yl}phenyl)[6-(pyridin-1-ium-1-yl) hexyl] amino] hexyl} pyridin-1-ium dibromide (Ziapin2). 12 mg of **Azo-Br2** are dissolved in 3 ml of pyridine and stirred at room temperature for 42 h. Then 3 ml of methanol are added and further stirred for 60 h. The excess of pyridine and methanol are removed from the reaction mixture under reduced pressure to give a solid in quantitative yield that is further washed with small portions of hexane.

^{1}H NMR: (400 MHz, DMSO) δ 9.09 (d, Pyr, 4H), 8.61 (t, Pyr, 2H), 8.16 (t, Pyr, 4H), 7.62 (d, J = 8.8 Hz, Ph, 4H), 6.78 (d, J = 8.8 Hz, Ph, 2H), 6.70 (d, J = 8.8 Hz, Ph, 2H), 4.60 (t, -CH_2-Pyr-, 4H), 3.54 (t, N-CH_2-, 4H), 2.97-1.24 (m, 24H). ^{13}C NMR: (400 MHz, DMSO) δ 150.29, 149.45, 145.97, 145.21, 143.00, 128.56, 124.38, 124.24, 111.65, 111.36, 61.22, 50.54, 49.50, 31.15, 27.27, 27.15, 26.75, 26.27, 25.86. MS: 618 (M -2Br)$^+$

The chromatographic analysis of Ziapin2 was performed by means of a Waters HPLC system equipped with a Waters 600 Controller, a Waters 996 Photodiode Array Detector and a Jupiter 5 µ C18 300A Phenomenex column. The measurement was carried out using a gradient programme with 25% CH_3CN/75% H_2O (both HiPerSolv Chromanorm grade solvents from VWR Chemicals) initial eluent mixture for 5 min progressively modified into 100% CH_3CN over a total period of 25 min. The spectrum of the isolated compound absorbs at nearly 470 nm.

UV–Vis absorption measurements. For the UV–Vis absorption measurements, we used a Perkin Elmer Lambda 1050 spectrophotometer equipped with deuterium (180–320 nm) and tungsten (320–3300 nm) lamps and three detectors (photomultiplier 180–860 nm, InGaAs 860–1300 nm and PbS 1300–3300 nm). For further details, see Supplementary Information.

Photoluminescence measurements. The PL measurements in solution (25 µM in DMSO, water and SDS; 100 mM) were taken with a Horiba Nanolog Fluorometer equipped with a xenon lamp, two monochromators and two detectors (photomultiplier and InGaAs). Hek293 cells, used as a source of cell membranes, were obtained from ATCC. The emission of azobenzene in the membrane environment at 450 nm was elicited by using a CW diode laser (excitation energy of 10 mW mm^{-2}, matching that of electrophysiology experiments). The emission was collected with an ×50 objective (Zeiss), filtered to remove the wavelength excitation and sent to the camera (Hamamatsu, acquisition time 100 ms). The system was illuminated for a shorter time (10 s) than the PL measurements in solution, to avoid cell damage. For further details see Supplementary Information.

MD simulations. All-atom MD simulations of Ziapin2 in *trans* and *cis* conformations in a model membrane bilayer of 1-palmitoyl-2-oleoyl-phosphatidylcholine (POPC) made of 160 lipid molecules (80 per leaflet) and water. A starting conformation for the bilayer in water was generated using pre-equilibrated lipid structures from the CHARMM-GUI web server[41]. All simulations were run with NAMD v2.12 code[42] using the CHARMM36 force field[43] and TIP3P model for water molecules. CHARMM-compatible topology and parameters for Ziapin2 were obtained using the CHARMM General Force Field (CGenFF), and atomic charges were calculated at the B3LYP/cc-pVTZ level. The total electrostatic charge of each system was neutralized by the addition of physiological concentrations of counter ions. The time step for integrating the equation of motion was 2 fs. Simulations were performed using periodic boundary conditions in the NPT ensemble, that is, at constant pressure (1 atm) and temperature (310 K), using a Langevin piston with a constant decay of 100 ps^{-1} and an oscillation period of 200 fs and a Langevin thermostat with a damping constant of 5 ps^{-1}. Flexible unit cell was used with constant ratio in the x–y plane. Long-range electrostatic interactions were computed using the particle-mesh Ewald method, with a fourth-order spline and 1 Å grid spacing. The PC/water system was simulated for 30 ns to equilibrate, and then the following simulations were performed: three runs of spontaneous *trans* Ziapin2 insertion in the membrane (two for 175 ns and one for 300 ns); two runs of a single Ziapin2 in the membrane, one in *trans* and one in *cis* conformation (200 ns each); two runs each with four copies of Ziapin2 in the membrane, in *trans* and *cis* conformation (200 ns each); two runs each with eight copies of Ziapin2 in the membrane, in *trans* and *cis* conformation (200 ns each); one run with 16 copies of Ziapin2 in the membrane in *trans* conformation (200 ns). When multiple copies of Ziapin2 were considered, they were distributing symmetrically in the upper and in the lower leaflet, aligned with the respective lipid headgroups. For the *cis* systems, the initial positions were determined by aligning the pyridine branches with those of the *trans* molecules. To determine the free energy profile for moving Ziapin2 from bulk water into the PC bilayer, we integrated a set of mean force values (that is, minus the derivative of the free energy) calculated at 34 different positions of the molecule along the axis normal to the bilayer. The different values of the mean force were computed by restraining the centre of mass of the pyridine nitrogen atoms of Ziapin2 at positions spaced by 1 Å along the normal with a force constant of 100 kcal mol^{-1} Å^{-2}. The centre of mass of the bilayer was kept fixed in all mean force simulations. At each position, the simulation lasted for 10–20 ns, until convergence of the mean force estimator was observed. To simulate the effect of light-induced *trans*→*cis* Ziapin2 conformational change on the membrane, we extracted a pinched bilayer conformation from the simulation with eight *trans* Ziapin2, deleted the photochromic molecules, inserted eight Ziapin2 in *cis* conformations and ran a standard MD trajectory for 200 ns. For further details on the raft simulations model[44] and MD technique[45], see Supplementary Information.

Atomic force microscopy. Atomic force microscopy data were acquired using an Oxford Instrument Cypher AFM equipped with a liquid droplet probe holder. AFM scans were acquired in liquid in AC mode (free amplitude ~6 nm) using BL-AC40TS cantilevers (Olympus), with a nominal resonance frequency in air of 110 kHz and a nominal spring constant of 0.09 N m^{-1}.

Liposomes were prepared as previously reported[16]. Bilayers were prepared starting from a 6 mg ml^{-1} large unilamellar vesicles (LUV) solution in phosphate buffer (150 mM NaCl, 15 mM sodium phosphate, pH 7.4), exposed to Ziapin2 (2 mM in DMSO) for 7 min at room temperature, at a molar ratio lipid/Ziapin2 of around 50. In control experiments, we added to the LUV solution, instead of the Ziapin2 solution, the same volume of pure DMSO. Samples were then diluted in phosphate buffer at a final lipid concentration of 2 mg ml^{-1} (PC bilayers) or of 1 mg ml^{-1} (ternary membranes, PC:SM:Chol 1:1:1 (mol)) and supplemented with 1 mM $CaCl_2$ to help the vesicle fusion on the mica substrate. Supported lipid bilayers were deposited on freshly cleaved mica discs (Ted Pella), incubating for 10 min a 100 µl droplet of the LUV/Ziapin2 (LUV/DMSO) suspension. The excess of vesicles was removed by gently washing the samples with phosphate buffer. At least three samples for every condition were analysed. Data were imported in ImageJ for image plane fitting and line-by-line flattening, rendering and analysis.

Planar lipid bilayer experiments. Solvent-free planar lipid membranes were formed over a 100–180 µm diameter hole sparkling drilled in a 25-µm-thick Teflon septum, thus separating two compartments, as previously described[47]. Each chamber was filled with 2 mL buffer solution (150 mM NaCl, 15 mM sodium phosphate, pH 7.4), and stable bilayers were formed between the two chambers. Micromolar concentrations of Ziapin2 (5 µM) were sequentially added to the *cis* and to the *trans* sides of a stable preformed bilayer. Lipid compositions used were pure PC or PC:CHO:SM 57:33:10 (molar ratio). Currents were recorded with a patch-clamp amplifier (Axopatch 200B, Axon Instruments), and a PC equipped

with a DigiData 1550A/D converter (Axon Instruments) was used for data acquisition. Current traces were filtered at 2 kHz and acquired at 10 kHz by the computer using Clampex 10.5 software (Axon Instruments). All measurements were performed in the dark at room temperature. Membrane capacitance was measured via continuous symmetrical triangular ramps (100 Hz in frequency), as summarized in Schmitt and Koepsell[48]. The membrane capacitance (C_m) is connected to the membrane characteristic features, for example area (A) and thickness (d), through the following equation (1):

$$C_m(\mathrm{pF}) = A(\mathrm{nm}^2)\ \epsilon_r\epsilon_0\ (\mathrm{pF/nm})/d(\mathrm{nm}) \quad (1)$$

For a stable membrane formed by a defined lipid class or composition, we can consider A and ϵ_r being constant for each experiment; therefore, a measured increase in the membrane capacitance reflects a linear reduction in the membrane thickness. The membrane capacitance (C_m) was obtained by subtracting the capacity of the septum, which is 30 pF in our conditions.

Electrophysiology. Whole-cell patch-clamp recordings of Hek293 cells and low-density primary hippocampal neurons (between 14 and 18 days in vitro) were performed at room temperature (22–24 °C) using 3–4 MΩ borosilicate patch pipettes (Kimble, Kimax, Mexico) and under GΩ patch seal. Cells with leak currents >200 pA or series resistance (R_s) >15 MΩ were discarded. The R_s was compensated 80% (2 µs response time), and the compensation was readjusted before stimulation. The shown potentials were not corrected for the measured liquid junction potential (9 mV). Voltage-clamp recordings were sampled at 20 kHz and low-pass filtered at 4 kHz. Current-clamp recordings were sampled at 50 kHz and low-pass filtered at 10 kHz. Patch-clamp recordings were carried out using either an Axopatch 200B (Molecular Devices, San José, CA) or an EPC10 (HEKA Elektronik, Reutlingen, Germany) amplifier.

For Hek293 cell recordings, patch electrodes (3–4 MΩ) were filled with an intracellular solution containing (in mM) 140 NaCl, 2 $MgCl_2$, 5 HEPES (pH 7.4). Cells were bathed during whole-cell recordings in an extracellular solution containing (in mM) 140 NaCl, 2 $MgCl_2$, 5 HEPES (pH 7.4) unless stated in the text. For recordings in primary neurons, the standard extracellular solution contained (in mM) 135 NaCl, 5.4 KCl, 1 $MgCl_2$, 1.8 $CaCl_2$, 5 HEPES, 10 glucose adjusted to pH 7.4 with NaOH. The standard intracellular solutions contained (in mM) 126 K-gluconate, 4 NaCl, 1 $MgSO_4$, 0.02 $CaCl_2$, 0.1 EGTA, 10 glucose, 5 HEPES, 3 ATP-Na_2, and 0.1 GTP-Na. When indicated, recordings were performed in the presence of the SB D-AP5 (50 µM)/CNQX (10 µM) and bicuculline (30 µM) (Tocris, Bristol, UK) to block excitatory and inhibitory synaptic transmission, respectively.

To investigate the contribution of ionic conductances in the capacitive currents evoked by light stimulation, the standard internal solution was used in combination with an extracellular solution where Na^+ was replaced by choline or, alternatively, an 'external blocking solution' containing (in mM) NaCl 130, TEA Cl 3, $CaCl_2$ 1.8, $MgCl_2$ 1, $CdCl_2$ 5, $NiCl_2$ 1, $GdCl_3$ 1, HEPES 5, glucose 10, ouabain 1, in the presence of 30 µM tetrodotoxin, in combination with an 'internal blocking solution', containing (mM) CsMES 120, NaCl 4, $CaCl_2$ 0.02, EGTA 0.1, $MgSO_4$ 1, phosphocreatine 10, ATP-Na_2 3, GTP-Na 0.1, HEPES 10. Solution exchange was performed using gravity flow controlled by pinch valves (Warner Instruments, Hamden, CT). All chemicals were purchased from Sigma Aldrich (St. Louis, MO, USA), except for tetrodotoxin from Tocris.

Capacitance recordings. Capacitance measurements were performed using the 'sine+dc' method[2,4,25,49] implemented as the 'sine 1 dc' feature of the PULSE lock-in module[50]. A sine wave function (1–5 mV peak-to-peak) was superimposed to the holding potential of −70 mV at a frequency of 150–300 Hz corresponding to the C_m sampling rates. To determine changes of membrane capacitance induced by light stimulation in Ziapin2-treated cells, the C_m was first averaged over 500 ms preceding the light stimulus and then subtracted from the peak value induced by the stimulation.

Equivalent circuit simulations. We numerically solved the equivalent circuit as shown in Supplementary Fig. 13, starting from the equilibrium position according to the input parameters $E = -60$ mV, starting capacity $C_m = 30$ pF, $1/g = 300$ MΩ. The resistor–capacitor (RC) time constant of the circuit was 90 µs. In the simulation, we changed C_m in time and calculated the predicted V_m by keeping g constant, according to the experimental observations.

Data analysis. Data were analysed using pCLAMP 10 or FitMaster v2x90.1, together with Prism 6.07 (GraphPad) and OriginPro 9 (OriginLab) softwares.

For further details, see Supplementary Information.

Photostimulation. Illumination of neurons during electrophysiological experiments for both Ziapin2 and ChETA was provided by an LED system (Lumencor Spectra X) fibre-coupled to an upright Nikon FN1 microscope. The light source emission peaked at 470 nm to match the Ziapin2 absorption spectrum and the power density of 20 mW mm^{-2}, as measured at the output of the microscope objective.

In vivo experiments. Surgery: Mice were anaesthetised with isoflurane and placed in a stereotaxic frame, where anaesthesia was maintained with an isoflurane flow. Ziapin2 (200 µM in 1 µl 10% DMSO in phosphate-buffered saline) or vehicle was injected with a 5 µl Hamilton syringe in the primary somatosensory cortex (S1ShNc) of the left hemisphere using the following stereotaxic coordinates: 2 mm anterior to lambda, 2 mm lateral to midline and −723 µm ventral to brain surface. Injection was done at a rate of 100 nl/min with a nano-jector (World Precision Instruments, Fl, USA). Five minutes after, to let the molecules diffuse within brain tissue, the craniotomy was extended by 1 mm laterally and 1 mm medially to accommodate the microwire array (16 electrodes in 2 rows of 8, 33 µm diameter, 250 µm pitch, 375 µm between rows (Tucker Davis Technologies)). The two central microwires were inserted at a depth of 723 µm, before being cleaned with saline and topped with silicone sealant (Kwik-cast, WPI). A hole was drilled 1 mm caudally to the injection hole, and a fibre optic cannula (MFC_400/430-0.66_10 mm_ZF1.25_FLT, Doric Lenses) was inserted at a depth of 1 mm and an angle of 65° from the vertical. Two surgical screws were inserted in the skull contralateral to the implants to be used as reference/ground for the microwires and support. The skull was then covered with dental cement, and diclofenac was systemically administered at a dose of 100 µl/20 g. In vivo recordings: For the evaluation of the acute effects of Ziapin2 loading, in vivo optical stimulations were performed in freely moving C57BL6 mice that had been previously injected with either DMSO ($N = 3$) or Ziapin2 ($N = 3$) and left to recover for 60 min before electrophysiological recordings. Light stimulation was delivered at 0.25 Hz with 40% jitter for either 20 or 200 ms at irradiances of 4, 25, 43 or 116 mW mm^{-2} with a 473 nm laser (Shanghai Dream Lasers) to the freely moving rats. Each condition was repeated 25 times. Extracellular signals in response to stimulation were amplified, digitized and sampled at 1,017 Hz by commercially available hardware (System 3, Tucker-Davis Technologies) before being saved for offline analysis using custom Matlab scripts (The Mathworks). During acquisition, data were high-pass (1 Hz) and low-pass (100 Hz) filtered to extract LFPs. The peak amplitude of the LFP waves, recorded within the correct latency range after the light onset, was normalized by the averaged noise amplitude calculated from the non-responding channels over the same epoch. For the analysis of the persistence of the Ziapin2 effects over time, implanted C57BL6 mice that had been injected with either DMSO ($N = 3$) or Ziapin2 ($N = 4$) at time = 0 were photostimulated and recorded as described above 1, 4 and 7 d after Ziapin2 administration. Mice that received Ziapin2 injection, but were not implanted, were euthanized at the same times after the injection and the brain processed for Ziapin2 fluorescence microscopy and immunohistochemical analysis of astro- and micro-glial reaction.

For further details about numerical model of the PL signal dynamics in solution, total internal fluorescence microscopy, primary neuron preparations, differentiation of human neurons from induced pluripotent stem cells, cell viability assays, fluorescence imaging of the plasma membrane, Immunofluorescence staining and statistical analysis, see Supplementary Information.

Reporting Summary. Further information on research design is available in the Nature Research Reporting Summary linked to this article.

Data availability

The datasets generated and analysed during the current study are available from the corresponding author on reasonable request.

References

41. Jo, S., Kim, T., Iyer, V. G. & Im, W. CHARMM-GUI: a Web-based graphical user interface for CHARMM. *J. Comput. Chem.* **29**, 1859–1865 (2008).
42. Phillips, J. C. et al. Scalable molecular dynamics with NAMD +. *J. Comput. Chem.* **26**, 1781–1802 (2005).
43. Huang, J. & MacKerell, A. D. Jr. CHARMM36 all-atom additive protein force field: validation based on comparison to NMR data. *J. Comput. Chem.* **34**, 2135–2145 (2013).
44. Bennett, W. F. & Tieleman, D. P. Molecular simulation of rapid translocation of cholesterol, diacylglycerol, and ceramide in model raft and nonraft membranes. *J. Lipid Res.* **53**, 421–429 (2012).
45. Maragliano, L. & Vanden-Eijnden, E. A temperature accelerated method for sampling free energy and determining reaction pathways in rare events simulations. *Chem. Phys. Lett.* **426**, 168–175 (2006).
46. Dalla Serra, M. & Menestrina, G. Liposomes in study of pore-forming toxins. *Meth Enzymol.* **372**, 99–124 (2003).
47. Dalla Serra, M. & Menestrina, G. Characterization of molecular properties of pore-forming toxins with planar lipid bilayers. *Meth Mol. Biol.* **145**, 171–188 (2000).
48. Schmitt, B. M. & Koepsell, H. An improved method for real-time monitoring of membrane capacitance in *Xenopus laevis* oocytes. *Biophys. J.* **82**, 1345–1357 (2002).
49. Pusch, M. & Neher, E. Rates of diffusional exchange between small cells and a measuring patch pipette. *Pflug. Arch.* **411**, 204–211 (1988).
50. Gillis, K. D. Admittance-based measurement of membrane capacitance using the EPC-9 patch-clamp amplifier. *Pflug. Arch.* **439**, 655–664 (2000).

Acknowledgements

We thank F. Fruscione and F. Zara (Giannina Gaslini Institute, Genova, Italy) for help in preparing iPSC-derived human neurons; P. Bianchini, M. Oneto and M. Scotto (Center for Nanoscopy and Nikon Imaging Center, Istituto Italiano di Tecnologia, Genova, Italy); L. Cingolani (Center for Synaptic Neuroscience and Technology, Istituto Italiano di Tecnologia, Genova, Italy) for providing the ChETA-encoding lentiviral vectors; A. Mehilli and G. Mantero (Center for Synaptic Neuroscience and Technology, Istituto Italiano di Tecnologia, Genova, Italy) for precious help in primary cultures and in vivo elelectrophysiology, respectively. This work was supported by the Italian Ministry of Health (project RF-2013-02358313 to G.P., G.L. and F.B.) and Istituto Italiano di Tecnologia (pre-startup project to G.L. and F.B.). The support of the Ra.Mo. Foundation (Milano, Italy), Fondazione 13 Marzo (Parma, Italy), Rare Partners srl (Milano, Italy) and Fondazione Cariplo (project 2018-0505) to G.L. and F.B. is also acknowledged.

Author contributions

C.B. designed and engineered Ziapin2. S.C., L.C. and F.O. performed the synthesis and characterization of Ziapin2. D.F. calculated the atomic charges and optimized coordinates. G.M.P. performed the spectroscopic characterization. L.M. performed molecular dynamics simulations. M.D.S., L.L. and M.M. performed planar lipid membrane and AFM studies. M.B., G.G. and E.C. studied the in vitro and in vivo distribution of the Ziapin compounds in neurons. M.L.D.F., P.B., E.C. and F.L. performed the in vitro patch-clamp experiments and analysed the data. V.V. elaborated the numerical RC model. J.F.M-V., E.C., D.S. and C.G.E. performed and analysed the in vivo experiments. M.L.D.F., E.C., P.B., G.M.P. and F.L. contributed to paper writing. G.L., C.B. and F.B. conceived the work. G.L. and F.B. planned the experiments, analysed the data and wrote the manuscript.

Competing interests

The authors declare no competing interests.

Additional information

Supplementary information is available for this paper at https://doi.org/10.1038/s41565-019-0632-6.

Correspondence and requests for materials should be addressed to G.L. or F.B.

Peer review information *Nature Nanotechnology* thanks Or Shemesh, Joao L. Carvalho-de-Souza and the other, anonymous, reviewer(s) for their contribution to the peer review of this work.

Reprints and permissions information is available at www.nature.com/reprints.

ADVANCED SCIENCE
Open Access
www.advancedscience.com

Membrane Environment Enables Ultrafast Isomerization of Amphiphilic Azobenzene

Giuseppe Maria Paternò, Elisabetta Colombo, Vito Vurro, Francesco Lodola, Simone Cimò, Valentina Sesti, Egle Molotokaite, Mattia Bramini, Lucia Ganzer, Daniele Fazzi, Cosimo D'Andrea, Fabio Benfenati, Chiara Bertarelli, and Guglielmo Lanzani**

The non-covalent affinity of photoresponsive molecules to biotargets represents an attractive tool for achieving effective cell photo-stimulation. Here, an amphiphilic azobenzene that preferentially dwells within the plasma membrane is studied. In particular, its isomerization dynamics in different media is investigated. It is found that in molecular aggregates formed in water, the isomerization reaction is hindered, while radiative deactivation is favored. However, once protected by a lipid shell, the photochromic molecule reacquires its ultrafast photoisomerization capacity. This behavior is explained considering collective excited states that may form in aggregates, locking the conformational dynamics and redistributing the oscillator strength. By applying the pump probe technique in different media, an isomerization time in the order of 10 ps is identified and the deactivation in the aggregate in water is also characterized. Finally, it is demonstrated that the reversible modulation of membrane potential of HEK293 cells via illumination with visible light can be indeed related to the recovered trans→cis photoreaction in lipid membrane. These data fully account for the recently reported experiments in neurons, showing that the amphiphilic azobenzenes, once partitioned in the cell membrane, are effective light actuators for the modification of the electrical state of the membrane.

The precise, fast, and efficient spatiotemporal control of cellular signaling via the use of external triggers has become an important topic in chemical biology[1] and photopharmacology.[2,3] In this regard, light-responsive systems offer the possibility to employ light as a clean, non-invasive, and spatio-temporally precise tool for controlling a variety of biological signals both in vitro and in vivo.[4–9] A plethora of photochromic systems allowing modulation of molecular responses in a reversible fashion have been developed.[10,11] Among them, azobenzenes[12] are widely employed as versatile photoresponsive element for conferring reversible sensitivity to bio(inspired) targets and drugs, such as artificial membranes,[13–15] peptides,[16,17] nucleic acids,[18,19] ion channels,[20,21] living organisms,[22] and antibacterial molecules.[23–25] These studies have demonstrated that effective and reversible photomodulation can be achieved both in vitro and in vivo, by the covalent binding of the azobenzene unit to the selected target. Alternatively, one can exploit non-covalent interactions to assist the incorporation of photoactive molecules in bio-systems.[26–30] Although this method is less specific than the covalent approach, the relatively weak non-covalent interactions still allow for driving affinity to various bio-interfaces, while ensuring full

Dr. G. M. Paternò, V. Vurro, Dr. F. Lodola, Dr. E. Molotokaite, Prof. C. D'Andrea, Prof. G. Lanzani
Center for Nano Science and Technology
Istituto Italiano di Tecnologia
Via Pascoli 70/3, 20133 Milano, Italy
E-mail: guglielmo.lanzani@iit.it

Dr. E. Colombo, Dr. M. Bramini, Prof. F. Benfenati
Center for Synaptic Neuroscience and Technology
Istituto Italiano di Tecnologia
Largo Rosanna Benzi 10, 16132 Genova, Italy

Dr. E. Colombo, Dr. M. Bramini, Prof. F. Benfenati
IRCCS Ospedale Policlinico San Martino
Largo Rosanna Benzi 10, 16132, Genova, Italy

The ORCID identification number(s) for the author(s) of this article can be found under https://doi.org/10.1002/advs.201903241.

DOI: 10.1002/advs.201903241

V. Vurro, Dr. L. Ganzer, Prof. C. D'Andrea, Prof. G. Lanzani
Dipartimento di Fisica
Politecnico di Milano
Piazza L. da Vinci 32, 20133 Milano, Italy

S. Cimò, V. Sesti, Prof. C. Bertarelli
Dipartimento di Chimica
Materiali e Ingegneria Chimica "Giulio Natta"
Politecnico di Milano
Piazza L. da Vinci 32, 20133 Milano, Italy
E-mail: chiara.bertarelli@polimi.it

Dr. D. Fazzi
Department of Chemistry
Institut für Physikalische Chemie
University of Cologne
Luxemburger Str. 116, D-50939 Köln, Germany

Dr. M. Bramini
Department of Applied Physics
Faculty of Sciences
University of Granada
C/Fuentenueva s/n 18071, Granada, Spain

reversibility and much lower invasiveness. For instance, the ability of amphiphilic azobenzenes to intercalate spontaneously in model artificial membranes and micelles has been used to guide their internalization into these systems, mostly to study intrinsic membrane properties,[15,31] to build up photoresponsive cargos for drug delivery applications,[32,33] or to provide novel antibacterial systems.[25] Very recently a new amphiphilic azobenzene molecule named ZIAPIN2 has been introduced. ZIAPIN2 predominantly localizes in the plasma membrane and potently modulates neuronal firing in vitro as well in vivo via an opto-mechanical effect.[34] In order to fully characterize the photostimulation mechanism of ZIAPIN2, here we report a detailed investigation of its photophysics and dynamics in different media. By combining steady-state and time-resolved optical spectroscopies, we observed that ZIAPIN2 in water lends itself to a radiative transition likely mediated by the formation of excimers, whereas it reacquires its conformational dynamics in membrane-mimicking environments. Characteristic time scales and reaction yields are reported, reconciling the fast response (ms) observed in functional studies and the apparent slow ensemble evolution(s) by determining the molecular conversion time in the tens of picosecond range. Finally, we validate this opto-mechanical phenomenon in a non-excitable cell line that has an intrinsically low concentration of ion channels, to single out the effect on the plasma membrane itself.

ZIAPIN2 was synthesized by reduction of the commercially available Disperse Orange 3 followed by the substitution of the amines with an excess of 1,6-dibromohexane. Full details about the synthesis can be found in ref. [34] and Supporting Information. The molecular structures and electronic transition energies of ZIAPIN2 were computed at the density functional theory (DFT) and time-dependent density functional theory (TDDFT) level (see Supporting Information), for both trans and cis isomers (**Figure 1**a). The trans species shows a quasi-planar structure with a dihedral angle between the phenyl rings of 14°; the cis shows a distorted structure, with a dihedral angle of 46°. The computed vertical transition energies well agree with the experimental UV–vis absorption spectra reported in Figure 1b. In vacuum, the trans species shows a vertical (i.e., Franck–Condon region) dipole active excited state at 430 nm ($f = 1.33$) featuring an n–π^* character with molecular orbitals delocalized over the azobenzene moiety. The cis species shows two vertical dipole active excited states computed at 537 nm ($f = 0.18$) and 367 nm ($f = 0.33$), associated with the n–π^* and π–π^* transitions, respectively. Note that the diamino substitution induces a red shift of the optical gap with respect to the unsubstituted azobenzene that is favorable to biological applications. As discussed in the following sections, the addition of water induces a broadening and a red-shift of the absorption spectrum of the trans species. To a first approximation, we performed DFT/conductor-like polarizable continuum model calculations on the single molecule. Considering water as a solvent, two active states are computed at 456 nm ($f = 1.34$) and 436 nm ($f = 0.15$), the former being red-shifted by 26 nm with respect to the active state in the vacuum case. We preliminary speculate that such a shift in the ground state absorption might be related to the solvent cage (in this case water) that can play a role in the molecular conformation. As shown later, however, modeling at the single molecule level is not sufficient to fully account for the observed phenomena.

We used UV–vis absorption and photoluminescence (PL) spectroscopies to investigate the behavior of ZIAPIN2 in the following media: i) DMSO that is a good solvent, as a control medium and vector for ZIAPIN2; ii) water that is the main component of extracellular and intracellular media; and iii) micelles of sodium dodecyl sulfate (SDS) to mimic the lipid bilayer environment.[34–36] The latter is useful for steady-state and transient absorption measurements (vide infra) that are difficult to perform in intact cells. We selected SDS as it spontaneously forms mixed micelles upon combination with single-tailed surfactants with oppositely charged head groups.[32,37,38] In the UV–vis absorption spectra (Figure 1b), we observe a large bathochromic shift when passing from DMSO to water (22 nm), in good agreement with the 26 nm shift computed at the TDDFT level, accompanied by the vanishing of the vibronic structure. On the other hand, suspension of ZIAPIN2 in the SDS micellar dispersion shows a reduced spectral shift and a marked recovery of the vibronic structure (peaking at 444 and 422 nm), which can be assigned to a more rigid conformation adopted by the azobenzene upon interaction with the alkyl chains of the surfactant.[39] PL spectra (Figure 1c) are more sensitive to the local environment as emission occurs after re-equilibration within the solvent cage. Accordingly, PL spectra reveal dramatic changes in both spectral position and relative emission quantum yield. Interestingly, we note the development of a new red-shifted and structureless PL band centered at 600 nm upon addition of water to the DMSO solution (Figure 1c and Figure S1a, Supporting Information), affording progressively higher relative intensity than in DMSO (up to almost one order of magnitude). Such a behavior, alongside the progressive and marked increase of the Stokes shift (100 nm; Figure S1b, Supporting Information) cannot be explained either by solvatochromic effects[40–42] or by TDDFT calculations performed on the single molecule level, and possibly indicates the occurrence of an excited state process. Interestingly, a propensity for ZIAPIN2 to aggregate in an anti-parallel stacking dimer configuration is computed by using semi empirical tight-binding quantum-chemical calculations (i.e., geometry, frequency, noncovalent, extended TB method;[43] see Supporting Information), carried out on ZIAPIN2 dimer in trans conformation. Semi-empirical excited state vertical transition energies (e.g., zerner's intermediate neglect of differential overlap level) were computed on the optimized dimer, resulting in an in- (i.e., high energy) and out-of-phase (i.e., low energy) splitting of the monomer bright state (see Figure S2, Supporting Information). Calculations for the Kasha-like dimer indicate the presence of a red-shifted and radiative active state that could be responsible for the enhanced emission at 600 nm. On the other hand, such a broad, structureless, and highly Stokes shifted PL band might also originate from an excimer.[44,45] The propensity to aggregate is further confirmed by scanning electron microscopy (SEM) images taken on azobenzene solid films drop-cast from water solution (Figure S3a,b, Supporting Information), which show the presence of circular micelle-like micron-sized clusters. Conversely, when SDS is added to the aqueous buffer, ZIAPIN2 emission peaks at 570 nm, and features a threefold decrease in the relative emission intensity if compared to the water solution, suggesting that it could reacquire its non-radiative pathway. As a reference, we acquired absorption and PL spectra in the culture medium (Dulbecco's modified

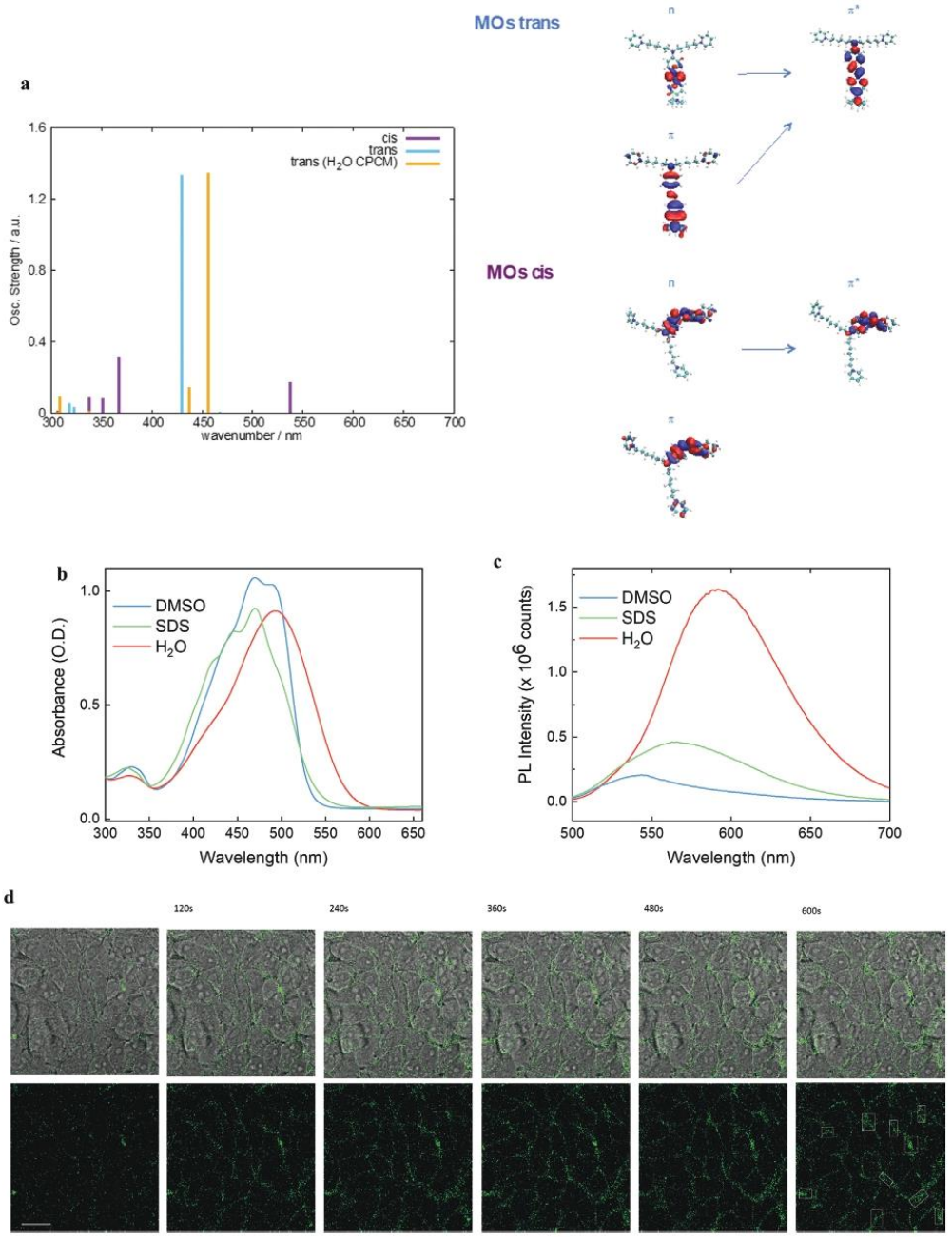

Figure 1. a) Computed UV–vis electronic transition and molecular structures for trans and cis ZIAPIN2 at the DFT and TDDFT level of theory (see Supporting Information for details). b) UV–vIS and c) PL spectra of ZIAPIN2 in DMSO, SDS 100 mM, and water (25 μM). PL spectra were normalized to both lamp intensity and ground state absorption, to obtain a relative PL quantum yield among the three solutions. d) Time-lapse bright-field and fluorescence confocal images of ZIAPIN2 (in DMSO 25 μM) loading in HEK293 cells (scale bar = 50 μm).

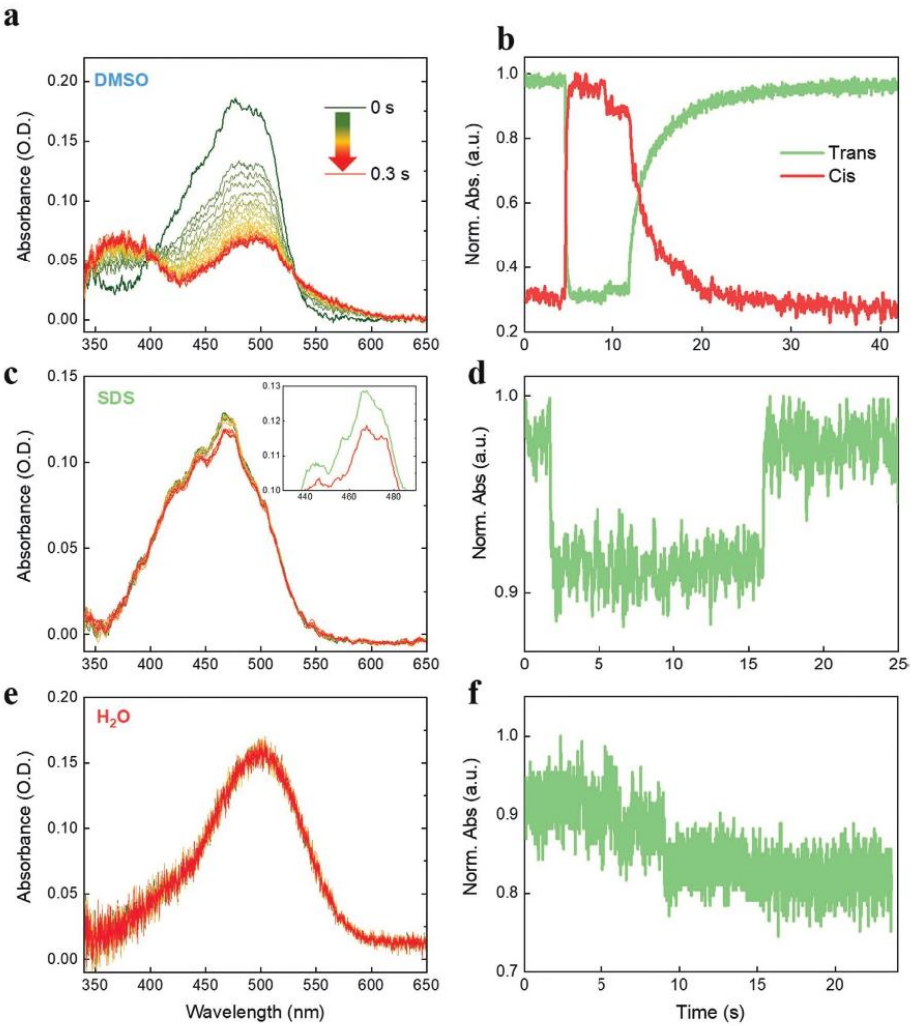

Figure 2. UV–vis absorption spectra of ZIAPIN2 in a) DMSO, c) SDS (100 mM), and e) water taken under illumination with a blue LED (470 nm). The inset in Figure 2c highlights the 10% decay in the trans absorption of ZIAPIN2 in SDS. Isomerization kinetics of ZIAPIN2 in DMSO taken at b) 490 nm, d) SDS (100 mM), and f) water as a function of illumination time.

Eagle's medium, see Supporting Information for cell culturing), which also display a clear red-shift of absorption/emission of ZIAPIN2 with respect to DMSO and SDS buffer (Figure S4, Supporting Information), suggesting that ZIAPIN2 aggregation is also occurring in such aqueous medium. Time-lapse confocal imaging on living HEK293 cells loaded with ZIAPIN2 in DMSO (Figure 1d) confirms the affinity of the molecule for lipid bilayers and its dynamics of incorporation. The sequence of bright-field and fluorescence images (488 nm excitation, 500–700 nm emission) demonstrates an increase in signal intensity at cell membrane level lasting approximately 7 min, and subsequently reaching a stable plateau (see Figure S5a,b, Supporting Information, for the 3D z-stack images of ZIAPIN2 fluorescence in HEK293 cells and co-localization data, and Figure S5c, Supporting Information, for the fluorescence intensity evolution during time-lapse acquisitions).

Steady-state absorption measurements of ZIAPIN2 in solution under an actinic light allow the assessment of the ensemble dynamics of isomerization. In **Figure 2**a,c,e, we present the absorption spectra of ZIAPIN2 under illumination with a blue LED (470 nm), alongside the photoswitching dynamics in DMSO, SDS 100 mM, and water (Figure 2b,d,f). In DMSO (Figure 2a,b), we observe a trans→cis isomerization reaction that leads to a cis-rich photostationary state in 200 ms (extracted

time constant τ = 60 ms) and a thermal cis→trans back relaxation that is completed in ≈20 s (τ = 3 s). The presence of the cis species is confirmed by the rising of the two absorption bands at 370 and 550 nm (Figure 2a), in good agreement with TDDFT calculations. Standard rate-equations allow extracting an isomerization rate $K = 4 \times 10^3$ cm^2 J^{-1}. This is indeed a measure of the trans-isomer absorption cross-section normalized by photon energy, yielding a value of 2×10^{-15} cm^2. This value is consistent with the direct evaluation by standard transmission measurements, validating the isomerization experiments. The thermal rate of back conversion from cis to trans is 0.06 s^{-1}. The absorption band centered at 500 nm accounts for the residual trans population (30%). In water (Figure 2e,f), ZIAPIN2 photoisomerization is totally suppressed, likely owing to the formation of micellar aggregates that hinder molecular switching. In SDS (Figure 2c,d), however, we see a recovery of the fast photoswitching ability (τ = 60 ms), although the photostationary state contains only 10% of the cis isomer (Figure 2a and inset). The reason of such decreased isomerization yield in SDS compared to DMSO can be ascribed to the convolution of two effects, namely: i) ZIAPIN2 molecules are not fully incorporated by SDS, with a fraction remaining in water and forming non-isomerizing aggregates; ii) a more constrained conformational freedom experienced by ZIAPIN2 inside the micellar environment than when solubilized in DMSO.[32] The time-dependent quenching of trans isomer PL upon illumination is an alternative proof of the isomerization reaction, based on the notion that isomerization competes with radiative recombination and the cis isomer is poorly or non-emitting.[34] This opens up the possibility to follow photoisomerization in biological media where absorption measurements, due to high scattering and reduced optical density, would not be feasible. Therefore, we recorded the isomerization reaction also in HEK293 living cells treated with 25 μM ZIAPIN2 by using a micro-PL set-up. The PL images (Figure S6a,b, Supporting Information) indicate that the photoinduced PL quenching occurs almost totally in the membrane region, while residual ZIAPIN2 molecules present in the aqueous extracellular buffer do not seem to undergo isomerization. This confirms that lipid environment allows restoration of ZIAPIN2 photoswitching ability.

In electrophysiology experiments, neurons reacted to short burst of light, between 20 and 200 ms. The prompt response seems in contradiction with the time evolution measured in solution, taking place in seconds. One should however notice that steady-state measurements allow accessing the isomer fraction population in the ensemble. In order to gain insights into the molecular isomerization event (expected to occur in the picosecond time scale[12]) it is necessary to employ ultrafast techniques.[46] We carry out a transient absorption (TA) experiment where a pump pulse brings population to the excited state, while a broadband probe pulse interrogates this state and tracks its temporal evolution. With this technique, we studied the ZIAPIN2 photodynamics in the three media of choice, namely water, DMSO, and SDS. The TA spectra at early delay-times (i.e., pump-probe delay 1 ps, **Figure 3**a) in all three media shows three main features: i) a positive peak centered at 470–500 nm that can be attributed to ground state bleaching ($S_0 \rightarrow S^*$, PB); ii) another positive peak at 570–610 nm that can be linked to stimulated emission ($S^* \rightarrow S_0$, SE), and iii) a negative feature at around 700 nm due to photoinduced absorption from excited states ($S^* \rightarrow S_n$, PA). To obtain quantitative insights into the complex convolution of the trans and cis spectra, we employed a global analysis algorithm. We describe our experimental data with two components (Figure 3b,c), with different decay associated spectra (DAS) and kinetics. In DMSO and SDS, the photodynamics is well consistent with the isomerization reaction,[12] in which the first component is the trans isomer that decays (τ = 6 and 12 ps for DMSO and SDS, respectively) into the second component, the long-living cis isomer metastable state (3 and 6 ns for DMSO and SDS, respectively). Conversely, in water, the first component evolves rapidly (τ = 2 ps) into a second red-shifted component (about 30 nm) with a relatively short lifetime (τ = 20 ps). This latter scenario can be consistent with the photoinduced formation of excimers[44] within the micellar aggregates. The first component can be related to the trans isomer that decays in the excimeric red-shifted state (second component) via vibrational relaxation. The second component is therefore assigned to the excimer state. This photophysics landscape (see Figure 3f for a sketch) is corroborated by the experimental transient dynamics at probe wavelengths corresponding to ground state bleaching (PB at 500–520 nm, Figure 3d) and at 550–580 nm (Figure 3e). The former shows an almost complete extinction of the PB signal in water due to rapid ground state re-population, while the latter highlights both the long-living nature of the photogenerated cis species in DMSO and SDS and the fast (20 ps) deactivation of the excimeric state in water. By working out the intrinsic radiative lifetime of 1.5 ns using the Strickler–Berg relation[47] and assuming isomerization as the only non-radiative decay pathway, we can estimate that the PL quantum yield (PLQY) in DMSO and SDS should not exceed 0.4% and 0.8%, respectively. This is in good agreement with the experimental data, as reported in Figure 1c, suggesting a ratio $PLQY_{DMSO}/PLQY_{SDS}$ = 0.43. On the other hand, the significant deviation between the expected ratio $PLQY_{DMSO}/PLQY_{H2O}$ (0.3) and the experimental value (0.12) for ZIAPIN2 in water (i.e., the enhanced PLQY in water) confirms the kicking in of a different deactivation mechanism in the aqueous buffer. We assign the breakdown of the Strickler–Berg rule to the formation of an aggregate excited state, possibly an excimer, with higher radiative rate. The findings in SDS are consistent with our steady-state spectroscopic data and suggest that ZIAPIN2 performs ultrafast isomerization reaction in membrane. The tiny changes observed in the ensemble measurements in SDS/cells are likely due to the presence of a mixed population in which only a fraction of ZIAPIN2 molecules is protected by water.

To further investigate the biological effect previously demonstrated in neurons both in vitro and in vivo,[34] here we study the photoreaction in a model system, namely non-excitable HEK293 cells. These have an intrinsically low concentration of ion channels that enables to probe the opto-mechanical effect on the cell membrane free from other effects possibly present in neurons. We proceed by loading with a DMSO/water solution of ZIAPIN2 (25 μM) in HEK293 cells, which represent a well-established cellular model. Possible cytotoxicity of ZIAPIN2 was evaluated by using the Alamar Blue standard test, which indicates that exposure to ZIAPIN2 does not have an appreciable impact on cell proliferation (Figure S7, Supporting Information). We measured

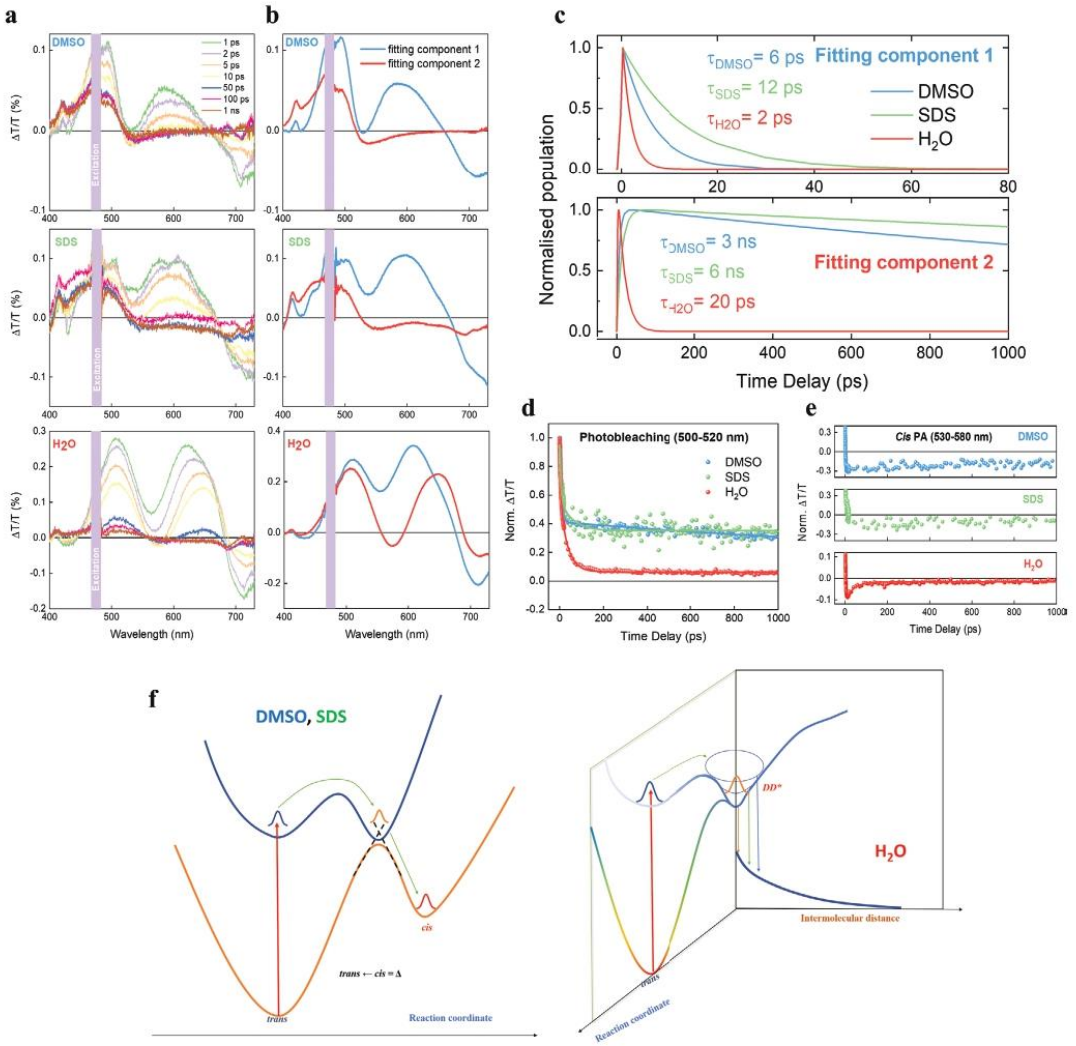

Figure 3. a) TA spectra in DMSO (top panel), SDS (100 mM, central panel) and water (bottom panel). The system was excited at 470 nm (π–π^*) and probed with a white light super continuum. The three solutions (25 µM) were flowed by means of a peristaltic pump, to permit relaxation from the cis state. b) Global analysis of the experimental TA spectra into two fitting components. The first and second components observed in DMSO and SDS can be associated with the trans and cis isomer spectra, respectively. In H_2O, this latter component can be linked to the excimer formation. c) Population evolution (normalized) of the two SVD components in DMSO, SDS, and H_2O. d) TA experimental dynamics of ZIAPIN2 in DMSO, SDS 100 mM, and H_2O (25 µM) excited at 470 nm and probed in the photobleaching region (500–520 nm) and e) in the 530–580 nm region. Solid lines represent the best-fit of the experimental data. f) Sketch of the photodynamics in DMSO, SDS, and water as suggested by the TA data.

the light-induced change in the resting plasma membrane potential (V_m) by applying the patch-clamp technique in current clamp mode ($I = 0$) (Figure S8, Supporting Information). In agreement with what has been found in neuronal cells,[34] photostimulation of ZIAPIN2-loaded HEK293 cells with either short (20 ms) or long (200 ms) visible light pulses (470 nm, 50 mW mm^{-2}) also generated a significant hyperpolarization of V_m that appeared immediately at the light onset and slowly returned to the physiological resting values after a slight rebound depolarization phase after the light offset (Figure S8a,b, Supporting Information). In our previous study, we have assigned this potential modulation to a photoinduced thinning/thickening of the cell membrane leading to an increase/decrease of the membrane capacitance.[34] To link ultimately such an effect to the ZIAPIN2

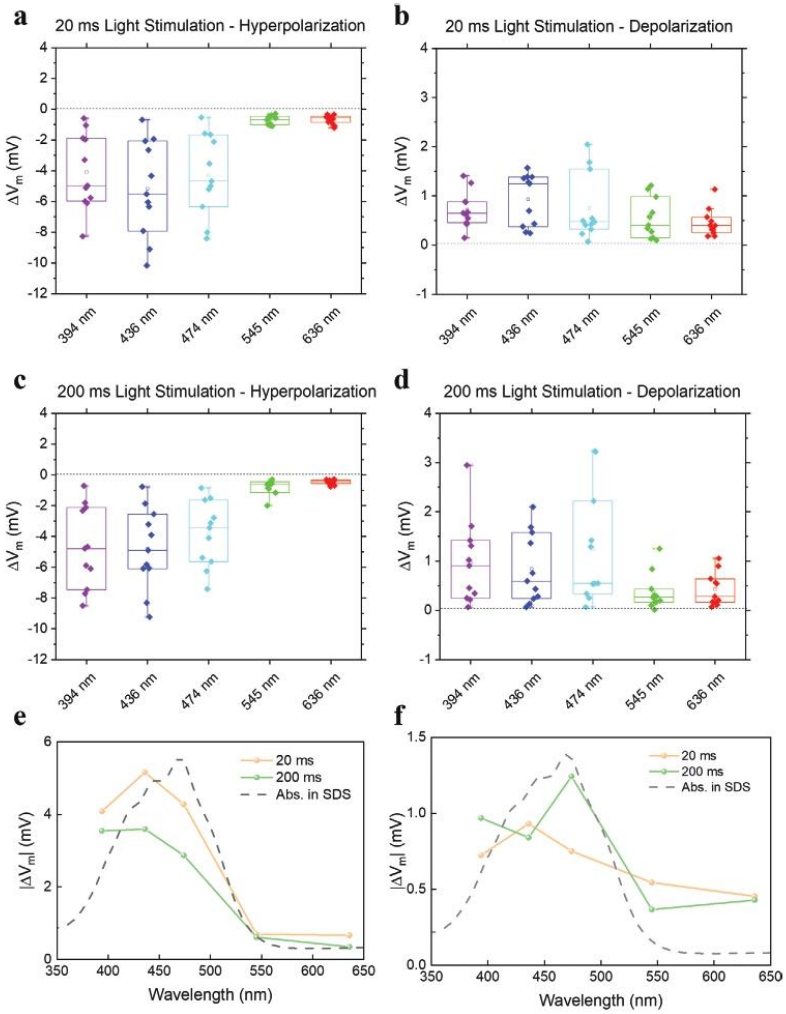

Figure 4. a–d) Box plots of the parameters investigated for voltage membrane modulation analysis as a function of illumination wavelength. Hyperpolarization (a,c) and depolarization (b,d) changes of HEK293 cells or exposed to DMSO/ZIAPIN2, subjected to 20 or 200 ms light stimulation ($n = 14$, 18, 20 for CTRL, DMSO, and ZIAPIN2, respectively). Hyperpolarization and depolarization were measured as the minimum and maximum voltage, respectively, reached within 350 ms from the light-onset. e,f) Action spectrum versus wavelength of the $|\Delta V|$ of hyperpolarization (e) and depolarization (f) in HEK293 treated with 25 µM ZIAPIN2, for both short (20 ms) and long (200 ms) light stimuli. We also report the absorption spectrum of ZIAPIN2 in SDS for comparison (dotted grey line). All experiments were carried out at 24 ± 1 °C. $^{**}p < 0.01$; $^{***}p < 0.001$; $^{****}p < 0.0001$, Kruskal–Wallis test.

ultrafast photoreaction occurring in the membrane environment, we therefore recorded the $|\Delta V_m|$ of hyperpolarization and depolarization as a function of the illumination wavelength for 20 and 200 ms light stimulation (**Figure 4**c–f). Remarkably, we observed an almost perfect overlap of $|\Delta V_m|$ with the absorption spectrum of ZIAPIN2 in SDS micelles, further confirming that the light-induced modulation of V_m is indeed related to the trans→cis photoreaction enabled by ZIAPIN2 internalization in the plasma membrane.

To summarize, the observed aggregation of photochromic molecules in water, where they lose their ability to photoisomerize, might represent an impediment to their application in biology as water is the main component of biological environments. However, here we find that it is not true if the molecules have a preferential affinity for the cell membrane. In particular, we show that an amphiphilic azobenzene (ZIAPIN2) with noncovalent affinity for cell membranes can act as an efficient, fast, and reversible modulator of the membrane potential via

visible light. By applying steady-state and time-resolved ultrafast spectroscopies, we note that in water a strong aggregation occurs, effectively hampering photoisomerization and opening up a deactivation path likely mediated by excimer formation. Alternatively, internalization in the cell membrane prevents self-aggregation and restores the intrinsic ultrafast response of the photo switch. This, ultimately allows light-triggering a large hyperpolarization in HEK293 cells whose magnitude follows the absorption profile of the trans state in membrane and, remarkably, permits evoking biological photoinduced effects in vivo.[34] Such actuators are new tools that could contribute to the development of opto-neuroscience, biophotonics, and photopharmacology.

Supporting Information

Supporting Information is available from the Wiley Online Library or from the author.

Acknowledgements

G.M.P. and E.C. contributed equally to this work. G.M.P. acknowledges the financial support from Fondazione Cariplo, grant no. 2018-0979. The authors thank the financial support from the EU Horizon 2020 Research and Innovation Programme under Grant Agreement No. 643238 (SYNCHRONICS). The authors also thank Dr. Daniele Viola for helping with the analysis of the TA data.

Conflict of Interest

The authors declare no conflict of interest.

Keywords

amphiphilic, azobenzene, cell membranes, cell stimulation, ultrafast isomerization

Received: November 14, 2019
Revised: January 24, 2020
Published online: March 6, 2020

[1] A. A. Beharry, G. A. Woolley, *Chem. Soc. Rev.* **2011**, *40*, 4422.
[2] W. A. Velema, W. Szymanski, B. L. Feringa, *J. Am. Chem. Soc.* **2014**, *136*, 2178.
[3] G. Cabré, A. Garrido-Charles, M. Moreno, M. Bosch, M. Porta-de-la-Riva, M. Krieg, M. Gascón-Moya, N. Camarero, R. Gelabert, J. M. Lluch, F. Busqué, J. Hernando, P. Gorostiza, R. Alibés, *Nat. Commun.* **2019**, *10*, 907.
[4] W. Szymański, J. M. Beierle, H. A. V. Kistemaker, W. A. Velema, B. L. Feringa, *Chem. Rev.* **2013**, *113*, 6114.
[5] M. R. Antognazza, N. Martino, D. Ghezzi, P. Feyen, E. Colombo, D. Endeman, F. Benfenati, G. Lanzani, *Adv. Mater.* **2015**, *27*, 7662.
[6] J. F. Zimmerman, B. Tian, *ACS Nano* **2018**, *12*, 4086.
[7] H. Acarón Ledesma, X. Li, J. L. Carvalho-de-Souza, W. Wei, F. Bezanilla, B. Tian, *Nat. Nanotechnol.* **2019**, *14*, 645.
[8] A. Splendiani, L. Sun, Y. Zhang, T. Li, J. Kim, C. Y. Chim, G. Galli, F. Wang, *Nano Lett.* **2010**, *10*, 1271.
[9] S. Chen, *Science* **2019**, *365*, 456.
[10] J. Zhang, J. Wang, H. Tian, *Mater. Horiz.* **2014**, *1*, 169.
[11] P. Gorostiza, E. Y. Isacoff, *Science* **2008**, *322*, 395.
[12] H. M. D. Bandara, S. C. Burdette, *Chem. Soc. Rev.* **2012**, *41*, 1809.
[13] M. Albota, D. Beljonne, J. L. Brédas, J. E. Ehrlich, J. Y. Fu, A. A. Heikal, S. E. Hess, T. Kogej, M. D. Levin, S. R. Marder, D. McCord-Maughon, J. W. Perry, H. Röckel, M. Rumi, G. Subramaniam, W. W. Webb, X. L. Wu, C. Xu, *Science* **1998**, *281*, 1653.
[14] D. Balasubramanian, S. Subramani, C. Kumar, *Nature* **1975**, *254*, 252.
[15] H. Fujiwara, Y. Yonezawa, *Nature* **1991**, *351*, 724.
[16] A. A. Beharry, L. Wong, V. Tropepe, G. A. Woolley, *Angew. Chem., Int. Ed.* **2011**, *50*, 1325.
[17] G. A. Woolley, *Acc. Chem. Res.* **2005**, *38*, 486.
[18] M. Zhou, X. Liang, T. Mochizuki, H. Asanuma, *Angew. Chem., Int. Ed.* **2010**, *49*, 2167.
[19] U. Kusebauch, S. A. Cadamuro, H. J. Musiol, M. O. Lenz, J. Wachtveitl, L. Moroder, C. Renner, *Angew. Chem., Int. Ed.* **2006**, *45*, 7015.
[20] M. Volgraf, P. Gorostiza, R. Numano, R. H. Kramer, E. Y. Isacoff, D. Trauner, *Nat. Chem. Biol.* **2006**, *2*, 47.
[21] M. Schönberger, M. Althaus, M. Fronius, W. Clauss, D. Trauner, *Nat. Chem.* **2014**, *6*, 712.
[22] C. Wyart, F. Del Bene, E. Warp, E. K. Scott, D. Trauner, H. Baier, E. Y. Isacoff, *Nature* **2009**, *461*, 407.
[23] W. A. Velema, J. P. Van Der Berg, M. J. Hansen, W. Szymanski, A. J. M. Driessen, B. L. Feringa, *Nat. Chem.* **2013**, *5*, 924.
[24] M. Wegener, M. J. Hansen, A. J. M. Driessen, W. Szymanski, B. L. Feringa, *J. Am. Chem. Soc.* **2017**, *139*, 17979.
[25] X. Fu, H. Bai, R. Qi, H. Zhao, K. Peng, F. Lv, L. Liu, S. Wang, *Chem. Commun.* **2019**, *55*, 14466.
[26] H. Yan, C. Catania, G. C. Bazan, *Adv. Mater.* **2015**, *27*, 2958.
[27] L. E. Garner, J. Park, S. M. Dyar, A. Chworos, J. J. Sumner, G. C. Bazan, *J. Am. Chem. Soc.* **2010**, *132*, 10042.
[28] C. Zhou, G. W. N. Chia, J. C. S. Ho, T. Seviour, T. Sailov, B. Liedberg, S. Kjelleberg, J. Hinks, G. C. Bazan, *Angew. Chem., Int. Ed.* **2018**, *57*, 8069.
[29] B. Wang, B. N. Queenan, S. Wang, K. P. R. Nilsson, G. C. Bazan, *Adv. Mater.* **2019**, *31*, 1806701.
[30] C. Zhou, G. W. N. Chia, J. C. S. Ho, A. S. Moreland, T. Seviour, B. Liedberg, A. N. Parikh, S. Kjelleberg, J. Hinks, G. C. Bazan, *Adv. Mater.* **2019**, *31*, 1808021.
[31] T. Sato, M. Kijima, Y. Shiga, Y. Yonezawa, *Langmuir* **1991**, *7*, 2330.
[32] S. Geng, Y. Wang, L. Wang, T. Kouyama, T. Gotoh, S. Wada, J. Y. Wang, *Sci. Rep.* **2017**, *7*, 1.
[33] C. Yao, P. Wang, X. Li, X. Hu, J. Hou, L. Wang, F. Zhang, *Adv. Mater.* **2016**, *28*, 9341.
[34] M. L. DiFrancesco, F. Lodola, E. Colombo, L. Maragliano, G. M. Paterno, M. Bramini, S. Cimo, L. Colella, D. Fazzi, C. G. Eleftheriou, J. F. Maya-Vetencourt, C. Bertarelli, G. Lanzani, F. Benfenati, *bioRxiv* **2019**, 711077.
[35] J. H. Fendler, *Acc. Chem. Res.* **1980**, *13*, 7.
[36] D. V. Tulumello, C. M. Deber, *Biochemistry* **2009**, *48*, 12096.
[37] E. W. Kaler, A. K. Murthy, B. E. Rodriguez, J. A. N. Zasadzinski, *Science* **1989**, *245*, 1371.
[38] F. P. Hubbard, G. Santonicola, E. W. Kaler, N. L. Abbott, *Langmuir* **2005**, *21*, 6131.
[39] K. Kano, Y. Tanaka, T. Ogawa, M. Shimomura, T. Kunitake, *Photochem. Photobiol.* **1981**, *34*, 323.
[40] J. Bahrenburg, K. Röttger, R. Siewertsen, F. Renth, F. Temps, *Photochem. Photobiol. Sci.* **2012**, *11*, 1210.

[41] G. M. Paternò, N. Barbero, S. Galliano, C. Barolo, G. Lanzani, F. Scotognella, R. Borrelli, *J. Mater. Chem. C* **2018**, *6*, 2778.
[42] G. M. Paternò, L. Moretti, A. J. Barker, C. D'Andrea, A. Luzio, N. Barbero, S. Galliano, C. Barolo, G. Lanzani, F. Scotognella, *J. Mater. Chem. C* **2017**, *5*, 7732.
[43] S. Grimme, C. Bannwarth, P. Shushkov, *J. Chem. Theory Comput.* **2017**, *13*, 1989.
[44] J. B. Birks, *Nature* **1967**, *214*, 1187.
[45] P. Sierocki, H. Maas, P. Dragut, G. Richardt, F. Vogtle, L. De Cola, F. Brouwer, J. I. Zink, *J. Phys. Chem. B* **2006**, *110*, 24390.
[46] A. Nenov, R. Borrego-Varillas, A. Oriana, L. Ganzer, F. Segatta, I. Conti, J. Segarra-Marti, J. Omachi, M. Dapor, S. Taioli, C. Manzoni, S. Mukamel, G. Cerullo, M. Garavelli, *J. Phys. Chem. Lett.* **2018**, *9*, 1534.
[47] S. J. Strickler, R. A. Berg, *J. Chem. Phys.* **1962**, *37*, 814.

14. REFERENCES

[1] P. Castesana e S. E. Puliafito, «Bottom-Up Analysis of Energy Consumption and Carbon Emissions, with Particular Emphasis on Human Capital Investment,» *Low Carbon Economy,* vol. 4, pp. 1-13, 2013.

[2] G. S. Becker, K. M. Murphy e R. Tamura, «Human Capital, Fertility, and Economic Growth,» *Journal of Political Economy,* vol. 98, n. 5, pp. 12-37, 1990.

[3] C. I. Jones, «R & D-Based Models of Economic Growth,» *Journal of Political Economy,* vol. 103, n. 4, pp. 759-784 , 1995.

[4] E. Puliafito, J. Puliafito e M. C. Grand, «Modeling population dynamics and economic growth as competing species: An application to CO2 global emissions,» *Ecological Economics,* vol. 65, n. 3, pp. 602-615, 2008.

[5] J. G. Canadell, C. L. Quéré, M. R. Raupach, C. B. Field, E. T. Buitenhuis, P. Ciais, T. J. Conway, N. P. Gillett, R. A. Houghton e G. Marland, «Contributions to accelerating atmospheric CO2 growth from economic activity, carbon intensity, and efficiency of natural sinks,» *Proceedings of the National Academy of Sciences of the United States of America,* vol. 104, n. 47, pp. 18866-18870, 2007.

[6] Y. Kaya, «Impact of carbon dioxide emission control on GNP growth: interpretation of proposed scenarios,» in *IPCC Energy and Industry Subgroup*, Paris, 1990.

[7] «Eurostat: Statistics Explained,» [Online]. Available: https://ec.europa.eu/eurostat/statistics-explained/index.php/Glossary:Carbon_dioxide_equivalent.

[8] T. E. P. A. T. C. O. T. E. Union, «Regulation (EU) No 517/2014 Of The European Parliment And Of The Council of 16 April 2014 on fluorinated greenhouse gases and repealing Regulation (EC) No 842/2006,» 2014.

[9] I. P. o. C. C. (IPCC), «Fourth Assessment Report (AR4),» 2007.

[10] P. F. e. al., «Global Carbon Budget 2020,» *Earth System Science Data,* vol. 12, p. 3270, 2020.

[11] «Statista,» [Online]. Available: https://www.statista.com/statistics/264699/worldwide-co2-emissions/.

[12] «United Nations/Framework Convention on Climate Change 21st Conf parties,» Paris, 2015.

[13] A. Valero, A. Valero, G. Calvo, A. Ortego, S. Ascaso e J. Palacios, «Global material requirements for the energy transition. An exergyflowanalysis of decarbonisation pathways,» *Energy,* vol. 159, pp. 1175 - 1184, 2018.

[14] J. Koornneef, P. Breevoort, C. Hamelinck, C. Hendriks, M. Hoogwijk, K.Koop, M. Koper, T. Dixon e A. Camps, «Global potential for biomass and carbon dioxide capture, transport and storage up to 2050,» *International Journal of Greenhouse Gas Control,* vol. 11, pp. 117 - 132, 2012.

[15] D. L.Coleman, «Transport infrastructure rationale for carbon dioxide capture & storage in the European Union to 2050,» *Energy Procedia,* vol. 1, n. 1, pp. 1673-1681, 2009.

[16] A. Valero, A. Valero, G. Calvo e A. Ortego, «Material bottlenecks in the future development of green technologies,» *Renewable and Sustainable Energy Reviews,* vol. 93, pp. 178 - 200, 2018.

[17] J. M. Cullen e J. M. Allwood, «Theoretical efficiency limits for energy conversion devices,» *Energy,* vol. 35, n. 5, pp. 2059-2069, May 2010.

[18] J. M. Cullen e J. M. Allwood, «The efficient use of energy: Tracing the global flow of energy from fuel to service,» *Energy Policy,* vol. 38, n. 1, pp. 75-81, January 2010.

[19] T. Kuroki, K. Kabeya, K. Makino, T. Kajihara, H. Kaibe, H. Hachiuma, H. Matsuno e A. Fujibayashi, «Thermoelectric Generation Using Waste Heat in Steel Works,» *Journal of Electronic Materials,* vol. 43, p. 2405–2410, 2014.

[20] A. Kumar, P. A. Vermeulen, B. J. Kooi, J. Rao, L. v. Eijck, S. Schwarzmüller, O. Oeckler e G. R. Blake, «Phase Transitions of Thermoelectric TAGS-85,» *Inorganic Chemistry,* vol. 56, pp. 15091 - 15100, 2017.

[21] K. Peng, Z. Zhou, H. Wang, H. Wu, J. Ying, G. Han, X. Lu, G. Wang, X. Zhou e X. Chen, «Exceptional Performance Driven by Planar Honeycomb Structure in a New High Temperature Thermoelectric Material BaAgAs,» *Advanced Functional Materials,* vol. 31, pp. 2100583 - 2100592, 2021.

[22] Y. Pei, H. Wu, J. Sui, J. Li, D. Berardan, C. Barreteau, L. Pan, N. Dragoe, W. Liu, J. He e L. Zhao, «High thermoelectric performance in n-type BiAgSeS due to intrinsically low thermal conductivity,» *Energy & Enviromental Science,* n. 6, pp. 1750 - 1755, 2013.

[23] T. J. Seebeck, Ueber den magnetismus der galvenische kette, Berlin: Wentworth Press, 1821.

[24] T. J. Seebeck, Ueber die magnetische Polarisation der Metalle und Erze durch Temperaturdifferenz, Berlin, 1823.

[25] «wikipedia.org,» [Online].

[26] L. E. Bell, «Cooling, Heating, Generating Power, and Recovering Waste Heat with Thermoelectric Systems,» *Science,* vol. 321, pp. 1457-1461, September 2008.

[27] O. Bubnova e X. Crispin, «Towards polymer-based organic thermoelectric generators,» *Energy & Environmental Science,* vol. 5, n. 11, pp. 9345 - 9362, October 2012.

[28] J. C. A. Peltier, Nouvelles experiences sur la caloricit´e des courants electrique, Paris: Bailly, 1834.

[29] Y. G. Gurevich e J. E. Velazquez-Perez, «Peltier Effect in Semiconductors,» in *Wiley Encyclopedia of Electrical and Electronics Engineering*, J. Webster, 2014, pp. 1-21.

[30] W. Thompson, «On a Mechanical Theory of Thermo-Electric Currents,» *Proceedings of the Royal Society of Edinburgh,* vol. 3, pp. 91 - 98, 1857.

[31] W. Thompson, «Account of Researches in Thermo-Electricity,» *Proceedings of the Royal Society of London,* vol. 7, pp. 49 - 58, 1854.

[32] W. Thompson, On the electro-dynamic qualities of metals:—Effects of magnetization on the electric conductivity of nickel and of iron, vol. 8, London: Royal Society, 1857.

[33] L. Onsager, «Reciprocal Relations in Irreversible Processes. I.,» *Physical Review,* vol. 37, p. 405, 1931.

[34] L. Onsager, «Reciprocal Relations in Irreversible Processes. II.,» *Physical Review,* vol. 38, p. 2265, 1931.

[35] H. B. Callen, «The Application of Onsager's Reciprocal Relations to Thermoelectric, Thermomagnetic, and Galvanomagnetic Effects,» *Physical Review,* vol. 73, p. 1349, 1948.

[36] «www.nobelprize.org,» [Online].

[37] C. B. Vinning, «The thermoelectric process,» in *Materials Research Society Symposium Proceedings*, Auburn, 1997.

[38] H. Ibach e H. Luth, Solid-State Physics: An introduction to principles of materials science, 3 a cura di, Berlin: Springer-Verlag, 2003.

[39] C. Goupil e M. Tadashi, Thermodynamics of Thermoelectricity, Thermodynamics, IntechOpen, 2011.

[40] C. Goupil, «Thermodynamics of the thermoelectric potential,» *Journal of Applied Physics,* vol. 106, p. 104907, 2009.

[41] A. Feldhoff, «Thermoelectric Material Tensor Derived from the Onsager–de Groot–Callen Model,» *Energy Harvesting and Systems,* vol. 2, n. 1, pp. 5 - 13, 2015.

[42] G. J. Snyder e T. S. Ursell, «Thermoelectric Efficiency and Compatibility,» *Physical Review Letters,* vol. 91, n. 14, pp. 148301-1, 2003.

[43] G. J. Snyder e A. H. Snyder, «Figure of merit ZT of a thermoelectric device defined from materials properties,» *Energy & Environmental Science,* vol. 10, n. 11, pp. 2280-2283, 2017.

[44] G. Benenti, G. Casati, K. Saito e R. S.Whitneye, «Fundamental aspects of steady-state conversion of heat to work at the nanoscale,» *Physics Reports,* vol. 694, pp. 1 - 124, 2017.

[45] M. N. Hasan, H. Wahid, N. Nayan e M. S. M. Ali, «Inorganic thermoelectric materials: A review,» *Energy research,* vol. 44, n. 8, pp. 6170-6222, 2020.

[46] M. Cutler, J. F. Leavy e R. L. FitzPatrick, «Electronic Transport in Semimetallic Cerium Sulfide,» *Physical Review,* vol. 133, n. 4A, pp. 1143 - 1152, February 1964.

[47] J. P. Heremans, C. M. Thrush, D. T. Morelli e M. C. Wu, «Thermoelectric Power of Bismuth Nanocomposites,» *Physical Review Letters,* vol. 88, n. 21, pp. 216801 - 216804, May 2002.

[48] G. J. Snyder e E. S. Toberer, «Complex thermoelectric materials,» *Nature Materials,* vol. 7, n. 2, pp. 105 - 114, February 2008.

[49] Q. Jin, S. Jiang, Y. Zhao, D. Wang, J. Qiu, D.-M. Tang, J. Tan, D.-M. Sun, P.-X. Hou, X.-Q. Chen, K. Tai, N. Gao, C. Liu, H.-M. Cheng e X. Jiang, «Flexible layer-structured Bi2Te3 thermoelectric on a carbon nanotube scaffold,» *Nature Materials,* vol. 18, n. 1, pp. 62 - 68, 2018.

[50] N. Hasan, H. Wahid, N. Nayan e M. S. M. Ali, «Inorganic thermoelectric materials: A review,» *International journal of Energy Research,* vol. 44, n. 8, pp. 6170 - 6222, 2020.

[51] B. Z. X. Ji, T. Tritt, J. Kolis e A. Kumbhar, «Solution-Chemical Syntheses of Nano-Structured Bi2Te3 and PbTe Thermoelectric Materials,» *Journal of Electronic Materials,* vol. 36, n. 7, pp. 721 - 726, 2007.

[52] A.Boyer e E.Cissé, «Properties of thin film thermoelectric materials: application to sensors using the Seebeck effect,» *Materials Science and Engineering: B,* vol. 13, n. 2, pp. 103 - 111, 1992.

[53] D. Beretta, N. Neophytou, J. M. Hodges, M. G. Kanatzidis, D. Narducci, M. Martin-Gonzalez, M. Beekman, B. Balke, G. Cerretti, W. Tremel, A. Zevalkink, A. I. Hofmann, C. Müller, B. Dörli, M. Campoy-Quiles e M. Caironi, «Thermoelectrics: From history, a window to the future,» *Materials Science and Engineering: R: Reports,* vol. 138, p. 100501, 2019.

[54] H. Jin, J. Li, J. Iocozzia, X. Zeng, P. Wei, C. Yang, N. Li, Z. Liu, J. H. He, T. Zhu, J. Wang, Z. Lin e S. Wang, «Hybrid Organic–Inorganic Thermoelectric Materials and Devices,» *Angewandte Chemie International Edition,* vol. 54, n. 43, pp. 15206-15226, 2019.

[55] T. Sun, B. Zhou, Q. Zheng, L. Wang, W. Jiang e G. J. Snyder, «Stretchable fabric generates electric power from woven thermoelectric fibers,» *Nature Communications,* vol. 11, p. 572, 2020.

[56] I. H. Eryilmaz, Y. Chen, G. Mattana e E. Orgiu, «Flexible organic thermoelectric generators,» *Organic Flexible Electronics,* pp. 335-351, 2021.

[57] B. Russ, A. Glaudell, J. J. Urban, M. L. Chabinyc e R. A. Segalman, «Organic thermoelectric materials for energy harvesting and temperature control,» *Nature Reviews Materials,* vol. 1, n. 10, pp. 1 - 14, August 2016.

[58] M. F. Sanad, A. E. Shalan, S. O. Abdellatif, E. S. A. Serea, M. S. Adly e M. A. Ahsan, «Thermoelectric Energy Harvesters: A Review of Recent Developments in Materials and Devices for Diferent Potential Applications,» *Topics in Current Chemistry,* vol. 378, n. 48, 2020.

[59] B. Zheng, Y. Liu, B. Zhan, Y. Lin, J. Lan e X. Yang, «Enhanced Thermoelectric Properties of BiCuSeO/Polyaniline Composites,» *Journal of Electronic Materials,* vol. 43, n. 9, p. pages3695–3700, 2014.

[60] B. Zheng, Y. Lin, J. Lan e X. Yang, «Thermoelectric Properties of Ca3Co4O9/Polyaniline Composites,» *Journal of Materials Science & Technology,* vol. 30, n. 4, pp. 423 - 426, 2014.

[61] Y. Li, Q. Zhao, Y.-G. Wang e K. Bi, «Synthesis and characterization of Bi2Te3/polyaniline composites,» *Materials Science in Semiconductor Processing,* vol. 14, n. 3-4, pp. 219 - 222, 2011.

[62] C. Meng, C. Liu e S. Fan, «A Promising Approach to Enhanced Thermoelectric Properties Using Carbon Nanotube Networks,» *Advanced Materials,* vol. 22, n. 4, pp. 535 - 359, 2010.

[63] H. Shirakawa, «The Discovery of Polyacetylene Film: The Dawning of an Era of Conducting Polymers (Nobel Lecture),» *Angewandte Chemie International Edition,* vol. 40, n. 14, pp. 2575 - 2580, 2001.

[64] H. Shirakawa, E. J. Louis, A. G. MacDiarmid, C. K. Chiang e A. J. Heeger, «Synthesis of electrically conducting organic polymers: halogen derivatives of polyacetylene, (CH)x,» *Journal of the Chemical Society, Chemical Communications,* n. 16, pp. 578 - 580, 1977.

[65] A. J. Heeger, «Semiconducting and Metallic Polymers: The Fourth Generation of Polymeric Materials,» *The Journal of Physical Chemistry B,* vol. 105, n. 36, pp. 8475 - 8491, August 2001.

[66] A. G. MacDiarmid, «"Synthetic Metals": A Novel Role for Organic Polymers (Nobel Lecture),» *Angewandte Chemie International Edition,* vol. 40, n. 14, pp. 2581 - 2590, July 2001.

[67] Y. Lu, J.-Y. Wang e J. Pei, «Strategies To Enhance the Conductivity of n-Type Polymer Thermoelectric Materials,» *Chemistry of Materials,* vol. 31, n. 17, pp. 6412 - 6423, 2019.

[68] S. Savagatrup, A. D. Printz, T. F. O'Connor, A. V. Zaretski e D. J. Lipomi, «Molecularly Stretchable Electronics,» *Chemistry of Materials,* vol. 26, n. 10, p. 3028 – 3041, 2014.

[69] S. E. Root, S. Savagatrup, A. D. Printz, D. Rodriquez e D. J. Lipomi, «Mechanical Properties of Organic Semiconductors for Stretchable, Highly Flexible, and Mechanically Robust Electronics,» *Chemical Reviews,* vol. 117, n. 9, p. 6467 – 6499, 2017.

[70] C. Ruiz, E. M. García-Frutos, G. Hennrich e B. Gómez-Lor, «Organic Semiconductors toward Electronic Devices: High Mobility and Easy Processability,» *The Journal of Physical Chemistry Letters,* vol. 3, n. 11, p. 1428 – 1436, 2012.

[71] I. Petsagkourakis, K. Tybrandt, X. Crispin, I. Ohkubo, N. Satoh e T. Mori, «Thermoelectric materials and applications for energy harvesting power generation,» *Science and Technology of Advanced Materials,* vol. 19, n. 7, p. 836 – 862, 2018.

[72] P. O. Morin, T. Buraa e M. Leclerc, «Realizing the full potential of conjugated polymers: innovation in polymer synthesis,» *Materials Horizons,* vol. 3, n. 1, pp. 11 - 20, 2016.

[73] K. Namsheer e S. R. Chandra, «Conducting polymers: a comprehensive review on recent advances in synthesis, properties and applications,» *RSC Adv.,* vol. 11, p. 5659, 2021.

[74] A. Facchetti, «Semiconductors for Organic Transistors,» *Materials Today,* vol. 10, n. 3, pp. 28 - 37, 2007.

[75] C. Tanase, P. W. M. B. e D. M. d. Leeuw, «Origin of the enhanced space-charge-limited current in poly(p-phenylene vinylene),» *Physical Review B,* vol. 70, n. 19, p. 193202, November 2004.

[76] L. Groenendaal, F. Jonas, D. Freitag, H. Pielartzik e J. R. Reynolds, «Poly(3,4-ethylenedioxythiophene) and Its Derivatives: Past, Present, and Future,» *Advanced Materials,* vol. 12, n. 7, pp. 481- 494, 2000.

[77] K. Lee, S. Cho, S. H. Park, A. J. Heeger, C. W. Lee e S. H. Lee, «Metallic transport in polyaniline,» *Nature,* vol. 441, n. 7089, pp. 65 - 68, 2006.

[78] I. Salzmann, G. Heimel, M. Oehzelt, S. Winkler e N. Koch, «Molecular Electrical Doping of Organic Semiconductors: Fundamental Mechanisms and Emerging Dopant Design Rules,» *Accounts of Chemical Research,* vol. 49, n. 3, p. 370–378, 2016.

[79] H. Méndez, G. Heimel, A. Opitz, K. Sauer, P. Barkowski, M. Oehzelt, J. Soeda, T. Okamoto, J. Takeya, J. B. Arlin, J. Y. Balandier, Y. Geerts, N. Koch e I. Salzmann, «Doping of Organic Semiconductors: Impact of Dopant Strength and Electronic Coupling,» *Angewandte Chemie International Edition,* vol. 52, n. 30, pp. 7751 - 7755, 2013.

[80] L. M. Cowen, J. Atoyo, M. J. Carnie, D. Baran e B. C. Schroeder, «Review—Organic Materials for Thermoelectric Energy Generation,» *ECS Journal of Solid State Science and Technology,* vol. 6, n. 3, pp. 3080 - 3088, January 2017.

[81] T. Le, Y. Kim e H. Yoon, «Electrical and Electrochemical Properties of Conducting Polymers,» *Polymers,* vol. 9, n. 4, p. 150, 2017.

[82] D. R. McCamey, S.-Y. P. S.-Y. Lee, J. M. Lupton e C. Boehme, «Spin-dependent dynamics of polaron pairs in organic semiconductors,» *Physical Review B,* vol. 82, p. 125206 , 2010.

[83] N. Lu, L. Li, D. Geng e M. Liu, «A review for polaron dependent charge transport in organic semiconductor,» *Organic Electronics,* vol. 61, pp. 223-234, 2018.

[84] V. I. Arkhipov, E. V. Emelianova, P. Heremans e H. Bässler, «Analytic model of carrier mobility in doped disordered organic semiconductors,» *Physical Review B,* vol. 72, n. 23, p. 235202, December 2005.

[85] D. Fazzi, S. Fabiano, T. Ruoko e K. Meerholza, «Polarons in p-conjugated ladder-type polymers: a broken symmetry density functional description,» *Journal of Materials Chemistry C,* vol. 7, p. 12876, 2019.

[86] H. Yan, Z. Chen, Y. Zheng, C. Newman, J. R. Quinn, F. Dötz, M. Kastler e A. Facchetti, «A high-mobility electron-transporting polymer for printed transistors,» *Nature,* vol. 457, n. 7230, pp. 679 - 687, February 2009.

[87] W. Zhang, J. Smith, S. E. Watkins, R. Gysel, M. McGehee, A. Salleo, J. Kirkpatrick, S. Ashraf, T. Anthopoulos, M. Heeney e I. McCulloch, «Indacenodithiophene Semiconducting Polymers for High-Performance, Air-Stable Transistors,» *Journal of the American Chemical Society,* vol. 132, n. 33, pp. 11437 - 11439, August 2010.

[88] J. Płocharski, W. Pukacki e S. Roth, «Electrical conductivity of iodine doped oriented polyacetylene,» *Synthetic Metals,* vol. 41, n. 1-2, pp. 133 - 136, 1991.

[89] R. L. Elsenbaumer, K. Y. Jen e R.Oboodi, «Processible and environmentally stable conducting polymers,» *Synthetic Metals,* vol. 15, n. 2-3, pp. 169 - 174, 1986.

[90] S. Hotta, «Electrochemical synthesis and spectroscopic study of poly(3-alkylthienylenes),» *Synthetic Metals,* vol. 22, n. 2, pp. 103 - 113, 1987.

[91] K. Hiraishi, A. Masuhara, H. Nakanishi, H. Oikawa e Y. Shinohara, «Evaluation of Thermoelectric Properties of Polythiophene Films Synthesized by Electrolytic Polymerization,» *Japanese Journal of Applied Physics,* vol. 48, p. 071501, 2009.

[92] G. Shi, S. Jin, G. Xue e C. Li, «A Conducting Polymer Film Stronger Than Aluminium,» *Science,* vol. 267, pp. 994 - 996, 1995.

[93] L. Zhou, Z. Q. Gao e H. Huang, «Poly-3-octylthiophene films with ultra high tensile strength and flexibility,» *Materials Letters,* vol. 37, pp. 182 - 186, 1998.

[94] Y. Hu, H. Shi, H. Song, C. Liu, J. Xu, L. Zhang e Q. Jiang, «Effects of a proton scavenger on the thermoelectric performance of free-standing polythiophene and its derivative films,» *Synthetic Metals,* vol. 181, n. 1, pp. 23 - 26, 2013.

[95] Y. Xuan, X. Liu, S. Desbief, P. Leclère, M. Fahlman, R. Lazzaroni, M. Berggren, J. Cornil, D. Emin e X. Crispin, «Thermoelectric properties of conducting polymers: The case of poly(3-hexylthiophene),» *Physical Review B,* vol. 82, p. 115454, 2010.

[96] «Two-dimensional charge transport in self-organized, high-mobility conjugated polymers,» *Nature,* vol. 401, pp. 685 - 689, 1999.

[97] D. T. Duong, C. Wang, E. Antono, M. F. Toney e A. Salleo, «The chemical and structural origin of efficient p-type dopingin P3HT,» *Organic Electronics,* vol. 14, pp. 1330 - 1336, 2013.

[98] E. F. Aziz, A. Vollmer, S. Eisebitt, W. Eberhardt, P. Pingel, D. Neher e N. Koch, «Localized Charge Transfer in a Molecularly Doped Conducting Polymer,» *Advanced Materials,* vol. 19, pp. 3257 - 3260, 2007.

[99] E. Lim, K. A. Peterson, G. M. Su e M. L. Chabinyc, «Thermoelectric Properties of Poly(3-hexylthiophene) (P3HT) Doped with 2,3,5,6-Tetrafluoro-7,7,8,8-tetracyanoquinodimethane (F4TCNQ) by Vapor-Phase Infiltration,» *Chemistry of Materials,* vol. 30, pp. 998 - 1010, 2018.

[100] Y. Xuan, X. Liu, S. Desbief, P. Leclère, M. Fahlman, R. Lazzaroni, M. Berggren, J. Cornil, D. Emin e X. Crispin, «Thermoelectric properties of conducting polymers: The case of poly(3-hexylthiophene),» *Physical Review B,* vol. 82, n. 11, p. 115454, 2010.

[101] Q. Zhang, Y. Sun, W. Xu e D. Zhu, «Thermoelectric energy from flexible P3HT films doped with a ferric salt of triflimide anions,» *Energy & Environmental Science,* vol. 5, n. 11, pp. 9639 - 9644, 2012.

[102] J. C. Bijleveld, A. P. Zoombelt, S. G. J. Mathijssen, M. M. Wienk, M. Turbiez, D. M. d. Leeuw e R. A. J. Janssen, «Poly(diketopyrrolopyrrole−terthiophene) for Ambipolar Logic and Photovoltaics,» *Journal of the American Chemical Society,* vol. 131, n. 46, p. 16616 – 16617, 2009.

[103] I. H. Jung, C. T. Hong, U.-H. Lee, Y. H. Kang, K.-S. Jang e S. Y. Cho, «High Thermoelectric Power Factor of a Diketopyrrolopyrrole-Based Low Bandgap Polymer via Finely Tuned Doping Engineering,» *Scientific Reports,* vol. 7, n. 1, p. 44704 , 2017.

[104] Q. Zhang, Y. Sun, W. Xu e D. Zhu, «What To Expect from Conducting Polymers on the Playground of Thermoelectricity: Lessons Learned from Four High-Mobility Polymeric Semiconductors,» *Macromolecules,* vol. 47, n. 2, p. 609 – 615, 2014.

[105] H. Li, M. E. DeCoster, R. M. Ireland, J. Song, P. E. Hopkins e H. E. Katz, «Modification of the Poly(bisdodecylquaterthiophene) Structure for High and Predominantly Nonionic Conductivity with Matched Dopants,» *Journal of the American Chemical Society,* vol. 139, n. 32, p. 11149 – 11157, 2017.

[106] K. Hiraishi, A. Masuhara, H. Nakanishi, H. Oikawa e Y. Shinohara, «Evaluation of Thermoelectric Properties of Polythiophene Films Synthesized by Electrolytic Polymerization,» *Japanese Journal of Applied Physics,* vol. 7, n. 48, p. 071501, 2009.

[107] A. M. Glaudell, J. E. Cochran, S. N. Patel e M. L. Chabinyc, «Impact of the Doping Method on Conductivity and Thermopower in Semiconducting Polythiophenes,» *Advanced Energy Materials,* vol. 5, n. 4, p. 1401072, 2015.

[108] S. N. Patel, A. M. Glaudell, K. A. Peterson, E. M. Thomas, K. A. O'Hara, E. Lim e M. L. Chabinyc, «Morphology controls the thermoelectric power factor of a doped semiconducting polymer,» *Science Advances,* vol. 3, n. 6, p. e1700434, 2017.

[109] F. Jonas e L. Schrader, «Conductive modifications of polymers with polypyrroles and polythiophenes,» *Synthetic Metals,* vol. 41, n. 3, pp. 831 - 836, 1991.

[110] J. E. McCarthy, C. A. Hanley, L. J. Brennan, V. G. Lambertini e Y. K. Gun'ko, «Fabrication of highly transparent and conducting PEDOT:PSS films using a formic acid treatment,» *Journal of Material Chemistry C,* vol. 2, n. 4, pp. 764 - 770, 2014.

[111] N. Rozlosnik, «New directions in medical biosensors employing poly(3,4-ethylenedioxy thiophene) derivative-based electrodes,» *Analytical and Bioanalytical Chemistry,* vol. 395, p. 637 – 645, 2009.

[112] R. A. GreenNigel, H. L. Gordon, G. W. Laura e A. P. Warren, «Conducting polymers for neural interfaces: Challenges in developingan effective long-term implant,» *Bio Materials,* vol. 29, p. 3393 – 3399, 2008.

[113] Y. Wen e J. Xu, «Scientific Importance of Water-Processable PEDOT–PSS and Preparation, Challenge and New Application in Sensors of Its Film Electrode: A Review,» *Polymer Chemistry,* vol. 55, pp. 1121 - 1150, 2017.

[114] H. Yao, Z. Fan, H. Cheng, X. Guan, C. Wang, K. Sun e J. Ouyang, «Recent Development of Thermoelectric Polymers,» *Macromolecular Rapid Communications,* vol. 39, n. 6, p. 1700727, 2018.

[115] K. Sun, S. Zhang, P. Li, Y. Xia, X. Zhang, D. Du, F. H. Isikgor e J. Ouyang, «Review on application of PEDOTs and PEDOT:PSS in energy conversion and storage devices,» *Journal of Materials Science: Materials in Electronics ,* vol. 26, p. 4438 – 4462, 2015.

[116] M. Z. Cetin e P. Camurlu, «An amperometric glucose biosensor based on PEDOT nanofibers,» *RCS Advances,* vol. 8, n. 35, pp. 19724 - 19731, 2018.

[117] Q. Pei, G. Zuccarello, M. Ahlskog e O. Inganäs, «Electrochromic and highly stable poly(3,4-ethylenedioxythiophene) switches between opaque blue-black and transparent sky blue,» *Polymer,* vol. 35, n. 7, pp. 1347 - 1351, 1994.

[118] M. Culebras, C. M. Gómeza e A. Cantarero, «Enhanced thermoelectric performance of PEDOT with different counter-ions optimized by chemical reduction,» *Journal of Materials Chemistry A,* vol. 2, n. 26, pp. 10109 - 10115, 2014.

[119] J. Štulík, R. Polanský, A. Hamáček, S. Nešpůrek, P. Slepička, Z. Kolská e V. Švorčík, «Comparison of organic thermistors based on PEDOT:PSS and PEDOT:tos thin films under various thermal and humidity conditions,» *Sensors and Actuators B: Chemical,* vol. 275, pp. 359 - 366, 2018.

[120] M. Bharti, A. Singh, S. Samanta e D. K. Aswal, «Conductive polymers for thermoelectric power generation,» *Progress in Materials Science,* vol. 93, pp. 270-310, 2018.

[121] L. Huang, Z. Hu, K. Zhang, P. Chen e Y. Zhu, «Dip-coating of poly(3,4-ethylenedioxythiophene):poly(styrenesulfonate) anodes for efficient polymer solar cells,» *Thin Solid Films,* vol. 578, pp. 161 - 166, 2015.

[122] F. Elya, C. O. Avellaneda, P. Paredez, V. C. Nogueira, T. Santos, V. Mammana, C. Molina, J. Brug, G. Gibson e L. Zhao, «Patterning quality control of inkjet printed PEDOT:PSS films by wetting properties,» *Synthetic Metals,* vol. 161, n. 19-20, pp. 2129 - 2134, 2011.

[123] T. C. Li e R. C. Chang, «Improving the performance of ITO thin films by coating PEDOT:PSS,» *International Journal of Precision Engineering and Manufacturing-Green Technology,* vol. 1, n. 4, p. 329 – 334, 2014.

[124] S. Jönsson, J. Birgerson, X. Crispin, G. Greczynski, W. Osikowicz, A. Denier van der Gon, W. Salaneck e M. Fahlman, «The effects of solvents on the morphology and sheet resistance in poly(3,4-ethylenedioxythiophene)–polystyrenesulfonic acid (PEDOT–PSS) films,» vol. 139, n. 1, pp. 1 - 10, 2003.

[125] A. Elschner, S. Kirchmeyer, W. Lovenich, U. Merker e K. Reuter, PEDOT: Principles and Application of an Intrinsically Conductive Polymer, T. &. F. Group, A cura di, CRC Press, 2010.

[126] J. Xiong, F. Jiang, W. Zhou, C. Liu e J. Xu, «Highly electrical and thermoelectric properties of a PEDOT:PSS thin-film via direct dilution–filtration,» *RCS Advances,* vol. 5, n. 75, pp. 60708 - 60712, 2015.

[127] O. Bubnova, M. Berggren e X. Crispin, «Tuning the Thermoelectric Properties of Conducting Polymers in an Electrochemical Transistor,» *Journal of the American Chemical Society,* vol. 134, n. 40, p. 16456 – 16459, 2012.

[128] S. H. Lee, H. Park, W. Son, H. H. Choi e J. H. Kim, «Novel solution-processable, dedoped semiconductors for application in thermoelectric devices,» *Journal of Materials Chemistry A,* vol. 2, n. 33, pp. 13380 - 13387, 2014.

[129] N. Massonnet, A. Carella, O. Jaudouin, P. Rannou, G. Laval, C. Cellea e J.-P. Simonato*a, «Improvement of the Seebeck coefficient of PEDOT:PSS by chemical reduction combined with a novel method for its transfer using free-standing thin films,» *Journal of Materials Chemistry C,* vol. 2, n. 7, pp. 1278 - 1283, 2014.

[130] J. Ouyang, «''Secondary doping'' methods to significantly enhance the conductivityof PEDOT:PSS for its application as transparent electrode of optoelectronic devices,» *Displays,* vol. 34, n. 5, pp. 423 - 436, 2013.

[131] J. Kim, J. Jung, D. Lee e J. Joo, «Enhancement of electrical conductivity of poly(3,4-ethylenedioxythiophene)/poly(4-styrenesulfonate) by a change of solvents,» *Synthetic Metals,* vol. 126, n. 2-3, pp. 311 - 316, 2002.

[132] M. Scholdt, H. Do, J. Lang, A. Gall, A. Colsmann, U. Lemmer, J. D. Koenig, M. Winkler e H. Boettner, «Organic Semiconductors for Thermoelectric Applications,» *Journal of Electronic Materials volume,* vol. 39, n. 9, p. 1589 – 1592, 2010.

[133] C. Yi, A. Wilhite, L. Zhang, R. Hu, S. S. C. Chuang, J. Zheng e X. Gong, «Enhanced Thermoelectric Properties of Poly(3,4-ethylenedioxythiophene):poly(styrenesulfonate) by Binary Secondary Dopants,» *ACS Applied Materials & Interfaces,* vol. 7, n. 17, pp. 8984 - 8989, 2015.

[134] D. A. Mengistie, C.-H. Chen, K. M. Boopathi, F. W. Pranoto, L.-J. Li e C.-W. Chu, «Enhanced Thermoelectric Performance of PEDOT:PSS Flexible Bulky Papers by Treatment with Secondary Dopants,» *ACS Applied Materials & Interfaces,* vol. 7, n. 1, pp. 94 - 100, 2015.

[135] Y. Lin, P. Cheng, Y. Li e X. Zhan, «A 3D star-shaped non-fullerene acceptor for solution-processed organic solar cells with a high open-circuit voltage of 1.18 V,» *Chemical Communications,* vol. 48, n. 39, pp. 4773 - 4775, 2012.

[136] Z. Fan, D. Du, Z. Yu, P. Li, Y. Xia e J. Ouyang, «Significant Enhancement in the Thermoelectric Properties of PEDOT:PSS Films through a Treatment with Organic Solutions of Inorganic Salts,» *ACS Applied Materials & Interfaces,* vol. 8, n. 35, p. 23204 – 23211, 2016.

[137] T.-C. Tsai, H.-C. Chang, C.-H. Chen e W.-T. Whang, «Widely variable Seebeck coefficient and enhanced thermoelectric power of PEDOT:PSS films by blending thermal decomposable ammonium formate,» *Organic Electronics,* vol. 12, n. 12, pp. 2159 - 2164, 2011.

[138] J. Luo, D. Billep, T. Waechtler, T. Otto, M. Toader, O. Gordan, E. Sheremet, J. Martin, M. Hietschold, D. R. T. Zahnd e T. Gessnerab, «Enhancement of the thermoelectric properties of PEDOT:PSS thin films by post-treatment,» *Journal of Materials Chemistry A,* vol. 1, n. 26, pp. 7576 - 7583, 2013.

[139] T.-C. Tsai, H.-C. Chang, C.-H. Chen, Y.-C. Huang e W.-T. Whang, «A facile dedoping approach for effectively tuning thermoelectricity and acidity of PEDOT:PSS films,» *Organic Electronics,* vol. 15, n. 3, pp. 641 - 645, 2014.

[140] H. Park, S. H. Lee, F. S. Kim, H. H. Choi, I. W. Cheongc e J. H. Kim, «Enhanced thermoelectric properties of PEDOT:PSS nanofilms by a chemical dedoping process,» *Journal of Materials Chemistry A,* vol. 2, n. 18, pp. 6532 - 6539, 2014.

[141] S. H. Lee, H. Park, S. Kim, W. Son, I. W. Cheong e J. H. Kim, «Transparent and flexible organic semiconductor nanofilms with enhanced thermoelectric efficiency,» *Journal of Materials Chemistry A,* vol. 2, n. 20, pp. 7288 - 7294, 2014.

[142] Z. Fan, P. Li, D. Du e J. Ouyang, «Significantly Enhanced Thermoelectric Properties of PEDOT:PSS Films through Sequential Post-Treatments with Common Acids and Bases,» *Advanced Energy Materials,* vol. 7, n. 8, p. 1602116, 2017.

[143] I. Petsagkourakis, E. Pavlopoulou, G. Portale, B. A. Kuropatwa, S. Dilhaire, G. Fleury e G. Hadziioannou, «Structurally-driven Enhancement of Thermoelectric Properties within Poly(3,4-ethylenedioxythiophene) thin Films,» *Scientific Reports,* vol. 6, n. 1, p. 30501, 2016.

[144] C. Yi, L. Zhang, R. Hu, S. S. C. Chuang, J. Zheng e X. Gong, «Highly electrically conductive polyethylenedioxythiophene thin films for thermoelectric applications,» *Journal of Materials Chemistry A,* vol. 4, n. 33, pp. 12730 - 12738, 2016.

[145] Y. H. Lee, J. Oh, S.-S. Lee, H. Kim e J. G. Son, «Highly Ordered Nanoconfinement Effect from Evaporation-Induced Self-Assembly of Block Copolymers on In Situ Polymerized PEDOT:Tos,» *ACS Macro Letters,* vol. 6, n. 4, p. 386 – 392, 2017.

[146] T. Park, C. Park, B. Kim, H. Shina e E. Kim, «Flexible PEDOT electrodes with large thermoelectric power factors to generate electricity by the touch of fingertips,» *Energy & Environmental Science,* vol. 6, n. 3, pp. 788 - 792, 2013.

[147] O. Bubnova, Z. U. Khan, A. Malti, S. Braun, M. Fahlman, M. Berggren e X. Crispin, «Optimization of the thermoelectric figure of merit in the conducting polymer poly(3,4-ethylenedioxythiophene),» *Nature Materials,* vol. 10, n. 6, p. 429 – 433, 2011.

[148] Z. U. Khan, O. Bubnova, M. J. Jafari, R. Brooke, X. Liu, R. Gabrielsson, T. Ederth, D. R. Evans, J. W. Andreasen, M. Fahlmanc e X. Crispin, «Acido-basic control of the thermoelectric properties of poly(3,4-ethylenedioxythiophene)tosylate (PEDOT-Tos) thin films,» *Journal of Materials Chemistry C,* vol. 3, n. 40, pp. 10616 - 10623, 2015.

[149] J. Wanga, K. Caia e S. Shenb, «A facile chemical reduction approach for effectively tuning thermoelectric properties of PEDOT films,» *Organic Electronics,* vol. 17, pp. 151 - 158, 2015.

[150] J. Wangab, K. Cai, H. Songa e S. Shenc, «Simultaneously enhanced electrical conductivity and Seebeck coefficient in Poly (3,4-ethylenedioxythiophene) films treated with hydroiodic acid,» *Synthetic Metals,* vol. 220, pp. 585 - 589, 2016.

[151] S. Bhadra, N. K. Singha e D. Khastgir, «Electrochemical synthesis of polyaniline and its comparison with chemically synthesized polyaniline,» *Journal of Applied Polymer Science,* vol. 104, n. 3, p. 1900 – 1904, 2007.

[152] Y. Yang, S. Chen e L. Xu, «Enhanced Conductivity of Polyaniline by Conjugated Crosslinking,» *Macromolecular Rapid Communications,* vol. 32, n. 7, pp. 593 - 597, 2011.

[153] J. Li, X. Tang, H. Li, Y. Yan e Q. Zhang, «Synthesis and thermoelectric properties of hydrochloric acid-doped polyaniline,» *Synthetic Metals,* vol. 160, n. 11-12, pp. 1153 - 1158, 2010.

[154] G. Qi, L. Huang e H. Wang, «Highly conductive free standing polypyrrole films prepared by freezing interfacial polymerization,» *Chemical Communications,* vol. 48, n. 66, pp. 8246 - 8248, 2012.

[155] N. T. Kemp, A. B. Kaiser, C. Liu, B. Chapman, O. Mercier, A. M. Carr, H. J. Trodahl, R. G. Buckley, A. C. Partridge, J. Y. Lee, C. Y. Kim, A. Bartl, L. Dunsch, W. T. Smith e J. S. Shapiro, «Thermoelectric power and conductivity of different types of polypyrrole,» *Journal of Polymer Science Part B: Polymer Physics,* vol. 37, n. 9, pp. 953 - 960, 1999.

[156] S. Wakim, B. Aïch, Y. Tao e M. Leclerc, «Charge Transport, Photovoltaic, and Thermoelectric Properties of Poly(2,7-Carbazole) and Poly(Indolo[3,2-b]Carbazole) Derivatives,» *Polymer Reviews,* vol. 48, n. 3, pp. 432 - 462, 2008.

[157] R. B. Aïch, N. Blouin, A. Bouchard e M. Leclerc, «Electrical and Thermoelectric Properties of Poly(2,7-Carbazole) Derivatives,» *Chemistry of Materials,* vol. 21, n. 4, p. 751 – 757, 2009.

[158] D.M.deLeeuw, M.M.J.Simenon, A.R.Brown e R.E.F.Einerhand, «Stability of n-type doped conducting polymers and consequences for polymeric microelectronic devices,» *Synthetic Metals,* vol. 87, pp. 53 - 59, 1997.

[159] X. Zhan, A. Facchetti, S. Barlow, T. J. Marks, M. A. Ratner, M. R. Wasielewski e S. R. Marder, «Rylene and Related Diimides for Organic Electronics,» *Advanced Materials,* vol. 23, pp. 268 - 284, 2011.

[160] S. Griggs, A. Marks, H. Bristowa e I. McCulloch, «n-Type organic semiconducting polymers: stability limitations, design considerations and applications,» *Journal of Materials Chemistry C,* vol. 9, p. 8099, 2021.

[161] A. Nollau, M. Pfeiffer, T. Fritz e K. Leo, «Controlled n-type doping of a molecular organic semiconductor: Naphthalenetetracarboxylic dianhydride (NTCDA) doped with bis(ethylenedithio)-tetrathiafulvalene (BEDT-TTF),» *Journal of Applied Physics,* vol. 87, n. 9, pp. 4340 - 4343, 2000.

[162] R. Schmidt, J. H. Oh, Y.-S. Sun, M. Deppisch, A.-M. Krause, K. Radacki, H. Braunschweig, M. Könemann, P. Erk, Z. Bao e F. Würthner, «High-Performance Air-Stable n-Channel Organic Thin Film Transistors Based on Halogenated Perylene Bisimide Semiconductors,» *Journal of the American Chemical Society,* vol. 131, n. 14, p. 6215 – 6228, 2009.

[163] Y. Fukutomi, M. Nakano, J.-Y. Hu, I. Osaka e K. Takimiya, «Naphthodithiophenediimide (NDTI): Synthesis, Structure, and Applications,» *Journal of the American Chemical Society,* vol. 135, n. 31, p. 11445 – 11448, 2013.

[164] M. Torben, R. Debdutta, M. Jan, L. Karl e R. Moritz, «n-situ conductivity and Seebeck measurements of highly efficient n-dopants in fullerene C60,» vol. 100, n. 9, p. 093304, 2012.

[165] N. Tea, R.-C. Yu, M. Salamon, D. Lorents, R. Malhotra e R. Ruoff, «Thermal conductivity of C60 and C70 crystals,» *Applied Physics A,* vol. 56, n. 3, pp. 219 - 225, 1993.

[166] B. Malhotra e M. A. Ali, Nanomaterials for Biosensors: Fundamentals and Applications, 2017, pp. 75 - 103.

[167] R. C. Haddon, A. F. Hebard, M. J. Rosseinsky, D. W. Murphy, S. J. Duclos, K. B. Lyons, B. Miller, J. M. Rosamilia, R. M. Fleming, A. R. Kortan, S. H. Glarum, A. V. Makhija, A. J. Muller, R. H. Eick, S. M. Zahurak, R. Tycko, G. Dabbagh e F. A. Thiel, «Conducting films of C60 and C70 by alkali-metal doping,» *Nature,* vol. 350, n. 6316, pp. 320 - 322, 1991.

[168] M. Sumino, K. Harada, M. Ikeda, S. Tanaka, K. Miyazaki e C. Adachi, «Thermoelectric properties of n-type C60 thin films and their application in organic thermovoltaic devices,» vol. 99, n. 9, p. 093308, 2011.

[169] S. Guo, S. B. Kim, S. K. Mohapatra, Y. Qi, T. Sajoto, A. Kahn, S. R. Marder e S. Barlow, «n-Doping of Organic Electronic Materials using Air-Stable Organometallics,» *Advanced Materials,* vol. 24, n. 5, pp. 699 - 703, 2011.

[170] B. D. Naab, S. Guo, S. Olthof, E. G. B. Evans, P. Wei, G. L. Millhauser, A. Kahn, S. Barlow, S. R. Marder e Z. Bao, «Mechanistic Study on the Solution-Phase n-Doping of 1,3-Dimethyl-2-aryl-2,3-dihydro-1H-benzoimidazole Derivatives,» *Journal of the American Chemical Society,* vol. 135, n. 40, pp. 15018 - 15025, 2013.

[171] P. Wei, J. H. Oh, G. Dong e Z. Bao, «Use of a 1H-Benzoimidazole Derivative as an n-Type Dopant and To Enable Air-Stable Solution-Processed n-Channel Organic Thin-Film Transistors,» *Journal of the American Chemical Society,* vol. 132, n. 26, pp. 8852 - 8853, 2010.

[172] J. Liu, B. Zee, R. Alessandri, S. Sami, J. Dong, M. I. Nugraha, A. J. Barker, S. Rousseva, L. Qiu, X. Qiu, N. Klasen, R. C. Chiechi, D. Baran, M. Caironi, T. D. Anthopoulos, R. W. A. H. G. Portale, S. J. Marrink, J. C. Hummelen e L. J. A. Koster, «N-type organic thermoelectrics: demonstration of zT > 0.3,» *Nature Communications,* vol. 11, p. 5694 , 2020.

[173] J. H. Burroughes, D. D. C. Bradley, A. R. Brown, R. N. Marks, K. Mackay, R. H. Friend, P. L. Burns e A. B. Holmes, «Light-emitting diodes based on conjugated polymers,» *Nature,* vol. 347, n. 6293, p. 539–541, 1990.

[174] G. Yu, J. Gao, J. C. Hummelen, F. Wudl e A. J. Heeger, «Polymer Photovoltaic Cells: Enhanced Efficiencies via a Network of Internal Donor-Acceptor Heterojunctions,» *Science,* vol. 270, n. 5243, pp. 1789 - 1791, 1995.

[175] L.-L. Chua, J. Zaumseil, J.-F. Chang, E. C.-W. Ou, P. K.-H. Ho, H. Sirringhaus e R. H. Friend, «General observation of n-type field-effect behaviour in organic semiconductors,» *Nature,* vol. 434, n. 7030, p. 194 – 199, 2005.

[176] T. Lei, J.-H. Dou, X.-Y. Cao, J.-Y. Wang, J e Pei, «Electron-Deficient Poly(p-phenylene vinylene) Provides Electron Mobility over 1 cm2 V–1 s–1 under Ambient Conditions,» *Journal of the American Chemical Society,* vol. 135, n. 33, p. 12168 – 12171, 2013.

[177] H. Un, S. A. Gregory, S. K. Mohapatra, M. Xiong, E. Longhi, Y. Lu, S. Rigin, S. Jhulki, C.-Y. Yang, T. V. Timofeeva, J.-Y. Wang, S. K. Yee, S. Barlow, S. R. Marder e J. Pei, «Understanding the Effects of Molecular Dopant on n-Type,» *Advanced Energy Materials,* vol. 9, n. 24, p. 1900817, 2019.

[178] Y. Sun, P. Sheng, C. Di, F. Jiao, W. Xu, D. Qiu e D. Zhu, «Organic Thermoelectric Materials and Devices Based on p - and n -Type Poly(metal 1,1,2,2-ethenetetrathiolate),» *Advanced Materials,* vol. 24, n. 7, 2012.

[179] a. F. Z. Yuanhui Sun, Y. Sun, C. Di, W. Xu e D. Zhu, «n-Type thermoelectric materials based on CuTCNQ nanocrystals and CuTCNQ nanorod arrays,» *Journal of Materials Chemistry A,* vol. 3, n. 6, pp. 2677 - 2683, 2015.

[180] D. Shukla, S. F. Nelson, D. C. Freeman, M. Rajeswaran, W. G. Ahearn, D. M. Meyer e J. T. Carey, «Thin-Film Morphology Control in Naphthalene-Diimide-Based Semiconductors: High Mobility n-Type Semiconductor for Organic Thin-Film Transistors,» *Chemistry of Materials,* vol. 20, n. 24, p. 7486 – 7491, 2008.

[181] T. Kakinuma, H. Kojima, M. Ashizawa, H. Matsumotoa e T. Mori, «Correlation of mobility and molecular packing in organic transistors based on cycloalkyl naphthalene diimide,» *Journal of Materials Chemistry C,* vol. 1, n. 34, pp. 5395 - 5401, 2013.

[182] H. E. Katz, J. Johnson, A. J. Lovinger e W. Li, «Naphthalenetetracarboxylic Diimide-Based n-Channel Transistor Semiconductors: Structural Variation and Thiol-Enhanced Gold Contacts,» *Journal American Chemistry Society,* vol. 122, n. 32, p. 7787 – 7792, 2000.

[183] M. Nakano, D. Hashizume e K. Takimiya, «N,N'-Bis(2-cyclohexylethyl)naphtho[2,3-b:6,7-b']dithiophene Diimides: Effects of Substituents,» *Molecules,* vol. 21, n. 8, p. 981, 2016.

[184] M. Nakano, I. Osaka, D. Hashizume e K. Takimiya, «α-Modified Naphthodithiophene Diimides - Molecular Design Strategy for Air-Stable n-Channel Organic Semiconductors,» *Chemistry of Materials,* vol. 27, n. 18, pp. 6418 - 6425, 2015.

[185] X. Zhan, A. Facchetti, S. Barlow, T. J. Marks, M. A. Ratner, M. R. Wasielewski e S. R. Marder, «Rylene and Related Diimides for Organic Electronics,» vol. 23, n. 2, pp. 268 - 284, 2011.

[186] B. Russ, M. J. Robb, B. C. Popere, E. E. Perry, C.-K. Mai, S. L. Fronk, S. N. Patel, T. E. Mates, G. C. Bazan, J. J. Urban, M. L. Chabinyc, C. J. Hawker e R. A. Segalman, «Tethered tertiary amines as solid-state n-type dopants for solution-processable organic semiconductors,» *Chemical Science,* vol. 7, n. 3, pp. 1914 - 1919, 2016.

[187] T. H. Reilly, A. W. Hains, H. Chen e B. A. Gregg, «A Self-Doping, O2-Stable, n-Type Interfacial Layer for Organic Electronics,» *Advanced Energy Materials,* vol. 2, n. 4, pp. 455 - 460, 2012.

[188] B. Russ, M. J. Robb, F. G. Brunetti, P. L. Miller, E. E. Perry, S. N. Patel, V. H. W. Segalman, B. C. Jeffrey, J. Urban, M. L. Chabinyc, C. J. Hawker e R. A. Segalman, «Power Factor Enhancement in Solution-Processed Organic n-Type Thermoelectrics Through Molecular Design,» vol. 26, n. 21, pp. 3473 - 3477, 2014.

[189] B. D. Naab, X. Gu, T. Kurosawa, J. W. F. To, A. Salleo e Z. Bao, «Role of Polymer Structure on the Conductivity of N-Doped Polymers,» *Advanced Electronic Materials,* vol. 2, n. 5, p. 1600004, 2016.

[190] Z. Chen, Y. Zheng, H. Yan e A. Facchetti, «Naphthalenedicarboximide- vs Perylenedicarboximide-Based Copolymers. Synthesis and Semiconducting Properties in Bottom-Gate N-Channel Organic Transistors,» *Journal of the American Chemical Society,* vol. 131, n. 1, pp. 8 - 9, 2009.

[191] A. Sanzone, S. Cimò, S. Mattiello, R. Ruffo, I. Facchinetti, G. E. Bonacchini, M. Caironi, M. Sassi, M. Sommer e L. Beverina, «Preparation of Naphthalene Dianhydride Bithiophene Copolymers by Direct Arylation Polycondensation and the Latent Pigment Approach,» *Chem Plus Chem,* vol. 84, n. 9, pp. 1346 - 1352, 2019.

[192] N. J. Snoeij, A. A. J. V. Iersel, A. H. Penninks e W. Seinen, «Toxicity of triorganotin compounds: Comparative in vivo studies with a series of trialkyltin compounds and triphenyltin chloride in male rats,» *Toxicology and Applied Pharmacology,* vol. 81, n. 2, pp. 274 - 286, 1985.

[193] V. Senkovskyy, R. Tkachov, H. Komber, M. Sommer, M. Heuken, B. Voit, W. T. S. Huck, V. Kataev, A. Petr e A. Kiriy, «Chain-Growth Polymerization of Unusual Anion-Radical Monomers Based on Naphthalene Diimide: A New Route to Well-Defined n-Type Conjugated Copolymers,» *Journal of the American Chemical Society,* vol. 133, n. 49, p. 19966 – 19970, 2011.

[194] A. Facchetti, L. Vaccaro e A. Marrocchi, «Semiconducting Polymers Prepared by Direct Arylation Polycondensation,» *Angewandte Chemie,* vol. 51, n. 15, pp. 3520 - 3523, 2012.

[195] R. Matsidik, H. Komber, A. Luzio, M. Caironi e M. Sommer, «Defect-free Naphthalene Diimide Bithiophene Copolymers with Controlled Molar Mass and High Performance via Direct Arylation Polycondensation,» *Journal of the American Chemical Society,* vol. 137, n. 20, pp. 6705 - 6711, 2015.

[196] E. Giussani, D. Fazzi, L. Brambilla, M. Caironi e C. Castiglioni, «Molecular Level Investigation of the Film Structure of a High Electron Mobility Copolymer via Vibrational Spectroscopy,» *Macromolecules,* vol. 46, n. 7, pp. 2658 - 2670, 2013.

[197] S. Wang, H. Sun, U. Ail, M. Vagin, P. O. Å. Persson, J. W. Andreasen, W. Thiel, M. Berggren, X. Crispin, D. Fazzi e S. Fabiano, «Thermoelectric Properties of Solution-Processed n-Doped Ladder-Type Conducting Polymers,» *Advanced Materials,* vol. 28, n. 48, pp. 10764 - 10771, 2016.

[198] C. J. Takacs, N. D. Treat, S. Krämer, Z. Chen, A. Facchetti, M. L. Chabinyc e A. J. Heeger, «Remarkable Order of a High-Performance Polymer,» *Nano Letters,* vol. 13, n. 6, p. 2522 – 2527, 2013.

[199] J. Rivnay, M. F. Toney, Y. Zheng, I. V. Kauvar, Z. Chen, V. Wagner, A. Facchetti e A. Salleo, «Unconventional Face-On Texture and Exceptional In-Plane Order of a High Mobility n-Type Polymer,» *Advanced Materials,* vol. 22, n. 39, pp. 4359 - 4363, 2010.

[200] J. Rivnay, R. Steyrleuthner, L. H. Jimison, A. Casadei, Z. Chen, M. F. Toney, A. Facchetti, D. Neher e A. Salleo, «Drastic Control of Texture in a High Performance n-Type Polymeric Semiconductor and Implications for Charge Transport,» *Macromolecules,* vol. 44, n. 13, pp. 5246 - 5255, 2011.

[201] K. Tremel, F. S. U. Fischer, N. Kayunkid, R. D. Pietro, R. Tkachov, A. Kiriy, D. Neher, S. Ludwigs e M. Brinkmann, «Charge Transport Anisotropy in Highly Oriented Thin Films of the Acceptor Polymer P(NDI2OD-T2),» *Advanced Energy Materials,* vol. 4, n. 10, p. 1301659, 2014.

[202] S. Fabiano, C. Musumeci, Z. Chen, A. Scandurra, H. Wang, Y. Loo, A. Facchetti e B. Pignataro, «From Monolayer to Multilayer N-Channel Polymeric Field-Effect Transistors with Precise Conformational Order,» *Advanced Materials,* vol. 24, n. 7, pp. 951 - 956, 2012.

[203] M. Brinkmann, E. Gonthier, S. Bogen, K. Tremel, S. Ludwigs, M. Hufnagel e M. Sommer§, «Segregated versus Mixed Interchain Stacking in Highly Oriented Films of Naphthalene Diimide Bithiophene Copolymers,» *ACS Nano,* vol. 6, n. 11, pp. 10319 - 10326, 2012.

[204] E. Giussani, L. Brambilla, D. Fazzi, M. Sommer, N. Kayunkid, M. Brinkmann e C. Castiglioni, «Structural Characterization of Highly Oriented Naphthalene-Diimide-Bithiophene Copolymer Films via Vibrational Spectroscopy,» *Physical Chemistry B,* vol. 119, n. 5, pp. 2062 - 2073, 2015.

[205] A. Lunzio, L. Criante, V. D'Innocenzo e M. Caironi, «Control of charge transport in a semiconducting copolymer by solvent-induced long-range order,» *Scientific Reports,* vol. 3, n. 1, p. 3425, 2013.

[206] Y. Qi, S. K. Mohapatra, S. B. Kim, S. Barlow, S. R. Marder e A. Kahn, «Solution doping of organic semiconductors using air-stable n-dopants,» *Applied Physics Letters,* vol. 100, n. 8, p. 083305, 2012.

[207] S. Fabiano, S. Braun, X. Liu, E. Weverberghs, P. Gerbaux, M. Fahlman, M. Berggren e X. Crispin, «Poly(ethylene imine) Impurities Induce n-doping Reaction in Organic (Semi)Conductors,» *Advanced Materials,* vol. 26, n. 34, pp. 6000 - 6006, 2014.

[208] R. A. Schlitz, F. G. Brunetti, A. M. Glaudell, P. L. Miller, M. A. Brady, C. J. Takacs, C. J. Hawker e M. L. Chabinyc, «Solubility-Limited Extrinsic n-Type Doping of a High Electron Mobility Polymer for Thermoelectric Applications,» *Advanced Materials,* vol. 26, n. 18, pp. 2825 - 2830, 2014.

[209] B. D. Naab, S. Zhang, K. Vandewal, A. Salleo, S. Barlow, S. R. Marder e Z. Bao, «Effective Solution- and Vacuum-Processed n-Doping by Dimers of Benzimidazoline Radicals,» *Advanced Materials,* vol. 26, n. 25, pp. 4268 - 4272, 2014.

[210] B. Saglio, M. Mura, M. Massetti, F. Scuratti, D. Beretta, X. Jiao, C. R. McNeill, M. Sommer, A. Famulari, G. Lanzani, M. Caironi e C. Bertarelli, «N-Alkyl substituted 1H-benzimidazoles as improved n-type dopants for a naphthalenediimide based copolymer,» *Journal of Materials Chemistry A,* vol. 6, n. 31, pp. 15294 - 15302, 2018.

[211] O. Bardagota, C. Aumaître, A. Monmagnon, J. Pécaut, P. A. Bayle e R. Demadrillea), «Revisiting doping mechanisms of n-type organic materials with N-DMBI for thermoelectric applications: Photo-activation, thermal activation, and air stability,» *Applied Physics Letters,* vol. 118, p. 203904, 2021.

[212] Y. Zeng, W. Zheng, Y. Guo, G. Hana e Y. Yi, «Doping mechanisms of N-DMBI-H for organic thermoelectrics: hydrogen removal vs. hydride transfer,» *Journal of Materials Chemistry A,* vol. 8, n. 17, pp. 8323 - 8328, 2020.

[213] S. Riera-Galindo, A. O. Biroli, A. Forni, Y. Puttisong, F. Tessore, M. Pizzotti, E. Pavlopoulou, E. Solano, S. Wang, G. Wang, T.-P. Ruoko, W. M. Chen, M. Kemerink, M. Berggren, G. d. Carlo e S. Fabiano, «Impact of Singly Occupied Molecular Orbital Energy on the n-Doping Efficiency of Benzimidazole Derivatives,» *ACS Applied Materials & Interfaces,* vol. 11, n. 41, p. 37981 – 37990, 2019.

[214] S. Wang, H. Sun, T. Erdmann, G. Wang, D. Fazzi, U. Lappan, Y. Puttisong, Z. Chen, M. Berggren, X. Crispin, A. Kiriy, B. Voit, T. J. Marks, S. Fabiano e A. Facchetti, «A Chemically Doped Naphthalenediimide-Bithiazole Polymer for n-Type Organic Thermoelectrics,» *Advanced Materials,* vol. 30, n. 31, p. 1801898, 2018.

[215] J. Liu, L. Qiu, R. Alessandri, X. Qiu, G. Portale, J. Dong, W. Talsma, G. Ye, A. A. Sengrian, P. C. T. Souza, M. A. Loi, R. C. Chiechi, S. J. Marrink, J. C. Hummelen e L. J. A. Koster, «Enhancing Molecular n-Type Doping of Donor–Acceptor Copolymers by Tailoring Side Chains,» *Advanced Materials,* vol. 30, n. 7, p. 1704630, 2018.

[216] A. Giovannitti, I. P. Maria, D. Hanifi, M. J. Donahue, D. Bryant, K. J. Barth, B. E. Makdah, A. Savva, D. Moia, M. Zetek, P. R. F. Barnes, O. G. Reid, S. Inal, G. Rumbles, G. G. Malliaras, J. Nelson, J. Rivnay e I.

McCulloch, «The Role of the Side Chain on the Performance of N-type Conjugated Polymers in Aqueous Electrolytes,» *Chemistry of Materials,* vol. 30, n. 9, p. 2945–2953, 2018.

[217] D. Kiefer, A. Giovannitti, H. Sun, T. Biskup, A. Hofmann, M. Koopmans, C. Cendra, S. Weber, L. J. A. Koster, E. Olsson, J. Rivnay, S. Fabiano, I. McCulloch e C. Müller, «Enhanced n-Doping Efficiency of a Naphthalenediimide-Based Copolymer through Polar Side Chains for Organic Thermoelectrics,» *ACS Energy Letters,* vol. 3, n. 2, pp. 278 - 285, 2018.

[218] J. Liu, G. Ye, B. v. d. Zee, J. Dong, X. Qiu, Y. Liu, G. Portale, R. C. Chiechi e L. J. A. Koster, «N-Type Organic Thermoelectrics of Donor–Acceptor Copolymers: Improved Power Factor by Molecular Tailoring of the Density of States,» *Advanced Materials,* vol. 30, n. 44, p. 1804290, 2018.

[219] D. Nava, Y. Shin, M. Massetti, X. Jiao, T. Biskup, M. S. Jagadeesh, A. Calloni, L. Duò, G. Lanzani, C. R. McNeill, M. Sommer e M. Caironi, «Drastic Improvement of Air Stability in an n-Type Doped Naphthalene-Diimide Polymer by Thionation,» *ACS Applied Energy Materials,* vol. 1, n. 9, pp. 4626 - 4634, 2018.

[220] I. Denti, S. Cimò, L. Brambilla, A. Milani, C. Bertarelli, M. Tommasini e C. Castiglioni, «Polaron Confinement in n-Doped P(NDI2OD-T2) Unveiled by Vibrational Spectroscopy,» *Chemistry of Materials,* vol. 31, n. 17, p. 6726 – 6739, 2019.

[221] R. M. Kluge, N. Saxena, W. Chen, V. Körstgens, M. Schwartzkopf, Q. Zhong, S. V. Roth e P. Müller-Buschbaum, «Doping Dependent In-Plane and Cross-Plane Thermoelectric Performance of Thin n-Type Polymer P(NDI2OD-T2) Films,» *Advanced Functional Materials,* vol. 30, n. 28, p. 2003092, 2020.

[222] J. Wang, Y. Liu, H. Li, S. Yan, X. Sun, D. Tu, X. Guo e Z. Ren, «Enhanced charge transport and thermoelectric performance of P(NDI2OD-T2) by epitaxial crystallization on highly oriented polyethylene substrates,» *Materials Chemistry Frontiers,* vol. 4, pp. 661 - 668, 2020.

[223] S. Riera-Galindo, A. O. Biroli, A. Forni, Y. Puttisong, F. Tessore, M. Pizzotti, E. Pavlopoulou, E. Solano, S. Wang, G. Wang, T.-P. Ruoko, W. M. Chen, M. Kemerink, M. Berggren, G. d. Carlo e S. Fabiano, «Impact of Singly Occupied Molecular Orbital Energy on the n-Doping Efficiency of Benzimidazole Derivatives,» *ACS Appl. Mater. Interfaces,* vol. 11, n. 41, p. 37981 – 37990, 2019.

[224] S. Wang, D. Fazzi, Y. Puttisong, M. J. Jafari, Z. Chen, T. Ederth, J. W. Andreasen, W. M. Chen, A. Facchetti e S. Fabiano, «Effect of Backbone Regiochemistry on Conductivity, Charge Density, and Polaron Structure of n-Doped Donor−Acceptor Polymers,» *Chemistry of Materials,* vol. 31, n. 9, pp. 3395 - 3406, 2019.

[225] Y. Shin, H. Komber, D. Caiola, M. Cassinelli, H. Sun, D. Stegerer, M. Schreiter, K. Horatz, F. Lissel, X. Jiao, C. R. McNeill, S. Cimò, C. Bertarelli, S. Fabiano, M. Caironi e M. Sommer, «Synthesis and Aggregation Behavior of a Glycolated Naphthalene,» *Macromolecules,* vol. 53, p. 5158−5168, 2020.

[226] S. Seiji e N. Takao, «Preparation of fluorescent compounds or their salts useful as detection agents for ionic compounds». Japan Brevetto JP 2016196447A, Nov 2016.

[227] J. National Institute of Advanced Industrial Science and Technology (AIST). [Online]. Available: https://sdbs.db.aist.go.jp/sdbs/cgi-bin/direct_frame_top.cgi.

[228] J. Zhou, J. Jin, Y. Zhang, Y. Yin, X.Chen e B. Xu, «Synthesis and antiproliferative evaluation of novel benzoimidazole-contained oxazole-bridged analogs of combretastatin A-4,» *European Journal of Medicinal Chemistry,* vol. 68, pp. 222 - 232, 2013.

[229] N. Elgrishi,́ . J. Rountree, B. D. McCarthy, E. S. Rountree, T. T. Eisenhart e J. L. Dempsey, «A Practical Beginner's Guide to Cyclic Voltammetry,» *Journal of Chemical Education,* vol. 95, pp. 197 - 206, 2018.

[230] I. Tochitsky, M. A. Kienzler, E. Isacoff e R. H. Kramer, «Restoring Vision to the Blind with Chemical Photoswitches,» *Chemical Reviews,* vol. 118, n. 21, p. 10748 – 10773, 2018.

[231] E. Merino, «Synthesis of azobenzenes: the coloured pieces of molecular materialsw,» *Chemical Society Reviews,* vol. 40, n. 7, pp. 3835 - 3853, 2011.

[232] M. A. Kienzler, A. Reiner, E. Trautman, S. Yoo, D. Trauner e E. Y. Isacoff, «A Red-Shifted, Fast-Relaxing Azobenzene Photoswitch for Visible Light Control of an Ionotropic Glutamate Receptor,» *Journal of the American Chemical Society,* vol. 135, p. 17683 − 17686, 2013.

[233] S. J. Brown, R. A. Schlitz, M. L. Chabinyc e J. A. Schuller, «Morphology-dependent optical anisotropies in the n-type polymer P(NDI2OD-T2),» *Physical Review B,* vol. 94, n. 16, p. 165105, 2016.

15. ACKNOWLEDGMENTS

Si ringrazia sentitamente la prof.ssa Chiara Bertarelli che mi ha dato la possibilità di portare avanti il mio percorso di dottorato presso il suo gruppo di ricerca. Desidero anche menzionare le mie colleghe Paola Moretti, Valentina Sesti e Alessia Arrigoni con cui ho condiviso gli spazi del laboratorio per molti mesi e che non si sono mai tirate indietro dall'aiutarmi, quando è stato necessario.

Un ringraziamento sentito va anche a Marco Cassinelli e Mario Caironi dell'Istituto Italiano di Tecnologia e alla prof.ssa Chiara Castiglioni, che mi hanno spesso aiutato con i loro preziosi pareri e consigli.

Una menzione speciale è dovuta anche a Ilaria Denti e Lorenzo Rossi, indispensabili compagni di interminabili ore di lavoro notturno, il cui aiuto è stato fondamentale alla stesura di questa tesi. In loro sono fiero di poter dire di aver trovato dei cari amici oltre che dei preziosi collaboratori.

Desidero ringraziare i miei genitori Francesca e Antonio, mio nonno Gaetano e mio fratello Fabrizio, che sono da sempre stati le solide fondamenta sulle quali cui ho potuto edificare tutta la mia vita.

Infine, desidero ringraziare la mia fidanzata Paola che più di ogni altra persona mi è stata accanto nei tanti momenti di gioia e di sconforto di cui è stata caratterizzata la mia carriera accademica. E' soprattutto grazie a lei, se sono riuscito a mantenere la rotta verso l'obbiettivo finale.